Imaging strategies for the detection of inflammation in atherosclerosis

Document status and date:
Published: 28/08/2020

Document Version:
Publisher's PDF, also known as Version of Record (includes final page, issue and volume numbers)

Please check the document version of this publication:

• A submitted manuscript is the version of the article upon submission and before peer-review. There can be important differences between the submitted version and the official published version of record. People interested in the research are advised to contact the author for the final version of the publication, or visit the DOI to the publisher's website.
• The final author version and the galley proof are versions of the publication after peer review.
• The final published version features the final layout of the paper including the volume, issue and page numbers.

[Link to publication](#)

Imaging Strategies for the Detection of Inflammation in Atherosclerosis

Esad Vucic, MD

PhD Thesis

Imaging Strategies for the Detection of Inflammation in Atherosclerosis

PROEFSCHRIFT

ter verkrijging van de graad van doctor aan de Technische Universiteit Eindhoven, op gezag van de rector magnificus prof.dr.ir. F.P.T. Baaijens, voor een commissie aangewezen door het College voor Promoties, in het openbaar te verdedigen op vrijdag 28 augustus 2020 om 16:00 uur

door

Esad Vucic

geboren te

Bar, Montenegro

Dit proefschrift is goedgekeurd door de promotoren en de samenstelling van de promotiecommissie is als volgt:

voorzitter:	prof.dr. M. Merkx
1e promotor:	prof.dr. W.J.M. Mulder
2e promotor:	prof.dr. Z.A. Fayad
copromotor(en):	dr. C. Calcagno
leden:	prof.dr.ir. Frans van der Vosse
	prof.dr. Tim Leiner (UMC Utrecht)
	prof.dr. Jan van Hest
	prof.dr.ir. G.J. Strijkers (Amsterdam UMC)
adviseur(s):	dr. E Kluza

Het onderzoek of ontwerp dat in dit wordt beschreven is uitgevoerd in overeenstemming met de TU/e Gedragscode Wetenschapsbeoefening.

Table of Contents

Chapter Summary

Chapter 1. Introduction

Chapter 2. Paramagnetic lipid and lipopeptide containing multi-modal nanoparticles for macrophage detection with fluorescence and MRI.

Chapter 3. Lipopeptide containing high-density lipoprotein (HDL)-nanoparticles for macrophage imaging with fluorescence and MRI.

Chapter 4. A crystalline iodine based nanoparticular contrast agent for the detection of macrophages in atherosclerotic plaques with computed tomography in a rabbit model of atherosclerosis.

Chapter 5. Introduction of a bimodal nanoparticular contrast agent for apoptosis imaging in atherosclerotic plaques with MRI and fluorescence.

Chapter 6. Characterization a small molecule conjugated gadolinium contrast agent targeting activated matrix metalloproteinases in a rabbit model of atherosclerosis.

Chapter 7. Reproducibility of black-blood delayed contrast enhancement (DCE)-MRI in a rabbit model of atherosclerosis.

Chapter 8. Multimodal imaging with DCE-MRI and FDG-PET/CT for monitoring atherosclerotic plaque inflammation upon intervention with Pioglitazone in atherosclerotic rabbits.

Chapter 9. Multimodal imaging with DCE-MRI and FDG-PET/CT for monitoring atherosclerotic plaque inflammation upon intervention with an LXR-agonsit R211945 in atherosclerotic rabbits compared to atorvastatin.

Chapter 10. Discussion

For my mother Atidža Vučić

Chapter 1

Introduction

1.1 Scope of the Thesis

Atherosclerosis is a chronic inflammatory disease that is triggered by the deposition of lipoproteins in the subendothelial space[1]. Monocytes-macrophages are the principal immune cells within atherosclerotic lesions or "plaques" and both the innate and the adaptive immune system drive the disease process[2]. Atherosclerosis is a slowly progressive sterile inflammatory disease that remains silent over long periods of time. Non–resolved inflammation through its destabilizing effects on atherosclerotic plaques triggers acute ischemic events leading to myocardial infarction and stroke. Both, are the principal causes of death worldwide and the incidence of atherosclerosis continues to increase despite effective lipid-lowering strategies[3]. Currently, no effective diagnostic techniques exist to identify at highest risk individuals. Novel imaging approaches that allow assessment of inflammatory plaque activity could help risk stratify populations and identify who benefits most from preventive intervention, monitor therapy responses and identify the most promising therapeutic interventions. In this thesis, I will explore various imaging strategies from nanoparticular and small molecule-based MRI- and CT-contrast agents to detect inflammatory activity in atherosclerotic plaques as well as employ clinically applicable MRI and PET/CT imaging techniques to monitor the effects of therapeutic interventions on atherosclerotic plaque inflammation in atherosclerotic disease models.

1.2 Atherosclerosis

Atherosclerosis was originally defined as a condition related to the arterial deposition of cholesterol[4]. Over the last decades, particularly, discoveries in vascular biology, immunology, and pathology establisched atherosclerosis as a chronic progressive and maladaptive inflammatory disease with monocyte/macrophage cells at the center of inflammation that is triggered by sub-endothelial lipoprotein accumulation[2]. Besides traditional risk factors, chronic inflammatory conditions (e.g. systemic lupus erythematosus, rheumatoid arthritis, psoriatic arthritis)[5] and infections (e.g. HIV)[6] increase the risk for

atherosclerosis disease. The disease process begins at early age[7]. It affects medium to large arteries and occurs at sites with impaired laminar flow, particularly arterial branch points and bifurcations[8]. Flow disturbances activate the endothelium and lead to subendothelial extracellular matrix proteoglycan deposition. The key pathogenic event is the deposition of apolipoprotein-B (apoB)-containing lipoproteins in the subendothelial compartment called- "intima"[1]. The necessary transfer of lipoproteins across the endothelium occurs via transcytosis and depends on caveolae, scavenger receptor B1 (SR-B1), activin receptor-like kinase 1 (ALK1), and LDL-receptor (LDLR)[9]. Upon retention, apoB-lipoproteins undergo various modifications including aggregation and oxidation (e.g. through myeloperoxidase and other oxidases) creating damage associated patterns (DAMPs) that trigger an innate immune response through interaction with pattern recognition receptors (PRR)[10,11]. The overlying endothelium then expresses surface adhesion molecule (selectins) and secretes chemoattractants (chemokines). The secreted chemokines interact with blood-borne monocytes leading to their recruitment from either bone marrow or spleen[12]. Upon recruitment, monocytes first bind and role, predominately through the interaction of monocyte P-selectin ligand and endothelial selectins predominantly, P-selectin, ICAM-1 and VCAM-1. Monocytes, then firmly attach through the interaction between monocyte integrins VLA-4 and LFA-1 and endothelial ligands VCAM-1 and ICAM-1 and, ultimately traverse the endothelium into the subendothelial space[13]. Transmigration is mediated by endothelial cell, intimal macrophage and smooth muscle cell secreted chemokines. Essential for the transcytosis, is the interaction of three monocyte chemokine receptors and chemokine pairs: CCR2-CCL2, CX3CR1-CX3CL1 and CCR5-CCL5[14]. Upon retention into the subendothelial space, monocytes can terminally differentiate into macrophages or differentiate and locally proliferate[15]. Monocyte to macrophage differentiation is orchestrated by cytokines, predominantly macrophage colony stimulating factor (M-CSF) and other factors[16]. In progressive plaque lesions, monocytes differentiate predominantly into pro-inflammatory phenotype macrophages[17]. The recruited inflammatory macrophages ingest cholesterol ester-rich apoB-lipoproteins via phagocytosis, pinocytosis, uptake via scavenger receptor and uptake via CD36 as part of an innate immune response[18]. Cholesterol uptake causes the inhibition of macrophage motility so-called "chemostasis", thereby, preventing egress of plaque macrophages from the vasculature[19]. Once ingested the cholesterol esters undergo hydrolysis and re-esterification and deposition as lipid droplets. This process creates the foam in "foam cells"-the hallmark cells of early atherosclerotic lesions-called "fatty streaks". The inflammatory

macrophage reaction, which at onset is an innate immune response, triggers an adaptive immune response mainly via the action of activated dendritic cells- which are locally present in atherosclerotic plaques[20]. The adaptive immune response is pro-inflammatory and characterized by T helper 1 (Th1) cells, Th17-cells, Th2-cells and B-cells. It is accompanied by a continuous decrease in regulatory T (Treg) cells in progressive plaque lesions[21]. Multiple other immune cells that promote atherosclerosis via various mechanisms are present in atherosclerotic plaques such as: neutrophils, platelet-neutrophil aggregates, natural killer cells, mast cells, eosinophil, and innate immune cells. Neutrophils participate in the initiation and progression of atherosclerotic plaques through close interaction and collaboration with monocytes/macrophages[22,23]. Simultaneously, to the macrophage centered immune reaction myofibroblast cells accumulate in the intima. The cells arise from medial smooth muscle cells and are a source of extracellular matrix proteins. Myocytes become activated through exposure to modified apoB-lipoproteins, cytokines and growth factors. The activation process ultimately causes the mycocytes to transform into a proliferating, migratory and extracellular matrix secreting phenotype. Additionally, myofibroblasts can develop a macrophage-like phenotype and take up apoB-lipoproteins and become foam cells that can make up a large portion of the cellular content in atherosclerotic plaques[24]. Continued macrophage lipid accumulation and inflammation leads to plaque progression - ultimately producing a "necrotic core" - the feature of complex plaque lesions. It develops when the accumulation of foam cells outnumbers its clearance. It is secondary to apoptosis and necrosis of foam cells that cannot effectively be cleared via phagocytosis - so-called "efferocytosis". A "fibrous cap" originates from the generation of extracellular matrix by myofibroblasts and surrounds the necrotic core. If inflammation persists in advanced plaques and acutely destabilizing factors are present, plaque rupture or plaque erosion and thrombosis causing acute ischemic events can occur[25].

1.2.1 Inflammation in Atherosclerosis

1.2.1.1 Pro-Inflammatory Macrophages

As part of the innate immune response differential macrophage phenotypes are present in atherosclerotic plaques[26]. Simplistically, a differentiation between pro-inflammatory LPS or IFN-γ activated - M1 and anti-inflammatory, alternatively activated (by IL-4 or IL 13) - M2 macrophages, exists. M1

macrophages express pro-inflammatory mediators, particularly, inducible nitric oxide synthase, tumor necrosis factor-alpha (TNF-α), Interleukin 1 beta (IL-1β), IL-6, IL-12, and proteolytic enzymes. Combined, these factors promote atherosclerotic plaque progression that ultimately can lead to plaque instability that can cause acute ischemic events. M2 macrophages, on the other hand, are characterized by expression of CD163, mannose receptor 1 (CD 206), FIZZ1 and arginase I. Additionally, M2 macrophages secrete anti-inflammatory cytokines: TGF-β, IL-1 Receptor antagonist, IL-10 and increased quantities of collagen. These factors favor M2 macrophages in tissue repair and healing. Applied to atherosclerotic plaques, M2 macrophages promote plaque stabilization and can induce plaque regression[17].

Instead of distinct macrophage phenotypes, however, a network of different macrophage phenotypes depending on the local microenvironment in the spectrum between the distinct M1 and M2 macrophage phenotypes exist[26]. Secondary to systemic and local micro-environmental factors-M1 type macrophages dominate over M2 macrophages in progressive atherosclerotic plaques[17,27]. Factors that contribute to a preponderance of pro-inflammatory M1 macrophages in atherosclerotic plaques are outlined below. The overarching theme relates to LDL-Cholesterol and its downstream effects on immune competent cells and organs.

Leukocyte lipoprotein uptake and Inflammasome activation
The continuous influx of LDL-cholesterol in the subendothelial space, its subsequent oxidative modification, and the uptake through macrophages during foam cell formation activates macrophages through multiple effects. Oxidized LDL and oxidized LDL derivatives activate Toll-like receptors (TLRs), particularly, TLR4-homodimers and TLR4/TLR6 heterodimers in conjunction with CD36 scavenger receptor[28,29]. Stimulation of TLR causes activation of nuclear factor - κB (NF-κB) and inflammatory cytokine secretion[16]. TLR activation, furthermore, primes the inflammasome for subsequent activation. Cholesterol crystals form already at an early stage in atherosclerotic plaques and can be ingested directly by macrophages or can manifest from free cholesterol within macrophages. The intracellular cholesterol crystals disrupt phagolysosomes, which causes the release of proteases and/or reactive oxygen species. Cholesterol crystals are the second factor necessary after priming that leads to the activation of NOD-like receptor family domain containing 3 (NLRP3) inflammasome - an intracellular protein complex. NLRP3 activation culminates in pyroptosis- a process of Caspase-1 dependent lytic cell death and pro-inflammatory cytokine-IL1-β and IL-18 release. IL1-β is the central proinflammatory cytokine of the innate immune response[30].

It orchestrates the inflammatory response in atherosclerosis and is essential for atherogenesis. Autophagy protects against inflammasome activation but is defective in plaque macrophages[31]. Other factors present in atherosclerotic plaque macrophages can lead to NLRP3 inflammasome activation: lysosomal cathepsins, mitochondrial reactive oxygen species (ROS) and extracellular ATP. IL1-β itself is a strong stimulator for IL1-β secretion. In addition to macrophages, neutrophils take up cholesterol crystal which leads to Neutrophil Extracellular Traps (NETs) formation that can prime macrophages for IL1-β and IL-18 release[32].

Leukocytosis, Inflammatory Phenotype Priming, and Trained Innate Immunity
Leukocytosis is present in atherosclerosis and correlates with cardiovascular risk[33]. Leukocytosis occurs through increased myelopoiesis. Multiple factors cause increased myelopoiesis, particularly cholesterol homeostasis and impaired cholesterol efflux as well as chronic systemic inflammation, diabetes mellitus (Types 1 and 2), sympathetic nervous system activation and lifestyle factors[33,34]. Besides, an increased number, increased myelopoiesis leads to the generation of pro-inflammatory monocytes (Ly6C high in mice, and CD 14_{++} in humans) in the bone marrow and spleen[14,35]. Ly6C^{hi} monocytes are the main source for pro-inflammatory M1 macrophages in progressive plaques[36]. $CD14_{++}$ cell numbers correlate directly with increased cardiovascular risk in humans[15].

A critical factor that causes increased myelopoiesis in hyperlipidemia is the impaired cholesterol efflux from hematopoietic stem and multipotential progenitor cells (HSPCs; precursors of monocytes and neutrophils)[37]. Cholesterol efflux is predominately medicated via ABCA-1 and ABCG-1-transport from the plasma membrane to apolipoprotein-A1 and high density lipoprotein (HDL), respectively and is regulated by apolipoprotein-E[38]. The induction of ABCA-1 and ABCG-1 is mediated by the sterol responsive nuclear transcription factor, liver-x-receptor (LXR)[39]. Mechanistically, impaired cholesterol efflux in HSPCs increases cell signaling through lipid "rafts" by increasing the density of the common β-subunit of the IL-3/GM-CSF receptor[37]. Additionally, splenic macrophages secrete M-CSF[38]. Both effects cause increased myelopoiesis. Recently, furthermore, a direct effect of Apolipoprotein-A-1 binding protein (AIBP)-mediated cholesterol efflux on HSPC expansion and mobilization was described[40].

Hypercholestorlemia, furthermore, through epigenetic reprogramming skews HSPCs towards myeloid lineages that differentiate preferentially into pro-

inflammatory monocytes and neutrophils[41-43]. Cholesterol accumulation in myeloid cells, moreover, activates the inflammasome directly and increases plaque neutrophil accumulation and NETosis[44].

Historically, immune memory was associated with an adaptive immune response. The Innate immune system, however, can form immune memory as well. It leads to an enhanced inflammatory response after re-exposure, so-called "trained" innate immunity. In atherosclerosis both oxidized LDL and lipoprotein (a) provoke a trained immune response[45,46]. Trained immunity has been, furthermore, observed on the level of myelopoiesis[47,48]. Mechanistically, epigenetic reprogramming is at the core of trained innate immunity. It causes a sustained shift in metabolic repertoire towards aerobic glycolysis via the activation of mammalian target of rapamycin (mTOR) through a dectin-1/Akt/HIF1α pathway[49]. A direct link between metabolic pathways and their intermediates and epigenetic modification exits[50,51]. Essential metabolic pathways for epigenetic modification in trained immunity are glycolysis (notably, via acetyl CoA), glutaminolysis (via fumarate) and cholesterol synthesis (via mevalonate)[52-54].

Aging is a major risk factor for atherosclerosis and it is associated with an increase in inflammation, so-called "inflammaging"[55]. Aging is associated with an increase of pro-inflammatory cytokines (e.g. interleukin-6, interleukin-1-receptor antagonist, and interleukin-18-binding protein)[56]. Other factors that contribute to an increase inflammation with aging are the pro-inflammatory effects of senescent cell accumulation[57], trained innate immunity[58] and clonal proliferation of mutated HSPCs (e.g. TET2 gene mutation) so-called clonal hematopoiesis of indeterminate potential (CHIP)[59].

Immunometabolism, Hypoxia and Reactive Oxygen
Macrophage polarization is accompanied by simultaneous changes in metabolic repertoire and distinct metabolic pathways determine immune function[60,61]. Inflammatory M1 macrophages use largely different metabolic pathways compared to reparative M2 macrophages[62]. M1-macrophage polarization is predominantly associated with aerobic glycolysis. Pro-inflammatory macrophage stimuli through stimulation of TLRs lead to activation and stabilization of HIF-1α via NF-κB. HIF-1α is also activated in hypoxia which is common in progressive plaques secondary to an increased atherosclerotic plaque size that results in increased oxygen diffusion distance[63]. Hypoxia, furthermore, leads to neovascularization via HIF-1α which increases immune cell influx and can cause plaque hemorrhage and thereby

further enhancing inflammation and causing acute plaque destabilization[64,65]. HIF-1α stabilization, furthermore, leads to an increased transcription of key glycolytic enzymes particularly Hexokinase II, Phosphofructokinase and cell surface GLUT-1 transporter expression in monocytes/ macrophages[66]. The metabolic shift towards glycolysis is already present in bone marrow HSPCs and is at the core of trained innate immunity[67].

Activated macrophages consume large quantities of glucose and secrete high quantities of inflammatory cytokines. The fact of increased glucose uptake of activated macrophages is used in imaging atherosclerotic plaques with the glucose analog fluorodeoxyglucose (^{18}F-FDG) with positron emission tomography (PET). In contrast M2 macrophages predominantly use oxidative Phosphorylation (oxPhos) and beta-oxidation[68].

Counterintuitive for cells with high-energy demands as glycolysis generates less ATP compared to oxPhos, this metabolic shift is well known for cancer cells so-called Warburg effect or shift[69]. It turns out, that aerobic glycolysis allows for the rapid increase in metabolic activity and that the glycolytic metabolites are essential to support inflammatory cell function as well as providing building blocks for cell proliferation. The functional consequences of induction of aerobic glycolysis are essential to support innate immune cell function. Glycolysis in cells with a Warburg shift generates succinate and citrate secondary to a metabolic blockade at both metabolites in the tricarboxylic acid cycle (TCA). Succinate directly stabilizes HIF-1α and causes increased secretion of IL1-β[70]. Citrate is essential for phospholipid and cholesterol synthesis. Glycolysis, furthermore, fuels the pentose phosphate pathway (PPP). This pathway is essential for the generation of NADPH, nucleotides and aromatic amino acids. The generated metabolic intermediates are essential for cell proliferation and the majority of plaque macrophages originates from cell proliferation[71]. NADPH is essential for the generation of reactive oxygen species (ROS). ROS contributes to inflammation in atherosclerotic plaques through oxidation of LDL and other proteins.

Mitochondrial dysfunction occurs as part of the atherosclerotic disease process[72]. Various oxidized products such as oxLDL as well as hypoxia interfere with mitochondrial function which causes the generation of reactive oxygen species (ROS) and thereby inflammation[73]. Defective autophagy of damaged mitochondria so-called mitophagy, furthermore, promotes inflammation via inflammasome activation[74]. Damaged mitochondria cause apoptosis and necrosis, thereby, further increasing inflammation[73].

Impaired mitochondrial function, furthermore, impedes with M2 macrophage function which is depended on oxPhos, thereby leading to a decrease in M2 macrophages[17].

1.2.1.2 Adaptive Immune Cell Response

In addition to the central role of the innate immune cell response in atherosclerosis, adaptive immune cells play are a critical role in the initiation and progression of atherosclerosis[75]. Atherosclerosis can be considered as an autoimmune condition with LDL as the antigen[76]. Central to the adaptive immune cells are T cells. Approximately 25-38% of leukocytes in mouse aortic and human atherosclerotic plaques are T cells (CD3$^+$)[76]. T-helper cells (CD3$^+$ CD4$^+$) account for about 10%. T cells predominantly localize in the fibrous cap. In the adventitia of advanced plaques, so-called arterial tertiary lymphoid organs (ATL) are formed and contain T cells and primary B cells. Antigen-presenting cells (APCs; i.e. plaque macrophages, and particularly dendritic cells) take up oxLDL/LDL via scavenger receptor and initiate the adaptive immune response[20]. Upon intracellular processing of oxLDL/LDL antigen peptide fragments are generated from apoB. The antigen peptide fragments are subsequently presented by APCs on MHC (major histocompatibility complex)-II to naïve CD4$^+$ Helper T cells by exiting the plaque and entering secondary lymphoid tissue (i.e. lymph nodes). As a result of antigen presentation, co-stimulation (i.e. CD28 on T cells) and cytokine stimulation, T cell clonal expansion into effector T cells, notably, Th1 cells and Th17 cells occurs. Of note, T cell expansion can be pro-atherogenic or atheroprotective depending on what T cell subtype is expanded [e.g. Type 1 regulatory (TR1) and T-regulatory (T$_{reg}$) are atheroprotective]. In general, atherosclerosis is considered a Th1 disease. Upon expansion, effector T cells migrate into atherosclerotic plaques where APCs present the same antigens and co-stimulators. This leads to effector T cell activation and expression of pro-inflammatory factors, particularly secreted TNF-α and IFN-γ as part of a Th-1 response. The secreted factors promote inflammation, plaque growth, and ultimately plaque instability.

T$_{reg}$ protect against autoimmune disease[77] and low T$_{reg}$ predict future cardiovascular events[78,79]. T$_{regs}$ reactive to apoB/LDL have been demonstrated in humans and mice and initially proliferate as a response to apoB/LDL[80]. The T$_{reg}$ number diminishes, however, with progressive disease[76].

B cells can be categorized into B1 and B2 cells. B1 cells are part of the innate immune system and secrete IgM antibodies in a T cell-independent manner. B2 cells, on the other hand, need to be activated by T cells to differentiate into plasma cells that secrete IgG antibodies and are part of the adaptive immune system. The B1 cell/IgM-response is atheroprotective and the effect of B2 cell/IgG response, on the other hand, appears to be pro-atherogenic[76].

1.2.1.3 Apoptosis, Necrosis, Defective Efferocytosis, and Impaired Resolution of Inflammation

Macrophage apoptosis occurs at all stages of atherosclerosis[24]. The effects of apoptosis on atherosclerotic plaques are dependent on the atheroma stage[81]. Macrophage apoptosis appears to be protective at early stages of atherosclerosis, as it is believed to limit plaque progression through the clearance of death cells and debris through efferocytosis. At later stages, however, through various factors, efferocytosis becomes defective and apoptotic cells undergo secondary necrosis, thereby exposing pro-inflammatory cell content[82]. This is, however, not the only process under which necrosis can occur[83]. A process named, necroptosis, or programmed necrosis, occurs in advanced atherosclerotic plaques and is regulated by receptor-interacting protein kinases 1 (RIP1) and 3 (RIP3) and mixed lineage kinase domain-like pseudokinase (MLKL)[83,84]. Both RIP3 and MLKL are present in human unstable carotid atherosclerotic plaques. Necroptosis in atherosclerotic plaques is triggered by oxLDL and its derivatives that are the predominant DAMPs in atherosclerotic plaques[85]. Necrosis and Necroptosis, through the release of pro-inflammatory cell components, trigger further necroptosis further enhancing inflammation[84,85]. In addition, the RIP1 and RIP3 complex enhances inflammation directly via inflammasome activation after TLR4 stimulation in macrophages[86].

Efferocytosis, the clearance of apoptotic cells, is a very effective process as evidenced by the lack of significant apoptotic cells in healthy tissue[87]. So-called "eat me" signals are presented on cells undergoing apoptosis. The best characterized "eat me" signal is phosphatidylserine and it is presented on the extracellular surface of cells undergoing apoptosis[88]. Various cell surface receptors recognize phosphatidylserine and mediate the phagocytosis of apoptotic cells[89]. In atherosclerotic plaques most prominently the tyrosine kinase MER (MER-TK) mediates, via bridging molecules (e.g. gas6), phagocytosis of apoptotic foam cell macrophages. Efferocytosis is

immunological inert[90] and inhibits inflammatory cytokine secretion and causes the secretion of anti-inflammatory factors notably, TGF-β and IL-10[91,92]. Phagocytosis of apoptotic cells is more efficient than necrotic cells phagocytosis which may explain the accumulation of necrotic cell debris in plaque[84]. Effective Efferocytosis is depended on lipid homeostasis and both peroxisome proliferators-activated receptors (PPARs) and LXR are critical regulators of lipid hemostasis[93,94].The ingestion of apoptotic cells activates cholesterol efflux pathways via the activation of LXR and defective cholesterol efflux impairs efferocytosis[95]. The alternate activated, M2-type, macrophages are effective phagocytes and promote plaque healing. The M2 macrophage phenotype correlates with PPAR-γ and PPAR-δ expression[96-99].

MerTK is of critical importance for efferocytosis[100,101]. Cleavage of MerTK occurs in progressive atherosclerotic plaques and leads to defective efferocytosis and plaque necrosis[102]. The metalloproteinase ADAM17 is expressed in inflammatory plaques and particularly in areas surrounding the necrotic core. It is associated with MerTK cleavage, thereby, creating soluble MerTK (sMer)[103,104]. Mechanistically, sMer inhibits the bridging molecule gas6 which results in the inhibition of efferocytosis[105]. Efferocytosis, is furthermore, impaired in atherosclerotic plaques through the increased expression of the "don't eat me" signal CD 47. Its expression is controlled by TNF-α[106]. Additionally, apoptotic cell binding is impaired in progressive atherosclerotic plaques by the increased presence of oxidized LDL and antibodies against oxidized LDL phospholipid through competition and masking of apoptosis receptors, respectively[107].

An imbalance between pro-inflammatory lipid mediators (Leukotrienes and Prostaglandin E$_2$) and pre-resolving factors so-called specialized pro-resolving mediators (SPMs) is present in progressive atherosclerotic plaques and promote inflammation and can cause plaque instability[108]. SPMs, are derived from docosahexaenoic acid (DHA) [e.g., resolvin D1,D2 (RvD1,RvD2), protectin D1 (PD1) and maresin 1 (MarR1)] or arachidonic acid [Lipoxins (e.g., LXA4 and LXB4)] and promote efferocytosis and resolution of inflammation in atherosclerotic plaques[108,109]. The administration of various SMPs in progressive plaques led to plaque stabilization in animal models[110].

1.2.2 Vulnerable Plaque

Plaques leading to acute cardiovascular syndromes so-called "vulnerable plaques" are predominately localized in proximal segments of the coronary artery[111]. Rupture-prone plaques underlie the majority of acute cardiovascular syndromes and are found in about two-thirds of cases and the remainder of cases are largely caused by plaque erosion[112]. Structurally, the rupture-prone plaques are characterized by a large and soft lipid-rich necrotic core associated with a thin fibrous cap (less the 65 μm) - so called thin cap fibroatheroma (TCFA)[113]. In the majority of cases, the necrotic core size is larger than 1 mm^2 and consists of more than 30 % of the plaque size[113,114]. Other features are a relatively large plaque size with expansive remodeling (therefore, the plaques are not obstructing the lumen on routine coronary angiography), neovascularization, intraplaque hemorrhage and a "spotty" pattern of calcification[111]. What ultimately leads to plaque rupture is not definitely known. A critical component, however, is the presence of macrophages in the fibrous cap and paucity of smooth muscle cells[115]. Pro-inflammatory macrophages are present in high density in rupture-prone plaques especially at the "neck" or hinge point of the fibrous cap and demonstrate a high degree of apoptosis/necrosis. Pro-inflammatory macrophages weaken the fibrous cap via the secretion and activation of matrix-degrading enzymes particularly matrix metalloproteinases (MMP)[116]. Additionally, the collagen secretion by myoblasts is suppressed by IFN-γ from activated T-helper cells[117] and smooth muscle cells apoptosis[118,119]. As a precursor to acute ischemic syndromes, a dysregulation of the adaptive immune response is, furthermore, present[120]. It results in increased inflammatory cytokine production (e.g IFN-γ and TNF-α) and increased cytotoxic activity, and can, ultimately, cause either directly or indirectly through actions on macrophages, smooth muscle cells, endothelial cells, and extracellular matrix, plaque instability and acute ischemic events.

Neovascularization in plaques occurs as a response to hypoxia and inflammation[121]. Neovessels, however, are fragile and can lead to plaque hemorrhage which represents a source of free cholesterol and cholesterol esters from erythrocyte membranes[122]. The free cholesterol and cholesterol esters contribute to rapid necrotic core expansion and plaque vulnerability[64]. Besides, neovascularization, plaque hemorrhage can also occur after partial plaque rupture[123]. Additionally, inflammatory cells, particularly monocyte/macrophages and neutrophils enter plaques through neovessels and promote plaque inflammation and instability[124].

Calcification, specifically spotty calcification rather then dense calcification is associated with plaque vulnerability[125]. The mechanism by which this occurs has not been entirely elucidated but it appears that spotty calcifications cause potential hinge points for plaque rupture. Dense calcifications, on the other hand, are protective[125]. Interestingly, M1 macrophages produce spotty calcification whereas M2 macrophages produce dense calcification[125]. Cholesterol crystals, furthermore, have also been implicated to mechanically cause plaque rupture[126].

1.3 Atherosclerotic Plaque and Inflammation Imaging

Inflammation is the driving force in atherosclerosis plaque initiation, progression, and vulnerability. It is, therefore, of great interest to develop tools that can reliably detect vascular inflammation. Various imaging approaches have been developed to assess atherosclerotic plaques and inflammation. One can broadly discriminate between non-invasive and invasive imaging tools and between anatomical and molecular imaging approaches.

1.3.1 Invasive imaging

Invasive imaging using intravascular ultrasound (IVUS), optical coherence tomography (OCT), near-infrared spectroscopy and lately high-resolution near-infrared fluorescence (NIRF) have been used for invasive coronary artery plaque assessment[127].

Grayscale IVUS acquisition allows for the assessment of plaque size and positive remodeling. IVUS with radiofrequency analysis so called virtual histology (VH-IVUS) permits, furthermore, the visualization of plaque components: fibrous plaque, fibrofatty plaque, necrotic core, and spotty calcification. Despite its axial resolution of 150-250 μm (depth penetration 7-10 mm), VH-IVUS allows the assessment of thin-cap fibroatheroma (TCFA) with good histological correlation[128]. VH-IVUS assessed TCFA and large plaque burden were demonstrated as independent predictors of major adverse cardiovascular events in human studies[129-131].

OCT uses low-coherence infrared light to visualize different plaque components with high axial resolution of 10-20 μm but limited depth penetration (0.1-2 mm). OCT can truly measure the fibrous cap. A fibrous cap thickness of ≤ 85 μm on OCT was found to be the optimal definition of a TCFA with OCT[128]. OCT can detect macrophages which appear as so-called "bright spots" with associated posterior plaque attenuation[132]. A correlation between bright spot amount on OCT and macrophage density in carotid[133] and coronary[134] plaques was detected. Macrophage density was found greater in: TCFA vs. non-TCFA[135], culprit vs. non-culprit plaques[136] and ST-segment elevation myocardial infarction vs. stable angina pectoris patients[137]. Interestingly, not all macrophages (CD68 positive cells) on histology demonstrate bright spots on OCT which was attributed to different macrophage phenotypes (M1 vs M2 macrophages)[138].

Plaque neovascularization[139] and adventitial vasa vasorum (VV)[140] can be detected with OCT as microchannels. Plaque neovascularization correlates with plaque vulnerability whereas adventitial VV correlate with plaque volume[141]. The presence of plaque neovessels correlates with plaque progression[142] and plaque rupture[143,144].

Near-infrared spectroscopy (NIRS) applies near-infrared laser light to the vasculature. The reflected spectrum is then collected and analyzed. Cholesterol has a distinct reflective spectrum and can be identified with NIRS[145]. NIRS has only limited anatomical information and is therefore used, most commonly, in combined with IVUS in a single catheter. The acquired data are presented as a chemogram, which is a two-dimensional display of the likelihood of the presence of lipid core plaque per millimeter. A lipid core burden index (LCBI) can then be calculated.

An LCBI above the median was found to be a significant predictor of adverse cardiovascular events[146,147]. LCBI of 4 mm lesion length ($LCBI_{4mm}$) represents the total lipid amount over the segment. An $LCBI_{4mm}$ of greater than 400 positively identified culprit lesions in ST-segment elevation myocardial infarction (STEMI)[148], non-STEMI and unstable angina patients[149] and positively correlated with future cardiovascular events[147].

High-resolution near-infrared fluorescence (NIRF) has emerged as an invasive molecular imaging tool[150]. In preclinical studies plaque inflammation detection (cysteine protease activity)[151] and lipid-rich area and macrophage content assessment [indocyanine green (ICG)][152] were demonstrated. A pilot human study, on ex-vivo carotid plaques samples [NIRF combined with OCT (NIRF-OCT)] demonstrated ICG uptake in atherosclerotic plaques with

increased endothelial permeability[153]. ICG localized within plaques in lipid-, and macrophage-rich areas and areas with plaque hemorrhage. The results were validated by in-vivo NIRF-OCT in atherosclerotic swine. In-vivo coronary non-contrast imaging with NIRF-OCT to assess near-infrared autofluorescence (NIRAF) demonstrated an association of NIRAF and high-risk plaques[154].

1.3.2 Non-Invasive Imaging

The invasive nature and potential complications related to invasive imaging preclude its use on a population basis. This is particularly important for preventive strategies as well as therapeutic response assessment. Multiple, non-invasive imaging approaches have been applied to image atherosclerotic plaques and inflammation. Of great clinical interest are Magnetic Resonance Imaging, Computed Tomography, and Positron Emission Tomography.

1.3.2.1 Magnetic Resonance Imaging[155,156]

Magnetic Resonance Imaging (MRI) generates images by the biophysical response of tissues placed in a strong static magnetic field that are transiently exposed to electromagnetic radiofrequency (RF) pulses. It is based on nuclear magnetic resonance (NMR) and uses the nuclear spin of elements (e.g. ^{1}H, ^{13}C, ^{19}F, ^{23}Na and ^{31}P) for image generation. In the human body hydrogen nuclei (= protons) are abundantly present as the body largely consists of water and lipids. Protons have a positive charge and through the property of nuclear spin induce a small magnetic field. Upon application of an external magnetic field, protons align either parallel or anti-parallel to the external field. The parallel alignment is a lower energetic state and, therefore, favored but only by a small fraction. This causes a net magnetization along the external magnetic field so-called "longitudinal magnetization". The application of an external magnetic field, furthermore, causes the protons to wobble or "precess" with a certain frequency along the lines of the external magnetic field. The precession frequency or resonance frequency is directly proportional to the external magnetic field strength and can be described with the Larmor equation:

$$\omega_0 = \gamma B_0$$

ω = precession frequency; γ = yromagnetic ratio (protons = 42.5 MHz/T); B_0 = magnetic field strength (T).

The Application of an external RF pulse at resonance frequency causes energy transfer between the RF pulse and nucleus. This causes more protons to align to the higher energy, anti-parallel state, and synchronizes proton precession (protons precess in "phase"). The combination of these effects causes "transverse magnetization". Once the RF pulse is turned off protons return or "relax" to their original state by two independent relaxation mechanisms: 1) longitudinal- or "spin-lattice" relaxation and 2) transverse- or "spin-spin" relaxation. Longitudinal relaxation is described by the constant T1. Transverse relaxation is described by constant the T2. Additionally, secondary to small magnetic field inhomogeneities and magnetic susceptibility effects within the tissue the decay of transverse magnetization is in reality much faster and expressed by the time constant T2*. During relaxation, a decaying RF signal is induced at the resonant frequency, so-called free induction decay (FID). The signal is then received by the magnetic resonance receiver or coil. From the received signals anatomical images can be generated. In practice, however, it is more common to detect MRI signals as an echo. Mainly, two echos are applied: spin echos and gradient echos.

Spin- and Gradient Echo
A spin-echo is generated by the application of a 180° refocusing RF-pulse after the initial 90° excitation RF-pulse. De-phasing caused by T2 relaxation is irreversible whereas de-phasing secondary to magnetic field inhomogeneities is potentially reversible. The application of the 180° pulse rotates the protons while still in the x-y plane into the opposite direction and precess. This ultimately leads to re-phasing secondary to the now differential effect of field inhomogeneities on each proton frequency. A maximal signal is reached once the protons have returned to phase so-called spin echo (SE). The time to the maximum signal is the echo time (TE) and to achieve maximal signal the 180° refocusing RF-pulse needs to be applied at half TE time (TE/2). Spin echo sequences generate black blood contrast when imaging fast blood through the imaging slice. This is secondary to the fact that the transverse magnetization of blood flowing through the imaging slice is not refocused (spin washout effect). Therefore, spin echo sequences have been widely used for black blood imaging approaches.

A gradient-echo is produced by replacing the 180° refocusing RF-pulse with magnetic field gradients. Magnetic field gradients cause a change in field strength and, therefore, in Larmor frequency in a particular direction. Upon application of a magnetic field gradient after an initial RF pulse, rapid de-phasing along the direction of the gradient occurs this causes a rapid decline in FID signal. The rapid loss of signal, however, can be reversed upon application of second magnetic field gradient with a slope of equal amplitude but in reverse direction. This ultimately results in re-phasing and causes a return in signal so-called gradient echo (GRE). The time between the beginning of FID generated by the initial RF pulse to the time which GRE reaches is maximum is the echo time (TE). As opposed to spin echo sequences, gradient echo sequences use only one single RF pulse and spin washout, therefore, does not occur. In fact, GRE sequences have increased signal from flowing blood and are used in bright blood imaging. The increased signal from moving blood is caused by partial suppression of tissue magnetization by rapid and repeat application of RF pulses whereas moving blood remains fully magnetized, thereby, leading to an increase in signal intensity. This effect is known as inflow enhancement. GRE sequences are also the basis for TOF magnetic resonance angiography (MRA).

Image reconstruction
In order to reconstruct images, the MR signal needs to be localized and encoded. This is achieved by the application of three separate field gradients: 1) slice-selection gradient, 2) phase encoding gradient (G_p) and 3) frequency encoding gradient (G_f)-applied perpendicular to G_p. The slice selection gradient alters B_0 along the chosen axis so that protons within the field have different Larmor frequencies, thereby, allowing slice selection. Upon selective slice excitation, the signals from each slice element (= pixels) need to be spatially encoded through the application of phase- and frequency encoding gradients. Upon the excitatory RF pulse, the protons precess in phase. The application of an additional magnetic gradient (phase encoding gradient) will cause a change in phase according to their position along the gradient and in direction of the applied gradient (= phase encoding direction). A magnetic gradient (frequency encoding gradient) perpendicular to and after the phase encoding gradient direction causes the protons to rotate at different frequency along the gradient direction. This permits the differentiation of the signal along the third axis. In order to sample sufficient phase encoding information, the pulse sequence is repeated many times (RP) with an incremental increase in phase encoding gradient. Each repetition generates a signal echo that is

digitized and deposited in a raw data matrix (k-space). The raw data is then converted into an image by a mathematical tool called Fourier transform.

Image Contrast
Variation in timing intervals on RF repetition (RP) and Echo times (TE) are used to generate the most commonly used T1-, T2- or Proton Density (PD) weighted MRI for spin echo sequences and T1 and T2* weighted MRI for gradient echo sequences. Contrast agents can be used to further enhance tissue contrast. Paramagnetic T1 agents shorten T1, which leads to signal enhancement on T1 imaging sequences. Superparamagnetic T2 agents shorten T2, and provide negative contrast (signal voids) on T2 (T2*) imaging sequences.

1.3.2.1.1 MRI for Atherosclerosis Imaging
MRI allows for high resolution [in-plane resolution of 0.5-1mm (maximum 0.25mm)] imaging of the vasculature. It has emerged as the preferred imaging modality for the characterization of atherosclerotic plaques[157,158]. MRI is preferably performed for the study of large and relatively immobile arteries, such as the aorta, femoral and carotid arteries. Because of their small dimensions and their continuous motion during data acquisition, coronary arteries remain more difficult to image. Recent advancements in instrumentation and imaging technique, however, continue to generate interest in coronary MRI and robust detection of proximal to mid portion of the coronaries is now standard[159]. At the current time, most of the data on the detection of atherosclerotic plaques with MRI have been obtained from carotid arteries. Multiple features of progressive carotid atherosclerotic plaque notably, lipid-rich necrotic core, fibrous cap, calcification as well as intra-plaque hemorrhage, can be effectively characterized using multi-contrast (MC-[T1-, T2-, PD-]) MRI using black blood and TOF-MRA bright blood imaging techniques[160]. Worse clinical outcomes have been observed in patients who have vulnerable plaque features on MRI and particularly the presence of intraplaque hemorrhage correlates with worse outcomes[161]. Additionally, plaque permeability and neovascularization (a marker of plaque inflammation/ hypoxia) can be assessed by dynamic contrast-enhanced (DCE)-MRI.

A drawback of carotid MC-MRI has been the relatively low resolution, as black blood imaging sequences require a relatively large slice thickness. Furthermore, limited reproducibility, difficult interpretability as well as its length of imaging acquisition as each sequence is acquired sequentially. To overcome these limitations a simultaneous multi-contrast 3D MRI was

introduced (Multi-contrast ATherosclerosis Characterization [MATCH]), recently[162]. It acquires three different contrast weightings in an interleaved fashion in 3D. A routine multi-contrast carotid imaging study using MATCH can be completed in about 5 min. The sequence appears to be at least as sensitive as traditional multi-contrast MR protocols for the assessment of different carotid plaque components.

Recently, furthermore, quantitative MRI applying T1 and T2 mapping approaches have been introduced for carotid artery plaque characterization [163]. In analogy to the MATCH sequence a 3D interleaved T1 and T2 mapping sequence, dubbed SIMPLE, was introduced[164]. It allows rapid (< 10 min) quantitative assessment of individual carotid plaques component. This approach could be particularly useful for serial imaging to assess plaque progression and in the assessment of the effectiveness of therapeutic interventions.

1.3.2.1.2 Molecular MRI of Atherosclerotic Plaque Inflammation

Compared to nuclear imaging, MRI has a magnitude lower sensitivity (micromolar range). In order to achieve molecular imaging the target contrast content needs to be relatively high at the local space. This can be achieved by imaging high abundance targets or by increasing contrast payload delivery to the target. Increased payload delivery has been achieved with various actively or passively targeted nanoparticles[165]. Nanoparticles are defined by the size of 1-100 nm in at least one dimension and can be constructed from various building blocks (i.e. biomacromolecules, polymers, metals, etc.)[166]. To improve biocompatibility and stability, polyethylene glycol (PEG) coating is frequently applied. Because of a favorable surface area to volume ratio many targeting ligands (i.e. small molecule, antibodies, antibody fragments, aptamers, etc.) can be attached to a single nanoparticle. Nanoparticles for imaging are extremely versatile as multiple imaging probes can be incorporated into a single particle (e.g. Nuclear, MRI, CT and fluorescence probes), thereby, permitting multi-modality imaging[167]. Additionally, therapeutic agents can be incorporated into the imaging nanoprobes (e.g. into the particle core) so-called "theranostic" probes. This permits targeted imaging and therapeutics delivery in one single agent[168].

Largely, two groups of MRI molecular probes can be discriminated: paramagnetic T1-shortening probes and superparamagnetic based T2 (T2*)-shortening probes. Paramagnetic molecular probes have most commonly used targeting ligands conjugated to gadolinium chelates (small molecule probes), as well as paramagnetic nanoparticles with or without targeting

ligands. Superparamagnetic probes are based on coated (most commonly heparan sulfates) iron oxide nanoparticles. Various targets associated with atherosclerotic plaque inflammation have been explored as outlined below.

Activated endothelium
Increased endothelial permeability secondary to endothelial activation is associated with atherosclerotic plaque inflammation. Gadofosveset is a small molecule agent composed of lipophilic biphenylcyclohexyl conjugated to a Gadolinium chelate (Gd-DTPA)[169]. It reversibly binds to serum albumin with moderate affinity and is commonly used as a blood pool agent for peripheral MR angiography. It has a plasma half-life of 18.5 h. In a murine model of atherosclerosis increased delayed vessel wall enhancement and relaxation rate R1 (assessed by quantitative T1 mapping) was demonstrated in atherosclerotic plaques[170]. Plaque enhancement correlated with Evans blue uptake (a marker for endothelial permeability). Additionally, a decrease in vessel wall enhancement was observed upon statin treatment. In a subsequent study in atherosclerotic rabbits, Gadofosveset enhancement and relaxation rate R1 was higher in rupture-prone plaques vs. stable plaques[171].

In a pilot human study, Gadofosveset enhanced carotid MRI was performed and demonstrated higher signal enhancement in symptomatic patients compared to asymptomatic patients[172]. Most recently, Gadofosveset was applied in human coronary MRI to enhance atherosclerotic plaque detection[173]. It identified culprit coronary lesions with high sensitivity (82%) and specificity (83%). Additionally, in a segmented analysis, thin-cap fibroatheroma (as detected invasively on OCT) showed increased enhancement post Gaodofosveset as compared with segments without coronary plaque or in early atherosclerotic lesions.

VCAM-1 is expressed on activated endothelium and leads to homing of immune competent cells into atherosclerotic plaque. Multimodal (fluorescence and MRI) dextran coated ultrasmall paramagnetic iron oxide (USPIO) nanoparticles (average size of about 38 nm) conjugated with a VCAM-1 binding peptide (peptide sequence: VHPKQHR) were applied to image activated endothelium in a murine model of atherosclerosis[174]. Changes in endothelial activation upon statin treatment were successfully monitored using this approach.

Microparticles of Iron Oxide (MION) with a size of 1 μm were used in atherosclerotic mice to detect activated endothelium[175]. Activated endothelium

targeting was achieved by applying a dual targeting strategy with antibodies against VCAM-1 and P-Selectin. MRI signal loss on T2 (T2*) weighted MRI upon targeted microparticles administration correlated with atherosclerotic plaque predilection sites and plaque macrophage content.

Neovascularization
Neovasculature promotes plaque inflammation and hemorrhage and is associated with plaque instability[176]. It is, furthermore, characterized by poor endothelialization and expression $\alpha v\beta 3$-Integrin. Lipid-perfluorocarbon nanoemulsions functionalized with a Arg-Gly-Asp (RGD)-peptide sequence to target $\alpha v\beta 3$-Integrin were applied in atherosclerotic rabbits[177]. Particle size was approx. 270 nm. The targeted particles led to a 47% signal enhancement on T1 weighted MRI compared to pre-contrast. In a subsequent study using the same nanoparticles a theranostic approach with the incorporation of the angiostatic agent, fumagillin was applied[178]. The treatment group showed an MRI signal decrease on post-therapy $\alpha v\beta 3$-Integrin MRI-imaging. Histologic analysis demonstrated a decreased neovessel count in the treatment group.

Macrophages
Macrophages are the most abundant cells in atherosclerotic plaques (around 40%). The cells are at the center of the inflammatory response and, therefore, attractive targets to inflammation imaging in atherosclerosis.

Paramagnetic PEG-lipid micelles were functionalized with an antibody against scavenger receptor A (expressed on macrophages)[179]. The nanoparticles had a size of 20 nm and led to signal enhancement on T1 weighted MRI. A quantum dot or fluorescent lipids were incorporated allowing multimodality detection (MRI and fluorescence). Macrophage targeting was validated on immune histological analysis.

Ultrasmall paramagnetic iron oxide (USPIO) nanoparticles are taken up by macrophages and macrophage foam cells[180]. Cellular uptake occurs through phagocytosis and receptor-mediated endocytosis uptake of larger particles, whereas smaller particles are internalized by pinocytosis. Besides the particle size and charge, the surface coating is particularly important. Most commonly dextran coating is applied to USPIOs. The small size of USPIOs largely prevents phagocytosis through the reticuloendothelial system (RES) and allows long blood circulation (14-30 h in humans)[181]. The particles, furthermore, are capable to pass through capillaries and accumulate in plaque neutrophils and macrophages.

Multiple pre-clinical animal studies in atherosclerotic mice and rabbits have demonstrated USPIO nanoparticle uptake in macrophages of atherosclerotic plaques[182]. A dextran coated USPIO nanoparticle, Ferumoxtran-10, with a particle size of 20-30 nm was applied in multiple human studies to image inflammation and macrophages in carotid plaques. A significant decrease in signal on T2* weighted MRI was observed upon Ferumoxtran administration in carotid plaques[183]. Macrophage USPIO uptake was validated where patients underwent carotid endarterectomy post-MRI[184]. A small statin intervention trial demonstrated a difference in plaque quadrant signal change on T2* weighted MRI over 12 weeks treatment between high dose (Atorvastatin 80 mg) and low dose statin (Atorvastatin 10 mg)[185]. Long term follow up demonstrated a trend towards an increase in cerebrovascular and cardiovascular events in patient with higher maximum signal change[186].

At the present time, the only USPIO nanoparticular agent approved by the FDA is ferumoxytol[187]. It has been mainly applied for vascular contrast MR angiography secondary to its T1 shortening properties and long plasma half-life (14-15 h). A proof of concept study, using ferumoxytol (particle size 20-30 nm) to image patients with carotid stenosis and controls was performed and compared to FDG-PET/CT[188]. It demonstrated a decrease R2* values on quantitative T2 mapping in patients with carotid stenosis. Interestingly, no association between ferumoxytol signal change and FDG uptake was found. It was attributed to the difference in what each probe detects: metabolism/inflammation (FDG) vs macrophage particle accumulation secondary to enhanced permeability (Ferumoxytol). This was presumed to be in analogy to the differential correlation between FDG PET/CT and DCE-MRI (see paragraph on DCE-MRI).

A completely different approach, using perfluorocarbon nanoemulsions (mean size: 130 nm), to identify macrophages in a murine atherosclerosis model with ^{19}F-MRI, was pursuit[189]. ^{19}F-MRI provides so-called "hot spot" imaging as there is no meaningful fluorine content in the body[190]. The detected signal, therefore, arises from the applied nanoparticles, alone.

Another innovative approach was demonstrated by hyperpolarized magnetic resonance (MR)[191]. This study applied [1-^{13}C]pyruvate to monitor the local cardiac inflammatory response of the innate immune system (predominantly macrophages) after myocardial infarction. Hyperpolarized magnetic resonance is an emerging imaging technology. It is based on hyperpolarizing nuclear spins and can generate contrast agents with up to > 10 000-fold

improvements in MR signal [192]. In this study, hyperpolarized [1-^{13}C]pyruvate was used in small and large animal models of myocardial infarction (MI) and in macrophage-like cell lines. MI caused intense [1-^{13}C]lactate signal in healing myocardial segments at both days 3 and 7 after rodent and pig MI. The in-vivo studies were validated by hyperpolarized [1-13C]pyruvate MR spectroscopy in macrophage-like cell suspensions in vitro. Currently, hyperpolarized MR image resolution is below the resolution of positron emission tomography.

Oxidation-specific Epitopes
Oxidation-specific epitopes (OSE) within atherosclerotic plaques are the principal antigens for the innate and adaptive immune responses in atherosclerosis[193]. Gadolinium or manganese-containing nanoparticular PEG-lipid micelles and PEG-lipid coated USPIO (LUSPIO)-nanoparticles were applied[194-196]. As targeting ligands served oxidation-specific epitope antibodies/antibody fragments. All formulations enhanced atherosclerotic plaque detection, which was dependent on oxidation-specific epitopes, and the particles co-localized with macrophage/foam cells.

Apoptosis
Apoptosis in atherosclerotic plaque is a feature of advanced plaque lesions and correlates with plaque vulnerability. USPIO nanoparticles functionalized with a phosphatidylserine binding peptide were applied in atherosclerotic mice[197]. The particles were about 27 nm in size. Significant particle uptake was observed in atherosclerotic plaques that correlated with apoptosis cell content.
A PEG-coated USPIO conjugated with Annexin V to target phosphatidylserine on apoptotic cells was applied[198]. A SPECT reporter was included to allow dual modality assessment. USPIO uptake correlated with lipid-rich plaque areas.

Proteolytic Enzymes
Plaque Myeloperoxidase (MPO) is associated with plaque inflammation and promotes plaque instability. Detection of MPO activity with a small molecule conjugated gadolinium chelate was associated with unstable plaque features in a murine atherosclerosis model[199]. The pharmacological inhibition of MPO led to a decrease in MPO targeted agent signal.

1.3.2.1.3 Dynamic Contrast-Enhanced MRI
Dynamic contrast-enhanced MRI has been widely used in oncology to quantify endothelial permeability and microvascular volume in tumors[200]. Neovascularization in atherosclerotic plaques plays a critical role in

atherosclerotic plaque progression, inflammation and is associated with plaque hemorrhage and correlates with plaque vulnerability[176]. Neovessels in humans are very small and measure ≤ 100 μm and have sparse endothelial cell coverage leading to enhanced permeability which leads to inflammatory cell and erythrocyte extravasation and plaque hemorrhage[64]. Dynamic contrast-enhanced (DCE)-MRI to assess atherosclerotic neovascularization and permeability was applied in multiple carotid artery imaging studies. DCE-MRI is based on the rapid sequential acquisition of T1-weighted MR images in the arterial vasculature during injection of a T1 shortening, Gadolinium-based, low molecular contrast agent[201]. Before contrast injection, an anatomical reference image is acquired that serves as a baseline for signal intensities in the vasculature. Upon contrast injection (rate: 0.5-2 ml/s), the contrast agent distributes first in the vascular lumen leading to signal enhancement in the vessel lumen and subsequently extravagates into the vessel wall. Vessel wall signal enhancement is dependent on overall vascular flow, amount of contrast agent extravasation from the neovasculature and reflux of contrast agent from the extravascular space back to plasma. Signal enhancement time curves can be generated from the DCE-MRI images and analyzed either by voxel or region of interest (ROI). From the analysis, a parametric map for K^{trans} can be created that describes the microvascular volume and permeability at each location. Both "black blood" and "bright blood" imaging sequences have been used for DCE-MRI in atherosclerosis imaging[201]. Black blood imaging sequences offer the advantage of better vessel wall delineation whereas bright blood imaging sequences allow individual luminal contrast concentration determination, corresponding to the arterial input function (AIF). Irrespective of imaging approach a compromise between spatial and temporal resolution is necessary. Specifically, for adequate vessel wall delineation DCE-MRI requires imaging with high resolution, which may impact on temporal resolution. Currently, an in-plane spatial resolution of 0.5x0.5 mm^2 is applied in clinical and pre-clinical (rabbit) studies with pre-clinical studies applying a temporal resolution of 5 s (rabbits) for 2D and 30 s for 3D approaches. Clinical studies apply a temporal resolution of about 15-30s.

In order to quantify individual contrast parameters, the local signal intensities need to be transformed to Gadolinium concentrations. For this purpose, several quantitative pharmacokinetic models have been developed to describe the accumulation kinetics[201]. The models are based on a two-compartment model and describe the relationship between blood plasma contrast concentration and the extracellular extravascular space[202]. The modified Tofts model with Patlak assumption was validated in carotid atherosclerotic plaques and is commonly used[203]:

$$C_{\text{tissue}}(t) = v_{\text{p}}C_{\text{p}}(t) + K^{\text{trans}} \int_0^t C_{\text{p}}(t')dt'.$$

The parameters, C_{tissue} is the tissue (= vessel wall) contrast concentration, C_p signifies the plasma contrast concentration, v_{p} (%) represents the fractional microvascular volume, K^{trans} denotes permeability (min^{-1}) and t is time.

Quantitative approaches have been validated in human studies. The first study by Kerwin et al.[204] applied a bright blood sequence and demonstrated a strong correlation between neovessel density on histological specimens of human carotid plaques and fractional microvascular volume (v_{p}) derived from DCE-MRI. It applied a 2D bright blood imaging sequence with Patlak pharmacokinetic modeling. The same group using the same approach, furthermore, demonstrated a strong positive correlation between v_{p}, K^{trans}, and plaque macrophage content, neovascularization and loose matrix[205]. This approach was extended to examine different plaque components including the necrotic core (NC), intraplaque hemorrhage (IPH), loose matrix (LM), fibrous tissue (FIB) and calcification (CA). LM and FIB demonstrated relatively high values for K^{trans} and v_{p} whereas NC, IPH and CA displayed significantly lower K^{trans} and v_{p} values[206].

As an alternative to quantitative model-based approaches, semi-quantitative non-model based approaches, most notably, area under the enhancement curve (AUC), have been applied as a surrogate marker for neovascularization in atherosclerosis[207]. The advantage of semi-quantitative approaches are the relatively easy implementation and analysis. A limitation is that the assessed AUC value is influenced by multiple pathophysiological factors e.g. neovessel density, neovessel permeability, neovessel flow, and contrast reflux. Thus, a difference in AUC may be related to any one or a combination of factors and it is, therefore, difficult to attribute a difference in AUC to a single underlying causative element.

The assessment of AUC as a surrogate marker of neovascularization has been specifically useful in combination with black blood imaging sequences where the blood plasma MR signal is suppressed and therefore the pharmacokinetic modeling cannot be easily performed. DCE-MRI assessing AUC values has been validated and a positive correlation with plaque neovessel count in atherosclerotic rabbits was demonstrated by Calcagno et al.[207]. Furthermore, a progressive increase of plaque AUC and K^{trans} was observed in atherosclerotic rabbit aortas between 3 and 6 months atherosclerotic diet[208].

1.3.2.1.4 DCE-MRI and Markers of Plaque Inflammation and Vulnerability

Macrophages are a critical component of atherosclerotic plaques and a correlation between plaque macrophage content and DCE-MRI was found in human and rabbit studies[205,207]. Several clinical studies investigated the association between DCE-MRI parameters and plaque inflammation as assessed by ^{18}F-fluorodeoxyglucose (FDG) PET/CT[209-212]. The results were mixed in that positive and negative correlations were observed. It appears that the correlation was dependent on the clinical state of the patients. Positive correlations were observed in symptomatic and advanced carotid plaques whereas early plaques or asymptomatic plaques showed a negative correlation or no correlation.

A link between intraplaque hemorrhage and neovascularization is present in pathological studies and was proposed as a marker of plaque vulnerability[64,114]. Indeed, an association between the presence of intraplaque hemorrhage and increase adventitial K^{trans} was observed in carotid arteries in symptomatic patients with moderate to severe carotid stenosis[213].

1.3.2.1.5 Monitoring Therapeutic Interventions with DCE-MRI

DCE-MRI to monitor therapeutic interventions was applied in rabbit and human studies. In an atherosclerotic rabbit study, a rapid and significant change in AUO was observed between pre- and post treatment with liposomal prednisolone administration in atherosclerotic rabbits[214]. A human, carotid artery study, demonstrated a reduction in K^{trans} upon intensive statin therapy in carotid arteries[215]. Another human DCE-MRI study as selected from the AIM High-trial[216] demonstrated an inverse relationship between the length of statin therapy and v_p (plaque microvascular function)[217]. Statins lower cholesterol and have anti-inflammatory properties and plaque stabilizing properties[218]. Other trials have applied DCE-MRI alongside ^{18}F-FDG-PET[211,219]. Overall, the results indicate that DCE-MRI can be used to monitor plaque changes upon therapeutic intervention.

1.3.2.1.6 Novel DCE-MRI Techniques

A limitation of the single or multi-slice DCE-MRI is the limited coverage along the vasculature. To overcome this limitation, 3D isotropic high-resolution DCE-MRI was introduced, recently. Atherosclerotic rabbit validation studies demonstrated a positive correlation between AUC by 3D black blood DCE-MRI and endothelial permeability as assessed by fluorescent albumin or Evans blue dye[220-222]. A human carotid study in patients with advanced carotid

artery disease demonstrated a significant correlation between bright blood 3D DCE-MRI determined permeability and ^{18}F-FDG PET/CT[210]. Additionally, K^{trans} demonstrated a significant correlation with histologically determined neovasculature (CD 31 immune staining) and inflammation [CD68 and major histocompatibility complex II (MHCII) immune staining]. Another human carotid study confirmed a correlation between vessel- and adventitial K^{trans} and plaque neovasculature[223].

Despite these advances a major limitation of vascular DCE-MRI is the precise quantification of atherosclerotic neovasculature and permeability. Black blood imaging approaches are limited by the lack of kinetic modeling. Bright blood imaging, on the other hand, may suffer from inaccuracies when estimating AIF from MR signal itself. This is related to an inadequate temporal resolution to assess the fast contrast agent kinetics within the vessel lumen and inadequate dynamic range for much lower T1 values within the vessel as compared to the vessel wall[224]. To overcome these limitations, so-called interleaved imaging approaches were applied with either 2D or 3D imaging[225-227]. This allows for optimized sampling of both blood and plaque compartments by applying optimized imaging sequences for each.

Most recently, a quantitative T1 mapping dynamic contrast-enhanced sequence was introduced[228]. A high temporal resolution as low as 500 ms was achieved and permits T1 mapping with high spatiotemporal resolution, thereby. enabling accurate modeling of AIF and plaque response curves. This approach could represent a significant advancement for DCE-MRI.

1.3.2.2 Computed Tomography

Computed tomography (CT) generates 3-dimensional images of a body portion. It is based on the principle that the density of the tissue passed by the x-ray beam can be determined from its attenuation coefficient. CT images, therefore, are a density representation of the imaged tissue. The basic setup is an x-ray source and detectors mounted on opposite sides of a gantry. The gantry continuously rotates and cross-sectional images are then obtained as the patient moves through the gantry. The acquired data is then processed ("stacked") to generate a three-dimensional volumetric dataset. Technical progress over the last decades has paved the way for coronary artery assessment using computed tomography secondary to dramatic increases in spatial and temporal resolution[229]. Particularly the introduction of faster gantry rotation speeds, increased number of detectors, decreased collimator slice thickness and use of dual x-ray sources have contributed to

this development[230]. Currently, multi-detector computed tomography (MDCT) systems for cardiac applications range from 64 up to 320 detectors and allow imaging of the heart in less than 1 sec. The temporal resolution can reach around 65–75 ms for a dual source system. The isotropic spatial resolution is around 0.5 mm (best achievable 0.35 mm). Recently, a novel high-resolution system was introduced with a resolution 0.25 mm which is comparable to invasive coronary angiography[231].

1.3.2.2.1 Coronary Calcium Scoring

Coronary calcium is a marker for coronary artery disease and correlates with cardiovascular risk[232]. Coronary artery calcium (CAC) scoring is a common and facile screening tool for atherosclerosis. It is used for improved risk stratification in asymptomatic patients with intermediate risk per Framingham score [10-20%, 10-year risk for major adverse cardiovascular events (MACE)]. CAC is most commonly determined with the Agatston scoring system[233]. It is a summed score, calculated by the product of calcium density factor (weighting factor derived from density in Hounsfield units [HU]) above a threshold of 130 HU) multiplied by the calcified area. It has an excellent negative predictive value and a score of 0 confers a low risk of coronary heart disease (CHD) death or myocardial infarction (0.4% over 3-5years)[234]. The relative risk for CHD death or myocardial infarction compared to a CAC score =0 increases significantly with increasing CAC scores. A CAC score ranging from 100 to 400 confers a relative risk (RR) = 4.3 (95% CI = 3.1 to 6.1; $p < 0.0001$). A high CAC scores of 400 to 1000 and very high, greater than 1000, imply a RR risk of 7.2 (95% CI = 5.2 to 9.9, $p < 0.0001$) and 10.8 (95% CI = 4.2 to 27.7, p less < 0.0001), respectively.

1.3.2.2.2 Coronary Computed Tomography Angiography (CCTA)

Coronary Computed tomography angiography (CCTA) can image the vessel lumen and detect a significant degree of stenosis with strong correlation with invasive coronary angiography and excellent sensitivity ($\geq 80\%$) and specificity (99%)[235]. It has an excellent negative predictive value with an event rate of ≈ 0.2/year[236]. CCTA has, furthermore, excellent diagnostic accuracy in plaque quantification with strong correlation with IVUS and slight overestimation of luminal area[237]. In contrast to invasive coronary angiography, CCTA has the ability to accurately delineate and quantify atherosclerosis plaque burden. Plaque burden has a high predictive value for adverse cardiovascular events and atherosclerosis extend positively correlates with cardiovascular risk[238]. This is in contrast to invasive assessment of thin cap fibroatheroma (TCFA) in the PROSPECT trial by VH-IVUS where low event rates (3.4% of

myocardial infarction or death) were observed[129]. Recently, computational fluid dynamics was introduced for cardiac CT to determine fractional flow reserve (FFR), FFR-CT. It is aimed at the identification of hemodynamic significant coronary stenosis, which may lead to further improvement in diagnostic CCTA capabilities as demonstrated in pilot studies[239].

1.3.2.2.3 Atherosclerotic Plaque Characterization with CCTA

Despite its low tissue contrast compared to MRI, CCTA was applied for plaque characterization and detection of high-risk plaque features. The most established CCTA-obtained high-risk plaque features are 1) positive remodeling (PR), lipid-rich low attenuation plaque (LAP; < 30 HU), napkin-ring sign (NRS) and spotty calcifications (< 3 mm)[236].

Positive remodeling, as determined by the remodeling index (RI) is determined by dividing the vasculature size at maximal narrowing through the divided by reference vessel size. A threshold of (RI) ≥ 1.1 was determined to be the most sensitive PR when comparing CCTA to IVUS[240]. Invasive studies demonstrate the correlation with PR and extent of necrotic core[241]. Concordant results were found in a human study when comparing CCTA and invasive imaging where PR positive plaques had larger necrotic cores and correlated with the presence of thin-cap fibroatheroma (TCFA) on VH-IVUS[242]. Low Fibrous cap thickness of 76 ± 24 μm as determined by OCT correlated with the presence of PR and low attenuation plaque (LAP) on CCTA[243]. Larger fibrous cap sizes occurred with the presence of either LAP or PR alone[243].

In terms of risk prediction, a significant larger plaque area and PR by CCTA was found in culprit lesions in patients with acute coronary syndromes (ACS)[244]. The simultaneous presence of both LAP and PR conferred a significantly increased risk of ACS as compared to the presence of either LAP or PR alone[245]. Currently, the role of spotty calcification remains unclear with some studies conferring positive risks whereas others showed no association[246].

The concept of napkin ring sign (NRS) as a signature CT feature of high-risk plaques has gained a lot of interest[247]. It is defined by the presence of a low attenuation area surrounded by an area of higher attenuation (but < 130 HU). As underlying pathophysiologic vascular components, were proposed: necrotic core, intra-plaque hemorrhage, contrast enhancement of vasa-vasorum, microcalcification as well as potentially healed plaque rupture. In a validation study, the presence of NRS in heart donors correlated with the

presence of plaque necrotic cores on autopsy[248] and demonstrated a high positive predictive value for the detection of advanced plaque and TCFA[249]. In-vivo studies comparing the CCTA derived NRS to OCT-derived TCFA have demonstrated in some studies a good correlation[250,251] whereas in another study no correlation[252] was observed. The discrepancy could be related to limitations of OCT for TCFA assessment[236]. In terms risk prediction, a prospective study demonstrated NRS by CCTA as an independent risk factor (hazard ratio 5.6, $p < 0.0001$) over a 2.3 year mean follow up[253].

1.3.2.2.4 Molecular Computed Tomography

Enhancing the diagnostic capabilities of computed tomography for molecular imaging is an attractive proposition as it would greatly enhance CT imaging capabilities[254,255]. The difficulty is to deliver enough contrast load to a relatively small target volume (e.g. atherosclerortic plaques) and the low sensitivity of computed tomography (millimolar range). Nanoparticle approaches appear to be the most promising in that respect as it allows the delivery of high payloads per target volume[256]. Traditionally, iodine-based contrast agents were used and recently, inorganic materials have been introduced. CT-contrast generation relies on the distinct attenuation coefficient. A higher atomic number with higher electron density results in a higher attenuation coefficient. Novel inorganic contrast agents carry high Z elements, such as ytterbium (Z = 70), gold (Z = 79), and bismuth (Z = 83) and, therefore, produce higher attenuation on CT. Higher Z elements are, furthermore, better suited for spectral CT. Spectral CT is an emerging imaging technology that besides traditional tomographic CT analysis allows the discrimination of metal-rich contrast agents based on the unique x-ray K-edge energy signatures of high Z -elements[255].

Molecular CT using gold-core high-density lipoprotein (HDL) was applied in atherosclerotic mice[257]. Gold-core HDL nanoparticle administration led to significant aortic plaque enhancement on μCT. Macrophage targeting was confirmed with histological analysis.
Hetero-bifunctional polyethyleneglycol coated gold nanoparticles targeted to CD4 have been applied in mice[258]. CD4 is expressed on macrophages and T cells and lymph node imaging was demonstrated with μCT. Ytterbium nanocolloids were proposed as thrombus imaging agents in atherosclerosis[259]. Bismuth nanoparticles were introduced as long-circulating contrast agents in mice[260].

Another approach to detect vascular inflammation by CT has been described, recently[261]. It is based on perivascular fat attenuation mapping and the calculation of a fat attenuation index (FAI). The pathophysiological basis is the paracrine effect of the inflamed vasculature on the surrounding perivascular fat. It causes phenotypic changes of peri-vascular adipose tissue secondary to the inhibition of the differentiation of small pre-adipocytes to large adipocytes. This is accompanied, by changes in the tissue composition and density (= increase in density). CT can be used to quantify the changes in tissue density and an FAI can be calculated. FAI showed excellent sensitivity and specificity for tissue inflammation when compared to FDG uptake. In-vivo, FAI identified subclinical coronary artery disease (CAD) as well as dynamic changes of perivascular fat secondary to changes in vascular inflammation as well as culprit plaques during acute coronary syndromes. This approach was validated in a post-hoc analysis of the CRISP-CT study[262]. A high FAI value of ≥ 70.1 HU around the right coronary artery conferred a large increase in cardiac mortality and all-cause mortality.

1.3.2.3 Positron Emission Tomography (PET)

Myocardial perfusion using single photon emission computed tomography (SPECT) is the most commonly used nuclear imaging in cardiovascular medicine. It has relatively poor spatial resolution and allows for only suboptimal quantification. Over the last decades, positron emission tomography (PET) has revolutionized nuclear imaging and has become the preferred molecular imaging tool[263]. Lately, PET has emerged as a molecular imaging technique for atherosclerosis. PET is a tomographic imaging technique based on detecting two time-coincident high- energy photons (511 keV), from the emission of a positron-emitting radioisotope. The photons are generated from an annihilation event with an electron that occurs 1-2 mm from the emitted positron. The photons travel at the opposite directions along a straight line with a resulting angle of 180°. Two simultaneous events are registered as "true" whereas other events are rejected as scatter. Registration is accomplished by a PET scanner outside the body that applies detectors consistent of scintillator crystals coupled to photomultipliers. PET has a resolution of currently 3-4 mm with experimental systems permitting < 1 mm resolution[264,265]. PET is most commonly combined as a hybrid imaging technique with computed tomography and lately with magnetic resonance imaging. CT and MRI provide anatomical information as well as attenuation

correction. The most widely used radioisotope is fluorine 18 (^{18}F). Various PET tracers have been applied for inflammation in atherosclerosis.

1.3.2.3.1 ^{18}F–fluorodeoxyglucose (FDG)–PET/CT

^{18}F-fluorodeoxyglucose (FDG) is the most commonly used PET imaging agent and has been applied for the detection of plaque inflammation[266]. It is based on avid uptake of ^{18}F-FDG in metabolically active cells such as activated macrophages and neutrophils. FDG competes with glucose and enters cells via glucose transporter (e.g. GLUT 1) and undergoes phosphorylation by hexokinase to yield FDG-6–phosphate but does not get further metabolized. ^{18}F-FDG-6–phosphate has low membrane permeability and it, therefore, progressively accumulates in cells in proportion of the cells glycolytic rate. The intracellular accumulation of ^{18}F-FDG-6–phosphate can then be imaged and quantified with PET with very high sensitivity in the picomolar range[265].

Pro-inflammatory macrophage activation and M1 polarization induces large increases in glycolysis[66] and vascular FDG uptake closely correlates with macrophage content in animal[267,268] and human[269-271] studies. ^{18}F-FDG PET/CT Imaging of large vasculature (aorta, iliac- and femoral arteries) is highly reproducible[272]. The degree of ^{18}F-FDG vascular uptake correlates with high risk features on CTA and histology in carotid plaques[273] and lipid rich plaques on MRI[274]. ^{18}F-FDG uptake, furthermore, can differentiate between symptomatic and asymptomatic carotid atheroma[271,275] and predict recurrence of cerebrovascular events[276].

Relatively small retrospective studies have demonstrated a positive predictive value of ^{18}F-FDG plaque uptake to determine future cardiovascular risk beyond calcium scoring and Framingham risk score[277,278]. In a prospective study of 1089 subjects, high carotid atheroma ^{18}F-FDG uptake predicted cardiovascular events independent of traditional risk factors and carotid intimal media thickness[279].

Inflammatory states are risk factors for atherosclerosis and patients with rheumatoid arthritis[280], Psoriasis[281], HIV[282] and Periodontitis[283] have increased vascular ^{18}F-FDG uptake. Additionally, a direct link between vascular ^{18}F-FDG uptake and ^{18}F-FDG uptake in hematopoietic tissues (particularly the spleen) exists and predicts future cardiovascular events[284].

^{18}F-FDG PET/CT was successfully applied in multiple drug intervention trials and was, furthermore, used as a surrogate marker for clinical outcomes[285].

A non-response on ^{18}F-FDG-PET-CT upon drug intervention anticipated a lack of efficacy in clinical outcomes trials[285].

^{18}F-FDG PET/CT, however, is limited to larger vessels as the detection of coronary ^{18}F-FDG uptake is impeded by the considerable ^{18}F-FDG uptake of the adjacent myocardium and cardiac motion[286]. Protocols using a low carbohydrate and high-fat diet to suppress myocardial ^{18}F-FDG uptake been developed to circumvent this limitation but have not gained widespread adaption[287].

1.3.2.3.2 ^{18}F-sodium fluoride (NaF)-PET/CT

Recently, a widely available PET agent, ^{18}F-sodium fluoride- ^{18}F-NaF, first introduced in 1962 for the detection of osseous metastasis[288] was introduced for imaging of arterial microcalcification[289,290]. Plaque microcalcification represents a vulnerable stage of plaque development. It occurs at regions with intense inflammation typically around the lipid pool/necrotic core. It is a site where macrophages undergo incomplete efferocytosis. The resulting apoptotic bodies and matrix vesicles surrounding the necrotic core form then a nidus for calcification[291].

Mechanistically, ^{18}F-NaF binds onto the surface hydroxyapatite crystals and subsequently exchanges its hydroxyl groups (OH-) with ^{18}F to form fluorapatite[292]. The ionic exchange requires a short distance between hydroxyapatite and capillary flow and binding is dependent on the surface area of hydroxyapatite[293]. Furthermore, [18]F -NaF binding to microcalcification is inversely correlated with the size of microcalcifications[294]. In clinical studies, NaF uptake co-localized in 88% with CT detected calcification but only 12% of CT positive calcification sites demonstrated NaF uptake as well[289]. Vascular NaF uptake, furthermore, is highest with the lowest density (< 210 HU) calcification, compared to medium- (211-510 HU) and dense (> 510 HU) calcification supporting the preferential binding of NaF to early calcification sites[295]. Interestingly, in a dual tracer study, poor congruence between vascular ^{18}F-FDG and ^{18}F-NaF uptake was observed as only 6.5% of lesions demonstrated co-localization between each tracer[296]. The results suggest, that ^{18}F-FDG and ^{18}F-NaF uptake is associated with different pathologic stages of atherosclerotic plaques. It appears that ^{18}F-FDG PET detects earlier more inflamed lesions whereas ^{18}F-NaF detects more advanced and potential more vulnerable lesions[297].

Coronary ^{18}F-NaF PET/CT imaging does not suffer the same limitations as coronary ^{18}F-FDG PET/CT as there is negligible myocardial uptake. Small scale clinical trials have demonstrated the effectiveness of ^{18}F-NaF PET/CT imaging of coronary atherosclerosis[298]. In this study, target to background activity (TBR) was higher in patients with coronary atherosclerosis and correlated with the calcium score (with the exemption that 40% of patients with scores of > 1,000 demonstrated normal uptake). Patients with higher NaF activity had a higher incidence of prior cardiovascular events and angina and had higher Framingham risk scores.

In a pilot study, post-myocardial infarction, 93% of culprit lesions showed strong NaF uptake[286]. In the same study, ^{18}F-NaF uptake was observed at the site of carotid plaque ruptures and was associated with active calcification, macrophage infiltration, apoptosis, and necrosis on histological specimens. Furthermore, 45% of patients with stable angina had atherosclerotic plaques with focal ^{18}F-NaF uptake and the plaques demonstrated high-risk features: vascular remodeling, microcalcification, and necrosis on invasive IVUS.

1.3.2.3.3 Novel PET Tracers
Novel PET tracers have been introduced and a selection is outlined, below.

^{68}Ga-DOTATATE
^{68}Ga-DOTATATE is widely used for the imaging of somatostatin-positive neuroendocrine tumors and binds the somatostatin receptor subtype 2 (SSTR2) on macrophages[299]. Coronary imaging using ^{68}Ga-DOTATATE is feasible as there is no significant myocardial uptake and was first demonstrated in a retrospective study in oncologic patients[300]. Its uptake in the coronary vasculature correlated strongly with coronary calcium content and atherosclerosis risk factor burden.
In a recent, prospective study of 42 patients ^{68}Ga-DOTATATE was compared against ^{18}F-FDG PET/CT for the detection of inflammation in coronary, carotid and aortic vessels[301]. The study applied a comprehensive validation of the imaging target. Preceding imaging the target SSTR2 gene expression was assessed in blood-derived macrophages. SSTR2 gene expression occurred exclusively in "proinflammatory" M1 macrophages. ^{68}Ga-DOTATATE mean of maximum tissue-to-blood ratios (mTBRmax) identified culprit versus non-culprit arteries in patients with acute coronary syndrome and transient ischemic attack. ^{68}Ga-DOTATATE ligand binding to SSTR2 was confirmed in CD68-positive macrophage-rich carotid plaque regions, and carotid SSTR2 mRNA correlated highly with in-vivo ^{68}Ga-DOTATATE uptake.

^{68}Ga-DOTATATE mTBRmax, furthermore, predicted high-risk coronary computed tomography features and correlated with Framingham risk and ^{18}F-FDG uptake. In line with ^{68}Ga-DOTATATE mTBRmax, ^{18}F-FDG mTBRmax correctly differentiated culprit from non-culprit carotid lesions and high-risk from lower-risk coronary arteries. Coronary ^{18}F-FDG scans, however, were un-interpretable in 64% of patients. In contrast, all coronary 68Ga-DOTATATE PET scans were interpretable.

[68]Ga-Pentixafor

[68]Ga-pentixafor binds with nanomolar affinity to cytokine receptor CXCR4[302]. CXCR4 mediates the homing of progenitor cells in the bone marrow and regulates their mobilization into peripheral tissues upon injury or stress[303]. It is expressed on monocytes, differentiated macrophages and lymphocytes migrating into arterial plaques. CXCR4 is, furthermore, expressed by different cell types including smooth muscle progenitors cells and endothelial progenitor cells which both contribute to plaque progression. In an atherosclerotic rabbit study Hybrid PET/MRI demonstrated uptake of ^{68}Ga-pentixafor into rabbit atherosclerotic plaques[304]. This was confirmed by ^{125}I-pentixafor autoradiographies which correlated with macrophage-rich regions in atheroma of atherosclerotic rabbits. A small human sub-study in patients with carotid stenosis demonstrated an increased focal ^{125}I-pentixafor carotid artery uptake in some patients with carotid stenosis > 50%. Immuno-histochemistry of human carotid plaques demonstrated CXCR4 expression mostly in macrophage-rich areas (CD-68–positive).
Pilot in-vivo studies demonstrate vascular ^{68}Ga-pentixafor uptake to correlate with vascular calcification as well as risk factors of atherosclerosis[305]. Coronary ^{68}Ga-pentixafor PET/CT was recently performed and demonstrated its feasibility for discrimination between culprit and non-culprit coronary lesions post myocardial infarction[306].

[18]F-fluorodeoxymannose

Another interesting agent, an analog to ^{18}F-FDG, ^{18}F-fluorodeoxymannose was evaluated in atherosclerotic rabbits[307]. The tracer uptake correlated strongly with plaque macrophage content and was comparable to ^{18}F-FDG uptake. Mannose receptors are expressed on alternate type activated-M2 macrophages and its in-vivo detection could contribute to monitoring plaque regression strategies.

Necrostatin-1
A PET tracer to detect necroptosis based on the necroptosis inhibitor necrostatin-1 (Nec-1) has been proposed[84].

Other agents target, neovascularization: ^{18}F-Galacto-RGD[308]/ ^{68}Ga-NOTA-RGD[309], macrophage proliferation: ^{18}F-FLT[310], apoptosis: ^{18}F-ML-10[311], plaque hypoxia: ^{64}Cu-ATSM[312]/ ^{18}F-FMISO[313] and Oxidation-specific Epitopes: ^{89}Zr-LA25[314].

1.3.2.4 Multimodality Imaging

Using two or more imaging modalities attempts to overcome the limitations of a single imaging modality and/or act synergistically as in ^{18}F-FDG PET/CT or ^{18}F-NaF PET/CT. The CT- imaging component provides anatomical detail and attenuation correction whereas PET provides high sensitivity. The combination of PET and CT, however, leads to overall significant radiation exposure (average up to 14 mSv) per single scan[315]. PET/CT does not allow simultaneous acquisition of CT and PET, which can lead to misregistration. CT, furthermore, only allows limited plaque component discrimination secondary to inferior tissue contrast when compared to MRI.

Lately, hybrid PET/MRI has gained significant interest as an improved imaging tool in cardiovascular disease[316]. PET/MRI provides high tissue contrast for anatomic delineation of plaque components with high sensitivity to detect molecular targets as PET Images can be acquired simultaneously on integrated PET/MR scanners, thereby improving co-registration. PET/MRI, furthermore, allows for improved motion and partial volume correction. More challenging, however, has been the attenuation correction with PET/MR as compared with PET/CT. Decreased radiation exposure can be achieved by only having the PET component as a radiation source and the ability to apply dose reduction protocols. In vivo coronary PET/MR with FDG/NaF was demonstrated using a sophisticated imaging protocol with an average radiation dose of 7.2 mSv per scan[317].

REFERENCES

1.   Williams, K. J. & Tabas, I., *Curr. Opin. Lipidol.* 9, 471–474 (1998).
2.   Ross, R., *N. Engl. J. Med.* 340, 115–126 (1999).
3.   *WHO-FACT Sheet Cardiovascular disease* Available at: https://www. who.int/news-room/fact-sheets/detail/cardiovascular-diseases-(cvds). (Accessed: 4 January 2019)
4.   *Anitschkow & S. Chalatow (translated by Mary Z. Pelias, 1913). Arteriosclerosis* 3, 178–182 (1983).
5.   Mason, J. C. & Libby, P., *Eur. Heart J.* 36, 482–9c (2015).
6.   Zimmer, S., Grebe, A. & Latz, E., *Circ. Res.* 116, 323–340 (2015).
7.   Strong, J. P., *et al. JAMA* 281, 727–735 (1999).
8.   Nigro, P., Abe, J.-I. & Berk, B. C., *Antioxid. Redox Signal.* 15, 1405–1414 (2011).
9.   Zhang, X., Sessa, W. C. & Fernández-Hernando, C., *Front Cardiovasc Med* 5, 130 (2018).
10. Glass, C. K. & Witztum, J. L., *Cell* 104, 503–516 (2001).
11. Lusis, A. J., *Nature* 407, 233 (2000).
12. Swirski, F. K. & Nahrendorf, M., *Science* 339, 161–166 (2013).
13. Ley, K., et al. *Nat. Rev. Immunol.* 7, 678–689 (2007).
14. Tacke, F., et al. *J. Clin. Invest.* 117, 185–194 (2007).
15. Hilgendorf, I., et al. *Arterioscler. Thromb. Vasc. Biol*. 35, 272–279 (2015).
16. Moss, J. W. & Ramji, D. P., *Future Med. Chem.* 8, 1317–1330 (2016).
17. Peled, M. & Fisher, E. A., *Front Immunol* 5, 579 (2014).
18. Moore, K. J., Sheedy, F. J. & Fisher, E. A., *Nat. Rev. Immunol.* 13, 709–721 (2013).
19. van Gils, J. M., et al. *Nat. Immunol.* 13, 136–143 (2012).
20. Cybulsky, M. I., Cheong, C. & Robbins, C. S., *Circ. Res.* 118, 637–652 (2016).
21. Tabas, I. & Lichtman, A. H., *Immunity* 47, 621–634 (2017).
22. Döring, Y., et al. *Arterioscler. Thromb. Vasc. Biol*. 35, 288–295 (2015).
23. Döring, Y., Soehnlein, O. & Weber, C. *Circ. Res.* 120, 736–743 (2017).
24. Rayner, K. J., *Arterioscler. Thromb. Vasc. Biol*. 37, e75–e81 (2017).
25. Hansson, G. K., Libby, P. & Tabas, I., *J. Intern. Med.* 278, 483–493 (2015).
26. Nahrendorf, M. & Swirski, F. K., *Circ. Res.*119, 414–417 (2016).
27. Decano, J. L. & Aikawa, M., *Front Cardiovasc Med* 5, 97 (2018).
28. Miller, Y. I., et al. *Arterioscler. Thromb. Vasc. Biol*. 25, 1213–1219 (2005).

29. Stewart, C. R., et al. *Nat. Immunol.* 11, 155–161 (2010).
30. Duewell, P., et al. *Nature* 464, 1357–1361 (2010).
31. Razani, B., et al. *Cell Metab.* 15, 534–544 (2012).
32. Warnatsch, A., et al. *Science* 349, 316–320 (2015).
33. Murphy, A. J. & Tall, A. R., *Eur. Heart J.* 37, 1113–1121 (2016).
34. Nahrendorf, M. & Swirski, F. K. *Circ. Res. 116:884-894* (2015).
35. Swirski, F. K., et al. *J. Clin. Invest.* 117, 195–205 (2007).
36. Robbins, C. S., et al. *Circulation* 125, 364–374 (2012).
37. Yvan-Charvet, L., et al. *Science* 328, 1689–1693 (2010).
38. Murphy, A. J., et al. *J. Clin. Invest.* 121, 4138–4149 (2011).
39. Lee, S. D. & Tontonoz, P., *Atherosclerosis* 242, 29–36 (2015).
40. Gu, Q., *et al.* A. *Science* 363, 1085–1088 (2019).
41. Murphy, A. J., Dragoljevic, D. & Tall, A. R., *Front Immunol* 5, 490 (2014).
42. Seijkens, T., et al. *FASEB J.* 28, 2202–2213 (2014).
43. van Kampen, E., et al. *J. Leukoc. Biol.* 96, 833–841 (2014).
44. Westerterp, M., et al. *Circulation* 138, 898–912 (2018).
45. Bekkering, S., et al. *Arterioscler. Thromb. Vasc. Biol*. 34, 1731–1738 (2014).
46. van der Valk, F. M., et al. *Circulation* 134, 611–624 (2016).
47. Mitroulis, I., et al. *Cell* 172, 147–161.e12 (2018).
48. Christ, A., et al. *Cell* 172, 162–175.e14 (2018).
49. Cheng, S.-C. et al. *Science* 345, 1250684–1250684 (2014).
50. Phan, A. T., Goldrath, A. W. & Glass, C. K., *Immunity* 46, 714–729 (2017).
51. Keating, S. T. & El-Osta, A., *Circ. Res.* 116, 715–736 (2015).
52. Arts, R. J. W., Joosten, L. A. B. & Netea, M. G., *Semin. Immunol.* 28, 425–430 (2016).
53. Arts, R. J. W., et al. *Cell Metab.* 24, 807–819 (2016).
54. Bekkering, S., et al. *Cell* 172, 135–146.e9 (2018).
55. Goldberg, E. L. & Dixit, V. D., *Immunol. Rev.* 265, 63–74 (2015).
56. Horst, ter, R., et al. *Cell* 167, 1111–1124.e13 (2016).
57. Ong, S.-M., et al. *Cell Death Dis* 9, 266 (2018).
58. Riksen, N. P. & Netea, M. G., *Aging* 10, 2218–2219 (2018).
59. Jaiswal, S., et al. *N. Engl. J. Med.* 377, 111–121 (2017).
60. Ganeshan, K. & Chawla, A., *Annu. Rev. Immunol.* 32, 609–634 (2014).
61. Koelwyn, G. J., Corr, E. M., Erbay, E. & Moore, K. J., *Nat. Immunol.* 19, 526–537 (2018).
62. Galván-Peña, S. & O›Neill, L. A. J., *Front Immunol* 5, 420 (2014).
63. Björnheden, T., et al. *Arterioscler. Thromb. Vasc. Biol*. 19, 870–876 (1999).

64. Kolodgie, F. D., et al. *N. Engl. J. Med.* 349, 2316–2325 (2003).
65. Sluimer, J. C., et al*. J. Am. Coll. Cardiol.* 51, 1258–1265 (2008).
66. Tawakol, A., et al. *Arterioscler. Thromb. Vasc. Biol*. 35, 1463–1471 (2015).
67. Sarrazy, V., et al*. Circulation Research* 118, 1062–1077 (2016).
68. Groh, L., et al*. Semin Immunopathol* 40, 203–214 (2018).
69. Warburg, O., *Science* 123, 309–314 (1956).
70. Tannahill, G. M., et al. *Nature* 496, 238–242 (2013).
71. Robbins, C. S., et al. *Nat. Med.* 19, 1166–1172 (2013).
72. Chen, Y., Zhou, Z. & Min, W., *Front Physiol* 9, 1487 (2018).
73. Madamanchi, N. R. & Runge, M. S., *Circ. Res.* 100, 460–473 (2007).
74. Zhou, R., Yazdi, A. S., Menu, P. & Tschopp, J., *Nature* 469, 221–225 (2010).
75. Lichtman, A. H., et al. *J. Clin. Invest.* 123, 27–36 (2013).
76. Wolf, D. & Ley, K., *Circ Res.* 124, 315–327 (2019).
77. Sakaguchi, S., *Annu. Rev. Immunol.* 22, 531–562 (2004).
78. Mor, A., *et al. Eur. Heart J.* 27, 2530–2537 (2006).
79. George, J., et al. *Atherosclerosis* 222, 519–523 (2012).
80. Kimura, T., et al*. Circulation* 138, 1130–1143 (2018).
81. Tabas, I., *Arterioscler. Thromb. Vasc. Biol*. 25, 2255–2264 (2005).
82. Tabas, I., *Nat. Rev. Immunol.* 10, 36–46 (2010).
83. Vandenabeele, P., et al. *Nat. Rev. Mol. Cell Biol.* 11, 700–714 (2010).
84. Karunakaran, D., et al. *Sci Adv* 2, e1600224 (2016).
85. Kaczmarek, A., Vandenabeele, P. & Krysko, D. V., *Immunity* 38, 209–223 (2013).
86. Najjar, M., et al*. Immunity* 45, 46–59 (2016).
87. Van Vré, E. A., et al*. Arterioscler. Thromb. Vasc. Biol*. 32, 887–893 (2012).
88. Balasubramanian, K. & Schroit, A. J., *Annu. Rev. Physiol.* 65, 701–734 (2003).
89. Poon, I. K. H., et al. *Nat. Rev. Immunol.* 14, 166–180 (2014).
90. Lauber, K., et al*. Mol. Cell* 14, 277–287 (2004).
91. Fadok, V. A., et al*. J. Clin. Invest.* 101, 890–898 (1998).
92. Fadok, V. A., et al. *The Journal of Immunology* 166, 6847–6854 (2001).
93. Han, C. Z. & Ravichandran, K. S., *Cell* 147, 1442–1445 (2011).
94. Chawla, A., *Circ. Res.* 106, 1559–1569 (2010).
95. A-Gonzalez, N., et al*. Immunity* 31, 245–258 (2009).
96. Bouhlel, M. A., et al. *Cell Metab.* 6, 137–143 (2007).
97. Odegaard, J. I., et al*. Nature* 447, 1116–1120 (2007).
98. Odegaard, J. I., et al. *Cell Metab.* 7, 496–507 (2008).

99. Kang, K., et al. *Cell Metab.* 7, 485–495 (2008).

100. Scott, R. S., et al. *Nature* 411, 207–211 (2001).

101. Thorp, E., et al. *Arterioscler. Thromb. Vasc. Biol*. 28, 1421–1428 (2008).

102. Cai, B., et al*. J. Clin. Invest.* 127, 564–568 (2017).

103. Thorp, E., et al*.* S *J. Biol. Chem.* 286, 33335–33344 (2011).

104. Garbin, U., et al*. Cardiovasc. Res.* 97, 125–133 (2013).

105. Sather, S., et al*. Blood* 109, 1026–1033 (2007).

106. Kojima, Y., et al. *Nature* 536, 86–90 (2016).

107. Yurdagul, A., et al. *Front Cardiovasc Med* 4, 86 (2017).

108. Kasikara, C., et al. *J. Clin. Invest.* 128, 2713–2723 (2018).

109. Bäck, M., et al. *Nat Rev Cardiol* (2019). doi:10.1038/s41569-019-0169-2 [Epub ahead of print]

110. Fredman, G., et al*. Nat. Commun.* 7, 12859 (2016).

111. Bentzon, J. F., et al. *Circ. Res.* 114, 1852–1866 (2014).

112. Falk, E., et al. *Eur. Heart J.* 34, 719–728 (2013).

113. Virmani, R., et al*. J. Interv. Cardiol.* 15, 439–446 (2002).

114. Kolodgie, F. D., et al. *Heart* 90, 1385–1391 (2004).

115. Davies, M. J., et al. *Heart* 69, 377–381 (1993).

116. Libby, P., *J. Clin. Invest.* 123, 3201–3203 (2013).

117. Libby, P., *N. Engl. J. Med.* 368, 2004–2013 (2013).

118. Geng, Y. J. & Libby, P., *Am. J. Pathol.* 147, 251–266 (1995).

119. Clarke, M. C. H., et al*. Nat. Med.* 12, 1075–1080 (2006).

120. Flego, D., *J. Am. Coll. Cardiol.* 68, 2107–2117 (2016).

121. Sluimer, J. C. & Daemen, M. J*., Pathol.* 218, 7–29 (2009).

122. Sluimer, J. C., et al. *J. Am. Coll. Cardiol.* 53, 1517–1527 (2009).

123. Crombag, G. A. J. C., et al. *J Cardiovasc Magn Reson* 21, 15 (2019).

124. Parma, L., et al. *Eur. J. Pharmacol.* 816, 107–115 (2017).

125. Shioi, A. & Ikari, Y., *J. Atheroscler. Thromb.* 25, 294–303 (2018).

126. Janoudi, A., et al*. Eur. Heart J.* 37, 1959–1967 (2016).

127. Michail, M., et al*. Eur. Heart J. Cardiovasc. Imaging* 18, 613–620 (2017).

128. Brown, A. J., et al*. Circ. Cardiovasc. Imaging* 8, e003487 (2015).

129. Stone, G. W., et al*. N. Engl. J. Med.* 364, 226–235 (2011).

130. Calvert, P. A., et al. *JACC Cardiovasc Imaging* 4, 894–901 (2011).

131. Cheng, J. M., et al. *Eur. Heart J.* 35, 639–647 (2014).

132. Tearney, G. J., et al*. J. Am. Coll. Cardiol.* 59, 1058–1072 (2012).

133. Tearney, G. J., et al. *Circulation* 107, 113–119 (2003).

134. Di Vito, L., et al. *Eur. Heart J. Cardiovasc. Imaging* 16, 807–813 (2015).

135. Raffel, O. C., et al*. Arterioscler. Thromb. Vasc. Biol*. 27, 1820–1827 (2007).

136. MacNeill, B. D., et al. *J. Am. Coll. Cardiol.* 44, 972–979 (2004).

137. Galon, M. Z., et al. *Catheter. Cardiovasc. Interv.* 85, E108–15 (2015).
138. Phipps, J. E., et al. *JACC Cardiovasc Imaging* 8, 63–72 (2015).
139. Vorpahl, M., Nakano, M. & Virmani, R., *Eur. Heart J.* 31, 1889 (2010).
140. Nishimiya, K., et al. *Circ. J.* 78, 2516–2518 (2014).
141. Taruya, A., et al. *J. Am. Coll. Cardiol.* 65, 2469–2477 (2015).
142. Uemura, S., et al. *Eur. Heart J.* 33, 78–85 (2012).
143. Kitabata, H., et al. *Am. J. Cardiol.* 105, 1673–1678 (2010).
144. Amano, H., et al. *Am. J. Cardiol* 119, 1512–1517 (2017).
145. Kilic, I. D., et al. *Eur. Heart J. Cardiovasc Imaging* 16, 1299–1306 (2015).
146. Oemrawsingh, R. M., et al. *J. Am. Coll. Cardiol.* 64, 2510–2518 (2014).
147. Karlsson, S., et al. *Open Heart* 6, e000917 (2019).
148. Madder, R. D., et al. *JACC Cardiovasc. Interv.* 6, 838–846 (2013).
149. Madder, R. D., et al. *Catheter. Cardiovasc. Interv.* 86, 1014–1021 (2015).
150. Suter, M. J., et al. *JACC Cardiovasc. Imaging* 4, 1022–1039 (2011).
151. Jaffer, F. A., et al. *J. Am. Coll. Cardiol.* 57, 2516–2526 (2011).
152. Vinegoni, C. et al. *Sci. Transl. Medicine* 3, 84ra45–84ra45 (2011).
153. Verjans, J. W., et al. *JACC Cardiovasc. Imaging* 9, 1087–1095 (2016).
154. Ughi, G. J. *et al. JACC Cardiovasc. Imaging* 9, 1304–1314 (2016).
155. Ridgway, J. P., *J Cardiovasc. Magn. Reson.* 12, 71 (2010).
156. Donald, W., Elizabeth, A. M. & Martin, R. P., *MRI from Picture to Proton*. (2003).
157. Sanz, J. & Fayad, Z. A., *Nature* 451, 953–957 (2008).
158. Walter, T. C., et al. *Curr. Radiol. Rep.* 2, 40 (2014).
159. Dweck, M. R., et al. *JACC Cardiovasc. Imaging* 9, 306–316 (2016).
160. Cai, J.-M., et al. *Circulation* 106, 1368–1373 (2002).
161. Brinjikji, W., et al. *Journal of Neurosurgery* 124, 27–42 (2016).
162. Fan, Z. et al., *J Cardiovasc. Magn. Reson.* 16, 53 (2014).
163. Coolen, B. F., et al. *Magn. Reson. Med.* 75, 1008–1017 (2016).
164. Qi, H. *et al. Magn. Reson. Med.* 80, 2598–2608 (2018).
165. Cormode, D. P., et al. *Arterioscler. Thromb. Vasc. Biol*. 29, 992–1000 (2009).
166. Boverhof, D. R., et al. *Regul. Toxicol. Pharmacol.* 73, 137–150 (2015).
167. Jarzyna, P. A., et al. *Wiley Interdiscip. Rev. Nanomed. Nanobiotechnol.* 2, 138–150 (2010).
168. Tang, J., et al. *Curr. Cardiovasc. Imaging Rep* 5, 19–25 (2011).
169. Aime, S. & Caravan, *J. Magn. Reson. Imaging* 30, 1259–1267 (2009).
170. Phinikaridou, A., et al. *Circulation* 126, 707–719 (2012).
171. Phinikaridou, A., et al. *Circ. Cardiovasc. Imaging* 9, 496 (2016).

172. Lobbes, M. B. I., et al. *Investigative Radiology* 45, 275–281 (2010).

173. Engel, L.-C., et al. JACC Cardiovasc. Imaging 12, 297-306 (2019).

174. Nahrendorf, M., et al*. Circulation* 114, 1504–1511 (2006).

175. McAteer, M. A., et al. *Arterioscler. Thromb. Vasc. Biol*. 32, 1427–1435 (2012).

176. Moreno, P., et al. *CMM* 6, 457–477 (2006).

177. Winter, P. M., et al. *Circulation* 108, 2270–2274 (2003).

178. Winter, P.M., et al*. Arterioscler. Thromb. Vasc. Biol*. 26, 2103-2109 (2006).

179. Mulder, W. J. M., et al. *Magn. Reson. Med.* 58, 1164–1170 (2007).

180. Weissleder, R., Nahrendorf, M. & Pittet, M. J., *Nat. Mater* 13, 125–138 (2014).

181. Alam, S. R., et al. *J. Cardiovasc. Magn. Reson.* 17, 83 (2015).

182. Tang, T. Y., et al. *Arterioscler. Thromb. Vasc. Biol*. 29, 1001–1008 (2009).

183. Sadat, U., Usman, A. & Gillard, J. H., *Curr. Opin. Cardiol.* 32, 437–440 (2017).

184. Trivedi, R. A., et al. *Arterioscler. Thromb. Vasc. Biol*. 26, 1601–1606 (2006).

185. Tang, T. Y. et al. *J. Am. Coll. Cardiol.* 53, 2039–2050 (2009).

186. Degnan, A. J., et al*. Cerebrovasc. Dis.* 34, 169–173 (2012).

187. Wáng, Y. X. J. & Idée, J.-M., *Quant. Imaging. Med. Surg.* 7, 88–122 (2017).

188. Smits, L. P., et al. *Atherosclerosis* 263, 211–218 (2017).

189. van Heeswijk, R. B., et al. *Radiology* 275, 421–429 (2015).

190. Bulte, J. W. M., *Nature Biotechnology 2005 23:11* 23, 945–946 (2005).

191. Lewis, A. J. M., et al. *Circ. Res.* 122, 1084–1093 (2018).

192. Ardenkjaer-Larsen, J. H., et al. *PNAS.* 100, 10158–10163 (2003).

193. Miller, Y. I. et al*. Circ. Res.* 108, 235–248 (2011).

194. Briley-Saebo, K. C., et al. *J. Am. Coll. Cardiol.* 59, 616–626 (2012).

195. Briley-Saebo, K. C., et al. *J. Am. Coll. Cardiol.* 57, 337–347 (2011).

196. Briley-Saebo, K. C., et al. *Circulation* 117, 3206–3215 (2008).

197. Burtea, C., et al. *Arterioscler. Thromb. Vasc. Biol.* 32, e36–48 (2012).

198. Cheng, D., et al*. D. ACS Appl. Mater. Interfaces* 7, 2847–2855 (2015).

199. Rashid, I., et al*. Eur. Heart J.* 39, 3301–3310 (2018).

200. Salem, A. & O'Connor, J. P. B., *Magnetic Resonance Imaging Clinics of North America* 24, 45–56 (2016).

201. van Hoof, R. H. M., et al. *Curr. Atheroscler. Rep.* 18, 33 (2016).

202. O'Connor, J. P. B., et al*. Br. J. Radiol.* 84 Spec No 2, S112–20 (2011).

203. Gaens, M. E., et al. *Radiology* 266, 271–279 (2013).

204. Kerwin, W., et al. *Circulation* 107, 851–856 (2003).
205. Kerwin, W. S. et al. *Radiology* 241, 459–468 (2006).
206. Chen, H. et al. *Magn. Reson. Med.* 64, 567–573 (2010).
207. Calcagno, C. et al. *Arterioscler. Thromb. Vasc. Biol.* 28, 1311–1317 (2008).
208. Chen, H., et al. *Magn. Reson. Med.* 69, 1712–1720 (2013).
209. Truijman, M. T. B., et al. *Stroke* 44, 3568–3570 (2013).
210. Taqueti, V. R. et al. *Circ. Cardiovasc. Imaging* 7, 920–929 (2014).
211. Calcagno, C., *et al. Eur. J. Nucl. Med. Mol. Imaging* 40, 1884–1893 (2013).
212. Wang, J., et al. *Stroke* 45, 1842–1845 (2014).
213. Sun, J., et al. *Stroke* 44, 1031–1036 (2013).
214. Lobatto, M. E., et al. *Mol. Pharm.* 7, 2020–2029 (2010).
215. Dong, L. et al. *Radiology* 260, 224–231 (2011).
216. AIM-HIGH Investigators et al. *N. Engl. J. Med.* 365, 2255–2267 (2011).
217. O'Brien, K. D., et al. *Atherosclerosis* 245, 74–81 (2016).
218. Kwak, B. R., Mulhaupt, F. & Mach, F., *Autoimmunity Reviews* 2, 332–338 (2003).
219. Calcagno, C., et al. *JACC Cardiovasc Imaging* 11, 291–301 (2018).
220. Calcagno, C., et al. *NMR Biomed* 28, 1304–1314 (2015).
221. Kim, Y. *et al. PNAS* 111, 1078–1083 (2014).
222. Lobatto, M. E., et al. *ACS Nano* 9, 1837–1847 (2015).
223. van Hoof, R. H. M., et al. *J. Magn. Reson. Imaging* 46, 1053–1059 (2017).
224. Coolen, B. F., et al. *Magn. Reson. Mater. Phy.* 31, 201–222 (2017).
225. Calcagno, C., et al. *J Cardiovasc Magn Reson* 15, 42 (2013).
226. Mendes, J., et al. *Magn. Reson. Med.* 72, 816–822 (2014).
227. Qi, H., et al. *Magn. Reson. Med.* 79, 1334–1344 (2018).
228. Wang, N. et al. *Magn. Reson. Med.* 81, 2302–2314 (2019).
229. Achenbach, S., *J. Am. Coll. Cardiol.* 48, 1919–1928 (2006).
230. Lewis, M. A., et al. *Br J Radiol* 89, 20160376 (2016).
231. Johns Hopkins Medicine First in U.S. to Install Canon Medical's Aquilion Precision. Available at: https://www.businesswire.com/news/home/20190319005267/en/Johns-Hopkins-Medicine-U.S.-Install-Canon-Medical%E2%80%99s. (Accessed: 4 May 2019)
232. Greenland, P., et al. *J. Am. Coll. Cardiol.* 72, 434–447 (2018).
233. Agatston, A. S., et al. *J. Am. Coll. Cardiol.* 15, 827–832 (1990).
234. Greenland, P., et al. *Circulation* 122, e584–636 (2010).
235. Sandfort, V., et al, *Circ. Cardiovasc. Imaging* 8, e003316 (2015).

236. Rodriguez-Granillo, G. A., et al. *Eur. Heart J. Cardiovasc. Imaging* 17, 481–491 (2016).
237. Voros, S., et al. *JACC Cardiovasc. Imaging* 4, 537–548 (2011).
238. Min, J. K., et al. *J. Am. Coll. Cardiol.* 50, 1161–1170 (2007).
239. Min, J. K., et al. *JACC Cardiovasc. Imaging* 8, 1209–1222 (2015).
240. Gauss, S., et al. *Heart* 97, 991–997 (2011).
241. Rodriguez-Granillo, G. A., et al. *Heart* 92, 388–391 (2006).
242. Kröner, E. S. J., et al. *Am. J. Cardiol.* 107, 1725–1729 (2011).
243. Sato, A., et al. *Int. J. Cardiol.* 182, 419–425 (2015).
244. Thomsen, C. & Abdulla, J., *Eur. Heart J. Cardiovas.c Imaging* 17, 120–129 (2016).
245. Motoyama, S., et al. *J. Am. Coll. Cardiol.* 66, 337–346 (2015).
246. Bom, M. J., et al. *Circ. Cardiovasc. Imaging* 10, 1166 (2017).
247. Maurovich-Horvat, P., et al. *JACC Cardiovasc Imaging* 3, 440–444 (2010).
248. Seifarth, H., et al. *Atherosclerosis* 224, 90–96 (2012).
249. Maurovich-Horvat, P., et al. *JACC Cardiovasc Imaging* 5, 1243–1252 (2012).
250. Ito, T., et al. *Am. J. Cardiol.* 107, 1270–1277 (2011).
251. Kashiwagi, M., et al. *JACC Cardiovasc. Imaging* 2, 1412–1419 (2009).
252. Nakazato, R., et al. *Eur. Heart J. Cardiovasc. Imaging* 16, 373–379 (2015).
253. Otsuka, K., et al. *JACC Cardiovasc. Imaging* 6, 448–457 (2013).
254. Lanza, G. M. & Pan, D., *Contrast Media & Molecular Imaging* 9, 1–2 (2014).
255. Danad, I., *et al. JACC Cardiovasc Imaging* 8, 710–723 (2015).
256. La Vega, De, J. C. & Häfeli, U. O., *Contrast Media & Molecular Imaging* 10, 81–95 (2015).
257. Cormode, D. P., et al. *Nano Lett.* 8, 3715–3723 (2008).
258. Eck, W., *et al. Nano Lett.* 10, 2318–2322 (2010).
259. Pan, D., et al. *ACS Nano* 6, 3364–3370 (2012).
260. Rabin, O., *et al. Nat. Mater* 5, 118–122 (2006).
261. Antonopoulos, A. S. et al. *Sci. Transl. Med.* 9, eaal2658 (2017).
262. Oikonomou, E. K., et al. *The Lancet* 392, 929–939 (2018).
263. Hess, S., et al. *Acad. Radiol.* 21, 232–249 (2014).
264. Vaquero, J. J. & Kinahan, P., *Annu. Rev. Biomed. Eng.* 17, 385–414 (2015).
265. Rudd, J. H. F., et al. *Arterioscler. Thromb. Vasc. Biol*. 29, 1009–1016 (2009).
266. Evans, N. R., et al. *Curr Atheroscler. Rep.* 18, 30 (2016).

267. Hyafil, F., et al. *J. Nucl. Med.* 50, 959–965 (2009).
268. Davies, J. R., et al. *Int. J. Cardiovasc. Imaging* 26, 41–48 (2010).
269. Tawakol, A., et al. *J. Am. Coll. Cardiol.* 48, 1818–1824 (2006).
270. Liu, J., *et al. Int J Cardiovasc Imaging* 32, 145–152 (2016).
271. Rudd, J. H. F., et al. *Circulation* 105, 2708–2711 (2002).
272. Rudd, J. H. F., et al. *J. Nucl. Med.* 49, 871–878 (2008).
273. Figueroa, A. L. et al. *Circ. Cardiovasc. Imaging* 5, 69–77 (2012).
274. Silvera, S. S., et al. *Atherosclerosis* 207, 139–143 (2009).
275. Skagen, K., et al. *Int. J. Stroke* 10, 730–736 (2015).
276. Marnane, M., et al. *Ann. Neurol.* 71, 709–718 (2012).
277. Rominger, A., et al. *J. Nucl. Med.* 50, 1611–1620 (2009).
278. Figueroa, A. L., et al. *JACC Cardiovasc. Imaging* 6, 1250–1259 (2013).
279. Moon, S. H., et al. *JACC Cardiovasc. Imaging* 8, 949–956 (2015).
280. Emami, H., et al. *JACC Cardiovasc. Imaging* 7, 959–960 (2014).
281. Rose, S., et al. *Arthritis Res. Ther.* 16, R161 (2014).
282. Subramanian, S., et al. *JAMA* 308, 379–386 (2012).
283. Fifer, K. M., et al. *J. Am. Coll. Cardiol.* 57, 971–976 (2011).
284. Emami, H., et al. *JACC Cardiovasc. Imaging* 8, 121–130 (2015).
285. Joseph, P. & Tawakol, A., *Eur. Heart J.* 37, 2974–2980 (2016).
286. Joshi, N. V., et al. *Lancet* 383, 705–713 (2014).
287. Wykrzykowska, J., et al. *J. Nucl. Med.* 50, 563–568 (2009).
288. Blau, M., Nagler, W. & Bender, M. A., *J. Nucl. Med.* 3, 332–334 (1962).
289. Derlin, T., et al. *J. Nucl. Med.* 51, 862–865 (2010).
290. Derlin, T., et al. *J. Nucl. Med.* 52, 362–368 (2011).
291. Nakahara, T., et al. *JACC Cardiovasc. Imaging* 10, 582–593 (2017).
292. Blau, M., Ganatra, R. & Bender, M. A., *Seminars in Nuclear Medicine* 2, 31–37 (1972).
293. Irkle, A., et al. *Nat. Commun.* 6, 7495 (2015).
294. Creager, M. D., et al. *Circ. Cardiovasc. Imaging* 12, 150 (2019).
295. Fiz, F., et al. *J. Nucl. Med.* 56, 1019–1023 (2015).
296. Derlin, T., et al. *J. Nucl. Med* 52, 1020–1027 (2011).
297. Nakahara, T., & Strauss, H. W., *Eur. J. Nucl. Med. Mol. Imaging* 44, 858–860 (2017).
298. Dweck, M. R., *et al. J. Am. Coll. Cardiol.* 59, 1539–1548 (2012).
299. Dalm, V. A. S. H., et al. *Am. J. Physiol. Endocrinol. Metab.* 285, E344–53 (2003).
300. Rominger, A. et al. *J J. Nucl. Med* 51, 193–197 (2010).
301. Tarkin, J. M. et al. *J. Am. Coll. Cardiol.* 69, 1774–1791 (2017).
302. Gourni, E. et al. *J. Nucl. Med.* 52, 1803–1810 (2011).
303. Döring, Y., et al. *Front Physiol* 5, 212 (2014).

304. Hyafil, F., et al. *J. Nucl. Med.* 58, 499–506 (2017).
305. Weiberg, D., et al. *J. Nucl. Med.* 59, 266–272 (2018).
306. Derlin, T., et al. *Eur. J. Nucl. Med. Mol. Imaging* 45, 1934–1944 (2018).
307. Tahara, N., et al. *Nat. Med.* 20, 215–219 (2014).
308. Beer, A. J., et al. *JACC Cardiovasc. Imaging* 7, 178–187 (2014).
310. Paeng, J., C. et al. *Ann. Nucl. Med* 27, 847–854 (2013).
311. Ye, Y.-X., et al. *Circ. Res.* 117, 835–845 (2015).
312. Hyafil, F. et al. *Mol. Imaging* 14, 433–442 (2015).
313. Nie, X. et al. *J. Nucl. Med.* 57, 2006–2011 (2016).
314. Mateo, J., et al. *Circ. Cardiovasc. Imaging* 7, 312–320 (2014)
315. Senders, M. L., et al. *J. Am. Coll. Cardiol.* 71, 321–335 (2018).
316. Kaushik, A., et al. *Indian J. Med. Res.* 142, 721–731 (2015).
317. Robson, P. M., et al. *JACC Cardiovasc. Imaging* 10, 1165–1179 (2017).
318. Robson, P. M., et al. *JACC Cardiovasc. Imaging* 10, 1103–1112 (2017).

Imaging Strategies for the Detection of Inflammation in Atherosclerosis

Chapter 2

Well-defined, multifunctional nanostructures of a paramagnetic lipid and a lipopeptide for macrophage imaging

Based on

Esad Vucic, Honorius M.H.F. Sanders, Francesca Arena, Enzo Terreno, Silvio Aime, Klaas Nicolay, Eik Leupold, Margitta Dathe, Nico A.J.M. Sommerdijk, Zahi A. Fayad, Willem J.M. Mulder

Author contribution: Esad Vucic: designed and performed experiments, analyzed data and revised the manuscript.

ABSTRACT

In the field of nanomedicine there is a great demand for technologies that allow the creation of self-assembled structures of which the size and morphology can be accurately controlled. In the current study, we report a nanoparticle platform that is composed of a paramagnetic lipid and a fluorescently labeled lipopeptide. By judiciously controlling the ratio of the aforementioned amphiphilic molecules a variety of well-defined nano-sized supramolecular structures with different sizes and morphologies could be created. The hydrodynamic radii of the different structures were determined by dynamic light scattering. Cryo-TEM revealed the aggregate morphology to vary from small micellar structures to plate-like and even full grown ribbons of which the aspect ratios varied from a diameter of 5-8 nm to structures with a width of up to 25 nm and infinite length. Interestingly, nuclear magnetic resonance dispersion profiling revealed excellent properties for MRI and also showed that the relaxivity of the structures was tunable and morphology dependent. Finally, macrophage cells were treated with two selected nanoparticles and were shown to be avidly taken up.
In conclusion we demonstrate a methodology to create structures that are (1) paramagnetic to enable their detection with MRI, (2) exhibit fluorescent properties, (3) can be tuned to defined sizes and shapes and (4) are efficiently taken up by macrophage cells in vitro.

INTRODUCTION

In the field of molecular imaging nanoparticulate structures are becoming increasingly important, since they can carry high payloads of contrast generating materials while their surface can be functionalized to improve bio-compatibility or to introduce specificity[1,2]. In addition to inorganic nanocrystals, such as quantum dots (QDs)[3] and iron oxide[4] or gold nanoparticles[5], self-assembled organic structures including liposomes[6], micelles[7] and microemulsions[8] have shown great potential for in vivo imaging. In the field of targeted imaging and therapy the pharmacokinetic profile as well as the tissue penetration potential of the nanovehicles is of paramount importance. Hence, there is a great demand for nanostructures of which the final morphology and size can be judiciously controlled. To this aim, we created a variety of well-defined nano-sized supramolecular structures based on two amphiphilic molecules: Gd-DTPA-DSA, a Gd^{3+} chelating lipid which exhibits paramagnetic properties for MRI[6,9,10], and P2fA2 a fluorescein

labeled apolipoprotein E derived lipopeptide that has been shown to enhance nanoparticle uptake into rat brain capillary endothelial cells *in vitro*[11-13]. Here we show how we can control the morphology and size of the imaging probes by varying the ratio of the two amphiphiles and thereby optimizing the molecular relaxivity of the resulting lipidic aggregates. The two most effective morphologies were selected for *in vitro* studies and were demonstrated to be effectively internalized by macrophage cells.

Figure 1. Schematic of the Molecular structure of Gd-DTPA-DSA and P2fA2

MATERIAL AND METHODS

Particle synthesis

The synthesis of the carboxyfluorescein-labeled P2A2, palmitoyl-K(palmitoyl)WK(carboxyfluorescein)G(LRKLRKRLLR)$_2$-NH$_2$ (P2fA2) has been described previously (Keller et al., 2005). Nanoparticular formulations were prepared by lipid film hydration. The fluorescent labeled lipopeptide P2fA2 and Gd-DTPA-DSA (gadolinium-diethylene triamine pentaacetic acid-distearyl amide) were dissolved in choloroform/methanol(1/1) in different ratios P2fA2/Gd-DTPA-DSA (see Table 1) and evaporated to dryness by rotary evaporation at 40°C. The obtained film was further dried under nitrogen for 15 min and heated to 65°C. Next, the film was hydrated with hot deionized water at 65°C under constant stirring. Subsequently, all preparations underwent 20 freeze-thaw-cycles until for the most preparations clear solutions were obtained (the formulation with a P2fA2/Gd-DTPA-DSA ratio of 1/9 was turbid at the end of the freeze-thawing cycles).

P2A2 / Gd-DTPA-DSA	1/0	2/1	1/1	1/2	1/3	1/4	7/40	3/20	1/8	1/9
% P2A2	100	66	50	33	25	20	17.5	15	12.5	10
size in nm (DLS)	7.4	7.7	9.8	10.8	18.6	15.5	34.3	39.1	51.4	338
cryo-TEM	x		x	x	x	x			x	x
NMRD			x	x	x	x			x	x

Table 1. Different formulations, their sizes and techniques applied indicated with 'x'.

Cryogenic transmission electron microscopy

Cryogenic transmission electron microscopy (cryo-TEM) was performed on an FEI Tecnai 20, type Sphera TEM instrument equipped with an LaB_6 filament operating at 200 kV. Images were recorded with a bottom-mounted 1k x 1k Gatan CCD camera. A Gatan cryoholder operating at ~ -170°C was used for the cryo-TEM measurements. The sample vitrification procedure was carried out using an automated vitrification robot (FEI Vitrobot Mark III). TEM grids, R2/2 Quantifoil Jena grids, were purchased from Aurion. The Quantifoil grids were surface plasma treated using a Cressington 208 carbon coater operating at 5 mA for 40 s prior to the vitrification procedure.

Confocal laser scanning microscopy, FACS and MRI of cells

Cell cultivation
Murine macrophage J774A.1 cells (ATTC®, Manassas, VA) were cultured in cell culture in DMEM (Cellgro, Mediatech Inc, Manassas, VA) supplemented with 2 mM glutamine, 100 U/ml penicillin, 0.1 mg/ml streptomycin, and 10% fetal bovine serum (FBS) (Cellgro, Mediatech Inc, Manassas, VA) at 37°C in a humidified atmosphere of 5% CO_2.

In vitro cellular uptake of nanoparticles and confocal laser scanning microscopy
Cells were plated on coverslips (diameter 15 mm) positioned in 20 mm plastic culture dishes and cultured for one day. The plates were washed with PBS at pH 7.4 and exposed to 50% - or 33% P2fA2 containing nanoparticles for 30 min at 37°C. After washing with PBS, the cells were fixed with 4% paraformaldehyde on ice for 10 minutes. Subsequently, the fixed cells were rinsed three times with PBS and mounted with DAPI containing VectaShield® (1.5 mg/ml DAPI) (Vector Laboratories, Burlingame) on microscopy slides. Imaging of cellular uptake was performed by using an LSM 510META inverted confocal laser scanning microscope equipped with a Plan-Neofluar 63×/1.4 oil objective (Carl Zeiss, Oberkochen, Germany). Fluorescein containing

P2fA2 was excited at 488 nm and emission was recorded using a BP505-550 bandpass filter. For detection of nuclei, DAPI was excited at 405nm and emission was recorded using a BP420-480 bandpass filter. Image data were captured and analyzed using Zeiss LSM 510 Meta and Image Browser software (Zeiss).

Fluorescence Assisted Cell Sorting (FACS) to determine uptake mechanism
FACS cell sorting was performed on two cell types, i.e. bovine adrenal capillary endothelial cells (BACE) and murine RAW macrophages, that were treated with 1 μM 100% P2fA2, 50% P2fA2 and 33% P2fA2 particles at 37 ºC. To demonstrate specificity the uptake as function of different inhibitory conditions was evaluated as well. These conditions included incubations at 4 ºC and in the presence of different endocytotic inhibitors (cytochalasin D, chlorpromacin and nystatin. Cytochalasin D is used to evaluate actin-dependent processes, while chlorpromacin inhibits clathin-dependent processes and nystatin inhbits caveolae mediated processes. A FACSCalibur fluorescence-activated cell sorter (BD Biosciences, Franklin Lakes, USA) was used to quantify uptake.

MR imaging
Loosely packed pellets of 1.5×10^6 cells were scanned using a 9.4 T MRI system supplied by Bruker Instruments. Cell pellets from cells incubated with media only, 50 μM 33% P2fA2 particles or 50% P2fA2 particles (n = 2) were imaged using a spin-echo sequence where the echo time was 10.5 ms, the repetition time 400 ms, the field of view 2.5 x 2.5 cm, the matrix size 96 x 128 and the no. of averages 4. The slice thickness was 0.5 mm and the total scan time 153 seconds.

RESULTS

Aqueous dispersions of mixtures of P2fA2 and Gd-DTPA-DSA were prepared (**Table 2**) and dynamic light scattering (DLS) revealed that the aggregates had narrow size distributions and that their mean hydrodynamic diameters increased with decreasing P2fA2/Gd-DTPA-DSA ratios (**Figure 2**).

P2A2 / Gd-DTPA-DSA	1/0	2/1	1/1	1/2	1/3	1/4	7/40	3/20	1/8	1/9
% P2A2	100	66	50	33	25	20	17.5	15	12.5	10
size in nm (DLS)	7.4	7.7	9.8	10.8	18.6	15.5	34.3	39.1	51.4	338
cryo-TEM	x		x	x	x	x			x	x
NMRD			x	x	x	x			x	x

Table 2. Different formulations, their sizes and techniques applied indicated with 'x'.
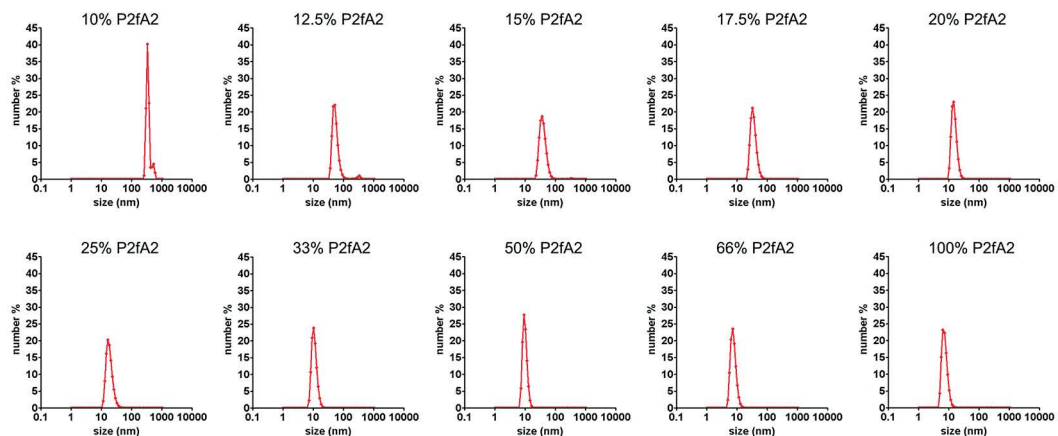
Figure 2. Individual DLS measurements of the different preparations.

At high P2fA2 contents of 50 mol% or more small structures with a mean diameter below 10 nm were observed, whereas a transition to larger aggregates (8-15 nm) was observed in case the P2fA2 content was lower than 33 mol%. Below 20 mol% P2fA2 the mean hydrodynamic diameter increased to ~ 60 nm for 12.5 mol% P2fA2 and to more than 300 nm for a formulation that contained 10 mol% P2fA2.

In line with the DLS measurements cryo-TEM revealed aggregates of which the size increased with decreasing P2fA2 concentration (**Figure 3**). At P2fA2 concentrations ≥ 50 mol% small micellar structures with diameters of 5-8 nm were observed. By decreasing the P2fA2 concentration plate-like morphologies appeared with a constant thickness of 5-8 nm of which the aspect ratios increased, from by 10 x 15-25 nm (33 mol% P2fA2) to 10-15 x 150 nm (25 mol% P2fA2) and up to 10-15 x 250 nm (20 mol% P2fA2). In the preparations that contained 10-12.5 mol% P2fA2 fully grown ribbons were present of up to 25 nm in width and with infinite lengths.
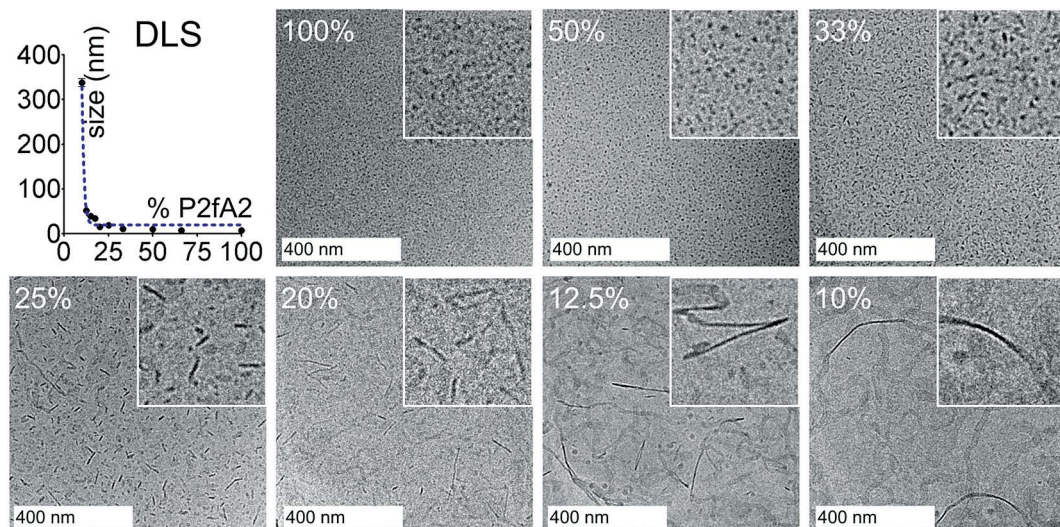
Figure 3. Dynamic light scattering (top, left) and cryo-TEM images of different P2fA2/Gd-DTPA-DSA preparations. The insets show a close up of the cryo-TEM images and represent 200 by 200 nm. The percentages refer to the amount of P2fA2 in the formulations.

Previously, in a study by Johnsson and Edwards it was demonstrated that by carefully mixing regular phospholipids and poly(ethylene glycol) (PEG) conjugated phospholipids a variety of structures, ranging from vesicular, discoidal and micellar, could be created[14]. The morphological changes were ascribed to the differences in geometry of the amphilphiles used. In our study Gd-DTPA-DSA tends to form bilayers with little curvature, while P2fA2 acts like a strong detergent and curves such that it forms micelles. Therefore aggregates of mixtures of such molecules can have morphologies that are more spherical, plate-like and even long elongated structures (**Figure 4**), depending on the ratio of both components.

Micelle forming lipid P2fA2   Bilayer forming lipid Gd-DTPA-DSA

High P2fA2 content   →   High Gd-DTPA-DSA content
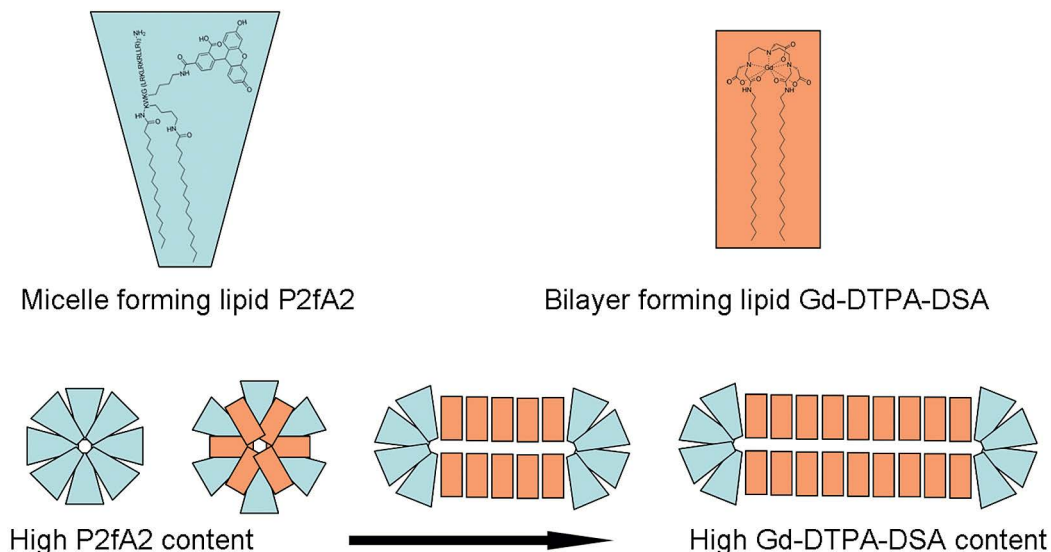
Figure 4. Possible amphiphilic organization of the different morphologies. **TOP:** P2fA2 has a structure that favors micelle formation, while Gd-DTPA-DSA has a structure that favors the formation of a bilayer with little curvature. **BOTTOM:** At high P2fA2/Gd-DTPA-DSA ratio micelle like structures will be formed. In case the ratio decreases the P2fA2 molecules will cluster and form regions with great curvature, while the regions with a high proportion of Gd-DTPA-DSA are relatively straight. Therefore, at lower ratios P2fA2/Gd-DTPA-DSA elongated structures are formed.

To assess the applicability of the different nanostructures for magnetic resonance imaging and to characterize their paramagnetic properties nuclear magnetic resonance dispersion profiles (NMRD-profiles) were obtained (**Figure 5**). Typical so-called macromolecular profiles with maximum intensities around 20 to 30 MHz were observed. These indicate a diminished mobility of the Gd^{3+} chelates in the lipidic aggregates which causes their tumbling rate τ_R to decrease. This result is typical for supramolecular and macromolecular contrast agents[15] at these moderate, but clinically relevant field strengths and is not observed for low molecular weight Gd^{3+} chelates. Moreover, these results further support the incorporation of Gd-DTPA-DSA in the lipidic aggregates. Our approach allowed the formation of structures with tunable ionic relaxivities, varying between 13 to 18 $mM^{-1}s^{-1}$ at 20 MHz (inset Figure 5), which is 3 to 5 times higher than commercially available Gd-DTPA at this field strength. Interestingly, the highest ionic relaxivity of 18 $mM^{-1}s^{-1}$ was observed for the formulation containing 33% P2fA2, the preparation with predominately small plate-like aggregates. In general such differences in relaxivity are largely determined by the variations in the interplay between the rotation correlation time (τ_R) and the exchange of water molecules

coordinated to a single Gd^{3+} chelate. At high P2fA2 concentrations, *i.e.* at low local concentrations of Gd-DTPA-DSA, it is unlikely that the water exchange rate is the limiting factor. Therefore the observed sub-optimal relaxivity at this composition is most likely due to the high τ_R, related to the small aggregate dimensions. Although the aggregate size increases with decreasing P2fA2 concentrations, a reduction in the relaxivity is observed upon further lowering of the P2fA2 content past the optimum value of 33 mol%. In this regime, the reduction in ionic relaxivity cannot be related to τ_R, as this parameter is expected to decrease further with the increasing dimensions of the aggregates. Rather, at the concomitant higher Gd-DTPA-DSA concentrations, the water exchange will become a limiting factor and the amount of water that is relaxed per Gd^{3+} chelate will be limiting the ionic relaxivity. Clearly at 33 mol% we find the morphology that optimally benefits from a low rotation correlation time associated with the aggregate dimensions and a Gd^{3+} surface concentration that allows a high enough water exchange rate.
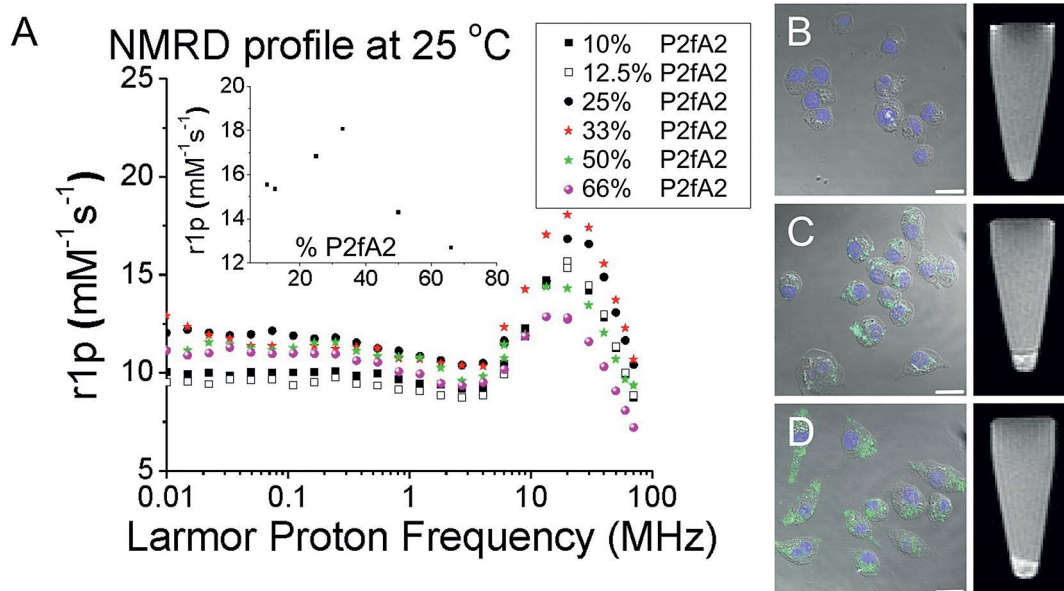
Figure 5. (A) NMRD-profiles of the different structures. The inset displays the relaxivity as function of%P2fA2 at 20 MHz. Confocal microscopy (left) and MRI of loosely packed cell pellets (right) of macrophage cells that were **(B)** left untreated, incubated with 33% **(C)** and **(D)** 50% P2fA2 nanoparticles. Scale bar: 20 µm

Based on these results we set out to test these P2fA2 containing nanostructures for their suitability as MR imaging probes for extravascular targets, such as macrophages. Since small nanoparticles are more likely to escape from the circulation and cross the diseased and permeable

endothelium, the two formulations with a high relaxivity and small size, *i.e.* those with 33 mol% (small platelets) and 50 mol% (micelles) P2fA2 were selected for further *in vitro* experiments with cultured mouse macrophage cells (J774A1). The incorporation of P2fA2 and Gd-DTPA-DSA allowed the visualization of nanoparticle uptake using fluorescence confocal laser scanning microscopy and MRI, respectively (**Figure 5B-D**). The CLSM images show nuclei in blue (DAPI) and P2fA2 in green, merged with bright field images of the macrophage cells. While control cells revealed no nanoparticle associated fluorescence or MRI contrast (**Figure 5B**), significant amounts of intracellular fluorescence as well as MRI signal enhancement were observed after 30 min of incubation for cells that were incubated with 50% (**Figure 5C**) and 33% (**Figure 5D**) P2fA2 nanoparticles. In addition, we performed quantitative uptake experiments under inhibitory conditions (**Figure 6**). The results revealed the particle uptake to be specific and further confirmed their multifunctional character. Uptake of P2fA2/Gd-DTPA 50/50 and 33/66 particles
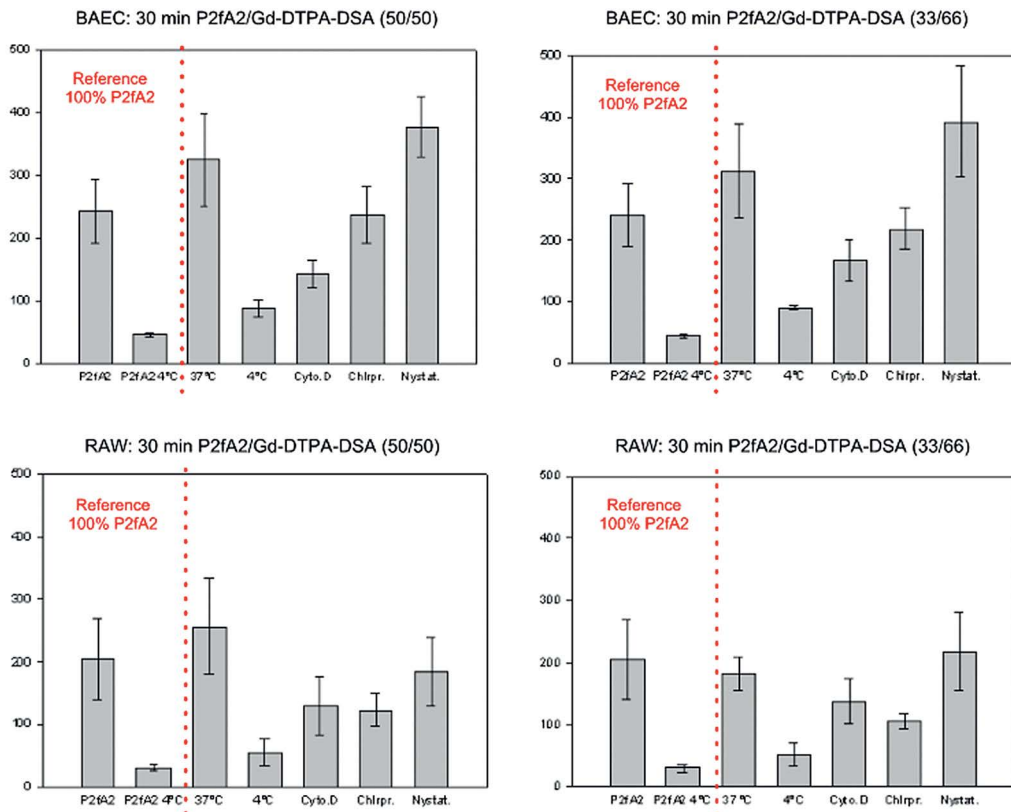
Figure 6. FACS determined uptake of 50/50 33/66 P2fA2/Gd-DTPA-DSA particles in endothelial cells (BAEC) and macrophages (RAW). Incubations of pure P2fA2 particles at 37 ºC and 4 ºC served as a reference.

in BAEC and RAW cells follows the same uptake pattern, but the uptake modes of the nanoparticles into RAW and BACE are different. Cytochalasin D, chlorpromacin and nystatin are inhibitors of different endocytotic pathways. Cytochalasin D is used to evaluate actin-dependent processes, while chlorpromacin inhibits clathrin-dependent processes and nystatin inhbits caveolae mediated processes. The uptake into RAW cells indicates the contribution of a clathin-dependent process (chlorpromacin reduces the uptake), but non-actin involving processes play also a role since cytochalasin D did not completely reduce the uptake. Nytatin has no influence which points out that the process is not caveolae mediated. Furthermore, the uptake into BAEC is also not caveolae-mediated. Furthermore, the uptake into BAEC is also not caveolae-mediated. The contribution of clathrin-mediated endocytosis is low, but incubations with cytochalasin D resulted in a significantly reduced uptake.

SUMMARY

In summary we have demonstrated that by carefully controlling the ratio of two functional amphiphiles Gd-DTPA-DSA and P2fA2, it was possible to create a variety of well-defined supramolecular structures, containing both fluorescein and Gd^{3+} chelates. Moreover, we showed that by changing the morphology we could optimize the relaxivity of the imaging probes, since NMRD-profiling disclosed excellent and tunable MRI properties for the different formulations, especially at clinically relevant field strengths.
We envision the application of these contrast agents for pathologies in which macrophage inflammation plays a key role, such as atherosclerosis, rheumatoid arthritis, or cancer[16-18].

REFERENCES

1.   Mulder, W.J., et al. *NMR Biomed*. 19, 142-164 (2006).
2.   Torchilin, V.P., *Nat.Rev.Drug Discov*. 4, 145-160 (2005).
3.   Medintz, I.L., et al. *Nat.Mater*. 4, 435-446 (2005).
4.   Bulte, J.W. & Kraitchman, D.L., *NMR Biomed*. 17, 484-499 (2004).
5.   Alric, C., *et al. J. Am. Chem. Soc*. 130, 5908-5915 (2008).
6.   Mulder, W.J., et al. *Bioconjug.Chem*. 15, 799-806 (2004).
7.   Amirbekian, V., et al. *PNAS* 104, 961-966 (2007).
8.   Lanza, G.M. et al*. Nanomedicine* 1, 321-329 (2006).
9.   Mulder, W.J., et al. *Nano.Lett*. 6, 1-6 (2006).
10. van Schooneveld, M.M., et al. *Nano.Lett*. 8, 2517-2525 (2008).
11. Keller, S., et al. *Angew. Chem. Int. Ed. Engl*. 44, 5252-5255 (2005).
12. Sauer, I., et al. *Biochim. Biophys. Acta* 1758, 552-561 (2006).
13. Sauer I et al. *Biochemistry* 44, 2021-2029 (2005).
14. Johnsson, M. & Edwards, K., *Biophys. J*. 85, 3839-3847 (2003).
15. Aime, S., et al. *Advances in Inorganic Chemistry - Including Bioinorganic Studies* 57,173-237 (2005).
16. Libby, P., et al. *Circulation* 105, 1135-1143 (2002).
17. Firestein, G.S., *Nature* 423, 356-361 (2003).
18. Mantovani, A., et al*. Nature* 454, 436-444 (2008).

Chapter 3

Incorporation of an apoE-derived lipopeptide in high-density lipoprotein MRI contrast agents for enhanced imaging of macrophages in atherosclerosis

Based on

Author contribution: Esad Vucic: designed and performed experiments, analyzed data and revised the manuscript.

ABSTRACT

Magnetic resonance (MR) imaging is becoming a pivotal diagnostic method to identify and characterize vulnerable atherosclerotic plaques. We previously reported a reconstituted high density lipoprotein (rHDL) nanoparticle platform enriched with Gd-based amphiphiles as a plaque specific MR imaging contrast agent. Further modification can be accomplished by inserting targeting moieties into this platform to potentially allow for improved intraplaque macrophage uptake. Since studies have indicated that intraplaque macrophage density is directly correlated to plaque vulnerability, modification of the rHDL platform may allow for better detection of vulnerable plaques. In the current study we incorporated a carboxyfluoresceine-labeled apolipoprotein E-derived lipopeptide, P2fA2, into rHDL. The *in vitro* macrophage uptake and *in vivo* MR efficacy were demonstrated using murine J774A.1 macrophages and the apolipoprotein E knock-out (apoE$^{-/-}$) mouse model of atherosclerosis. The *in vitro* studies indicated enhanced association of murine macrophages to P2fA2 enriched rHDL (rHDL-P2A2) nanoparticles, relative to rHDL, using optical techniques and MR imaging. The *in vivo* studies showed a more pronounced and significantly higher signal enhancement of the atherosclerotic wall 24 hours after the 50 μmol Gd/Kg injection of rHDL-P2A2 relative to administration of rHDL. The normalized enhancement ratio for atherosclerotic wall of rHDL-P2A2 contrast agent injection was 90% while that of rHDL was 53% 24 h post injection. Confocal laser scanning microscopy revealed that rHDL-P2A2 nanoparticles co-localized primarily with intraplaque macrophages. The result of the current study confirm the hypothesis that intraplaque macrophage uptake of rHDL may be enhanced by the incorporation of the P2fA2 peptide into the modified HDL particle.

INTRODUCTION

Atherosclerosis is a chronic inflammatory disease that is the major contributor to coronary artery disease, myocardial infarction, cerebrovascular disease, peripheral vascular disease, mesenteric ischemia and stroke[1-3]. The accumulation of modified low-density lipoproteins, including oxidized LDL (oxLDL) in the vessel wall initiates the development of early atherosclerotic lesions. These modified lipoproteins are critical for plaque progression and are directly responsible for monocyte activation, foam cell formation, and macrophage apoptosis[4]. The plaques may be stabilized by the migration of smooth muscle cells from the media to the subendothelial space, resulting

in the formation of a fibrous cap with deposition of extracellular matrix components, such as proteoglycans, collagens, tenascin and fibronectins[1]. However, the activation of macrophages by continued uptake of modified lipoproteins stimulates the production of metalloproteinases (MMPs) that are thought to degrade the fibrous cap and de-stabilize the lesion. De-stabilization may eventually result in plaque rupture and cause myocardial infarction or other acute clinical events by the formation of large thrombi that occlude the artery. Vessel wall narrowing, determined by angiography, has traditionally been used as a risk indicator[5]. Currently, intraplaque hemorrhage, angiogenesis, inflammatory activity and plaque composition, e.g. a thin cap with a large lipid necrotic core, are considered to be important indicators for the risk of plaque rupture that may lead to an adverse clinical event[6-14].

Several techniques have been developed to evaluate the burden of atherosclerosis. The luminal narrowing can be diagnosed by conventional luminography (mainly angiography)[15,16]. Nanoparticle agents have been developed to image angiogenesis, for example microemulsions targeted to the $\alpha v\beta 3$ integrin as a surrogate for angiogenesis[9,10] or microbubbles to evaluate perfusion density in intravascular ultrasound[11,12]. Plaque composition can be assessed by magnetic resonance (MR) imaging[4]. However, no clinically robust, noninvasive method is available to detect the biological activity of atherosclerotic plaques. Cellular and molecular imaging techniques, such as positron emission tomography (PET), optical imaging, and molecular MR imaging, are currently being explored to evaluate plaque activity[17-21]. MR imaging, which enables submillimeter resolution imaging of the arterial wall, has emerged as one of the most promising techniques for the evaluation of plaque composition and biological activity[5,22]. Despite these promising features of MR imaging for functional plaque characterization, the low concentration of biomarkers and inherently low sensitivity of MR usually requires contrast agents of high relaxivity that carry high pay-load of contrast generating materials to enable the visualization of specific biological activities[17,23].

The apolipoprotein E (apoE) derived peptide (A2), which has the amino acid sequence (LRKLR KRLLR)$_2$, is a tandem dimer (141–150)$_2$ derived from the low density lipoprotein receptor (LDLR) binding domain of apoE. Previously, this cationic and membrane penetrating peptide has been covalently attached to PEGylated liposomes, which were taken up by primary rat brain capillary endothelial cells in an energy dependent fashion[24,25] but not through LDLR pathway. As a further modification, two palmitoyl chains have been conjugated to A2 to create a so called "lipopeptide" (palmitoyl-

WK(palmitoyl)G(LRKLRKRLLR)$_2$-NH$_2$), named P2A2. P2A2 can be easily and efficiently incorporated into lipid-based particles[26]. This strategy has been demonstrated to be effective in promoting endosomal uptake of the P2A2 containing liposomes into rat brain capillary endothelial cells[26]. Unspecific interactions between the P2A2-bearing liposomes and membrane constituents predominate the uptake process[27]. In addition, cell surface heparan sulfate proteoglycans (HSPGs) are involved in the internalization process of P2A2-bearing liposomes[27]. The lipopeptide P2A2 can be further modified with carboxyfluoresceine, termed P2fA2, which can be tracked by Fluorescence[26,28].

We have previously reported that reconstituted high density lipoprotein (rHDL) nanoparticles can be modified to serve as a molecular MR contrast agent for the detection of atherosclerotic plaques[29-31]. These Gd-loaded rHDL nanoparticles accumulate in atherosclerotic plaques *in vivo* and substantially enhance the MR signal intensity of the vessel wall. In order to increase the delivery and retention of rHDL nanoparticles within the arterial wall, targeting molecules may be incorporated via different routes, e.g. anchored in the lipid layer or conjugated to apolipoprotein A I (apoAI). In the current study we hypothesize that incorporation of the cationic and membrane penetrating P2fA2 into rHDL nanoparticles (rHDL-P2A2) can increase the detection of intraplaque macrophages that are associated with plaque vulnerability. Our primary aims were to: 1) evaluate the ability of P2fA2 to mediate the uptake of rHDL nanoparticles by macrophages *in vitro* and 2) evaluate the efficacy of this enhanced rHDL platform for molecular MR imaging of atherosclerotic plaques *in vivo* using apolipoprotein E knockout (apoE$^{-/-}$) mouse models of atherosclerosis.

MATERIALS AND METHODS

Materials
1,2-Dipalmitoyl-*sn*-glycero-3-phosphocholine (DPPC), 1,2-dimyristoyl -*sn*-glycero-3-phosphoethanolamine-N-(lissamine rhodamine B sulfonyl) (Rhodamine-PE) were obtained from Avanti Polar Lipids (Albaster, AL). Gadolinium diethylenetriaminepentaacetate-bis(stearylamide) (Gd-DTPA-BSA) was purchased from IQSynthesis (St. Louis, MO). A carboxyfluoresceine-modified fluorescently labeled P2A2 derivative (Palmitolyl-K(Palmitoyl) WK(Fluo)G (LRKLRKRLLR)$_2$-NH$_2$, P2fA2, 90% purity) was synthesized as described previously[26,28]. All other chemicals were of analytical grade or the best grade available.

Preparation of reconstituted HDL (rHDL) and P2fA2 incorporated rHDL (rHDL-P2A2) nanoparticles

Gd-DTPA-BSA, Rhodamine-PE, and DPPC were dissolved in chloroform/ethanol (3:1 mol/mol, chloroform: ethanol), then dried initially under airflow at room temperature, then under vacuum overnight. The dried lipid film was dissolved in a sodium cholate buffer (0.15 M NaCl, 1 mM EDTA, pH 7.5) at 55°C so that the lipid film was fully hydrated. Apolipoprotein A-I (apoAI, purified from human HDL) solution in PBS was then added to the cooled lipid solution on ice. The molar ratio was 1:123:25:2:200 for apoAI:DPPC:Gd-DPTA-BSA: Rhodamine-PE:sodium cholate. After incubation at 0-5°C in an ice water bath for 2 h, the mixture was dialyzed against buffer (0.15 M NaCl, 1 mM EDTA, pH 7.5) to remove the sodium cholate. The dialysate was then filtered through 0.22 μm syringe filter (Fisherbrand, Fisher Scientific, Pittsburgh, PA), concentrated and the buffer exchanged to 1% sucrose with a Vivaspin 6 Centrifugal Filter Device (membrane cutoff range: 10,000 kDa; Sartorius Corporation, Edgewood, NY).

The protocol described above was used to create the P2fA2 incorporated rHDL (rHDL-P2A2), but the quantity of DPPC was reduced commensurately with the addition of P2fA2 in order to keep the total molar amount of lipid constant. The molar ratio was 1:113:10:25:2:200 for apoAI:DPPC:P2fA2:Gd-DPTA-BSA:Rhodamine-PE:sodium cholate.

The mean size of the different nanoparticles was determined by photon correlation spectroscopy performed with a Malvern light scattering instrument (Malvern Instruments, Malvern, UK). The zeta potential of the different nanoparticles was measured with a Malvern Zetasizer Nano ZS (Malvern Instruments, MA, US). All samples were analyzed at 25°C in filtered water (30 nm size cut-off).

Gadolinium content and relaxivity determinations

The Gd concentration of the rHDL and rHDL-P2A2 were analyzed by inductively coupled plasma mass spectrometry (ICP-MS). The relaxivity measurements were done on a Minispec (Bruker Medical BmbH, Ettingen) operating at 60 MHz and 40°C.

In vitro macrophage targeting of rHDL-P2A2

Murine macrophage J774A.1 cells (American Type Culture Collection, Manassas, VA) were cultured at 37°C with 5% CO_2 in cell culture flasks (BD Falcon™) in DMEM (Cellgro, Mediatech Inc, Manassas, VA) with 2 mM

glutamine, 100 U/ml penicillin, 0.1 mg/ml streptomycin, and 10% FBS (Mediatech Inc, Manassas, VA). J774A.1 cells were grown to ~ 90% of confluence in tissue culture flasks. Cells were incubated for 24 h at 37°C with the either rHDL or rHDL-P2A2 nanoparticles at concentration of 0.01 mM or 0.05 mM Gd. After incubation, cells were washed with PBS, collected, and centrifuged at 4000 rpm (x18 g) for 5 min. The cell pellet was further redispersed and washed by PBS twice. Finally, approximately 5×10^6 cells were dispersed in 500 μl PBS and lysated by sonication for 30 sec followed by centrifugation at 4000 rpm for 5 min. The *T1* relaxation times of the lysates were assessed using a Brucker Minispec at 60 MHz and 40°C. The *R1* relaxation times were calculated according to *R1 = 1/T1*. The fluorescent intensities of Rhodamine-PE of the lysates were measured using a BioTek Synergy 2 microplate reader with Gen5™ software using a 540 ± 20 nm excitation filter and a 590 ± 20 nm emission filter. The protein concentrations of lysates were measured by the Bradford assay[51] (Bio-Rad Protein Assay, Hercules, CA) according to the protocol.

For MR imaging of cell pellets, macrophages were incubated for 24 h at 37°C with either rHDL or rHDL-P2A2 nanoparticles at concentrations of 0.01 mM or 0.05 mM Gd. Subsequently, the cells were washed twice with PBS; harvested, and collected in 15 ml falcon tubes and washed twice in PBS by centrifugation. Finally, 4% paraformaldehyde solution was added to a final volume of ~ 200 μl and the dispersed cells were collected in small PCR cups and left overnight to form loosely packed cell pellets. MR imaging was performed on a preparation of 10^6 packed cells.

The cups containing cell pellets were placed in a custom-made sample holder, capable of carrying three PCR cups. A T1-weighted sequence (MSME) (TR/TE = 800 ms/10.5 ms, FOV = 2.0×2.0 cm, matrix size = 256×256, number of average = 8, scan time = 20min, slice thickness = 0.5 mm) was used to generate T1-wighted images. For absolute quantification of T1, a saturation recovery spin-echo sequence was used with 8 different inversion times, ranging from 200 ms to 5000 ms (TE = 10.5 ms, FOV = 2.0×2.0 cm, matrix size = 128×128, number of averages = 8, slice thickness = 0.5 mm).

The Institutional Animal Care and Use Committee approved the animal protocols and procedures. Six-month-old apoE^{-/-} mice (n = 6 for rHDL; n = 5 for rHDL-P2A2) were used for this study (all in the C57BL6 strain and purchased from Jackson Laboratory, Bar Harbor, Maine). The apoE^{-/-} animals were fed a Western diet (21% fat and 0.15% cholesterol, Diet D01022601,

Research Diets, Inc., New Brunswick, NJ) for a period of at least 4.5 months. The animals underwent *in vivo* MR imaging of the abdominal aorta using a 9.4 T, 89 mm bore magnet system (Bruker Instruments, Billerica, MA). The animals were anesthetized with a 4% isoflurane/O_2 gas mixture (400 cc/min initial dose) and maintained with a 1.5% isoflurane/O_2 gas mixture (100 cc/min maintenance dose) delivered through a nose cone and positioned in a 30 mm birdcage coil. A respiratory sensor connected to a monitoring and gating system (SA Instruments, Inc, Stony Brook, NY) was placed on the abdomen to monitor the depth and frequency of respiration. The abdominal aorta was identified in a coronal section on a localizing sequence. High resolution T1-weighted images were generated using a black blood spin echo (SE) sequence (TR/TE = 800 ms/8.6 ms, FOV = 3.0×3.0 cm, matrix size = 256×256, 22 contiguous 500 μm-thick axial slices, number of averages = 16, total scan time = 54 min). After pre-contrast imaging the animals were administered either an rHDL contrast agent (50 μmol of Gd/kg; n = 6) or an rHDL-P2A2 contrast agent (50 μmol of Gd/kg; n = 5) via the tail vein. Post-contrast imaging with the same parameters was performed on each animal at 24, 48 and 72 h after injection. At each time-point, the slices were matched to the baseline pre-contrast scan by using unique vertebral and para-spinous muscular anatomy as landmarks. Since MR images were acquired contiguously from the aortic bifurcation to the level of the renal arteries, accurate registration was achieved for all the slices during pre- and post-contrast imaging.

Immunohistochemistry
Abdominal aortas matching the MR imaging area from apoE^{-/-} mice were removed and embedded in TissueTek®. Eight-micrometer frozen sections were fixed in 4% paraformaldehyde and washed in PBS twice. The tissue sections were permeabilized in PBS with 0.5% Triton X-100 at room temperature for 30 min and washed with PBS twice. The sections were blocked in 2% goat serum in PBS for 45 min at room. After blocking, the sections were incubated in 2% goat serum in PBS with a primary antibody: rat anti-mouse CD 68 (Serotec, Raleigh, NC) for 120 min at room temperature, and washed by PBS twice. Thereafter the sections were incubated with a secondary antibody: Alexa Fluor 647 conjugated goat anti-rat Ab (Serotec, Raleigh, NC) for 60 min at room temperature, and washed by PBS twice again. Finally, the sections were mounted with DAPI-containing VectaShield mounting media and sealed with cover slips, shielded from light, and kept at 4°C until laser-scanning confocal fluorescence microscopy imaging was performed within 48 h. One section without any antibody and one section with secondary antibody only were used

as negative controls. Confocal imaging was performed using a Leica SP5DM microscope. The system is equipped with four lasers: a 405-nm blue diode, an Argon (488 nm), a green HeNe (543 nm) and a red HeNe (633 nm). For H&E staining sections were immersed in Harris Hematoxylin for six minutes, then rinsed in tap water, and immersed in Eosin solution (Eosin Y, 1 gram in 100 ml distilled water) for 2 min. Sections were again rinsed, dehydrated in a graded ethanol series, mounted in Cytoseal XYL mounting medium (Stephans Scientific, Kalamazoo, MI). Lastly, cover slips were placed.

Imaging analysis

For *in vitro* MR images of cell pellets, the signal intensities were normalized to control cell pellet by the equation that normalized enhancement ratio (NER) = $(I_{treatment}-I_{control})/I_{control}\times100\%$; The contrast-to-noise ratio (CNR) were calculated by CNR = $(I_{treatment}-I_{control})/I_{noise}$, where $I_{treatment}$ is the signal intensity of cell pellet with rHDL or rHDL-P2A2 incubation, $I_{control}$ is the signal intensity of control cell pellet, and I_{noise} is the standard deviation outside the cell pellet.

For *in vivo* MR images, the signal-to-noise ratio (SNR) of the region of interest (ROI) is defined by $SNR_{ROI} = I_{ROI}/I_{noise}$ where I_{ROI} is the intensity of either aortic vessel wall (SNR_w) or surrounding muscle (SNR_m); I_{noise} is the standard deviation outside the animal. The contrast-to-noise ratio (CNR_w) to muscle is defined as $CNR_w = SNR_w-SNR_m$. The normalized enhancement ratio of aortic wall (NER_w) to muscle is defined as $NER_w = [(SNR_w/SNR_m)_{post}-(SNR_w/SNR_m)_{pre}]/(SNR_w/SNR_m)_{pre} \times100\%$. Five aortic MR images of the matched (pre- and post-injection) slices for each mouse were used for analysis. The mean ± S.D. of NER_w for rHDL (n = 6 mice) and rHDL-P2A2 (n = 5 mice) were reported.

Statistics

Data are presented as the mean ± standard deviation (S.D.). For differences between groups, two-way ANOVA was used. Multiple comparisons with Bonferroni correction after ANOVA were used to distinguish the groups of significant difference. A value of $p < 0.05$ was considered statistically significant. The analysis was performed on Matlab® R2007b.

RESULTS

Physical properties

rHDL-P2A2 nanoparticles had a mean diameter of 11.6 ± 3.7 nm in aqueous solution as determined by dynamic light scattering, which was similar to

and not significantly different from the size of apoAI-containing rHDL (rHDL) nanoparticles: 9.5 ± 0.5 nm. The longitudinal relaxivity (r_1) measurements of the nanoparticles were performed on a 60 MHz Bruker Minispec operating at 40°C. The values for r_1 were 11.3 and 10.5 mM^{-1}s^{-1} for rHDL and rHDL-P2A2 nanoparticles, respectively. The Gd/nanoparticle ratios were 22 for rHDL and 19 for rHDL-P2A2, which were measured by [Gd] and protein concentration (mainly apoAI). Therefore relativities per nanoparticles were 249 mM^{-1}s^{-1} and 200 mM^{-1}s^{-1} for rHDL and rHDL-P2A2, respectively. In comparison, the relaxivity of the Gd-DTPA (Magnevist®, without the stearyl chains) was approximately 3 mM^{-1}s^{-1}. The physical properties of rHDL were consistent with our previous reports[29,30]; thus the physical similarities between rHDL and rHDL-P2A2 nanoparticles allow a direct comparison of their applicability as MR contrast agents for atherosclerosis. The positively charged P2fA2 peptide changed the zeta potential of the nanoparticle. The zeta potentials of rHDL and rHDL-P2A2 nanoparticles were -20.3 ± 1.8 and +15.6 ± 0.8 mV, respectively.

rHDL-P2A2 enhanced the delivery of Gd contrast agent to macrophages *in vitro*

The association of rHDL and rHDL-P2A2 with macrophage J774A.1 cells was compared quantitatively by fluorescent intensity measurements. After a 24 h incubation with the nanoparticles, J774A.1 cells were washed, lysed, and studied with respect to fluorescent intensity of 1,2-dimyristoyl-*sn*-glycero-3-phosphoethanolamine-N-(lissamine rhodamine B sulfonyl) (Rhodamine-PE) using a microplate reader. A significantly higher level of association of fluorescently labeled rHDL-P2A2 nanoparticles with J774A.1 in culture was observed, relative to cells incubated with rHDL (**Figure 1A**). The normalized fluorescent intensities of lysates from cells incubated with rHDL-P2A2 were approximately 2 and 3 times of that of cells incubated with rHDL nanoparticles at 0.01 mM and 0.05 mM Gd concentrations, respectively. The longitudinal relaxation rates (R_1) of lysates from cells were measured on a 60 MHz Bruker Minispec at 40°C to quantitatively determine the delivery of Gd to cells by both types of nanoparticles (**Figure 1B**). The lysates of J774A.1 macrophages incubated with rHDL nanoparticles had a R_1 of 0.266 ± 0.016 s^{-1} and 0.281± 0.008 s^{-1}, while the cells incubated with rHDL-P2A2 nanoparticles had a R_1 of 0.310 ± 0.013 s^{-1} and 0.412 ± 0.006 s^{-1} for 0.01 mM and 0.05 mM [Gd], respectively. The low R_1 values in cell lysates are due to the dilution effect of lysate buffer. The volume of lysate buffer is much larger than the volume of cells, which diluted the Gd from cells. It is worth pointing out that the observed low R_1 values of cell lysates are not equal to the R_1 values of cell

pellets. The observed R_1 values are dependent on several factors including concentration of material taken up by the cell, compartmentalization within the cell, transmetallation of gadolinium ions due to intracellular uptake, and interaction with endogenous cellular components. Since the number of cells lysed was constant and all cells were completely homogenized prior to analysis (to eliminate the effects of compartmentalization), the R_1 values may be used to estimate the amount of gadolinium uptake (assuming that the degree of transmetallation and/or interaction with endogenous cellular components is similar for the various formulations). The R_1 values strongly suggest that greater gadolinium uptake was observed for the rHDL-P2A2 than rHDL nanoparticles. These results are consistent with the fluorescent intensities of the lysates (**Figure 1A**).
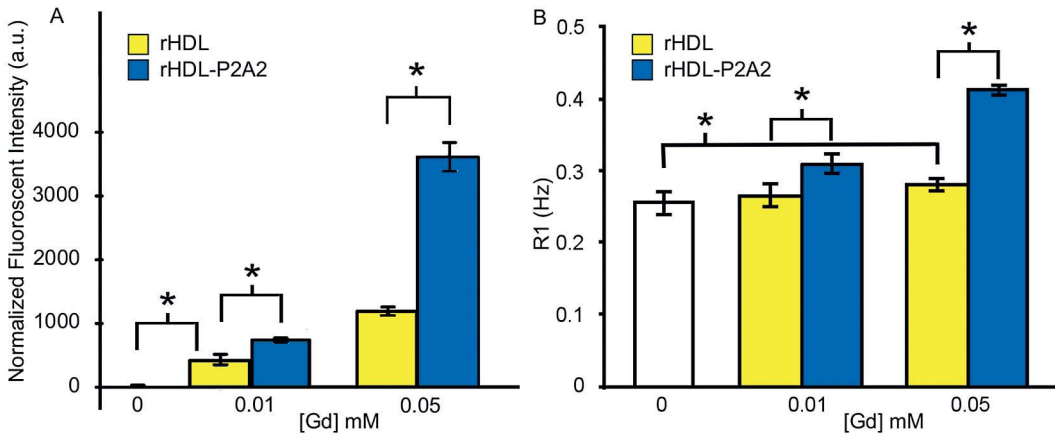
Figure 1. (**A**) Rhodamine-PE fluorescence of sonicated lysates of J774A.1 cells after incubation with rHDL, rHDL-P2A2 for 24 hr at 37 °C. The fluorescent intensities were measured for three independent experiments and normalized to protein concentrations by (Intensity$_{raw}$-Intensity$_{control}$)/ Protein concentration. (**B**) R_1 relaxation rate (60MHz, 40 °C) of sonicated lysates of J774A.1 cells after incubation with rHDL, rHDL-P2A2 for 24 hr at 37 °C. The R_1 relaxation rates were measured for three independent experiments with about 5 million cells in 500 µl PBS for each experiment. Significant differences of fluorescent intensity and R_1 relaxation rate were observed between J774A.1 cells treated by rHDL and rHDL-P2A2 after 24hr incubations at both 0.01 mM and 0.05 mM [Gd]. Bars present mean± standard deviation (S.D.); * indicates statistical significance.

The J774A.1 macrophage cell pellets were imaged using high field MR and their T1 values were determined by a saturation recovery sequence. The T1 mapping showed that both rHDL and rHDL-P2A2 treatment reduced the T1 time for macrophages (**Figure 2A** and **B**). The pellet of macrophages incubated with rHDL-P2A2 had T1 = 894 ± 84 ms and 717± 82 ms, while the cells incubated with rHDL had T1 = 1976 ± 103 ms and 1289 ± 168 ms for 0.01 mM and 0.05 mM [Gd], respectively. Cells that were incubated

with media only had a T1 = 2560 ± 347 ms. These data demonstrate that the rHDL-P2A2 treatment resulted in a significant reduction in the T1 relaxation time relative to both controls. In the T1-weighted image (**Figure 2C** and **D**) the pellets of cells incubated with rHDL-P2A2 nanoparticles cause greater increases in MR signal enhancement relative to cells incubated with rHDL nanoparticles or media only (control). These results are indicative of a more pronounced uptake of rHDL-P2A2, as compared to both controls. Quantitatively, the J774A.1 macrophage cells incubated with rHDL nanoparticles had *NER* = 13 ± 5% and 18 ± 7%, while the cells incubated with rHDL-P2A2 nanoparticles had a significantly higher *NER* = 27 ± 4% and 49 ± 16% for 0.01 mM and 0.05 mM [Gd] concentration, respectively.
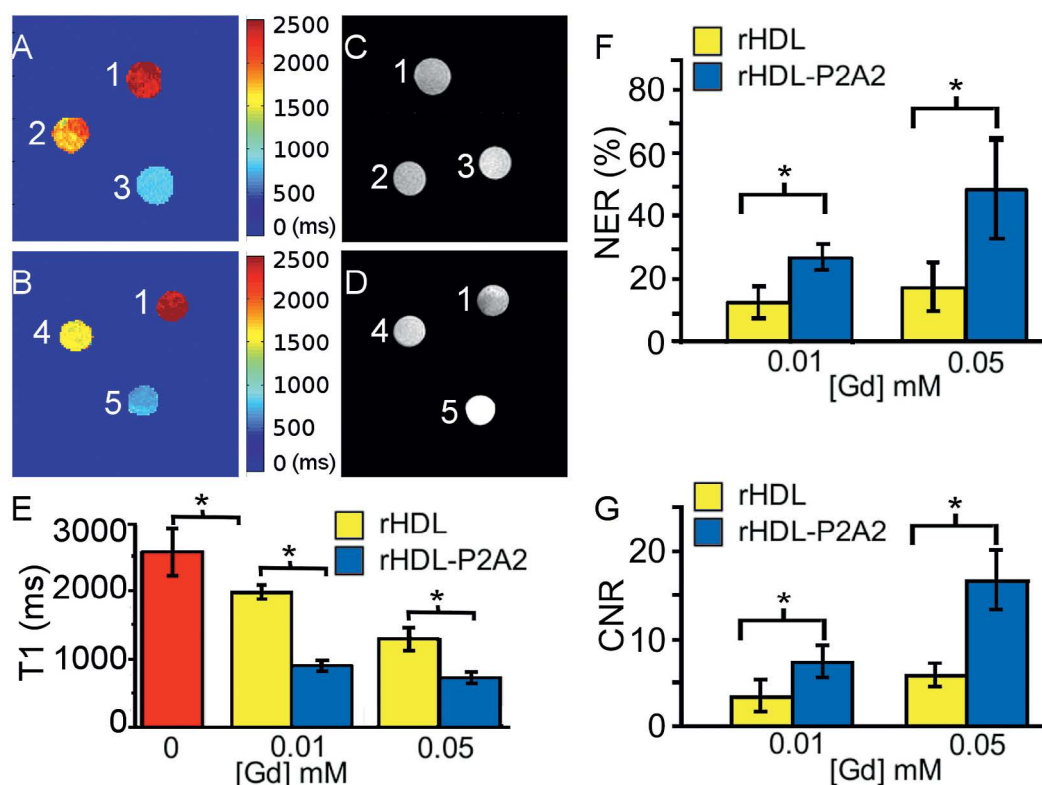
Figure 2. Typical (**A, B**) T1 mapping and (**C, D**) T1-weighted MR images of three pellets of J774A.1 macrophage after incubation at 37 °C with (**1**) media only (control), (**2**) rHDL at 0.01 mM [Gd], (**3**) rHDL-P2A2 at 0.01 mM [Gd], (**4**) rHDL at 0.05 mM [Gd], and (**5**) rHDL-P2A2 at 0.05 mM [Gd]. A brighter cell pellet has a shorter T1 and hence a higher uptake of nanoparticles. (**E**) T1 values of control, rHDL, and rHDL-P2A2treated macrophages determined by T1 mapping with a saturation recovery sequence (n = 3). (**F**) Normalized enhancement ratio (NER, to control macrophages) of rHDL or rHDL-P2A2 treated macrophages in the T1-weighted MR images (n = 3) (G) Contrast-to-noise ratio (CNR, to control macrophages) of rHDL or rHDL-P2A2 treated macrophages in the T1-weighted MR images (n = 3). Bars present mean ± S.D.; * indicates statistical significance.

Endocytosis of both rHDL and rHDL-P2A2 into J774A.1 macrophages was confirmed by confocal images (**Figure 3**).
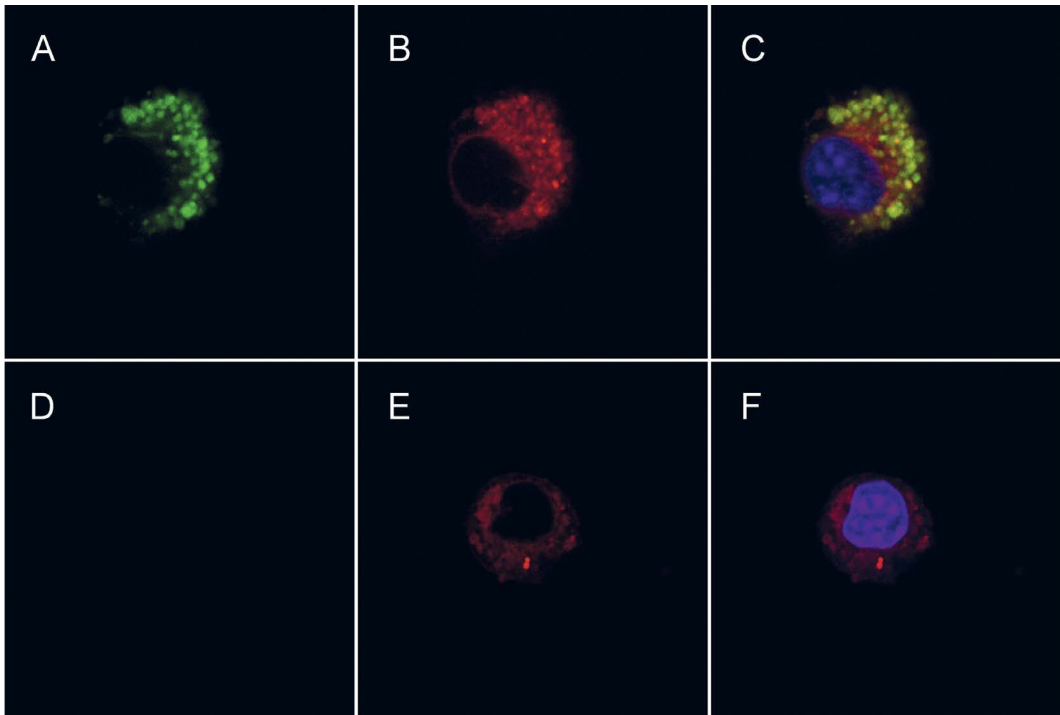
Figure 3. Confocal microscopy of J774A.1 macrophages after incubation with (A-C) rHDL-P2A2 or (D-F) rHDL nanoparticles at 0.01 mM Gd concentration for 24h. (A-B) Separate channels and (C) merged image of DAPI-stained cell shows uptake of the rhodamine-labeled rHDL-P2A2 by macrophages. (D-E) Separate channels and (F) merged image of DAPI-stained cell shows uptake of the rhodamine-labeled rHDL by macrophages. Green: P2fA2; Red: Rhodamine-PE; Blue: DAPI.

rHDL-P2A2 exhibited improved *in vivo* MR imaging signal enhancement in atherosclerotic mice

In vivo MR imaging was carried out on 6-month old apoE$^{-/-}$ mice that were placed on a high fat and high cholesterol diet for 4.5 months. Animals were injected with either rHDL or rHDL-P2A2 nanoparticles at a dose of 50 μmol Gd/Kg which we have previously established to be sufficient for rHDL nanoparticles[31] . The bi-exponential fitting was used to evaluate the elimination of nanoparticles. For HDL, the two time constants were 125 ± 21 min and $3.9 \times 10^6 \pm 1.3 \times 10^{10}$ min. For HDL-P2A2, the two time constants were 39 ± 14 min and 723 ± 487 min. These data suggest HDL-P2A2 might have another long circulating component. All blood samples were drawn from the saphenous vein over a 72 h time period post injection (n > 7).

The variation in the blood half-lives may be due to several causes including variations in charge (P2fA2 peptides more positively charged), clearance of P2fA2 by the LDL receptor expressed on many cells, and/or increased reticuloendothelial system uptake due to general targeting of macrophages.

The signal enhancement of the arterial vessel wall was evaluated 24 h after contrast agent administration. A slight enhancement of the arterial vessel wall was observed at 4 h after contrast agent injection in a pilot scan, but the maximum enhancement appeared at 24 h post injection. Therefore, the abdominal aortas were imaged 24 h after injection despite the relatively short half- lives of these nanoparticles. Representative MR images of atherosclerotic plaques of apoE$^{-/-}$ mice pre- and post-injection are depicted (**Figure 4A** and **B**). Sequential MR images showed that the both rHDL and rHDL-P2A2 caused increase arterial vessel wall enhancement 24 h post injection. The mean NER$_w$ of rHDL-P2A2 contrast agent injection was 90% while that of rHDL was 53% 24h post injection. The signal with the rHDL nanoparticles was substantially reduced to 24% by 48h. In contrast, the enhancement of rHDL-P2A2 nanoparticles remained high; 66% at 48 h post injection. The CNR$_w$ of rHDL-P2A2 contrast agent injection was 14 ± 5 significantly higher than that of rHDL contrast agent injection (6 ± 5) at 24 h post injection. The vessel to the left of the aorta is the inferior vena cava. Although arterial flow was saturated to allow delineation of the arterial wall, some enhancement in the inferior vena cava may be observed because of slow flow[32]. In contrast, no significant enhancement of the vessel wall of WT mice was observed following administration of either rHDL or rHDL-P2A2 nanoparticles (**Figure 4C** and **D**, **Table 1**). In addition, no significant enhancement of the vessel wall of ApoE$^{-/-}$ or WT mice was observed after 24 h of administration of Gd-DTPA (up to 100 umol Gd/Kg)[33,34]. Injection of Gd-DTPA-DMPE/DMPE mixture (1:1 by weight, 50 μmol Gd/Kg) into apoE$^{-/-}$ mice didn't show considerable enhancement in vessel wall (less than 20%)[31]. Since a Gd-DTPA-BSA/DPPC mixture (i.e. the lipids without the apoAI) has similar chemical and physical properties as Gd-DTPA-DMPE/DMPE, no significant enhancement in vessel wall will be expected. It seems that apoAI is required for successful plaque targeting.
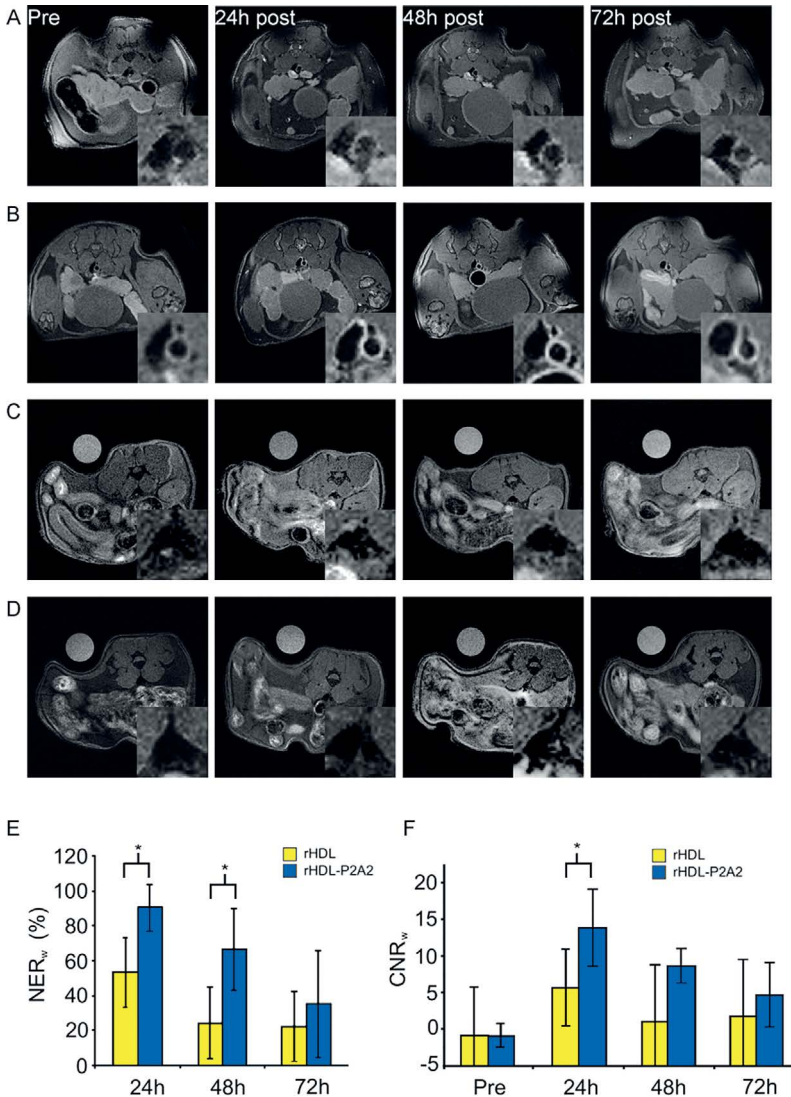
Figure 4. Representative *in vivo* MR images of apoE$^{-/-}$ mice injected with the rHDL and rHDL-P2A2 nanoparticle contrast agents. Pre- and post-injection MR images at the indicated time points after injection of 50 μmol Gd/Kg (**A**) rHDL nanoparticles and (**B**) rHDL-P2A2 nanoparticles into apoE$^{-/-}$ mice. Pre- and post-injection MR images at indicated time points after injection of 50 μmol Gd/Kg (**C**) rHDL nanoparticles and (**D**) rHDL-P2A2 nanoparticles into WT mice. (**E**) Normalized enhancement ratio of aortic wall (NER$_w$, to muscle in comparison with pre-injection image) *in vivo* after injection of rHDL (n = 6) or rHDL-P2A2 (n = 5) at 50 μmol Gd/Kg. (**F**) Contrast-to-noise ratio of aortic wall (CNR$_w$, to muscle) *in vivo* pre- and post-injection of rHDL (n = 6) or rHDL-P2A2 (n = 5) at 50 μmol Gd/Kg. Bars represent mean ± S.D.; * indicates statistical significance. The vessel to the left of the aorta is the inferior vena cava. Although arterial flow was saturated to allow delineation of the arterial wall, some enhancement in the inferior vena cava may be observed because of slow flow.

Agent	NER%			CNR			
	24h	48h	72h	Pre	24h	48h	72h
rHDL	5±28	-19±28	1±21	-7±3	-6±3	-9±4	-7±2
rHDL-P2A2	1±19	1±27	-5±27	-7±2	-7±2	-5±2	-7±2

Table 1. Percentage of normalized enhancement ratio (NER%) and contrast noise ratio (CNR) of aortic vessel wall to muscle in WT mice (n=3) injected with rHDL or rHDL- P2A2 nanoparticles.

After *in vivo* MR imaging, one mouse was sacrificed from each group and the aortas excised for optical and histological analysis at 24 hrs post injection of contrast agent, the time point of maximal MR enhancement. The rHDL-P2A2 nanoparticles were labeled with Rhodamine-PE (red) while P2fA2 itself contained carboxyfluoresceine (green). The aorta section was stained for macrophages by primary rat anti-mouse CD68 antibody and Alexa Fluor 647 (magenta) conjugated secondary goat anti-rat antibody. The co-localization between the P2fA2 and Rhodamine-PE fluorescence signals confirmed that P2fA2 lipopeptides remained incorporated into the rHDL-P2A2 nanoparticles *in vivo*. The rHDL-P2A2 nanoparticles were found to mainly localize with macrophages as shown by the co-localization of CD68-stained macrophages with both P2fA2 and Rhodamine-PE (**Figure 5A-E**). The rHDL-P2A2 nanoparticles were retained inside the core of plaques but not in the endothelial cap (**Figure 5A-E**). No uptake of rHDL-P2A2 was observed in normal arterial vessel wall (Figure 5F). The rHDL nanoparticles were partially co-localized with macrophages (**Figure 5G**, **Figure 6** for separate channels), which was consistent with our previous results[29,30]. The corresponding aorta regions from the same mice that were used for confocal microscopy were evaluated with histopathology by H&E staining, which confirmed the presence of atherosclerotic plaques in the aortas (**Figure 5H and I**).
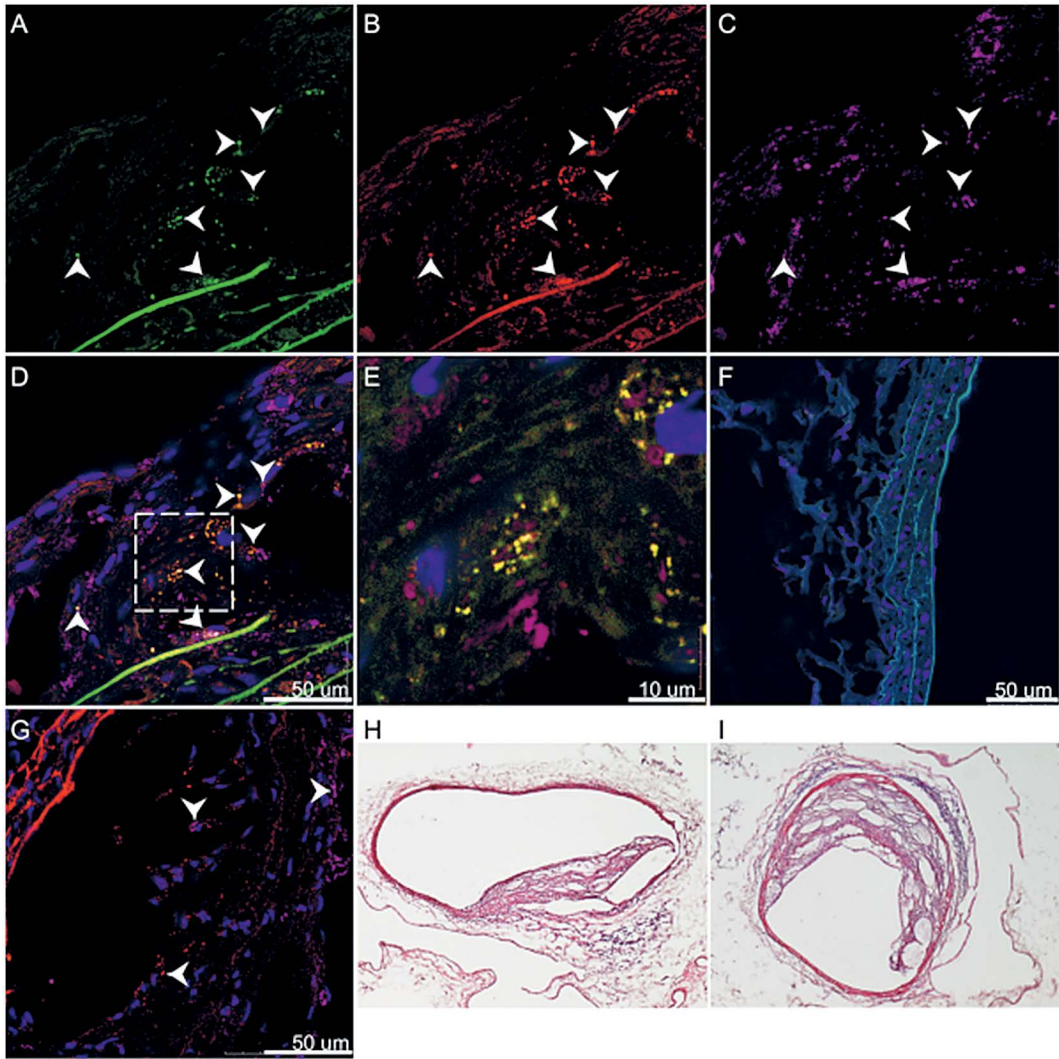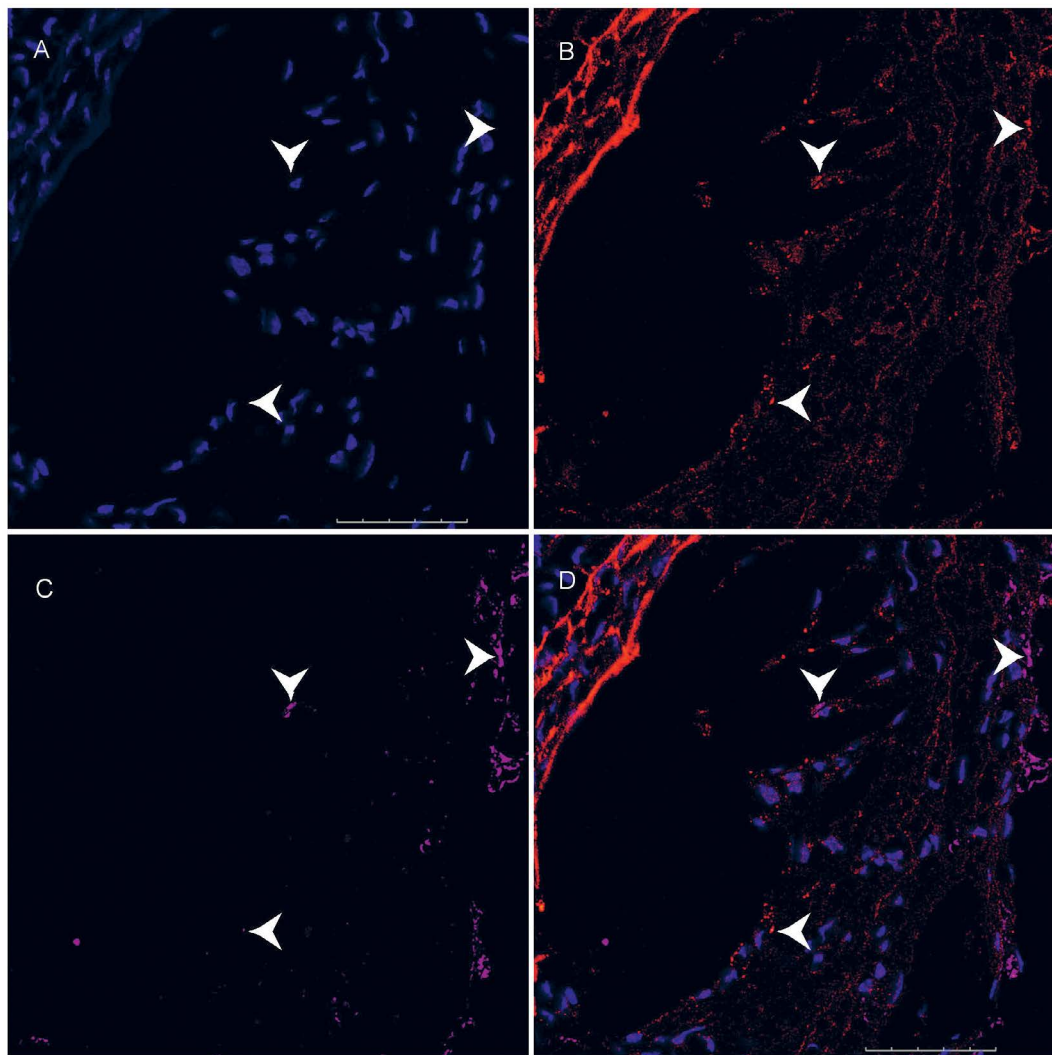
Figure 5. Confocal microscopy and H&E staining of aorta sections. (**A-C**) Separate channels and (**D**) merged image of DAPI-stained plaque section shows uptake of the rhodamine-labeled rHDL-P2A2 by macrophages. (**E**) A zoomed-in area of dashed box shown in (**D**); (**F**) An aortic vessel wall without plaque showed no uptake of rHDL-P2A2. (**G**) Merged image of DAPI-stained plaque section shows uptake of the rhodamine-labeled rHDL by macrophages (see Supplemental Information for separate channels). Green: P2fA2; Red: Rhodamine-PE; Magenta: anti-CD68; Blue: DAPI. Macrophages were identified by a CD68-specific antibody probe. The arrows indicate areas where nanoparticles co-localized with macrophages in the plaque. (**H**) H&E staining of an aorta section from the same region as section used for confocal microscopy from a mouse injected with rHDL-P2A2 nanoparticles; (**I**) H&E staining of an aorta section from the same region as section used for confocal microscopy from a mouse injected with rHDL nanoparticles.

Figure 6. Confocal microscopy of an aorta section. (**A–C**) Separate channels and (**D**) merged image of DAPI-stained plaque section shows uptake of the rhodamine-labeled rHDL by macrophages. Red: Rhodamine-PE; Magenta: anti-CD68; Blue: DAPI. Macrophages were identified by a CD68-specific antibody probe. The arrows indicate areas where nanoparticles co-localized with macrophages in the plaque.

DISCUSSION

This study demonstrates that incorporation of P2fA2 lipopeptides into the lipid layer of high density lipoprotein nanoparticles (rHDL-P2A2) can significantly enhance *in vitro* uptake in the J774A.1 murine macrophages. *In vivo* MR

imaging revealed that incorporation of P2fA2 into the rHDL nanoparticles led to greatly signal enhancement of the arterial vessel wall of atherosclerotic mice, which strongly suggests a more pronounced intraplaque uptake.

We provided evidence that rHDL-P2A2 uptake by macrophages was significantly higher than rHDL *in vitro* (**Figure 1A**) resulting in enhanced the MR signal of the rHDL-P2A2 cell pellet (Figure 2) in comparison with rHDL treated and untreated macrophages. Although the current study was not designed to explore the mechanism of uptake, the enhanced macrophage uptake of rHDL-P2A2 might be explained by the highly positively charged peptide of P2fA2 through unspecific interactions between P2fA2 and membrane constituents of macrophages, which is similar to liposomes/micelles[27]. Actually, nonspecific interactions of P2A2-carriers provide a substantial contribution to cellular accumulation and uptake. However, we found, that the uptake mode and cell selectivity distinctly depends upon the carrier architecture and the conformation of the vector peptide. Thus, P2A2 liposomes enter both capillary endothelial cells as well as endothelial cells of large vessels whereas P2A2 micelles are selectively internalized into brain capillary endothelial cells. Each particle activates different uptake modes[27,35]. Differences in uptake efficiency into macrophages were also found between P2A2 liposomes and PEG micelles with covalently attached A2, demonstrating that not only the vector but the complex formulation determines the interaction with the cell. We also found that the uptake of oligo-R and oligo-K micellar particles is distinctly different to the uptake of P2A2 micelles at least into brain capillary endothelial cells. The observation leads to the conclusion that stereo specific components are involved. Studies to further elucidate the structural basis of these differences are under way. In addition, the homing function to macrophages can be provided by apoAI in the rHDL-P2A2 particle, through the endogenous pathway of HDL and macrophage interactions. Our preliminary data also showed that the inhibitors of LDLR didn't significantly affect the uptake of P2fA2-bearing liposomes/micelles (not shown). Therefore, the down regulation of LDLR expression of macrophages after cholesterol accumulation might not affect the uptake of rHDL-P2A2. Future studies are planned to identify the exact mechanism of uptake. In addition, the results of the current study show that rHDL-P2A2 nanoparticles enhance the MR signal of atherosclerotic plaques *in vivo* in apoE$^{-/-}$ mice in comparison with rHDL nanoparticles (**Figure 4**). The increased enhancement within the arterial wall is most likely a result of increased intraplaque macrophage uptake that may be mediated by P2fA2 as suggested by confocal microscopy (**Figure 5**). Although uptake of the positively charged peptide of P2fA2

in liposomes or micelles into mouse brain capillary endothelial cells was observed *in vitro*[24,26,28], we didn't observe uptake of rHDL-P2A2 by vascular endothelial cells in the plaques *in vivo* at 24 h post injection (**Figure 4**). A variety of reasons may explain this discrepancy, including differences in the *in vivo* environment, the relatively short circulation time, and differences in phenotype of the endothelial cells.

We selected macrophages as a target because this cell type plays an essential role in the formation, pathogenesis, and vulnerability of atherosclerotic plaques. Several methods have been developed to noninvasively detect macrophages in atherosclerotic plaques both in animal models and in humans. Dextran-coated ultrasmall superparamagnetic particles of iron oxide (USPIO) are taken up by macrophages and cause strong T2*-shortening effects that can be detected as signal voids in MR images[19,36,37], which is referred to as negative contrast. Although the use of iron oxides for the detection of intraplaque macrophages has several advantages (i.e. safety and sensitivity) interpretation of the signal loss generated by iron particles may be challenging due to presence of artifacts (partial volume, perivascular effects) that cause the loss of MR signal. On the other hand, Gd-based contrast agents generate positive contrast by reducing T1 relaxation times in tissue or volumes containing the agent. However, the lower efficacy of the gadolinium based agents, relative to iron oxides, often necessitates delivery vehicles, such as liposomes, micelles, and dendrimers to achieve high-paramagnetic payloads[36].

We have previously developed Gd-based micelles to target macrophages in plaques. Micelles and liposomes have the advantages of high lipid capacity and high pay-load of Gd-based agents[22,32,36,38]. Targeting moieties such as antibodies have been conjugated to this platform. For example, antibodies to mouse macrophage scavenger receptors (MSRs, CD204) has been conjugated to micelles to form immunomicelles[22,34,38] that provided excellent in vivo enhancement of atherosclerotic plaques, which was thoroughly validated by histology. However, these immunomicelles targeting MSRs are rapidly removed from the circulation by the liver because Kupffer's cells also express scavenger receptors and play a prominent role in uptake of a wide variety of ligands. Therefore targeting the macrophage with inexpensive ligands for the MSR appears to be much more attractive than using monoclonal antibodies, which are expensive to produce and purify. In comparison to other Gd-based macrophage targeting platforms (e.g. immunomicelles)[32,34,38], rHDL nanoparticles have several advantages: they contain an endogenous protein component (apoAI) that does not trigger immunoreactions, and

they play a key role in reverse cholesterol transport by removing excess cellular cholesterol from the macrophages, and have therapeutic potential[39,40] in addition to their imaging function. Furthermore, synthetic apoAI mimic peptide (e.g. 18A and 37paA) can be used instead of purified apoAI from plasma, which avoids contaminations from blood products and provides ease for scale-up[31].

Previous studies using rHDL nanoparticles showed about 35% enhancement at 24h post-injection in 13-month-old apoE^{-/-} mice at about 10μmol Gd/Kg dose[30]. In 6-month-old apoE^{-/-} mice, we did not observe any significant enhancement (less than 30%) for rHDL nanoparticles at the dosages less than 20 μmol Gd/Kg (data not shown). The lower dosage required for older mice is due to the higher uptake of rHDL nanoparticles, which is attributable to many factors, such as lesion size, extracellular matrix, and macrophage density. The older mice have larger lesion size of plaques[41] with higher deposition of proteoglycans[41,42] and increased accumulation of macrophages[43]. In addition to promoting the uptake of HDL by macrophages, proteoglycans, especially biglycan and perlecan, are reported to help the retention of lipoproteins including HDL in plaques of apoE^{-/-} mice[41,42]. ApoAI is also found to localize in the lipid pools[44-46] and around necrotic cores[47] in human atherosclerotic plaques, which suggests a facilitated homing of rHDL in advanced plaques. The lipid exchange between lipoproteins also plays a role for rHDL based contrast agent[48,49]. Our preliminary data showed that the Gd migrates from HDL to the other lipoproteins and plasma proteins. VLDL and plasma proteins that receive the Gd-phospholipid are most likely not involved in delivering the imaging agent to the plaques. On the other hand, HDL-based lipids do transfer to other HDL endogenous particles as well as endogenous LDL. These classes of lipoproteins can then deliver Gd to the plaques. The exact amount of Gd delivered by HDL relative to LDL is still under investigation, but we observed that the enhancement due to the amount delivered by HDL is still very significant. Although LDL contributes to the signal enhancement, using rHDL to deliver contrast agent instead of LDL has definite advantages, because it not only avoids injection of atherogenic LDL but also provides therapeutic potential for atherosclerosis.

In order to achieve the early detection of plaque formation and to increase the performance of this platform, P2fA2 was incorporated into the lipid layer of rHDL nanoparticles. P2fA2 has been demonstrated to target macrophages in atherosclerotic plaques[50] . The rHDL-P2A2 nanoparticles showed 90% enhancement within the arterial vessel wall while 53% enhancement was

observed for rHDL 24 hrs after administration of a 50μmol Gd/Kg dose (Figure 4). These data suggest that rHDL-P2A2 may be more effective than rHDL nanoparticles for the *in vivo* detection of macrophage-rich vulnerable atherosclerotic plaques.

Visualization of molecular and cellular events in atherosclerosis represents a new goal for noninvasive identification of vulnerable atherosclerotic lesions[17]. We showed the rHDL-P2A2 nanoparticles had higher efficacy than rHDL nanoparticles for *in vivo* detection of macrophages in atherosclerotic plaques using high-resolution MR in the apoE$^{-/-}$ mouse model of atherosclerosis. Overall, these data suggest that rHDL-P2A2 may become a valuable contrast agent for noninvasive detection of macrophages in the evaluation of atherosclerosis.

REFERENCES

1. Fuster, V., et al. *J. Am. Coll. Cardiol.* 46, 937-954 (2005).
2. Stary, H.C., et al. *Arterioscler. Thromb. Vasc. Biol*. 20, 1177-1178 (2005).
3. Rosamond, W., et al*. Circulation* 115, e69-e171 (2007).
4. Fuster, V., et al. *J. Am. Coll. Cardiol*. 46,1209-1218 (2005).
5. Saam, T., et al. *Radiology* 244, 64-77 (2007).
6. Yuan, C., et al. *Circulation* 104,2051-2056 (2005).
7. Albuquerque, L.C., et al. *Journal of Vascular Surgery* 46,1130-1137 (2007).
8. Kang, H.W., et al. *Lab. Invest.* 86, 599-609 (2006).
9. Winter, P.M., et al. *Arterioscler. Thromb. Vasc. Biol*. 26, 2103-2109 (2006).
10. Winter, P.M., et al. *Circulation* 108, 2270-2274 (2003).
11. Vavuranakis, M., et al. *Int. J. Cardiol*. 130, 23-29 (2008).
12. Papaioannou, T.G., et al. *Int. J. Cardiol*. 134, e110-e112 (2009).

13. Cornily, J.C., et al. *Journal of Magnetic Resonance Imaging* 27, 1406-1411 (2008).
14. Virmani, R., et al. *Arterioscler. Thromb. Vasc. Biol*. 25, 2054-2061 (2005).
15. Stepansky, F., et al. *RadioGraphics* 28, e28-e28 (2008).
16. Dellegrottaglie, S., et al. *Nat. Clin. Pract. Cardiovasc. Med.* 4, 677-687 (2007).
17. Sanz, J. & Fayad, Z. A., *Nature* 451, 953-957 (2008).
18. Jaffer, F.A., et al. *J. Am. Coll. Cardiol*. 47, 1328-1338 (2006).
19. Jaffer, F.A., et al. *Circ. Res.* 94,4433-4445 (2004).
20. Warburton, L. & Gillard, J., *J. Neuroimaging* 16, 293-301 (2006).
21. Wu, J.C., et al. *Radiology* 244, 337-355 (2007).
22. Mulder, W.J.M., et al*. Magn. Reson. Med*. 58,1164-1170 (2007).
23. Choudhury, R.P., et al. *Nat. Rev. Drug Discov.*3, 913-925 (2004).
24. Sauer, I., et al. *Biochemistry* 44, 2021-2029 (2005).
25. Sauer, I., et al*. Journal of Liposome Research* 13, 81-82 (2003).
26. Sauer, I., et al. *Biochim. Biophys. Acta.*1758, 552-561 (2006).
27. Leupold, E., et al. *Biochim. Biophys. Acta* 1778, 2781-9 (2008)
28. Keller, S., et al. *Angew. Chem. Int. Ed. Engl*. 44,5252-5255 (2006).
29. Frias, J.C., et al. *Nano Lett.* 6, 2220-2224 (2006).
30. Frias, J.C., et al. *J. Am. Chem. Soc.* 126,16316-16317 (2004).
31. Cormode, D.P., et al. *Small* 4, 1437-1444 (2008).
32. Briley-Saebo, K.C., et al. *Circulation* 117, 3206-3215 (2008).
33. Briley-Saebo, K.C., et al. *Magn. Reson. Med*. 56,1336-1346 (2006).
34. Amirbekian, V., et al*. PNAS* 104, 961-966 (2007).
35. Leupold, E., et al. *Biochim. Biophys. Acta*. 1788, 442-9 (2009).
36. Briley-Saebo, K.C., et al. *Journal of Magnetic Resonance Imaging* 26, 460-479 (2007).
37. Mani, V., et al. *Magn. Reson. Med*. 56, 1096-1106 (2006).
38. Lipinski, M.J., et al. *Magn. Reson. Med.* 56, 601-610 (2006).
39. Forrester, J.S., et al. *Am. J. Cardiol.* 98, 1542-1549 (2006).
40. Williams, K.J., et al. *Curr. Opin. Lipidol.* 18,443-450 (2007).
41. O'Brien, K.D., et al. *Arterioscler. Thromb. Vasc. Biol.* 25, 785-790 (2007).
42. Kunjathoor, V.V., et al. *Arterioscler. Thromb. Vasc. Biol.* 22, 462-468 (2002).
43. Swirski, F.K., et al. *PNAS* 103,10340-10345 (2006).
44. Hoff, H.F., et al. *Circ. Res.* 37,72-79 (1975).
45. Hoff, H.F., et al. *Stroke* 7, 390-393 (1976).
46. Carter, R.S., et al. *J. Pathol*. 153, 31-36 (1987).

47. Bedossa, P., et al. *Arch. Pathol. Lab. Med.* 113, 777-780 (1989).
48. Barazza, A., et al. *Joint Molecular Imaging Conference*. Providence, RI; 2007.
49. Barazza, A., et al. *Bioconjug. Chem*. 24,1039-1048 (2013).
50. Vucic, E., et al. Apolipoprotein E derived peptide (A2) containing lipid nanoparticles as molecular imaging agents for the detection of macrophages in atherosclerotic lesions. Submitted.
51. Bradford, M.M., *Anal. Biochem.* 72, 248-254 (1976).

Imaging Strategies for the Detection of Inflammation in Atherosclerosis

Chapter 4

Noninvasive detection of macrophages using an iodanated nanoparticulate contrast agent for computed tomography

Based on

ABSTRACT

Sudden fibrous cap disruption of "high-risk" atherosclerotic plaques can trigger the formation of an occlusive thrombus in coronary arteries causing acute coronary syndromes. High-risk atherosclerotic plaques are characterized by their specific cellular and biological content (in particular, a high density of macrophages), rather than by their impact on the vessel lumen. Early identification of high-risk plaques may be useful to prevent ischemic events. One major hurdle in detecting high-risk atherosclerotic plaques in coronary arteries is the lack of an imaging modality that allows for the identification of atherosclerotic plaque composition with high spatial and temporal resolutions. We show here for the first time that macrophages can be detected with a clinical X-ray computed tomography (CT) scanner in atherosclerotic plaques of rabbits after the intravenous injection of a novel contrast agent formed of iodinated nanoparticles dispersed with surfactant. This contrast agent may become an important adjunct to the clinical evaluation of coronary arteries with CT.

INTRODUCTION

Macrophages are an essential component of the immune system but are also involved in several pathological processes, including atherosclerosis and autoimmune diseases. Acute coronary syndromes (unstable angina, acute myocardial infarction, sudden death) are caused, in about two thirds of patients, by the fibrous cap disruption of so-called "high-risk" or "vulnerable" atherosclerotic plaques[1,2]. The sudden exposure of the underlying atheromatous content of plaques to blood triggers the formation of a thrombus, that can occlude the coronary artery leading to myocardial ischemia and necrosis[3,4]. These high-risk atherosclerotic plaques are characterized by their specific cellular and biological composition rather than by their impact on the vessel lumen[5].

Macrophages play a key role in acute plaque destabilization and thrombus formation. They secrete proteases that digest the extra-cellular matrix and weaken the protective fibrous cap covering the atheromatous core, and release in atherosclerotic plaques large amounts of tissue factor that accelerate thrombus formation following plaque rupture[6]. Moreover, macrophage density measured on immuno-histology was found to be higher in atherosclerotic plaques obtained from patients with recent acute coronary syndromes as compared to plaques from patients with stable cardiovascular

disease[7]. Therefore, atherosclerotic plaques with high macrophage densities could be at higher risk of rupture and subsequent arterial thrombosis. Based on the assumption that early identification of high-risk atherosclerotic plaques could preclude ischemic events, both invasive and non-invasive imaging techniques aimed at detecting the composition of atherosclerotic plaques are growing at a rapid pace[8]. One of the most promising techniques for non-invasive imaging of coronary arteries is contrast-enhanced multi-detector computed tomography (CT). Thanks to the faster rotation times and increasing number of detectors, the spatial and temporal resolutions of CT scanners are continuously improving. An intravenous bolus of small iodinated molecules, effective in absorbing X-rays, is injected simultaneously to the acquisition of CT coronary angiography. Hence, the X-ray absorption of the vascular lumen is temporarily increased allowing for an optimal discrimination between the arterial lumen and surrounding tissues on CT. Using contrast-enhanced CT, stenosis of the coronary arteries, caused by atherosclerotic plaques protruding into the arterial lumen, are detected with an increasing accuracy in comparison to the results obtained with invasive angiography[9,10]. Furthermore, recent studies[11,12] have demonstrated the potential of CT to directly measure the size of atherosclerotic plaques in coronary arteries. Atherosclerotic plaques can be characterized on CT as hypo-dense, dense or calcified by measuring their X-ray absorption values[13,14] (densities expressed in Hounsfield units). Low densities detected in hypo-dense atherosclerotic plaques could be related to the lower X-ray absorption of lipids present in the atheromatous core and has been suggested as a marker of high-risk plaques on CT. However, densities of atherosclerotic plaques are also strongly influenced by the intensity of luminal enhancement[15] that can vary depending on many factors, such as cardiac blood flow and time delay between the injection of contrast agent and CT acquisition. This high variability of luminal enhancement represents a clear limitation for the characterization of atherosclerotic plaques by measuring their densities on CT angiographies[16]. Therefore, CT contrast agents designed for the assessment of plaque composition, especially the density of macrophages, would clearly improve the identification of high-risk coronary atherosclerotic plaques.

In this study, we tested a novel iodinated nanoparticulate contrast agent, N1177, for the detection of macrophages with CT. First, we characterized the physical and chemical properties of N1177 and tested its uptake by macrophages *in vitro*. Subsequently, we studied on CT the *in vivo* kinetics and distribution of N1177 in the blood and in macrophage-rich tissues after intravenous injection in rabbits. Finally, we tested N1177 in a model of atherosclerotic plaques generated by balloon injury in the aorta of

hypercholesterolemic rabbits. Atherosclerotic plaques in this animal model contain high levels of macrophage infiltration[17] and are similar in size to human coronary atherosclerotic plaques. We show here for the first time that macrophage infiltration can be detected in atherosclerotic plaques with a clinical CT scanner and intravenous injection of the novel contrast agent N1177.

MATERIAL AND METHODS

N1177 synthesis

N1177 (generously provided by Nanoscan Imaging) is composed of 150 mg/ml of an iodinated aroyloxy ester, 150 mg/ml of polyethylene glycol 1450 (BASF), 30 mg/ml of poloxamer 338 (Union Carbide) and 0.36 mg of tromethamine. The iodinated aroyloxy ester with the empirical formula $C_{19}H_{23}I_3N_2O_6$ and the chemical name 6-ethoxy-6-oxohexy-3,5-bis(acetylamino)-2,4-trioodobenzoate was synthesized by condensation of 6-bromohexanoate with sodium diatrizoate in DMF followed by precipitation of the product with DMSO and washing with ethanol (Sigma Aldrich Fine Chemicals). Poloxamer 338 was used after purification by diafiltration to reduce the level of low-molecular weight polymer. Nanoparticulate suspension was obtained by milling the iodinated aroyloxy ester and poloxamer 338 in presence of inert beads (Elan). After the milling, the suspension was separated from the beads by membrane filtration (membrane pore size in the range of 2 to 5 μm). Polyethylene glycol 1450 and tromethamine were added to the suspension to stabilize particle size and to buffer the solution to neutral pH, respectively.

Characterization of N1177

The size of nanoparticles was measured by laser light scattering (LA 910, Horiba Instruments Ltd). Iodine concentration was measured by ICP-MS (Elemental Research Inc.). N1177 was converted in a fine aerosol by a nebulizer, carried by an argon gas stream into the plasma region of the ICP-MS and ionized prior to analysis in the mass spectrometer. TEM imaging was performed using a Hitachi 7000 microscope operating at 80 kV after staining with a saturated aqueous solution of uranyl acetate.

Cell culture

RAW 264.7 mice macrophages (a generous gift from Ines Pineda Torra, PhD, New York University School of Medicine) were grown on twelve 75 cm^2-

culture plates in MEM media supplemented with fetal bovine serum, sodium pyruvate, L-glutamine, penicillin, streptomycin and non-essential amino acids. Macrophages were washed with PBS once and incubated for one hour with media containing either N1177 (n = 6) or iopamidol (n = 6) at a final concentration equivalent to 1 mg iodine/ml. After incubation, cell-plates were washed four times with PBS and imaged in phase-contrast with an optical microscope. Macrophages were then manually scraped from plates. Cell pellets (n = 12) were collected after centrifugation at 4,000 rpm for five minutes, weighted and digested with TMAH. Iodine content was measured in the liquid sample solution with ICP-MS and expressed as mean weight of iodine/mg wet weight tissue.

Animal protocol

Twenty male New Zealand White (NZW) rabbits (mean age, four months; mean weight = 3.1 ± 0.2 kg; Covance) were included in this study. Kinetic studies were performed in eight non-atherosclerotic NZW rabbits. Aortic atherosclerosis plaques were induced in eight NZW rabbits by a combination of 4 months of high cholesterol diet (4.7% palm oil and 0.3% cholesterol-enriched diet; Research Diet Inc.) and a repeated balloon injury of the aorta (two weeks and six weeks after starting the high-cholesterol diet). Aortic injury was performed from the aortic arch to the iliac bifurcation with a 4F Fogarty embolectomy catheter introduced through the femoral artery. All procedures were performed under general anaesthesia by an intramuscular injection of ketamine (20 mg/kg; Fort Dodge Animal Health) and xylazine (10 mg/kg; Bayer Corp.). Four non-injured rabbits, fed a normal chow diet, were used as controls. All experiments were approved by the Mount Sinai School of Medicine Institute Animal Care and Use Committee.

Imaging protocol

After anaesthesia with an intra-muscular injection (ketamine: 20 mg/kg, xylazine: 10 mg/kg and acepromazine: 0.5 mg/kg) and placement of a 22-gauge catheter in the marginal ear vein, rabbits were imaged with a 64-slice multi-detector computed tomography scanner (Sensation 64; Siemens Medical Solutions with the following parameters: tube voltage, 120 kV; current intensity, 180 mA; rotation time, 330 ms; detector collimation, 32 x 0.6 mm collimation; and table feed, 15 mm per rotation. The in-plane resolution of this CT protocol is evaluated at 0.4 x 0.4 mm. Axial 0.4 mm-thick slices were reconstructed on the scanner with a 30f medium smooth Kernel. The field of view was 100 x 100 mm and the data were acquired into a 512 x 512 data matrix, giving a pixel size of 0.2 x 0.2 mm. After a pre-

contrast CT scan, N1177 was injected intravenously at a dose equivalent of 250 mg iodine per kg body weight (final injected volume: 11 ml). At one week interval, the same rabbits underwent a second imaging session with intravenous injection of a conventional iodinated contrast agent at a dose equivalent to 250 mg iodine per kg body weight (iopamidol, Bracco Diagnostics; with a 1:4 dilution with saline, yielding a concentration of 75 mg iodine/ml; final injected volume: 10 ml). For quantitative analysis of CT images, densities were measured in regions of interest (ROI) using the dedicated CT workstation (Leonardo; Siemens Medical Solutions) and expressed in Hounsfield units. For kinetic studies, CT scans were acquired before, during and at different time points after the injection of each contrast agent. The densities were measured in ROI placed on selected organs of the rabbits ($n = 8$) on the CT scans acquired at each time point. For the evaluation of the aortic wall, CT scans were acquired before, during and two hours after the injection of each contrast agent. Densities of the aortic wall were evaluated every 10 mm on eleven axial CT slices of the abdominal aorta of eight atherosclerotic rabbits ($n = 88$) and four control rabbits ($n = 44$). Series of axial slices were matched using the vertebrae as landmarks. After delineation of the aortic lumen, twelve circular ROIs of 12 pixels each were placed adjacent to the lumen on the CT scan acquired during the injection of contrast agent. The densities were then measured in the same ROIs on the CT scans acquired before and two hours after the injection of each contrast agent and expressed as the average of the 12 ROIs placed on each slice. Multiplanar reformations and three-dimensional reconstructions were obtained with a Terarecon workstation (Terarecon Inc.).

Histology

Following CT imaging, rabbits were euthanized by an intravenous injection of 120 mg/kg of sodium pentobarbital (Sleepaway; Fort Dodge Animal Health). A bolus of heparin was injected prior to euthanasia to prevent clot formation. Aortas were excised, fixed for 24 hours in 4% paraformaldehyde and embedded in paraffin. Five-μm-thick slices were sectioned in the same direction as CT slices and stained with Masson's trichrome. Macrophages were detected on adjacent slices by immunohistochemistry. Arterial sections were incubated with 0.3% hydrogen peroxide to block endogenous peroxidase, then with a monoclonal mouse antibody to RAM-11, a marker of rabbit macrophage cytoplasm[17] (dilution 1:50, Dako). Biotinylated polyclonal anti-mouse secondary antibody and peroxidase-conjugated streptavidin were applied for 30 minutes each with the use of the ABC Kit (Dako). Peroxidase activity was visualized by diaminobenzidine to yield brown cytoplasmic reaction products.

Sections were counterstained with hematoxylin. Images of randomly selected sections of atherosclerotic plaques ($n = 40$) were obtained using an optical microscope (magnification x 2) coupled to a digital camera. On each image, the luminal area, the area bound by the internal elastic lamina and the macrophage-rich area (RAM-11 positive) of the intima were measured using ImageProPlus software (Media Cyberbetics). Intimal area was calculated as the difference between the area bound by the internal elastic lamina and the luminal area. For TEM imaging, tissue samples were cut in small pieces and fix overnight in a 2.5% glutaraldehyde solution. After several washes, tissue fragments were post-fixed in 1% osmium tetroxide solution, dehydrated and embedded in epoxy resin. Semi-thin (1-µm) serial sections were stained for hematoxylin-eosin to locate the macrophage-rich regions. Subsequently, ultra-thin sections from macrophage-rich regions were cut and mounted on Formvar-coated copper grids and counterstained with a solution of saturated uranyl acetate before analysis in TEM. For energy dispersion spectroscopy, 10-µm-thick cryosections of atherosclerotic plaques were cut, freeze-dried on a carbon holder and covered by a thin film of carbon. The absorption spectrum of electron-dense granules was analyzed with scanning electron microscopy using dedicated software (NanoAnalysis; Evex Inc.).

Statistical analysis

All probabilities were two-sided and expressed as mean ± standard error mean. Values of $p < 0.05$ were considered as significant. Statistical analysis was conducted with SPSS software (SPSS Inc.). Iodine content in cell pellets was compared using a non parametric Wilcoxon test. For kinetics studies, densities before and two hours after the injection of contrast agent were compared in each organ using a Wilcoxon test for paired samples. Densities of the arterial wall before and two hours after the injection of a contrast agent were compared using a Student t-test for paired samples. The enhancement of the arterial wall after the injection of N1177 and iopamidol was compared using a Student t-test.

RESULTS

Properties of the contrast agent N1177

N1177 is a suspension composed of crystalline iodinated particles dispersed with surfactant. Iodinated particles are composed of ethyl-3,5-bis(acetylamino)-2,4,6-triiodobenzoate (**Figure 1a**), an esterified derivative of the X-ray contrast agent diatrizoic acid with a very low aqueous solubility

(≈ 2 µg/ml). Biocompatible surfactants were added to the iodinated particles to prevent aggregation and to stabilize the nanoparticle size. Nanoparticulate suspension was prepared by milling the iodinated particles with the surfactants in the presence of inert beads. Final hydrodynamic diameter of N1177 was measured at a mean 259 nm by laser-light scattering with a broad spectrum of sizes (90% of diameters in the range of 153 to 408 nm) and remained stable for eight months. Iodine concentration of N1177 was measured by inductively coupled plasma mass spectrometry (ICP-MS) at 67 mg iodine/ml. Transmission electron microscopy of N1177 revealed a core with several electron-dense granules covered with molecules of polymer detected as negative prints after staining with aqueous uranyl acetate (**Figure 1b**). N1177 formed nanoparticles of various sizes and shapes. Analysis of the absorption spectrum with TEM confirmed the presence of
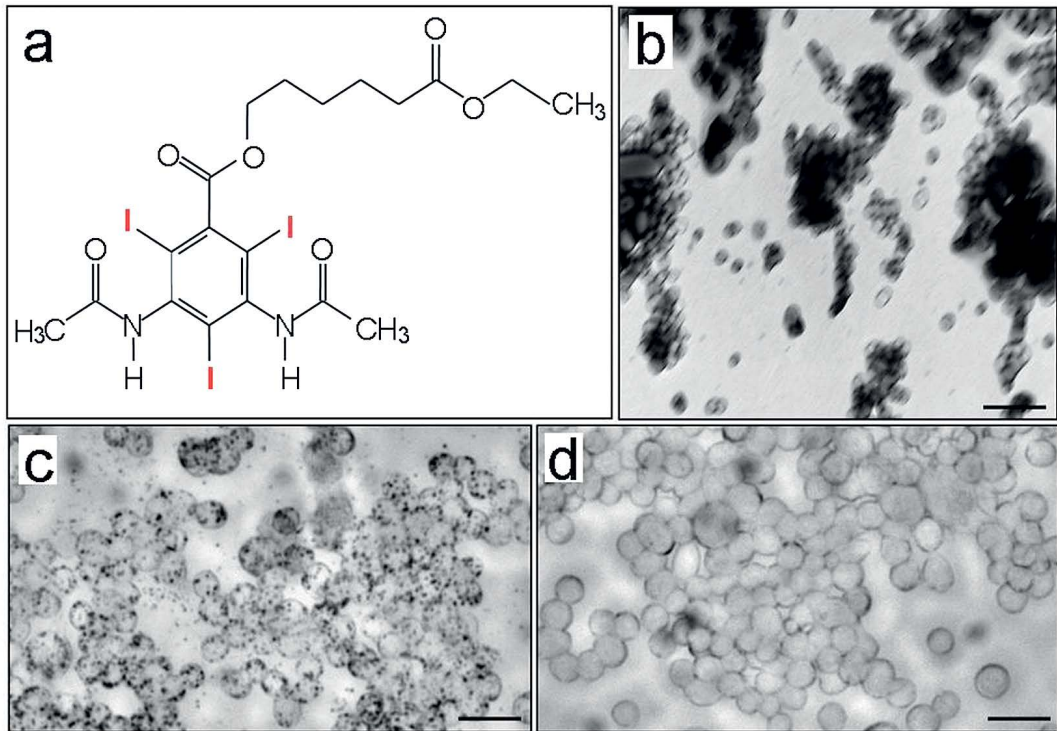
Figure 1. Properties of the contrast agent N1177. (**a**) Schematic representation of the iodinated compound of the contrast agent N1177 with the three iodine atoms in red. (**b**) Electron microscopic view of N1177 showing electron-dense iodinated granules coated by polymers appearing as negative prints after staining with a solution of uranyl acetate. Note the various sizes and shapes of nanoparticles found in the suspension. Bar width, 100 nm. (**c,d**) Optical microscopy in a phase-contrast mode of macrophages after one hour incubation *in vitro* with N1177 (**c**) or with the conventional CT contrast agent (**d**). Numerous dark granules were visualized only in the cytoplasm of macrophages incubated with N1177. Bar width, 100 µm.

iodine in the electron-dense granules (data not shown). We tested *in vitro* the uptake of N1177 by macrophages. Mice macrophages were incubated one hour with either N1177 or a conventional CT contrast agent adjusted to obtain the same concentration of iodine. On optical microscopy in a phase-contrast mode, numerous dark granules were visualized only in the cytoplasm of macrophages incubated with N1177 (**Figure 1c**,**d**). Quantification of iodine in cell pellets with ICP-MS confirmed the higher uptake of N1177 by macrophages as compared to a conventional CT contrast agent (4,920 ± 1,019 vs. 56 ± 11 μg iodine/g wet weight, respectively; *p* = 0.03).

In vivo kinetics and distribution of N1177

We performed serial CT imaging of eight non-atherosclerotic New Zealand White (NZW) rabbits to study the enhancement obtained in the blood and in macrophage-rich tissues after an intravenous injection of N1177 (corresponding to 250 mg iodine/kg body weight). As a control, the same rabbits were imaged one week later using the same CT protocol after injection of a conventional clinically-used iodinated contrast agent (iopamidol) at a dose adjusted to 250 mg iodine/kg body weight. We first tested if the larger size of N1177 compared to conventional CT contrast agents would lengthen its half-life in blood and allow for delayed arterial and venous angiographies. Indeed, five minutes after the intravenous injection of N1177, the density of the aortic lumen was measured at 125.3 ± 14.1 HU (vs. 61.8 ± 13.9 HU with the conventional CT contrast agent) and this enhancement was sufficient to obtain a clear delineation of all major arterial and venous contours on CT (**Figure. 2a**,**b**). However, the vascular enhancement decreased rapidly and, two hours after the injection of N1177, the density measured in the aortic lumen was not significantly different from pre-contrast values (42.3 ± 3.7 vs. 42.6 ± 5.5 HU, respectively; *p* = 0.80). At this time point, N1177 had distributed to organs containing macrophages (**Figure 2c**,**d**). Hence, densities measured in the spleen and in the liver were significantly higher two hours after the injection of N1177 compared to pre-contrast values (106.7 ± 6.5 vs. 65.0 ± 2.2 HU respectively in the spleen, *p* = 0.01; 114.4 ± 10.3 vs. 63.1 ± 5.1 HU respectively in the liver, *p* = 0.01), whereas no enhancement was detected in these organs two hours after the injection of a conventional CT contrast agent (**Figure 2e**). Organs devoid of macrophages (e.g., muscle) showed no enhancement on CT acquisitions after the injection of N1177. Of note, a weak contrast was found in the kidneys and in the urinary tract from one hour after the injection of N1177 and was presumably attributable to the renal excretion of iodine molecules contained in N1177. However, no residual enhancement was detectable in the rabbits 24 hours after the injection of N1177.
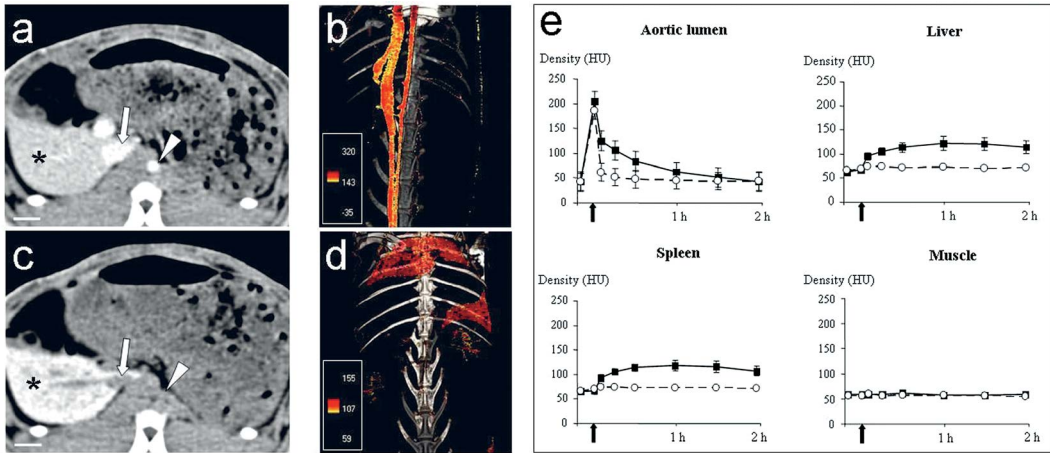
Figure 2. Kinetics and distribution of N1177 in non-atherosclerotic rabbits. (**a,b**) Axial view on computed tomography (CT) of a non-atherosclerotic rabbit five minutes after the injection of N1177 (**a**) showing the enhancement of the aorta (white arrowhead) and vena cava (white arrow) allowing for the reconstruction of three-dimensional CT angiograms (**b**). (**c,d**) Two hours after the injection of N1177, a strong enhancement was detected in the spleen (asterisk) on an axial CT view of the rabbit (**c**). The regions of high densities were identified on a three-dimensional reconstruction of the CT scan using a color scale. Note the strong enhancement of the spleen and the liver two hours after the injection of N1177 (**d**). The same level and width windows were used for images **a** and **c**. Inserts in **b** and **d** indicate the color scale of densities in Hounsfield units (HU). (**e**) Densities in HU of the different organs on CT before and at different time points after the injection of N1177 (■) or a conventional iodinated contrast agent (O). Densities measured in macrophage-rich organs were significantly higher two hours after the injection of N1177 compared to pre-contrast values, whereas no enhancement was detected in these organs two hours after the injection of a conventional CT contrast agent. Black arrows denote the time of injection.

Detection of macrophages in atherosclerotic plaques

Atherosclerotic plaques were generated in eight NZW rabbits by the combination of a double balloon injury in the aortas (one month apart) and four months of hypercholesterolemic diet. Atherosclerotic plaques in this animal model contain high levels of macrophage infiltration[17] and are similar in size to human coronary atherosclerotic plaques. Furthermore, this animal model has been extensively used to study the effects of anti-atherosclerotic drugs on atherosclerotic plaque size[18] and composition[19]. Four non-injured NZW rabbits, fed a chow diet, were used as controls. The same rabbits *(n = 12)* were first imaged with a conventional iodinated contrast agent (iopamidol) and, one week later, with N1177. From the previous kinetics studies, the optimal imaging time for the detection of macrophages in atherosclerotic plaques on CT was estimated to be two hours after the injection of N1177. At this time point, enhancement of macrophage-rich tissues was high and the density of the aortic lumen was back to its baseline

value. Hence, enhancement of macrophage-rich atherosclerotic plaques could be discriminated from the density of the aortic lumen on CT images. Densities measured in atherosclerotic plaques increased from 29.7 ± 6.0 HU before injection to 43.0 ± 7.3 HU two hours after the injection of N1177 compared to 31.5 ± 6.9 HU and 35.6 ± 8.1 HU after injection of the conventional contrast agent, respectively. The enhancement of atherosclerotic plaques after the injection of N1177 was significantly higher than after injection of a conventional CT contrast agent (13.3 ± 1.0 vs. 4.1 ± 0.9 HU, respectively; $p < 0.001$) and could reach up to 48 HU in certain regions of atherosclerotic plaques (**Figure 3**). No significant enhancement was detected in the arterial wall of control non-atherosclerotic rabbits two hours after the injection of N1177 or a conventional CT contrast agent (0.9 ± 1.2 HU and 0.3 ± 1.3 HU, respectively).
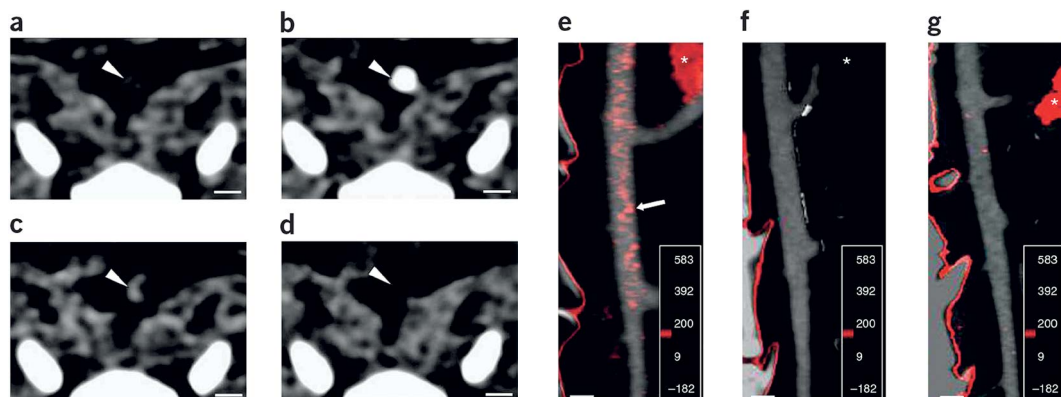
Figure 3. Imaging of macrophages in atherosclerotic plaques. Axial views of the same atherosclerotic plaque (white arrowheads) in the aorta of a rabbit on computed tomography (CT) obtained before (**a**), during (**b**) and two hours after the injection of N1177 (**c**) or a conventional contrast agent (**d**). These images were acquired in two separate imaging sessions. Before the injection of contrast agent, the atherosclerotic plaque could not be differentiated from the surrounding tissues, whereas a strong enhancement was detected in the atherosclerotic plaque only after the injection of N1177. The same level and width windows were used for all views. (**e-g**) Regions of high densities on the CT scan acquired two hours after the injection of N1177 were identified using a color scale and fused to the aortic angiography obtained in the same rabbit during the injection of contrast agent. Intense red spots were detected in atherosclerotic plaques after the injection of N1177 (**e**) but neither in atherosclerotic plaques after injection of a conventional contrast agent (**f**), nor in the aortic wall of a control rabbit injected with N1177 (**g**). The insert indicates the color scale of densities in Hounsfield units. White asterisk: spleen. Bar width, 5 mm.

At the end of the imaging protocol, the aortas were excised and sectioned in segments corresponding to the reconstructed CT axial slices. After staining sections with Masson's trichrome to detect the fibrous cap and lipid-rich core of atherosclerotic plaques, the distribution of macrophages was analyzed by

immunostaining of adjacent sections using a specific monoclonal antibody to RAM-11, a marker of rabbit macrophage cytoplasm. Correlations were observed between the increase in density of atherosclerotic plaques on CT two hours after the injection of N1177 and the intensity of macrophage infiltration in the lipid-rich core on the corresponding histological sections (**Figure 4a,b**).
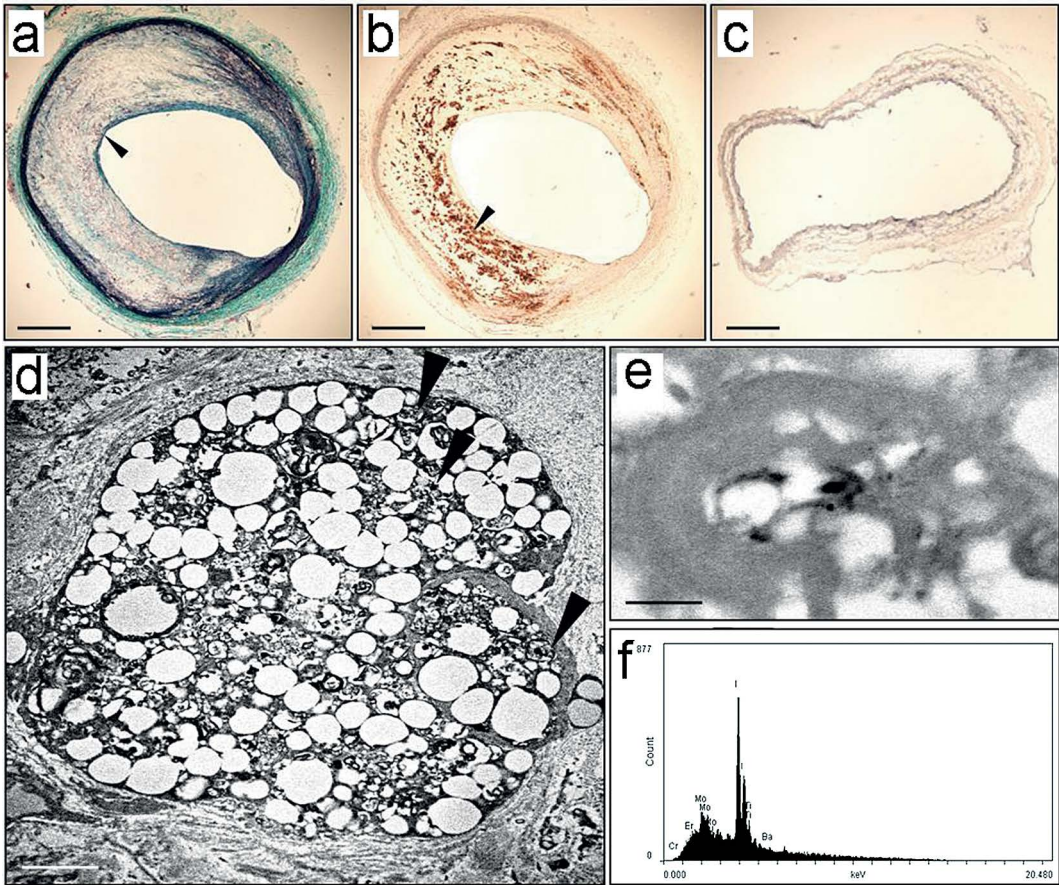

Figure 4. Histology. (**a**) Axial section of the atherosclerotic plaque corresponding to the CT images shown in Figure 3 showing the presence of a large lipid-rich core covered by a thin cap of collagen (black arrowhead) stained in green with Masson's trichrome. (**b,c**) Immunohistochemistry for macrophages with a monoclonal RAM-11 antibody counterstained with hematoxylin. Note the intense macrophage infiltration (**b**, black arrowhead) in the lipid-rich core of the section adjacent to (**a**), that was absent on the aortic section from a non-atherosclerotic rabbit (**c**). Bar width, 1 mm. (**d**) Numerous electron-dense granules (white arrowheads) were detected with transmission electron microscopy (TEM) next to lipid inclusions in lysosomes of macrophages from atherosclerotic plaques of rabbits sacrificed two hours after the injection of N1177. Bar width, 5 µm. (**e**) Higher magnification of the image showing electron-dense granules similar to the aspect of N1177 on TEM in **Fig. 1b**. Bar width, 500 nm. (**f**) Characteristic absorption spectrum of iodine (**I**) detected with energy dispersion spectroscopy in the area of electron-dense granules.

Hence, atherosclerotic plaques with an enhancement higher than 13.3 HU on N1177-enhanced CT demonstrated a macrophage area extending to more than 20% of the intimal area on 90% of corresponding histological sections. No macrophages were detected on immunohistochemistry in the aortic wall of control rabbits (**Figure 4c**) that showed no significant enhancement on N1177-enhanced CT. Transmission electronic microscopy demonstrated the presence of a large number of electron-dense granules in the lysosomes of macrophages in atherosclerotic plaques of rabbits sacrificed two hours after the injection of N1177 (**Figure 4d**,**e**). Energy dispersion spectrometry in the area of electron-dense granules showed the characteristic profile of iodine (**Figure 4f**) confirming that N1177 accumulates in macrophages of atherosclerotic plaques.

DISCUSSION

The results presented here demonstrate the feasibility of non-invasive detection of macrophages in atherosclerotic plaques of rabbits using a clinical CT scanner and the novel iodinated nanoparticulate contrast agent N1177. First, *in vitro* studies confirmed the high uptake of N1177 by macrophages. We then confirmed that the intravenous administration of N1177 lead to a significant enhancement of macrophage-rich organs using *in vivo* CT. After performing kinetic studies of N1177 distribution in macrophage-rich organs and in the blood, we demonstrated that an increase in density can be detected in atherosclerotic plaques of rabbits two hours after intravenous injection of N1177 and correlated with macrophage infiltration on corresponding histological sections.

Several non-invasive techniques have been tested both in animal models and in patients for the detection of macrophages in atherosclerotic plaques. Dextran-coated ultrasmall superparamagnetic particles of iron oxide (USPIO) are taken up by macrophages causing strong T2*-shortening effects[20,21] that can be detected as signal voids on magnetic resonance imaging (MRI). In carotid atherosclerotic plaques[22,23], focal signal voids could be detected on MRI after the injection of USPIO and were localized to the macrophage-rich regions that accumulated iron particles on histology. However, the small size of coronary arteries and the constant cyclic cardiac motion require both high spatial and temporal imaging resolutions that are currently not achievable with MRI. Furthermore, the optimal imaging time after the injection of USPIO was evaluated to be 24 to 48 hours[12], which shall clearly limit the

practical use of this technique as a screening tool. Another approach to detecting macrophages in atherosclerotic plaques uses the glucose analog ^{18}F-fluorodeoxyglucose (FDG), a positron emission tomography (PET) contrast radiotracer. FDG competes with glucose for uptake into metabolically active cells, including macrophages in atherosclerotic plaques, and is trapped inside cells after phosphorylation. Interestingly, a recent clinical PET study[24] has found higher FDG uptake in carotid atherosclerotic plaques of symptomatic patients as compared to plaques of asymptomatic patients. However, the very intense FDG uptake of normal myocardium present in about half of the patients represents a clear limitation of this technique for imaging coronary atherosclerotic plaques[25].

A CT contrast agent similar to N1177 has been previously tested for the detection of lymph nodes after subcutaneous or intra-peritoneal administrations[26,27]. In our study, we demonstrated that N1177 administrated intravenously can be used initially as an intra-vascular CT contrast agent and accumulates thereafter in macrophages. This route of administration was well tolerated in rabbits. Compared to other described CT intra-vascular contrast agents[28-32], N1177 combines the double advantage of a fast clearance from blood together with a rapid and high accumulation in macrophage-rich tissues. After performing kinetic studies, the optimal imaging time point for a dose of 250 mg iodine/kg body weight of N1177 was two hours after the injection. At this time point, increased densities in macrophage-rich atherosclerotic plaques could be discriminated from the density of the vascular lumen. Hence, N1177-enhanced CT has demonstrated significant advantages for the detection of macrophages in atherosclerotic plaques, relative to previously reported USPIO-enhanced MRI or PET imaging with ^{18}F-FDG. Namely, that N1177-enhanced CT allows for the detection of macrophage-rich tissues with a positive enhancement (i.e. increase in signal intensity) as soon as two hours after the intravenous injection of N1177 as compared to the detection of a negative enhancement (i.e. decrease in signal intensity) 24 hours after the injection of USPIO on MRI. Furthermore, N1177-enhanced CT does not require the injection of a radioactive tracer and offers higher spatial and temporal resolutions than PET. Therefore, the novel contrast agent N1177 may be useful for the detection of macrophages in high-risk atherosclerotic plaques and become an important adjunct to the clinical evaluation of coronary arteries with CT.

This novel imaging technique presents a few limitations for the detection of macrophages in atherosclerotic plaques. First, kinetics of N1177 in atherosclerotic plaques and the optimal dose of N1177 to be injected will need to be evaluated in additional studies. Second, in comparison to other

techniques such as MRI, computed tomography studies require to irradiate patients with X-rays. Radiation burden could be a concern in patients, particularly in case of repeated CT acquisitions. Third, whether high densities due to the accumulation of N1177 could be discriminated from calcifications in complex atherosclerotic plaques of humans needs to be determined. However, future technological developments in computed tomography scanners could help to overcome these current limitations. The use of highly efficient flat-panel detectors[33] may allow to decrease the intensity of X-ray beams and subsequently the level of patient irradiation. In addition, dual-energy beam technology[34,35], based on simultaneous CT acquisitions using two beams at different energy levels, may allow to discriminate between the X-ray absorption properties of iodine and calcium in atherosclerotic plaques.

In conclusion, we described the *in vivo* detection of macrophages in rabbits using a clinical CT scanner after intravenous injection of a suspension of iodinated nanoparticles. The technique described in the present study may have broad clinical applications. *In vivo* imaging of macrophage infiltration using N1177-enhanced CT may be helpful for diagnosis and prognosis in a number of pathological states, including atherosclerosis or infectious and autoimmune diseases. In addition, the underlying technology, which allows for the targeting of iodinated nanoparticles to macrophages, may be used to specifically dispense therapeutic agents (e.g., anti-atherosclerotic, anti-infectious, anti-inflammatory drugs) to diseased tissues with minimal systemic toxicity.

REFERENCES

1. Naghavi, M., et al. *Circulation* 108, 1664–1672 (2003).
2. Virmani, R., et al. *J. Am. Coll. Cardiol.* 47, C13–18 (2006).
3. Libby, P., *Circulation* 104, 365–372 (2001).
4. Fuster, V., et al. *J. Am. Coll. Cardiol.* 46, 937–954 (2005).
5. Topol, E.J. & Nissen S.E., *Circulation* 92, 2333–2342 (1995).
6. Libby, P., *Nature* 420, 868–874 (2002).
7. Mauriello, A., et al. *J. Am. Coll. Cardiol.* 45, 1585–1593 (2005).

8. Fayad, Z.A. and Fuster, V., *Circ. Res.* 89, 305–316. (2001).
9. Hoffmann, U., et al. *Circulation* 110, 2638–2643 (2004).
10. Leber, A.W., et al. *J. Am. Coll. Cardiol*. 46, 147–154 (2005).
11. Achenbach, S., et al. *Circulation* 109, 14–17 (2004).
12. Leber, A.W., et al. *J. Am. Coll. Cardiol.* 47, 672–677 (2006).
13. Viles-Gonzalez, J.F., et al. *Circulation* 110, 1467–1472 (2004).
14. Leber, A.W., et al. *J. Am. Coll. Cardiol.* 43, 1241–1247 (2004).
15. Schroeder, S., et al. *Clin. Radiol.* 56, 466–474. (2001).
16. Pohle, K., et al. Atherosclerosis. 2007 Jan;190(1):174-80.
17. Zhang, Z., et al. *BMC Nucl. Med* 6, 3 (2006).
18. Helft, G., et al. *Circulation* 105, 993–998. (2002).
19. Aikawa, M., et al. *Circulation* 97, 2433–2444 (1998).
20. Ruehm, S.G., et al. *Circulation* 103, 415–422 (2001).
21. Hyafil, F., et al. *Arterioscler. Thromb. Vasc. Biol* .26, 176–181 (2006).
22. Kooi, M.E., et al. *Circulation* 107, 2453–2458 (2003).
23. Trivedi, R.A., et al. *Stroke* 35, 1631–1635 (2004).
24. Rudd, J.H., et al. *Circulation* 105, 2708–2711 (2002).
25. Dunphy, M.P., et al. *J. Nucl. Med* 46, 1278–1284 (2005).
26. Wisner, E.R., et al. *Acad. Radiol.* 1, 377–384 (1994).
27. McIntire, G.L., et al. *Invest. Radiol.* 35, 91–96 (2000).
28. Krause, W., *Adv. Drug. Deliv. Rev*. 37, 159–173 (1999).
29. Rabin, O., et al. *Nat Mater* 5, 118–122 (2006).
30. Mukundan, S. Jr, et al. *AJR* 186, 300–307 (2006).
31. Zheng, J., et al. *Invest. Radiol.* 41, 339–348 (2006).
32. Fu, Y., et al. *Bioconjug. Chem*. 17, 1043–1056 (2006).
33. Gupta, R., et al. *Eur. Radiol.* 16, 1191–1205 (2006).
34. Flohr, T.G., et al. *Eur. Radiol.* 16, 256–268 (2006).
35. Boll, D.T., et al. *J. Comput. Assist. Tomogr.* 30, 804–811 (2006).

Chapter 5

Annexin A5-functionalized bimodal nanoparticles for MRI and fluorescence imaging of atherosclerotic plaques

Based on

Author contribution: Esad Vucic: designed and performed experiments, analyzed data and revised the manuscript.

ABSTRACT

Apoptosis and macrophage burden are believed to correlate with atherosclerotic plaque vulnerability and are therefore considered important diagnostic and therapeutic targets for atherosclerosis. These cell types are characterized by the exposure of phosphatidylserine (PS) at their surface. In the present study we developed and applied a small micellar fluorescent annexin A5-functionalized nanoparticle for non-invasive magnetic resonance imaging (MRI) of PS exposing cells in atherosclerotic lesions. Annexin A5-mediated target-specificity was confirmed with ellipsometry and *in vitro* binding to apoptotic Jurkat cells. *In vivo* T_1-weighted MRI of the abdominal aorta in atherosclerotic ApoE$^{-/-}$ mice revealed enhanced uptake of the annexin A5-micelles as compared to control-micelles, which was corroborated with *ex vivo* near infrared fluorescence images of excised whole aortas. Confocal laser scanning microscopy (CLSM) demonstrated that the targeted agent was associated with macrophages and apoptotic cells, whereas the nonspecific control agent showed no clear uptake by such cells. In conclusion, the annexin A5-conjugated bimodal micelles displayed potential for non-invasive assessment of cell types that are considered to significantly contribute to plaque instability, and therefore may be of great value in the assessment of atherosclerotic lesion phenotype.

INTRODUCTION

Annexin A5, a 36 kDa protein belonging to the annexin family, is known to bind to the negatively charged phospholipid phosphatidylserine (PS) in the presence of Ca^{2+} [1,2]. In almost all homeostatic cells this phospholipid is restricted to the cytoplasmic leaflet of the plasma membrane and therefore inaccessible from the extracellular compartment[3]. However, dying and activated cells, such as apoptotic cells, activated platelets[4,5] and activated macrophages[6], are known to expose PS also in the exoplasmic layer of the cell membrane. Furthermore, membrane integrity is lost during the process of necrosis, thereby allowing extracellular proteins to enter the cell[7]. Therefore, annexin A5 has been proposed and exploited to function as a ligand to target apoptotic, necrotic and other PS exposing cells for a variety of applications, including cell sorting, imaging, and drug targeting[8-11].

In atherosclerosis, a high occurrence of apoptosis and necrosis, as well as high macrophage burden are believed to contribute significantly to plaque vulnerability and rupture[12-15]. Consequently, identification of these markers

using annexin A5-targeted non-invasive diagnostic imaging may contribute to discrimination between atherosclerotic lesions with a stable and unstable phenotype, which would be of great clinical value. To this aim, there have been a number of studies where technetium- (^{99}Tc) or indium-labeled (^{111}In) annexin A5 has been used for imaging of vulnerable plaque or the effect of therapy with nuclear techniques in both experimental[16-20] and human atherosclerosis[21]. Importantly, these studies demonstrated significant correlations between the extent of annexin A5 uptake, macrophage content and the amount of apoptosis. Furthermore, all of these values were shown to increase with more advanced lesions, as classified according to the American Heart Association.

Although nuclear imaging is a very sensitive technique, it suffers from poor spatial resolution and the images lack detailed anatomical information. MRI is an imaging modality with a high spatial resolution and can discriminate between different plaque components[22]. Nevertheless, MRI suffers from relatively low sensitivity[23]. In targeted molecular MRI the latter drawback is frequently compensated for by using high relaxivity (super)paramagnetic imaging probes[24]. These probes, usually nanoparticulate in nature, contain either (multiple) iron oxide crystals or a high payload of gadolinium. We and others previously reported on a number of such nanoparticles that have been successfully applied for MRI-based molecular imaging of atherosclerosis. These include target-specific lipid-based nanoparticles within the size range of 10-300 nm, such as micelles[25, 26], high-density lipoproteins (HDL) (*27*), liposomes[28] and microemulsions[29], in which large numbers of Gd-DTPA moieties were incorporated in the lipid (bi)layer. Alternatively, iron oxide-based nanoparticles have been developed to enable molecular MRI of lipoproteins[30] or adhesion molecule expression in atherosclerotic plaques[31]. For validation and co-localization purposes the aforementioned nanoparticles can include additional fluorescent dyes, such as fluorescent lipids or quantum dots[32].

In the present study we developed and characterized a small annexin A5-conjugated micellar nanoparticle, carrying multiple Gd-labeled lipids for MRI and fluorescent lipids for fluorescence microscopy or imaging. Target-specificity of this nanoparticle for PS was examined with ellipsometry of PS-containing membranes as well as MRI and CLSM of apoptotic Jurkat cells *in vitro*. Furthermore, in a pilot study, the nanoparticles were applied for *in vivo* MR imaging of phosphatidylserine exposing cells in atherosclerotic lesions of ApoE knockout (ApoE^{-/-}) mice. *Ex vivo* near infrared fluorescence imaging of intact aortas was used to validate and quantify nanoparticle uptake in the

lesions, while CLSM was employed to investigate which specific cell types bound the contrast agent.

MATERIAL AND METHODS

Materials

1,2-distearoyl-*sn*-glycero-3-phosphoethanolamine-*N*-[methoxy(poly(ethylene glycol))-2000] (PEG2000-DSPE), 1,2-distearoyl-*sn*-glycero-3-phosphoethanolamine-*N*-[maleimide(poly(ethylene glycol))2000] (Mal-PEG2000-DSPE), 1,2-distearoyl-*sn*-glycero-3-phosphoethanolamine-*N*-[amino(poly(ethylene glycol))2000] (Amine-PEG2000-DSPE) and 1,2-dioleoyl-*sn*-glycero-3-phosphoethanolamine-N-(lissamine rhodamine B sulfonyl) (Rhodamine-PE) were obtained from Avanti Polar Lipids (Albaster, AL). Cy5.5 mono-reactive NHS ester was obtained from GE Healthcare Europe GmbH (Amersham CyDye™ value packs, Diegem, Belgium). Gd-DTPA-di(stearylamide) (Gd-DTPA-DSA) was purchased from Gateway Chemical Technology (St. Louis, MO). HEPES was purchased from Merck (Darmstadt, Germany). All other chemicals were of analytic grade or of the best grade available. A Bradford protein assay kit was purchased from Bio-Rad laboratories (Veenendaal, the Netherlands).

Cy5.5-PEG2000-DSPE

Cy5.5-PEG2000-DSPE lipid was prepared by covalent conjugation of Cy5.5 mono-reactive NHS ester to micellar amine-PEG2000-DSPE. First, amine-PEG2000-DSPE micelles were prepared by lipid film hydration. In short, 10 μmol amine-PEG2000-DSPE was dissolved in 0.5 ml chloroform. Subsequently, a lipid film was obtained by rotary evaporation of the solvent, followed by additional drying under nitrogen flow. Next, the film was gently hydrated in 5 ml sodium bicarbonate solution (0.1 M NaHCO$_3$, pH 8.0) at 65 ˚C, until a clear solution was obtained. Once micelles were formed, 5 mg Cy5.5 mono-reactive NHS ester was dissolved in 100 μl dimethyl sulfoxide (DMSO) and immediately added to the micelle-containing suspension. Coupling was performed via overnight incubation at 4 ˚C on a moving table. The resulting micelles were sequentially concentrated and resuspended in ultra pure water, using 20 ml vivaspin concentrators (Vivascience, Sartorius Stedim Biotech, 10,000 MWCO) at 3000 x g and 4 ˚C. At least 5 wash cycles were required to remove non-bound Cy5.5. Following the washing procedure, the Cy5.5-PEG2000-DSPE-micelle suspension was dried with a FreeZone 4.5 liter benchtop freeze dry system for three days (Labconco). The obtained lipid powder was dissolved in

a 2:1 (v/v) mixture of chloroform and methanol, to a final Cy5.5-PEG-DSPE concentration of 1 μmol/ml.

Micellar contrast agent

Bimodal micelles were obtained by lipid film hydration of a lipid mixture, typically containing a total amount of 50 μmol lipids. Gd-DTPA-DSA, PEG2000-DSPE and Mal-PEG2000-DSPE were added at a molar ratio of 0.5/0.4/0.1, and dissolved in chloroform/methanol 2:1 (v/v). Next, 1 mol% Cy5.5-PEG-DSPE or rhodamine-PE was added to the lipid mixture for near infrared fluorescence imaging or confocal microscopy, respectively. The solvent was removed by rotary evaporation and additional drying of the lipid film was performed under nitrogen flow. Next, the lipid film was gently dissolved in 4 ml of warm HEPES buffered saline (20 mM HEPES and 135 mM NaCl, pH 6.7, 65 °C) during continuous heating at 65 °C until a clear solution was obtained.

Annexin A5 coupling

The micellar contrast agent was functionalized with a variant of annexin A5 that has a single cysteine residue in the N-terminal tail (annexin A5-cys). The PS and apoptotic cell binding properties of annexin A5-cys are identical to those of recombinant human annexin A5 as previously shown by ellipsometry[1] and flow cytometry[33], respectively. Annexin A5-cys (~ 36 kDa) was covalently conjugated to the Mal-PEG2000-DSPE-containing micelles by sulfhydryl-maleimide coupling, as previously described for other lipid-based agents[34]. In short, annexin A5-cys was re-activated with 10mM DTT for 1.5 hours at 37 °C. Next, 10 mM EDTA was added and DTT and EDTA were removed by extensive dialysis using a 12-14 kDa membrane (Pierce). Activated annexin A5-cys was added to the micelle-suspension at a final concentration of 750 μg/μmol total lipid and coupling was performed overnight at 4 °C. Subsequently the annexin A5-micelles (AnxA5-micelles) were concentrated and resuspended at least 5 times in HEPES buffered saline (20 mM HEPES and 135 mM NaCl, pH 6.7) to remove non-conjugated annexin A5-cys, using 20 ml vivaspin concentrators (Vivascience, Sartorius Stedim Biotech, MWCO 100,000) at 3000 x g and 4 °C. Untargeted micelles were concentrated using the same protocol. A schematic of the preparation procedure of the annexin A5-micelles is shown in **Figure 1**.
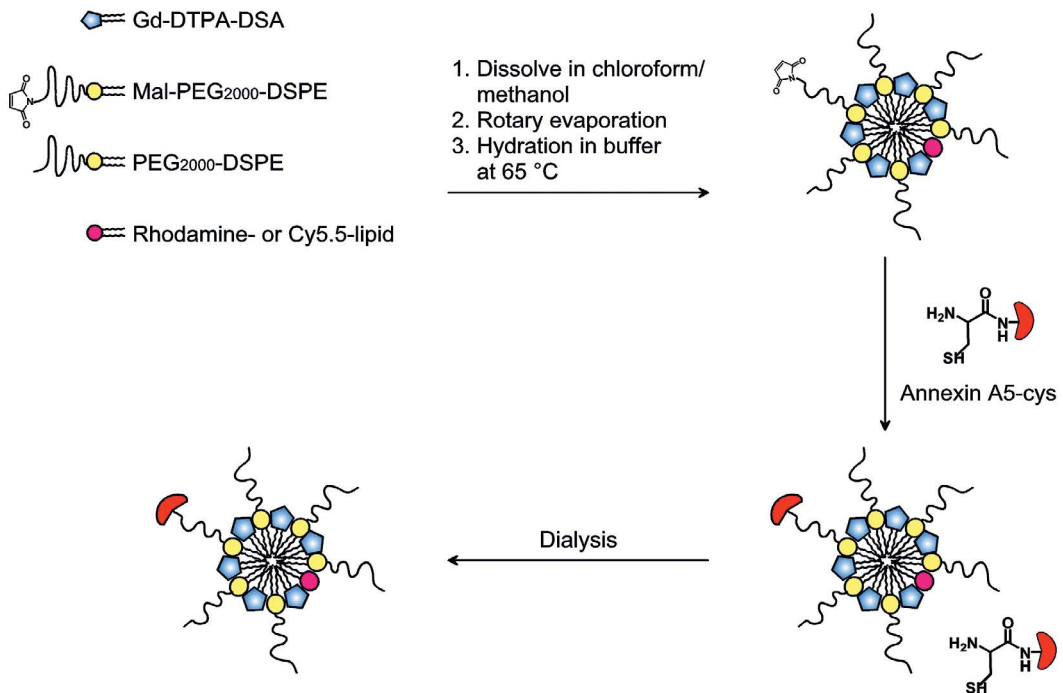
Figure 1. Schematic of nanoparticle preparation.

Contrast agent characterization

Dynamic light scattering was performed on a Malvern instrument (Zetasizer, Nano-S) to determine the hydrodynamic diameter of control- and anxA5-micelles in HEPES buffered saline (20 mM HEPES and 135 mM NaCl, pH 7.4), as deduced from the intensity-weighted particle size distribution. Final micelle concentration was determined by a phosphate analysis according to Rouser[35] after complete destruction with perchloric acid. Protein content of the AnxA5-micelles was measured according to a modified Bradford method[36], which corrects for lipid-associated background absorption at 750 nm by adding equivalent concentrations of control micelles to calibration samples containing a known amount of annexin A5-cys. Relaxivity measurements were performed on a 60 MHz table top NMR spectrometer (Bruker, Minispec), at 25 $^{\circ}$C and 37 $^{\circ}$C. Relaxivities were obtained by measuring T_1 and T_2 values for serial dilutions of the Cy5.5-labeled micelles in the range of 0.4 - 3.4 mM total lipid. T_1 relaxation times were obtained with an inversion recovery sequence, whereas T_2 values were measured using a CPMG sequence.

In vitro targeting
Ellipsometry

The interaction of the Cy5.5-labeled annexin A5-micelles with phosphatidylserine (PS) was monitored with ellipsometry as described in detail elsewhere[34]. Untargeted micelles and unconjugated annexin A5-cys served as a control. In short, a silicium plate was coated with a lipid bilayer of PS and phosphatidylcholine (PC) at a molar ratio of 20:80. The lipid-coated silicium plate was placed in a sample container, filled with 5 ml of Ca^{2+}-containing binding buffer (10 mM HEPES, 150 mM NaCl, 5 mM KCl, 1 mM $MgCl_2$, 2.5 mM $CaCl_2$, pH 7.4). Micelles were added at a final concentration of 280 µM total lipid, while the final concentration of free annexin A5-cys protein was 56 nM. Binding of the particles was assessed by continuously measuring the polarization angle of the reflected elliptically polarized light. Once the polarization angle reached a steady state value, 5 mM EDTA was added to investigate Ca^{2+} dependent membrane association.

Apoptotic cells

Target-specificity for apoptotic cells was examined in the T-lymphoma cell line Jurkat (ATCC). Cells were grown in RPMI1640 medium (Gibco) at 37 °C in a humidified atmosphere and 5% CO_2. Medium was supplemented with 10% fetal calf serum and a mixture of antibiotics (100 units/ml penicillin and 0.1 mg/ml streptomycin; Biochrom AG). In order to induce a high level of apoptosis, Jurkat cells were resuspended to $1·10^6$ cells/ml medium and treated with 200 ng/ml anti-Fas (CD95 human monoclonal antibody, Beckman Coulter B.V.) for 3 hours at 37 °C in a humidified atmosphere and 5% CO_2. Following this procedure, which initiated apoptosis in approximately 40-50% of the cells, cells were harvested and resuspended in Ca^{2+}-containing binding buffer to a final concentration of $2.5·10^6$ cells/ml. Next, the cell suspensions were incubated with the Cy5.5-labeled annexin A5- or control micelles for 30 minutes at a final concentration of 1 mM total lipid. An additional apoptotic cell sample was left untreated for comparison. Incubations were performed on a roller bench at room temperature. After the incubation procedure, cells were collected and washed for at least three times in 2 ml of Ca^{2+}-containing binding buffer (300 x g, 5 minutes). Last, cells were fixed in 200 µl of 4% paraformaldehyde containing 2.5 mM $CaCl_2$.

For confocal laser scanning microscopy (CLSM), 5 µl of the resuspended fixed cell pellets were applied to poly-L-lysine microscopy slides (Menzel-Gläser) and dried for 20 minutes at 55 °C. Next, the adhered cells were washed in PBS, counterstained for nuclei with DAPI (15 minutes; 0.1 µg/ml in PBS), washed in PBS and mounted with Mowiol mounting medium. CLSM was

performed on a Zeiss LSM 510 META NLO system (Carl Zeiss AG, Oberkochen, Germany), equipped with a multi-photon Chameleon laser and a HeNe633 laser. The Chameleon laser (780 nm) allowed excitation of DAPI, whereas the HeNe633 laser (633 nm) was used for Cy5.5 excitation. All images were obtained at 630x magnification and imaging settings remained unchanged to allow a direct comparison of the different samples.

In vivo experiments
Animals
A total of 10 ApoE$^{-/-}$ and 2 wild-type (WT) male C57BL/6 mice were included for *in vivo* MRI experiments and additional *ex vivo* fluorescence imaging or microscopy. One additional apoE$^{-/-}$ mouse was included for *ex vivo* fluorescence imaging only. ApoE$^{-/-}$ mice were placed on a high-cholesterol diet (0.2% total cholesterol, Harlan Teklad, Madison, Wis) ad libitum beginning at 6 weeks until 60 to 68 weeks of age, while WT mice were maintained on a normal murine diet (Research Diets, Inc, New Brunswick, NJ). All animal experiments were approved by the ethics committee of Mount Sinai Hospital.

MRI
In vivo MRI measurements were performed with an 89 mm vertical bore MRI system, operating at 9.4T (Bruker Instruments, Billerica, MA, USA). Mice were initially anesthetized with 4% isoflurane in oxygen (0.4 l/min), and placed head-up in a 30 mm birdcage coil for imaging (Bruker). During MRI, anesthesia was maintained using 1.5-2.0% isoflurane in oxygen (0.4 l/min) supplied through a face mask. The respiratory signal was monitored using a pressure sensor to regulate the depth of the anesthesia.

At the onset of the experiment, pre-contrast T_1-weighted images of the abdominal aorta in the area between the renal and iliac bifurcations were acquired using a fat suppressed black blood spin echo sequence with the following parameters: TR = 800 ms, TE = 8.6 ms, NEX = 16, matrix = 256 x 256, FOV = 2.6 x 2.6 cm^2, and slice thickness = 0.5 mm. For flow suppression, an inflow saturation slab of 4 mm, consisting of a 90° pulse followed by a 2 ms spoiler gradient, was positioned superior to the imaging area.

Following the pre-contrast scans anesthetized mice were injected with the micellar contrast agent through the tail vein at a dose of 2.5 μmol per mouse (100 μl; 25 mM total lipid concentration). A total of 6 ApoE$^{-/-}$ mice received annexin A5-micelles fluorescently labeled with either rhodamine-PE (n = 3) or Cy5.5-PEG2000-DSPE (n = 3). Control-micelles were administrated to

4 ApoE$^{-/-}$ mice (rhodamine-PE, n = 2; Cy5.5-PEG2000-DSPE, n = 2) and 2 WT mice received Cy5.5-labeled annexin A5-micelles.

At 24 hours post administration of the contrast agent, mice were again prepared for MR measurements. First, imaging slices were carefully matched to the pre-contrast images by using the unique anatomy of individual vertebrae as anatomical landmarks. Next, T_1-weighted MR images were obtained with the same parameters as used for the pre-contrast scans. For 2 ApoE$^{-/-}$ mice, the same MR protocol was additionally repeated at 48 hours and 7 days after injection of the annexin A5-micelles.

Mice that underwent their last MR measurement at 24 hours post injection were immediately sacrificed by saline perfusion after the scanning procedure. Blood samples were obtained and spleen, liver, kidney and lung tissues were removed to investigate nanoparticle biodistribution. The abdominal aortas from mice that received rhodamine-labeled micelles were isolated using microscopic dissection, and snap frozen in optical cutting temperature compound (Tissue Tek, Sakura Finetech) for confocal fluorescence microscopy (n = 2/group). Alternatively, whole aortas from mice that received Cy5.5-labeled micelles were excised and placed on a microscopy slide for near infrared fluorescence imaging (NIRF, n = 2/group). For the latter procedure the fat surrounding the abdominal aorta was carefully removed.

MR data analysis

Images were analyzed using Mathematica 6 (Wolfram Research, Inc., USA). Prior to analysis pre and 24 hours post contrast injection measured slices were matched by the shape of the vertebrae. Slices that could not be matched were excluded from data analysis. Typically, for each ApoE$^{-/-}$ mouse 15 to 19 slices with orientations perpendicular to the abdominal aorta were analyzed. Circular regions of interest (ROIs) were drawn on the pixels in the thickened atherosclerotic vessel wall surrounding the lumen (S_w), while excluding the vessel lumen. A second ROI was drawn in a portion of the surrounding muscle (S_m). Wall signal was divided by the muscle signal to yield a normalized signal intensity $S_{norm} = S_w/S_m$ that could be compared pre and 24 hrs post contrast as well as between mice. Signal enhancement (SE) was calculated as the average percentile difference between S_{norm} of all pre and 24 hrs post contrast slices: $[(S_{norm\_post} - S_{norm\_pre})/(S_{norm\_pre})]\cdot100\%$. WT mice were not analyzed using the above procedure as the aortic wall in these animals could not be discriminated from surrounding tissue. Alternatively, images from WT mice were visually inspected for possible signal enhancement in the aortic wall.

Near infrared fluorescence imaging

For whole-aorta near infrared fluorescence imaging (NIRF) 1 ApoE$^{-/-}$ mouse, which received no contrast agent, was used as a control. Aortas from ApoE$^{-/-}$ mice that were injected with either control-micelles (n = 2) or annexin A5-micelles (n = 2) were collected following the *in vivo* MRI experiments. The dissected aortas were placed on a microscope slide and covered with gauze submerged in PBS, placed at 4 °C and imaged within 2 hours. Aortas were placed in the IVIS 200 system (Xenogen) and the Cy5.5 label was excited using a wavelength filter with a range of 615-665 nm, while the emission was recorded using a 695-770 nm filter. Fluorescent reflectance images were acquired with identical exposure times for all groups. Total photon count was determined within identical windows around the whole aorta. The mean increase in fluorescence intensity was calculated as the average percentile difference between the total photon count from the contrast-receiving group (PC_{CA}) and the total photon count from the control ApoE$^{-/-}$ mouse that received no contrast agent ($PC_{control}$): $[(PC_{CA} - PC_{control})/(PC_{control})]\cdot100\%$.

Confocal fluorescence microscopy

8-μm-thick frozen tissue sections were cut for confocal microscopy. Individual sections were air dried for 10 minutes and blocked (PBS containing 1% BSA and 5% horse serum) for 45 minutes at room temperature. DNA fragmentation was detected with the TdT-mediated dUTP Nick End Labeling (TUNEL) technique, using the In Situ Cell Death Detection Kit with fluorescein isothiocyanate (FITC)-labelled dUTP (Roche, Mannheim, Germany) according to manufacturer instructions. Cells with fragmented DNA will be referred to as apoptotic. Macrophages were fluorescently stained with Alexa® 647 labeled anti-CD68 antibodies (Serotec, Inc.). After washing with PBS the sections were directly mounted with VectaShield® containing 1.5 µg/ml DAPI (VectorLaboratories, Burlingame, CA) to stain cell nuclei. The sections were covered with cover slips and imaged within 12 hours.

Rhodamine-labeled annexin A5-micelles and control-micelles (red) were detected and co-localized with respect to both DNA-fragmentation (green) and macrophages (green) within the vessel wall 24 hours after contrast agent administration using confocal laser scanning microscopy (Zeiss LSM 510 META microscope, Carl Zeiss AG, Oberkochen, Germany) in an inverted configuration. The system was equipped with 4 lasers and 3 confocal detectors and data was captured and analyzed using Zeiss LSM 510 Meta and post processed with Image Browser software (Carl Zeiss AG, Oberkochen, Germany). All images were obtained with the same laser power and detector gain settings.

Statistics

Statistical analysis was performed for experiments with $n \geq 3$ per group. Comparisons between the two groups were performed with a Student's t-test for independent samples in SPSS 16.0. $P < 0.05$ was considered significant.

RESULTS

Characterization of the micelles

The hydrodynamic diameters of control- and anxA5-micelles were 19.5 ± 0.7 nm and 22.3 ± 0.2 nm, respectively. Protein and phosphate determinations showed that on average 2 annexin A5-cys proteins were covalently conjugated per micelle, assuming that each micellar nanoparticle contains approximately 80 lipids[37]. Based on the initial lipid composition, this also implies that each micelle contains approximately 1 fluorescent dye and 40 gadolinium-based lipids. The potency of a MRI contrast agent to reduce the intrinsic tissue T_1 and T_2 relaxation times, and thereby introduce tissue contrast on MR images, is described by the relaxivity values r_1 and r_2, which are expressed in $mM^{-1}s^{-1}$. Relaxivities r_1 and r_2 of the paramagnetic Cy5.5-labeled control-micelles and annexin A5-micelles were measured at 60 MHz and different temperatures. Importantly, similar r_1 and r_2 values were observed for the targeted versus the non-targeted micelles (Table 1). At 25 °C the relaxivities of control-micelles were: $r_1 = 11.8 \pm 0.1$ $mM^{-1}s^{-1}$ and $r_2 = 18.5 \pm 0.1$ $mM^{-1}s^{-1}$, whereas for annexin A5-micelles relaxivities were: $r_1 = 11.4 \pm 0.1$ $mM^{-1}s^{-1}$ and $r_2 = 19.4 \pm 0.1$ $mM^{-1}s^{-1}$. These values, which are based on gadolinium concentration, are relatively high compared to clinically approved gadolinium complexes such as Gd-DTPA, for which $r_1 = 3.3$ and $r_2 = 3.9$ at 1.5 T (64 MHz) and 37 °C (38). An increase in temperature to 37 °C was shown to slightly elevate the r_1 and r_2 for both micellar agents (**Table 1**).

	25 °C		37 °C	
	r_1 ($mM^{-1}s^{-1}$)	r_2 ($mM^{-1}s^{-1}$)	r_1 ($mM^{-1}s^{-1}$)	r_2 ($mM^{-1}s^{-1}$)
Control-micelles	11.8 ± 0.1	18.5 ± 0.1	13.4 ± 0.1	20.4 ± 0.1
AnxA5-micelles	11.4 ± 0.1	19.4 ± 0.1	12.4 ± 0.1	19.9 ± 0.1

Table 1. Relaxivities of nonspecific control-micelles and annexin A5-micelles (AnxA5-micelles) in HEPES buffered saline at 60 MHz and different temperatures. Relaxivity values are based on Gadolinium concentration.

In vitro targeting

Ellipsometry measurements clearly demonstrated binding of the annexin A5-micelles to a bilayer consisting of 20 mol% PS and 80 mol% phosphatidylcholine (PC), as observed by the gradually increasing polarization angle, which is known to correlate with layer thickness. The polarization angle reached a steady state at higher values compared to free annexin A5-cys (**Figure 2**). Binding was shown to strictly depend on annexin A5 as the polarization angle remained at baseline levels after addition of control-micelles. Furthermore, association was Ca^{2+} dependent, as annexin A5-cys as well as annexin A5-micelles instantly dissociated from the bilayer upon addition of Ca^{2+}-chelating EDTA.
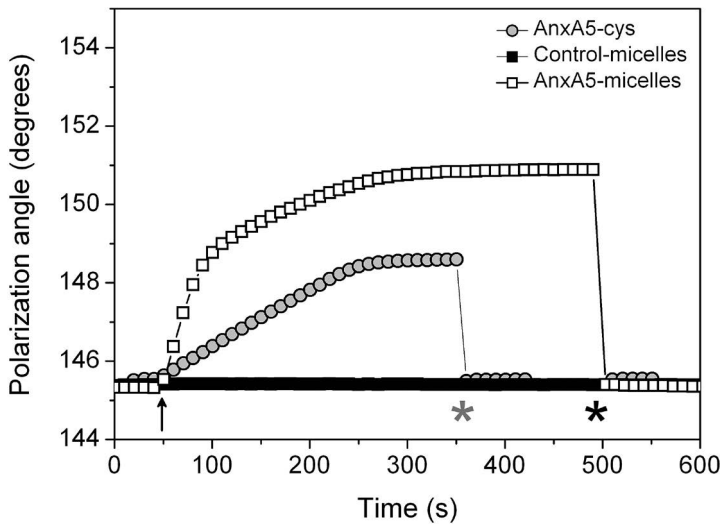
Figure 2: Ellipsometry measurements of a PS/PC (20:80) bilayer in the presence of 2.5 mM Ca^{2+} upon addition of annexin A5-cys (AnxA5-cys), annexin A5-micelles (AnxA5-micelles) and control-micelles. Micelles or protein was added at the time point indicated by the arrow. 5 mM EDTA was added at the time points indicated by the asterisks (*) to assess Ca^{2+}-dependence of binding.

Micelle binding to PS-expressing cells was also examined on a Jurkat cell line using confocal laser scanning microscopy (CLSM). Apoptotic cell suspensions that were untreated (**Figure 3A**) or incubated with control-micelles (**Figure 3B**) exhibited negligible levels of Cy5.5 fluorescence, while apoptotic cells incubated with the annexin A5-micelles showed a clear cell-associated Cy5.5 signal (**Figure 3C**).
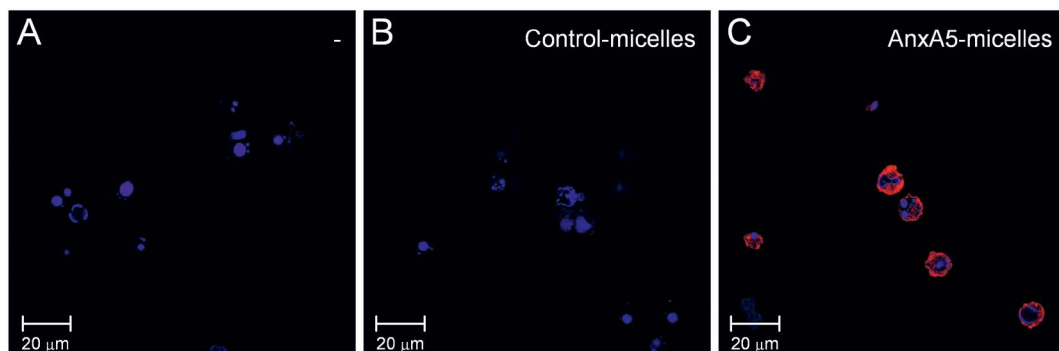
Figure 3: CLSM images of fixed apoptotic Jurkat cells after incubation with (**A**) no contrast agent, (**B**) untargeted paramagnetic control-micelles or (**C**) paramagnetic annexinA5-micelles (AnxA5-micelles). Micelles contained Cy5.5-PEG2000-DSPE (red) and adhered cells were counterstained with DAPI (blue). Magnification: 630x.

MRI and NIRF

In vivo pre-contrast T_1-weighted MR images of atherosclerotic ApoE$^{-/-}$ mice clearly revealed extensive atherosclerotic lesions in their abdominal aorta (**Figure 4A, C**), whereas aortas of wild type (WT) C57BL/6 mice showed normal vessel wall morphology within the same region (**Figure 4E**). At 24 hours post injection of annexin A5-micelles, T_1-weighted images of the same ApoE$^{-/-}$ mice showed increased signal intensity within the thickened aortic vessel wall (compare **Figure 4C** and **4D**). Contrast enhancement within these mice persisted up to at least 7 days after injection (data not shown). Atherosclerotic lesions of ApoE$^{-/-}$ mice that were injected with control-micelles showed less signal enhancement at 24 hours post injection (compare **Figures 4A** and **4B**). Moreover, no contrast changes were observed in WT mice that received annexin A5-micelles (compare **Figures 4E** and **4F**).
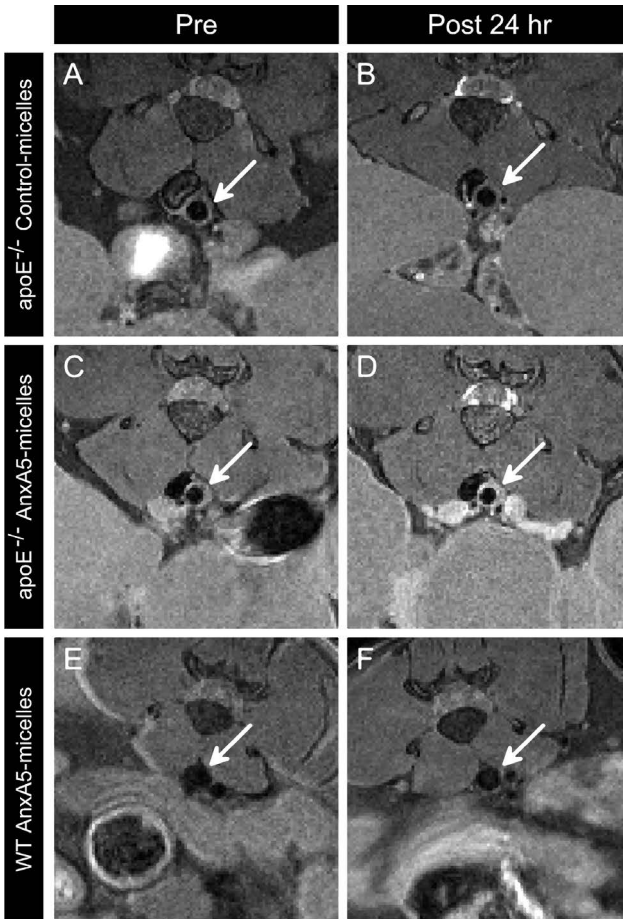
Figure 4. T_1-weighted in vivo MR images at the level of the abdominal aorta (arrow). Scans were made before (left panel) and 24 hours after contrast agent injection (right panel). ApoE^{-/-} mice received either control-micelles (**A-B**) or annexin A5-micelles (**C-D**). Wild type (WT) C57BL/6 mice only received annexinA5-micelles (**E-F**).

E*x vivo* near infrared fluorescence imaging was performed on excised aortas from ApoE^{-/-} mice that underwent *in vivo* MRI experiments and were sacrificed 24 hours post contrast agent injection. The aorta of an ApoE^{-/-} mouse that received no contrast agent served as a control, and showed marginal fluorescence signal due to autofluorescence (**Figure 5A**). In contrast, the aortas from ApoE^{-/-} mice that received control-micelles (**Figure 5B**) or annexin A5-micelles (**Figure 5C**) displayed strong fluorescence signal, which was heterogeneously distributed over the entire aorta. Interestingly, aortas from mice injected with annexin A5-micelles showed multiple intense fluorescent hotspots, whereas aortas from the control-micelle group revealed considerably less fluorescence in a reduced number of areas. Importantly,

these hotspots were predominantly observed in areas where extensive atherosclerotic lesions were expected as described by Nakashima *et al.*[39]. These areas included the aortic arch, the branching points of the renal arteries and the aortic bifurcation (**Figure 5C**).
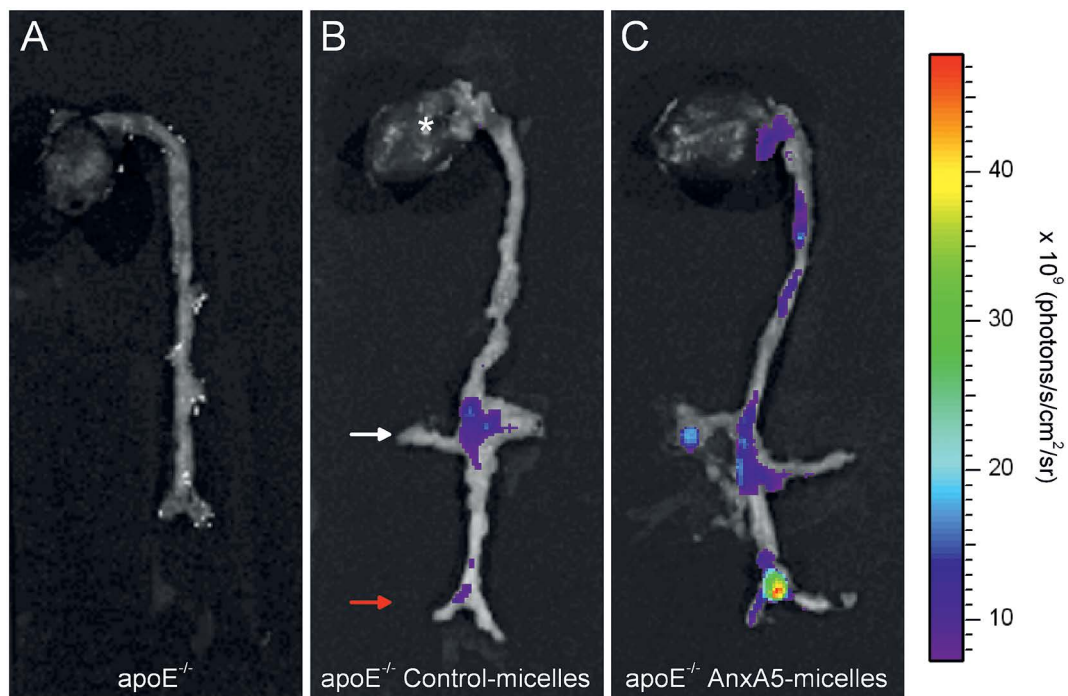
Figure 5. Ex vivo near infrared fluorescence imaging (NIRF) of whole aortas from ApoE^{-/-} mice (**A**) without contrast agent injection and at 24 hours after injection of (**B**) control-micelles and (**C**) annexin A5-micelles. Micelles contained Cy5.5-PEG2000-DSPE. The orientation of the aorta is indicated by characteristic regions in (B), such as the heart (*), a renal branch (white arrow) and the aortic bifurcation (red arrow). In vivo MR images were acquired in the area between the white and the red arrow.

MR signal enhancement in the aortic wall also appeared highly heterogeneous throughout the examined abdominal area. Nevertheless, all slices that were measured with *in vivo* MRI were used to calculate the mean signal enhancement within the vessel wall to prevent any bias by analyzing only specific slices. Mean MR signal within the examined abdominal aortic wall was calculated to be increased by $6.7 \pm 3.4\%$ and $10.7 \pm 1.7\%$ at 24 hours post administration of control- or annexin A5-micelles, respectively (**Figure 6A**). At the same time point, the total photon count in the entire aorta was enhanced by $113.1 \pm 4.4\%$ for the control-micelle group and $257.1 \pm 9.1\%$ for the annexin A5-micelle group (**Figure 6B**).
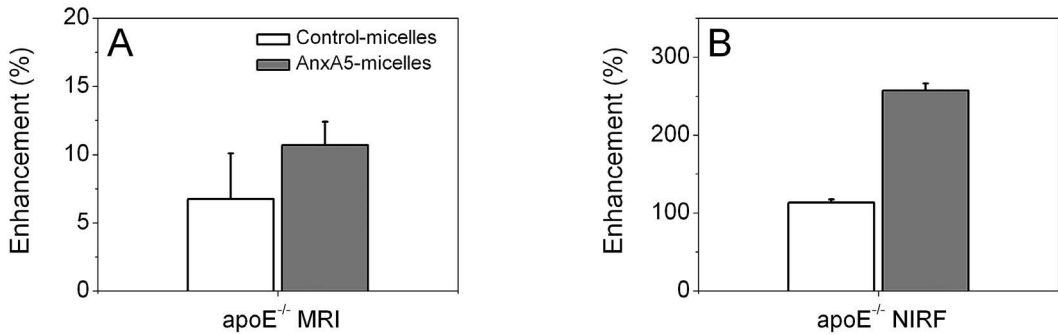
Figure 6. Quantitative analysis of MR signal enhancement in T_1-weighted images (A) and NIRF enhancement at 24 hours after injection of the contrast agent in ApoE$^{-/-}$ mice (B). Bars represent mean values ± SE. (**A**) MRI: control-micelles (n = 4), annexin A5-micelles (n = 6), (**B**) NIRF: control-micelles (n = 2), annexin A5-micelles (n = 2).

Confocal fluorescence microscopy

Tissue sections from the abdominal aortas of the mice were examined with confocal fluorescence microscopy. Atherosclerotic lesions from ApoE$^{-/-}$ mice injected with rhodamine-labeled control-micelles demonstrated only weak and diffuse red fluorescent signal at 24 hours post injection (Figure 7A and 7B), whereas bright red fluorescent hotspots were observed for ApoE$^{-/-}$ mice that received annexin A5-micelles (**Figure 7C** and **7D**). In these latter mice the annexin A5-micelles clearly co-localized with macrophages (**Figure 7C**) and apoptotic cells (**Figure 7D**) in the center of the intima. Presumably, a fraction of these macrophages are apoptotic, as previously described elsewhere[17]. No obvious association to macrophages (Figure 7A) or apoptotic cells was observed for control-micelles (**Figure 7B**).
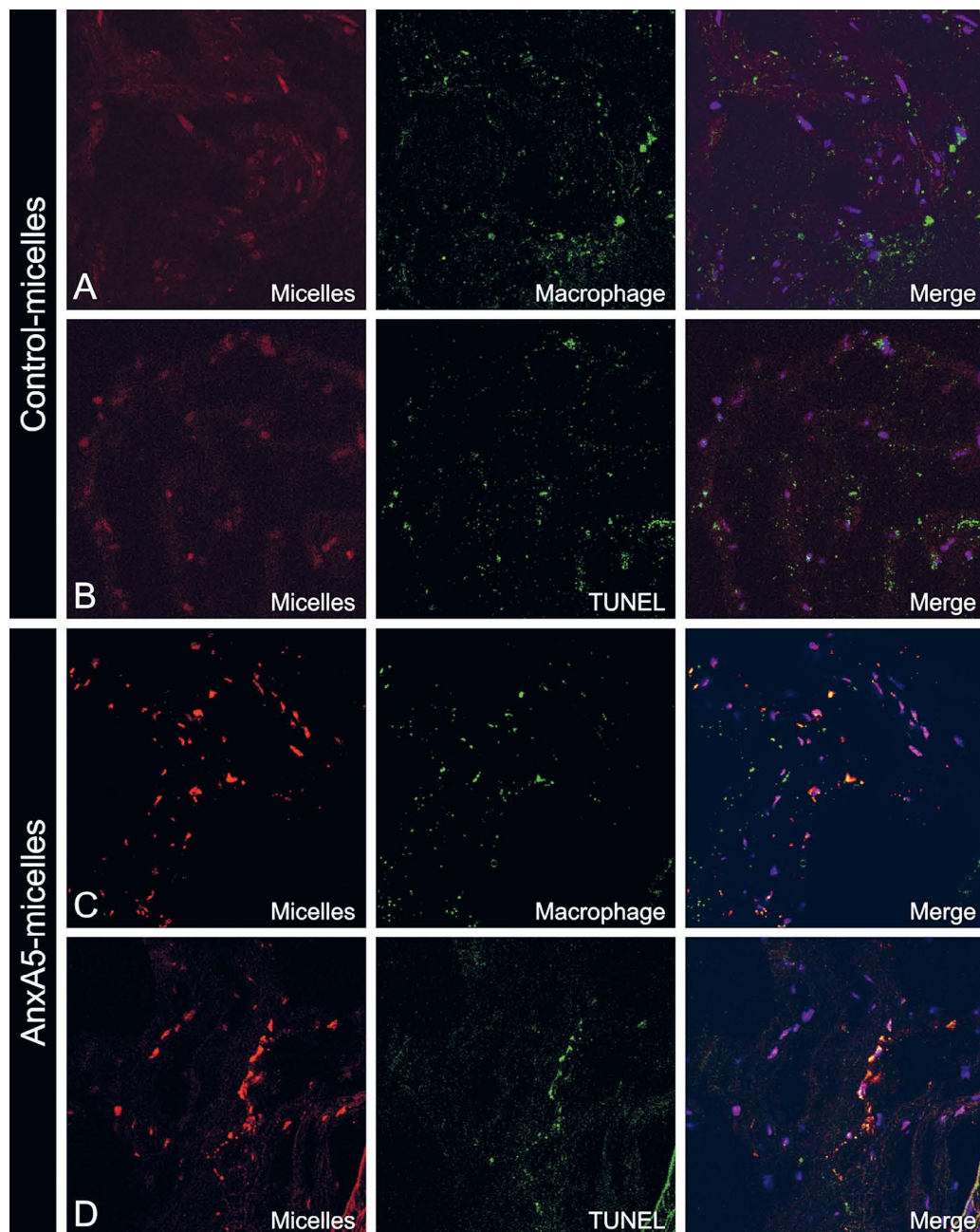
Figure 7. Confocal fluorescence microscopy of frozen sections from abdominal aortas of ApoE^{-/-} mice at 24 hours after administration of (**A,B**) control-micelles or (**C,D**) annexin A5-micelles (red). Sections were counterstained for (**A,C**) macrophages with anti-CD68 (green) or (**C,D**) apoptotic cells with TUNEL (green). Nuclei were stained with DAPI. Magnification: 400x.

Biodistribution

At 24 hours post injection of control-micelles in ApoE$^{-/-}$ mice, the Gd content of liver and spleen was shown to be higher than that of kidneys and lungs (**Figure 8A**). Similar amounts of Gd were measured in the kidneys and lungs of mice that received the annexin A5-functionalized micellar contrast agent (**Figure 8B**). In contrast, Gd content in the liver and spleen of these mice was approximately 100% and 219% higher, respectively, compared to control-micelles. These results are in agreement with previous studies that demonstrated PS specific uptake of radiolabeled annexin A5 by the liver and spleen, while kidney accumulation appeared to be non-specific[40]. Importantly, preliminary studies in ApoE$^{-/-}$ mice, which were injected with the same contrast agents at equal dose, displayed similar blood clearance kinetics for control- and annexin A5-micelles (data not shown). Consequently, this allows a direct comparison of the collected data from both agents.
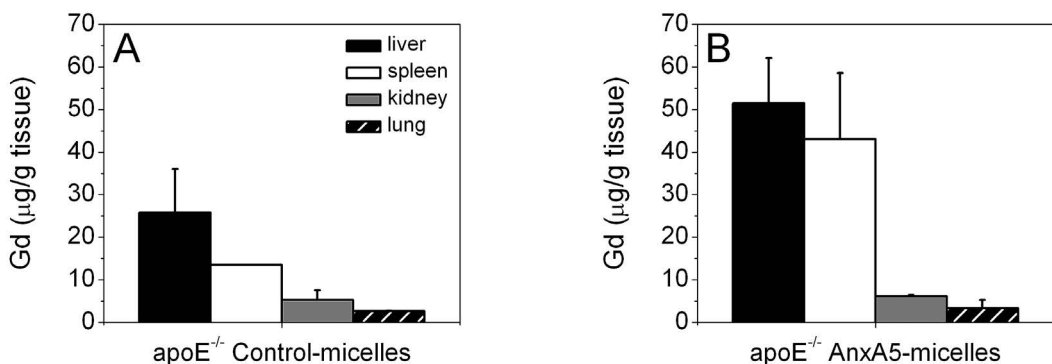
Figure 8. Biodistribution of control-micelles (**A**) and annexin A5-micelles (**B**) at 24 hours post injection in ApoE$^{-/-}$ mice, as measured by ICP-MS of Gd content indicated in µg per g tissue. Bars represent average ± SD (n = 2/group).

DISCUSSION

In the current study we developed, characterized and evaluated the use of annexin A5-conjugated micelles for targeted MRI of atherosclerotic plaques of ApoE$^{-/-}$ mice. The micelles were composed of a paramagnetic amphiphile (Gd-DTPA-DSA) and PEGylated lipids (PEG-DSPE) in a 1:1 molar ratio. Above the so-called critical micelle concentration (CMC) lipid mixture forms aggregates with micellar morphology. A near infrared fluorophore (Cy5.5) and annexin A5 proteins were covalently conjugated to the distal ends of the PEG chains of the micelles for fluorescence imaging and target-specificity, respectively. Alternatively rhodamine-PE, instead of Cy5.5-PEG2000-DSPE,

was incorporated in the lipid monolayer for confocal fluorescence microscopy. Ellipsometry measurements on PS/PC bilayers and experiments with apoptotic Jurkat cells were performed to assess the target-specificity of the annexin A5-micelles *in vitro.* Furthermore, *in vivo* MRI of the abdominal aortas from apoA$^{-/-}$ mice and *ex vivo* fluorescence methods on excised aortas of the same mice were used to image the uptake of control- and annexin A5-micelles in atherosclerotic lesions, as well as to validate their cellular targets following intravenous injection.

MR molecular imaging of vascular targets is usually done with nanoparticles that carry a high payload of contrast-generating material[41, 42]. After intravenous administration such nanoparticulate agents do not require extravasation from the vasculature to bind to their target and therefore nanoparticle size is less critical. However, when extravascular targeting is to be accomplished, *e.g.* intraplaque targeting, a small particle size is more favorable, to allow penetration of the endothelium. Recently, Burtea *et al.*, reported on a novel PS-specific peptide that was conjugated to a single Gd-DTPA, which successfully allowed MRI of PS exposing cells in atherosclerotic plaques[43]. Furthermore, Schellenberger *et al.* reported on a PS-specific superparamagnetic iron oxide-based MRI contrast agent with a hydrodynamic diameter of approximately 15 nm, *i.e.* annexin A5-VSOP[44]. However, this nanoparticle was only applied in an *in vitro* setting. In the current study we developed and applied annexin A5-functionalized paramagnetic micellar nanoparticles of similar size. This relatively small size facilitates extravasation in areas with enhanced endothelial permeability, such as atherosclerotic lesions.

Ellipsometry measurements revealed a Ca^{2+}-dependent affinity of the annexin A5-conjugated micelles for a lipid bilayer that contained 20% of PS, whereas non-specific control-micelles did not bind to a similar bilayer. These results were corroborated by CLSM images of apoptotic cells, which showed abundant association of annexin A5-functionalized micelles, whereas control micelles were barely detected.

For *in vivo* MRI experiments we used a dosage that is typical for targeted MR contrast agents, *i.e.* 50 µmol Gd per kg body weight. MRI revealed pronounced and heterogeneously distributed hyperintense areas throughout plaque rich regions in the abdominal aorta at 24 hours after administration of annexin A5-functionalized micelles. Such enhanced regions were also observed in the untargeted control-micelle group, but to a lower extent. To enable comparison of both groups, the signal enhancement for each slice was calculated and averaged for all acquired imaging slices, thereby disregarding

heterogeneous distribution of the contrast agent. Data analysis revealed that the mean signal enhancement throughout the abdominal aorta was non-significantly higher for mice that received annexin A5-micelles than for control-micelle-injected mice. In both cases, the enhancement was however modest compared to macrophage scavenger receptor (MSR) targeted micellar contrast agents that were applied at a dose of 75 μmol Gd per kg body weight[26].

In vivo MRI observations were compared to *ex vivo* fluorescence imaging of excised aortas. The mean photon count of aortas that originated from mice injected with annexin A5-micelles was at least twice that of the aortas from control-micelle injected mice. In addition near infrared fluorescence imaging allowed us to investigate the entire aorta. The most pronounced uptake of annexin A5-micelles was observed in the aortic arch, at principal branches of the abdominal aorta, such as the renal arteries, and at the aortic bifurcation into the iliac arteries. Isobe *et al.* observed distinct uptake of ^{99m}Tc-labeled annexin A5 in similar regions of the aorta in ApoE^{-/-} mice[17]. Importantly, these regions are known to correspond with high plaque burden[39], which was the case in this study as well. However, one should note that the *in vivo* MR images were acquired in the abdominal aorta in the area between the renal and iliac bifurcations. This implies that certain regions with intense uptake of the micellar contrast agent were not included in the *in vivo* MRI scans, which could partially explain the observed difference in signal enhancement between MRI and NIRF imaging. Future imaging studies should therefore cover a larger area of the abdominal aorta or alternatively, another animal model could be used, with well-defined locations and phenotype of atherosclerotic plaque within the carotid artery[45].

Ex vivo confocal fluorescence microscopy revealed association of annexin A5-micelles to PS-expressing cells, such as apoptotic cells and macrophages, within atherosclerotic lesions in the abdominal aorta. A large fraction of these apoptotic cells are considered dying macrophages, whereas the remaining fraction most likely consists of smooth muscle cells[46]. The annexin A5-functionalized contrast agent was most probably also associated to viable macrophages, as previously observed for biotinylated annexin A5[17]. Macrophages in atherosclerotic lesions are also known to non-specifically engulf nanoparticulate agents such as USPIOs[47]. Nevertheless, CLSM images of tissue sections from control-micelle injected mice revealed no macrophage-associated micellar fluorescence. Presumably, the cell-associated contrast agents observed in the CLSM images were internalized, which may have led to a quenched T_1 effect due to limited water exchange with the bulk[48,49]. Such

an effect may provide a second explanation for the apparent discrepancy between the modest signal enhancement of annexin A5-micelles in the *in vivo* MR images and the large difference in micellar fluorescence from control- and annexin A5-micelles in the *ex vivo* CLSM images.

At present, there is an urgent need to discriminate vulnerable atherosclerotic lesions from stable lesions. Current diagnostic methods used in the clinic are primarily focused on visualizing narrowing of the lumen, but do not reveal plaque composition and thus do not predict risk of rupture accurately[23]. In the past decade traditional high resolution MRI techniques have been developed to enable plaque characterization by visualizing features such as the lipid-rich core and fibrous cap size. The biochemistry that lies at the basis of plaque formation may be investigated using MRI-based molecular imaging techniques. For example, MR imaging of macrophage burden has been investigated with ultrasmall iron oxide nanoparticles (USPIO)[47], while the expression of cell adhesion molecules was visualized using VCAM-1 targeted cross linked iron oxide nanoparticles (CLIO)[31]. Furthermore, annexin A5-functionalized iron oxide particles were applied to image PS-expressing cells in a preliminary study on a limited number of animals[50]. The disadvantage of such strategies is that iron oxide-based imaging relies on the use of so-called $T_2^{(*)}$-weighted MRI, in which regions of high iron oxide content appear dark. These spots are hard to localize in images that usually already have a low signal-to-noise ratio. Therefore, more recent investigations primarily focus on the application of T_1-reducing agents that appear bright in T_1-weighted MR images[25,29,43], as is the case in our study. The paramagnetic nanoparticulate agent introduced in the present study exhibited enhanced accumulation in plaque by conjugation of annexin A5. This phenomenon may also be applied to shuttle therapeutically active compounds, such as anti-inflammatory agents or nucleotides, into plaque.

In the present study a dose of 1.9 mg annexin A5 was administered per mouse, which was well tolerated by the animals. However, this dose is considered unfeasible in clinical studies. Ideally, small molecules such as peptides or peptidomimetics, with a high affinity for PS, need to be developed for clinical translation. Alternatively, and despite the previously mentioned disadvantages, small iron oxide nanoparticles may be employed. These nanoparticles represent a more sensitive MRI contrast agent and are typically injected at a 100-fold lower particle dose, which also decreases the Annexin A5 dose by a factor 100.

In conclusion, the present study demonstrated the potential of an annexin A5-functionalized micellar contrast agent for target-specific imaging of PS-expressing cells in atherosclerotic lesions of ApoE$^{-/-}$ mice. Such imaging strategies are of great diagnostic potential as the abundance of PS expressing cells is considered an important prognostic marker of plaque vulnerability. Interestingly, the presented nanoparticulate platform may be simultaneously exploited for therapeutic purposes, thereby facilitating a wide range of clinically relevant applications for improved diagnostics as well as therapeutic interventions in atherosclerotic cardiovascular disease.

REFERENCES

1. Andree, H. A., et al. *J. Biol. Chem.* 265, 4923-8 (1990).
2. Gerke, V., and Moss, S. E. *Physiol. Rev.* 82, 331-71 (2002).
3. Devaux, P. F., and Zachowski, A. *Chemistry and Physics of Lipids* 73, 107-120 (1994).
4. Zwaal, R. F., et al, *Cell. Mol. Life Sci.* 62, 971-88 (2005).
5. Schroit, A. J., and Zwaal, R. F. *Biochim. Biophys. Acta* 1071, 313-29 (1991).
6. Callahan, M. K., et al, *Cell. Death Differ.* 7, 645-53 (2000).
7. van Engeland, M., et al. *Cytometry* 31, 1-9 (1998).
8. Halbreich, A., et al, *Biochimie* 80, 379-90 (1998).
9. Vermes, I., et al, *J. Immunol. Methods* 243, 167-90 (2000).
10. Boersma, H. H., et al, *J. Nucl. Med.* 46, 2035-50 (2005).
11. Kenis, H., et al, *Cell. Mol. Life. Sci.* 64, 2859-62 (2007).
12. Davies, M. J., et al, *Br. Heart J.* 69, 377-81 (1993).
13. Kolodgie, F. D., et al, *Am. J. Pathol.* 157, 1259-68 (2000).
14. Libby, P., et al, *Cur.r Opin. Lipidol.* 7, 330-5 (1996).

15. Li, W., et al, *J. Mol. Cell. Cardiol.* 37, 969-78 (2004).
16. Kolodgie, F. D., et al, *Circulation* 108, 3134-9 (2003).
17. Isobe, S., et al, *J. Nucl. Med.* 47, 1497-505 (2006).
18. Haider, N., et al, *J. Nucl. Cardiol*. 16, 753-62 (2009).
19. Hartung, D., et al, *J. Nucl. Med*. 46, 2051-6 (2005).
20. Sarai, M., et al, *J. Am. Coll. Cardiol.* 50, 2305-12 (2007).
21. Kietselaer, B. L., et al, *N. Engl. J. Med.* 350, 1472-3 (2004).
22. Cappendijk, V. C., et al, *Radiology* 234, 487-92 (2005).
23. Sanz, J., and Fayad, Z. A. *Nature* 45*1*, 953-7 (2008).
24. Mulder, W. J., et al, *NMR Biomed.* 19, 142-64 (2006).
25. Amirbekian, V., et al, *PNAS* 104, 961-6 (2007).
26. Mulder, W. J., et al, *Magn. Reson. Med.* 58, 1164-70 (2007).
27. Cormode, D. P., et al, *Bioconjug. Chem.* 20, 937-943 (2008).
28. Mulder, W. J., et al, *Magn. Reson. Med.* 55, 1170-4 (2006).
29. Winter, P. M., et al, *Circulation* 108, 2270-4 (2003).
30. Cormode, D. P., et al, *Nano Lett.* 8, 3715-23 (2008).
31. Nahrendorf, M., et al, *Circulation* 114, 1504-11 (2006).
32. Mulder, W. J., et al, *Nanomed.* 2, 307-24 (2007).
33. Vermes, I., et al, *J Immunol Methods* 184, 39-51 (1995).
34. van Tilborg, G. A., et al, *Bioconjug Chem* 17, 741-9 (2006).
35. Rouser, G., et al, *Lipids* 5, 494-6 (1970).
36. Bradford, M. M. *Anal Biochem.* 72, 248-54 (1976).
37. Ashok, B., et al, *J. Pharm. Sci.* 93, 2476-87 (2004).
38. Port, M., et al, *Biometals* 21, 469-90 (2008).
39. Nakashima, Y., et al, *Arterioscler. Thromb.* 14, 133-40 (1994).
40. Tait, J. F., et al, *J. Nucl. Med.* 46, 807-15 (2004).
41. Mulder, W. J., et al *FASEB J.* 19, 2008-10 (2010).
42. Winter, P. M., et al, *Cancer Res.* 63, 5838-43 (2003).
43. Burtea, C., et al. *Mol. Pharm.* 6, 1903-19 (2009).
44. Schellenberger, E., et al. *Small* 4, 225-30 (2008).
45. Cheng, C., et al. *Circulation* 113, 2744-53 (2006).
46. Harada, K., et al, *Atherosclerosis 135*, 235-9 (1997).
47. Ruehm, S. G., et al, *Circulation 103*, 415-22 (2001).
48. Strijkers, G. J., et al, *Magn. Reson. Med. 61*, 1049-58 (2009).
49. Terreno, E., et al, *Magn. Reson. Med. 55*, 491-7 (2006).
50. Smith, B. R., *Biomed. Microdevices 9*, 719-27 (2007).

Chapter 6

Monitoring of arterial wall remodeling in atherosclerotic rabbits with an magnetic resonance imaging contrast agent binding to matrix metalloproteinases

Based on

ABSTRACT

Aims

P947 is a gadolinium-based MRI contrast agent with high affinity for several matrix metalloproteinases (MMPs) involved in arterial wall remodeling. We tested whether the intensity of enhancement detected *in vivo* in the arterial wall with P947 and MRI correlates with actual tissue MMP-related enzymatic activity measured in a rabbit atherosclerotic model subjected to dietary manipulations.

Methods and Results

Aortas of 15 rabbits in which atherosclerotic lesions were induced by balloon-angioplasty and 4 months of hypercholesterolemic diet were imaged at "baseline" with P947-enhanced MRI. Atherosclerotic rabbits were divided into three groups: 5 rabbits were sacrificed ("baseline" group); 5 rabbits continued to be fed a lipid-supplemented diet ("high-fat" group); and 5 rabbits were switched from atherogenic to a purified chow diet ("low-fat" group). Four months later, a second P947-enhanced MRI was acquired in the 10 remaining rabbits. A significantly lower signal was detected in the aortic wall of rabbits from the "low-fat" group as compared to rabbits from "baseline" and "high-fat" groups ($21 \pm 6\%$ vs. $52 \pm 5\%$ and $46 \pm 3\%$, respectively; $p < 0.05$). Such differences were not detected with the contrast agent P1135, which lacks the MMP-specific peptide sequence. In addition, the intensity of aortic wall enhancement detected with MRI after injection of P947 strongly correlated with actual MMP-2 gelatinolytic activity measured in corresponding aortic segments using zymography ($r = 0.87$).

Conclusion

P947-enhanced MRI can distinguish dietary induced variations in MMP-related enzymatic activity within plaques in an experimental atherosclerotic model, supporting its utility as a clinical imaging tool for *in vivo* detection of arterial wall remodeling.

INTRODUCTION

Acute coronary syndromes and ischemic strokes are most often caused by the fibrous cap disruption of atherosclerotic plaques[1]. Sudden exposure of the underlying atheromatous content to blood triggers the formation of a thrombus that can occlude the artery or embolize distally leading to

myocardial or cerebral necrosis[2, 3]. Identification of atherosclerotic plaques at risk of rupture could be useful for risk stratification and early implementation of therapies aimed at plaque stabilization.

Matrix metalloproteinases (MMPs) are a broad family of zinc-dependent endopeptidases, which play a key role in the degradation and remodeling of the extra-cellular matrix network. Previous histological studies demonstrated strong expression of MMPs and *in situ* matrix-degrading gelatinolytic activity in the fibrous cap of human atherosclerotic plaques[4], as well as in atherosclerotic lesions that were induced in experimental models[5]. Therefore, MMPs are thought to play a key role in the pathological remodeling associated with the natural history of the atherosclerotic plaques, from the initial formation of lesions and the outward arterial remodeling to the thinning and weakening of the extra-cellular matrix scaffold forming the fibrous cap favoring plaque rupture[6]. Hence, noninvasive imaging of MMP activity in atherosclerotic plaques represents an attractive approach to monitor changes in the atherosclerotic plaques and identify those prone to rupture.

Magnetic resonance imaging (MRI) allows for the discrimination of atherosclerotic plaque components (fibrous cap, lipid core, hemorrhage) with a high spatial resolution[7, 8]. Using an approach similar to nuclear medicine, contrast agents targeting specific molecules are developed for the detection of biological activities with MRI. This new field known as "molecular MRI" offers the opportunity to image biological activities with a high spatial resolution[9]. P947 is a novel gadolinium-based MRI contrast agent with a high affinity for several MMPs. Our group has recently demonstrated that P947 accumulates in MMP-rich atherosclerotic plaques of ApoE^{-/-} mice[10,11]. In a previous work[12], variations of MMP-related enzymatic activity in atherosclerotic plaques of rabbits subjected to dietary changes was detected *ex vivo*. In this study, we advanced toward testing the utility of the technique for clinical imaging of atherosclerotic plaques by testing whether, i) such effects can be distinguished *in vivo* using P947-enhanced MRI, ii) the intensity of enhancement detected in the aortic wall with P947 and MRI correlates with actual MMP activity.

MATERIAL AND METHODS

MR contrast agents

P947 (Guerbet) was synthesized by binding covalently a broad-spectrum MMP inhibitor[13] formed of four amino-acids (Gly-Pro-Leu-Ala) to a gadolinium chelate (gadolinium-DOTA) at a 1:1 molar ratio with a thio-urea function. The MMP inhibitor forming P947 was selected with a micro-molar affinity for MMPs

to allow for fast clearance of P947 from tissues. P947 has a molecular weight of 1,210 Daltons and an r1 relaxivity of 5.5 mM^{-1}s^{-1} at 1.5 Tesla in 37°C water. Blood half-life of P947 was measured at 30 minutes in rabbits.

P1135 has the same properties as P947 (identical molecular weight, relaxivity and blood half life) except that the sequence of four amino-acids constitutive of the MMP-inhibiting moiety was scrambled. Concentrations of P947, P1135 and a broad-spectrum MMP inhibitor ilomastat (Calbiochem) yielding a 50% inhibition (IC$_{50}$) of MMP activity *in vitro* with an MMP inhibitor profiling kit (QuantiZyme Assay system; Biomol International) are displayed in (**Table 1)**.

	P947	P1135	Ilomastat
MMP-1	1.0	> 10^3	0.002
MMP-2	1.0	> 10^3	0.003
MMP-3	10	> 10^3	0.010
MMP-8	0.1	> 10^3	< 0.001
MMP-9	10	> 10^3	< 0.001
MMP-13	1.0	> 10^3	< 0.001
MMP-14	100	> 10^3	0.003

Table 1. Concentrations yielding a 50% inhibition of MMP activity (µM)

Animal model

Atherosclerotic plaques were induced in the abdominal aorta of 15 New Zealand White rabbits (mean age: 4 months; mean weight: 3.1 ± 0.2 kg, Covance) by a combination of 4 months of an atherogenic diet (4.7% coconut oil and 0.3% cholesterol-enriched diet, Research Diet) and a repeated balloon injury of the aorta (two weeks and six weeks after starting the high-cholesterol diet), as previously described[14]. Rabbits from the "high-fat" group were fed a lipid-supplemented diet (4.85% coconut oil and 0.15% cholesterol). Rabbits from the "low-fat group" were fed a purified chow diet without cholesterol. All experiments were approved by the Mount Sinai School of Medicine Institute Animal Care and Use Committee.

Plasma cholesterol levels

Peripheral blood was collected from the ear vein under local anesthesia for measurement of plasma cholesterol concentrations by enzymatic assays (Sigma Diagnostics).

Magnetic resonance imaging

General anaesthesia was induced with an intra-muscular injection of 20 mg/kg ketamine (Fort Dodge Animal Health), 10 mg/kg xylazine (Bayer Corp.) and 0.5 mg/kg acepromazine (Fort Dodge Animal Health). A 22-gauge catheter was placed in the marginal ear vein. Rabbits were imaged before injection and at 5, 30, 60, 90 minutes after the injection of 50 μmol Gd/kg of P947 or P1135 using a 1.5 Tesla MRI system (Siemens Sonata, Siemens Medical Solutions) with a conventional phased-array knee coil. Care was taken in placing rabbits in identical positions in the coil for the different imaging. Ten sequential, 2-mm-thick, axial slices of the aorta were acquired from the celiac trunk to the iliac bifurcation using a fast spin-echo T1-weighted sequence giving an in-plane resolution of 400 x 400 μm (repetition time: 800 ms; echo time: 5.6 ms; field of view: 10 x 10 cm; matrix: 256 x 256; echo train length: 8; signal averages: 4; inter-slice gap: 3 mm). Inferior and superior radiofrequency saturation pulses were added to null the signal from flowing blood in the inferior vena cava and aorta, and spectral fat suppression to null the signal from the peri-adventitial fat.

Study protocol

After 4 months of atherogenic diet, the rabbits (n = 15) underwent a first MRI with injection of P947 (Figure 1). Rabbits were divided by a random drawing into three groups: 5 atherosclerotic rabbits were sacrificed one week after the first MRI to evaluate baseline lesions ("baseline" group); 5 rabbits continued to be fed a lipid-supplemented diet ("high-fat" group); and 5 rabbits were switched from atherogenic to a purified chow diet ("low-fat" group). Four months later, rabbits from the "low-fat" and "high-fat" groups underwent a second MRI session. MRI was performed in rabbits (n = 10) with injection of P947 and, one week later, with injection of P1135. The 10 remaining atherosclerotic rabbits were sacrificed one week after the last MRI. Rabbits were sacrificed at least one week after the last MRI with P947 in order to avoid any residual MMP inhibition of P947 in atherosclerotic plaques.
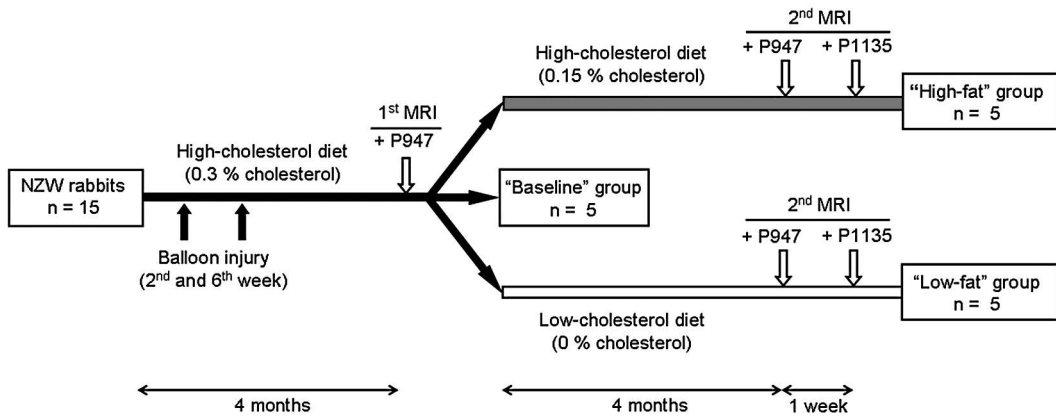
Figure 1. Study design. Atherosclerotic plaques were induced in 15 New Zealand White rabbits by a combination of an atherogenic diet and repeated endothelial abrasion of the aorta four weeks apart (black arrows). After four months of atherogenic diet, a first MRI (white arrow) was performed at baseline in all the rabbits after injection of the MMP-specific contrast agent P947. After this first MRI, 5 rabbits were sacrificed and formed the "baseline" group. The 10 remaining rabbits were split into two groups: 5 rabbits were left on the hyperlipidemic diet and composed the "high-fat" group; and 5 rabbits were switched to a chow diet and formed the "low-fat" group. Four months later, the 10 remaining animals were imaged with MRI, first, after injection of the MMP-specific contrast agent P947 and, one week later, after injection of the non-specific contrast agent P1135 (white arrows).

Image analysis

MR images were analyzed with ImagePro Plus (Media Cybernetics). Signal intensities were measured in each rabbit on 10 sequential axial T1-weighted images before, 5, 30, 60 and 90 minutes after injection of each contrast agent. Origin of the left renal artery and iliac bifurcation were identified on each MRI acquisition and were used to ensure identical slice position between pre- and post-contrast images and between the different MRI performed in the same rabbit. Regions of interest (ROI) encompassing the aortic wall were drawn manually on the MR acquisition obtained 5 minutes after the injection of contrast agent. Preliminary work confirmed that regions of interest of the aortic wall identified on post-contrast acquisitions were close to the ones obtained on T2-weighted acquisitions previously validated for measurements of plaque area[15]. These regions of interest were then copied on each axial slice of the acquisitions obtained before and at the different time points after the injection of contrast agent. Areas and mean signal intensity (SI) of the aortic wall were then measured in these ROIs by an operator (JC.C.) blinded to rabbit group and injected contrast agent. Standard deviation (SD) of noise was measured in a ROI located outside of the rabbit. The following parameters were calculated for each axial slice:

- Signal to Noise Ratio (SNR) of aortic wall = SI of aortic wall / SD of noise.
- Aortic wall enhancement (%) = ((SNR post-contrast - SNR pre-contrast)/ SNR pre-contrast) x 100

Aortic wall area, SNR and aortic wall enhancement were expressed for each rabbit as the mean value of the 10 sequential axial slices. Aortic wall area and enhancement were measured in all rabbits by a second operator (FH) to evaluate inter-operator reproducibility.

SDS-PAGE gelatin zymography of conditioned media

Rabbits were euthanized by an intravenous injection of 120 mg/kg of sodium pentobarbital (Sleepaway, Fort Dodge Animal Health) one week after the last MRI. A bolus of heparin was injected prior to euthanasia to prevent clot formation. Abdominal aortas were excised, washed with saline and cut into ten 5 mm-length segments. Three segments were randomly chosen for *in situ* zymography. The seven remaining segments were first weighted then incubated for 24 hours in 250 µL of serum-free Dulbecco's Modified Eagle Medium (Biomedia) at 37°C in humidified 5% CO_2 / 95% air. Gelatinolytic activities of conditioned media were measured as previously described[16]. Pro-forms of MMPs undergo a conformational change in presence of sodium dodecyl sulfate revealing their catalytic site, which allows for their detection with zymography. Densitometric analysis of scanned gelatinolytic bands was performed with Quantity One software (Bio-Rad). Results are expressed as mean densitometric units / mg wet weight.

In situ gelatin zymography

Aortic segments chosen for *in situ* zymography were snap-frozen with Optimal Cutting Temperature compound in isopentane prechilled with liquid nitrogen and sectioned in serial 8-µm-thick slices. For optimal matching with MRI slices, the location of each segment along the aorta was defined by measuring the distance between the segment and the origin of the left renal artery or the iliac bifurcation. *In situ* gelatin zymographies were performed using the quenched substrate DQ-gelatin (Invitrogen), which becomes fluorescent after cleavage by MMPs. Reagent solution was obtained by dissolving at a 1/1 ratio DQ gelatine at a concentration of 0.5 g/L with 1% agarose[17]. Cryosections of atherosclerotic plaques were covered with 50 µL of the solution using a coverslip. After 24-hour incubation, fluorescence signal of DQ-gelatin was captured using a confocal laser microscope (excitation wavelength: 488 nm, emission wavelength: 505-560 nm, Zeiss LSM 510 META microscope). In addition, adjacent cryosections were fixed in paraformaldehyde and colored with combined Masson's elastin staining.

For inhibition studies, reagent solution was brought to a 200 µM concentration of P947 or P1135 in reaction buffer (0.5 M Tris HCl, 1.5 M NaCl, 50.0 mM CaCl$_2$, 2.0 mM sodium azide, pH 7.6). As control for inhibition studies, initial reagent solution underwent a similar dilution with reaction buffer. As control for auto-fluorescence, cryosections were incubated in the same conditions with a solution lacking DQ-gelatin.

Statistics
All probabilities were two-sided and expressed as mean ± standard deviation. Values of p < 0.05 were considered as statistically significant. Statistical analysis was conducted with SPSS software (SPSS Inc.). Differences in weights, cholesterol levels, aortic wall areas and aortic wall enhancements were tested in three independent groups using a non parametric Kruskall-Wallis test, in two independent groups using a non parametric Mann-Whitney test and in two non independent groups using a non parametric Wilcoxon signed ranked test. Kinetics of aortic wall enhancement after injection of P947 and P1135 were compared using a two-way ANOVA test for multiple time points and a post-hoc Bonferroni test. Differences in MMP activities between the three groups of rabbits were tested using a one-way ANOVA test and a post-hoc Bonferroni t-test. Correlations were calculated with a Pearson test.

RESULTS

Rabbit weights and cholesterol levels
At baseline, mean weights and plasma cholesterol were similar between the 3 groups of rabbits ("baseline", 3.6 ± 0.2 kg, 4.1 ± 0.9 mg/100 dL; "high-fat", 3.7 ± 0.3 kg, 4.2 ± 1.0 mg/100 dL; "low-fat ", 3.5 ± 0.2 kg, 4.0 ± 0.6 mg/100 dL, respectively; p = 0.25 for rabbit weight and p = 0.61 for plasma cholesterol). Four months later, plasma cholesterol was significantly lower in rabbits from the "low-fat" group compared to rabbits from the "high-fat" group (0.6 ± 0.3 mg/100 dL vs. 3.6 ± 1.6 mg/ 100 dL; p = 0.04), whereas mean rabbit weights were identical in both groups (3.6 ± 0.4 kg).

Magnetic resonance imaging of the arterial wall
On the first MRI, aortic wall areas measured 5 minutes after injection of P947 were similar in the three groups of rabbits ("baseline", 8.6 ± 0.5 mm²; "high-fat", 8.4 ± 0.3 mm²; "low-fat", 8.5 ± 0.4 mm²; p = 0.89). Ninety minutes after the injection of P947, a strong enhancement was detected in the aortic wall (Figure 2), but was not significantly different between the three groups of

rabbits (**Figure 3A**; "baseline", 52 ± 5%; "high-fat", 47 ± 5%; "low-fat", 47 ± 10%; p = 0.47).

Four months later, aortic wall area increased in rabbits from the "high-fat" group which pursued the high-cholesterol diet (9.5 ± 1.3 mm² vs. 8.4 ± 0.3 mm²; p = 0.22) and decreased in rabbits from the "low-fat group which were switched to a chow diet (7.8 ± 0.5 mm² vs. 8.5 ± 0.4 mm²; p = 0.14). Ninety minutes after the injection of P947, aortic wall enhancement of rabbits from the "low-fat" group was significantly lower (**Figures 2** and **3B**) as compared to, i) the first MRI acquired in same rabbits 4 months earlier (21 ± 6% vs. 47 ± 10%, respectively; p = 0.04); ii) the second MRI performed in rabbits from the "high-fat" group given the hyperlipidemic diet (21 ± 6% vs. 46 ± 3%, respectively; p = 0.04). Aortic wall enhancement of rabbits from the "high-fat" group was not significantly different between the first and second MRI (46 ± 3% vs. 47 ± 5%; p = 0.59). Inter-operator reproducibility of aortic wall enhancement after injection of P947 per rabbit was excellent (r = 0.97). In contrast to results achieved with P947, no significant difference in aortic wall enhancement was detected between "low-fat" and "high-fat" groups of rabbits when MRI was performed after injection of P1135, the scrambled version of P947 (22 ± 3% vs. 21 ± 2%, respectively; p = 0.89).

To evaluate the proportion of aortic wall enhancement that can be attributed to a specific binding of P947 to MMPs, kinetics of P947 and P1135 were compared in "low-fat" and "high-fat" groups of rabbits. Five minutes after the injection of either P947 or P1135, a diffuse enhancement was present in the aortic wall (**Figure 4A**). Aortic wall areas defined at this time point were similar after injection of P947 or P1135 in the "high-fat" group (9.5 ± 1.3 mm² vs. 9.4 ± 1.4 mm², respectively; p = 0.65) or the "low-fat" group (7.8 ± 0.5 mm² vs. 7.8 ± 0.3 mm², respectively; p = 0.98). SNR of the aortic wall 5 minutes after injection of P947 was higher in the "high-fat" group than in "low-fat" group (16.4 vs. 15.0; p = 0.04) but the absolute difference in SNR between the two groups increased with time (15.6 vs. 12.8 at 90 minutes; p < 0.001).

In rabbits from the "high-fat" group, kinetics of aortic wall enhancement was significantly different after injection of P947 or P1135 (**Figure 4B**; P947 vs. P1135, p < 0.001). Signal to noise ratios (SNRs) of the aortic wall was higher at 5 minutes after injection of P947 than after injection of P1135 and decreased slower at later time points (p < 0.001 for all time points), in favor of a specific retention of P947 in the aortic wall. In contrast, kinetics of aortic wall enhancement in rabbits from the "low-fat" group were similar after injection of each contrast agent (P947 vs. P1135, p = 0.76).
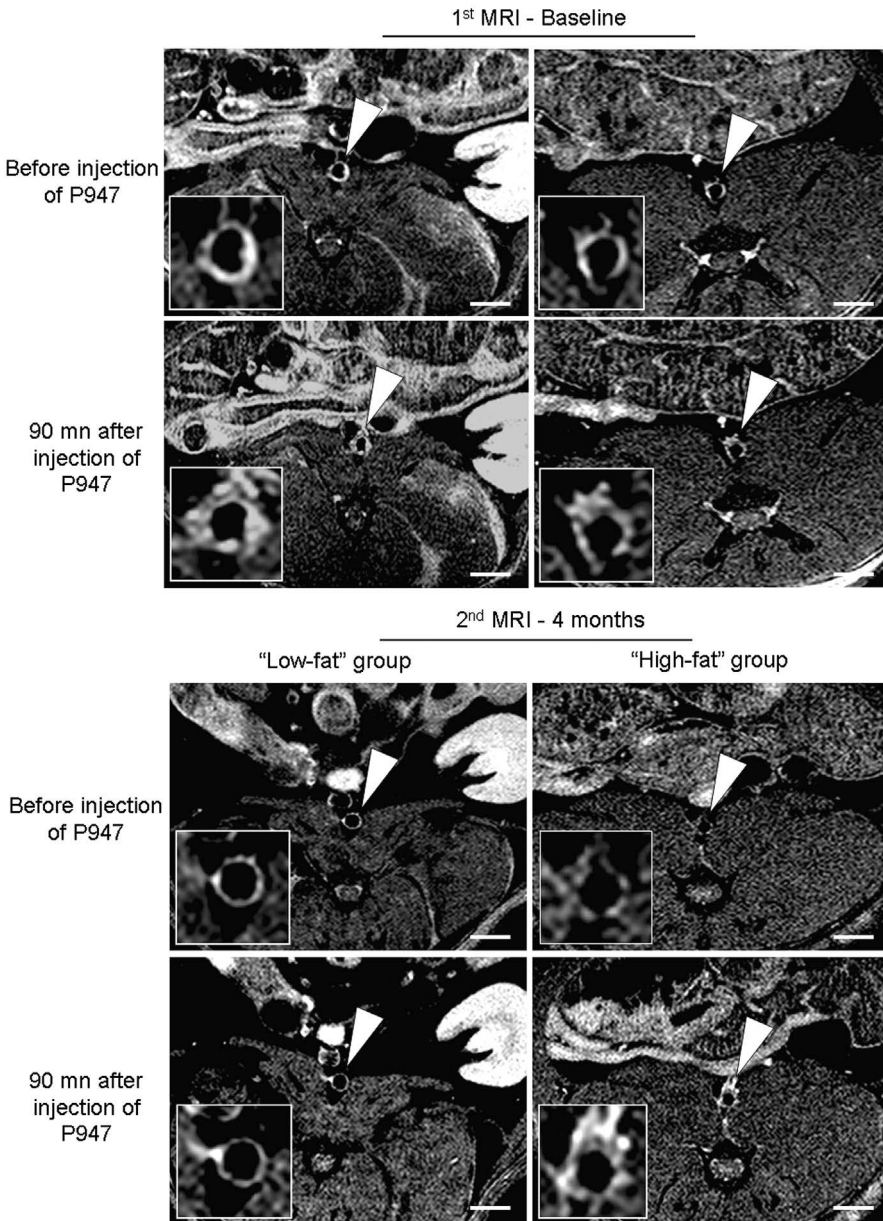
Figure 2. Monitoring of arterial wall remodeling with P947-enhanced MRI. Representative axial views of aortic walls imaged at baseline and four months later in a rabbit from the "low-fat" group (left panels) and the "high-fat" group (right panels) with P947-enhanced MRI. At baseline, note the strong enhancement detected with MRI after the injection of P947 in the aortic wall of both rabbits. Four months later, the enhancement detected in the aortic wall of the rabbit from the "low-fat" group, which had been switched to a chow diet, strongly decreased after injection of P947. In contrast, the enhancement detected in the rabbit from the "high-fat" group, which pursued a hyperlipidemic diet, was strong and similar to the first MRI. Inserts are magnifications of aortas. White arrowheads denote the rabbit aorta. Bar width, 10 mm.

A

Aortic wall enhancement (%)

*

*

*

60
50
40
30
20
10
0

1st MRI - P947   2nd MRI - P947   2nd MRI - P1135

- ■ "Baseline" group
- ▨ "High-fat" group
- ☐ "Low-fat" group

B

Aortic wall enhancement (%)

70
60
50
40
30
20
10
0

1st MRI - P947   2nd MRI - P947

- ◆—◆ "High-fat" group
- ◆- -◆ "Low-fat" group
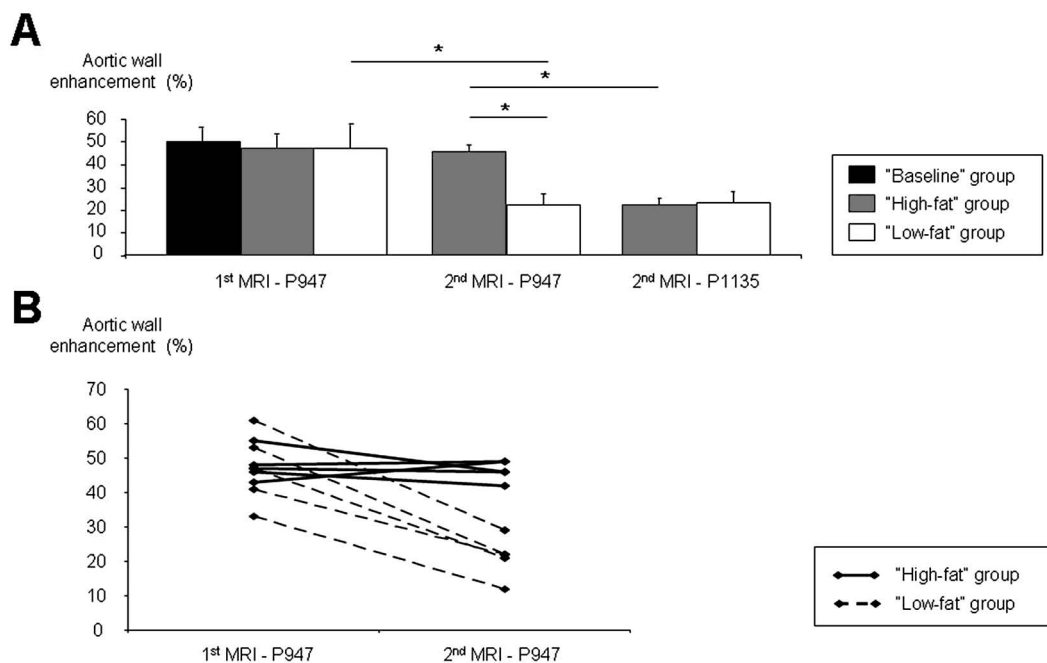
Figure 3. Quantification of aortic wall enhancement with MRI after injection of P947 or P1135. (**A**) At baseline, no significant difference in aortic wall enhancement was measured between "baseline", "high-fat" and "low-fat" groups after injection of the MMP-specific contrast agent P947. Four months later, the enhancement detected in the aortic wall with P947-enhanced MRI was significantly lower in rabbits from the "low-fat" group, which had been switched to a chow diet, as compared to the same rabbits four months earlier, and to rabbits from the "high-fat" group which pursued a hyperlipidemic diet. No significant difference in aortic wall enhancement could be detected between "high-fat" and "low-fat" groups after injection of the non-specific contrast agent P1135. *, $p < 0.05$. (**B**) Changes in aortic wall enhancement 90 minutes after injection of P947 between the first and second MRI in each rabbit from the "high-fat" and "low-fat" groups.
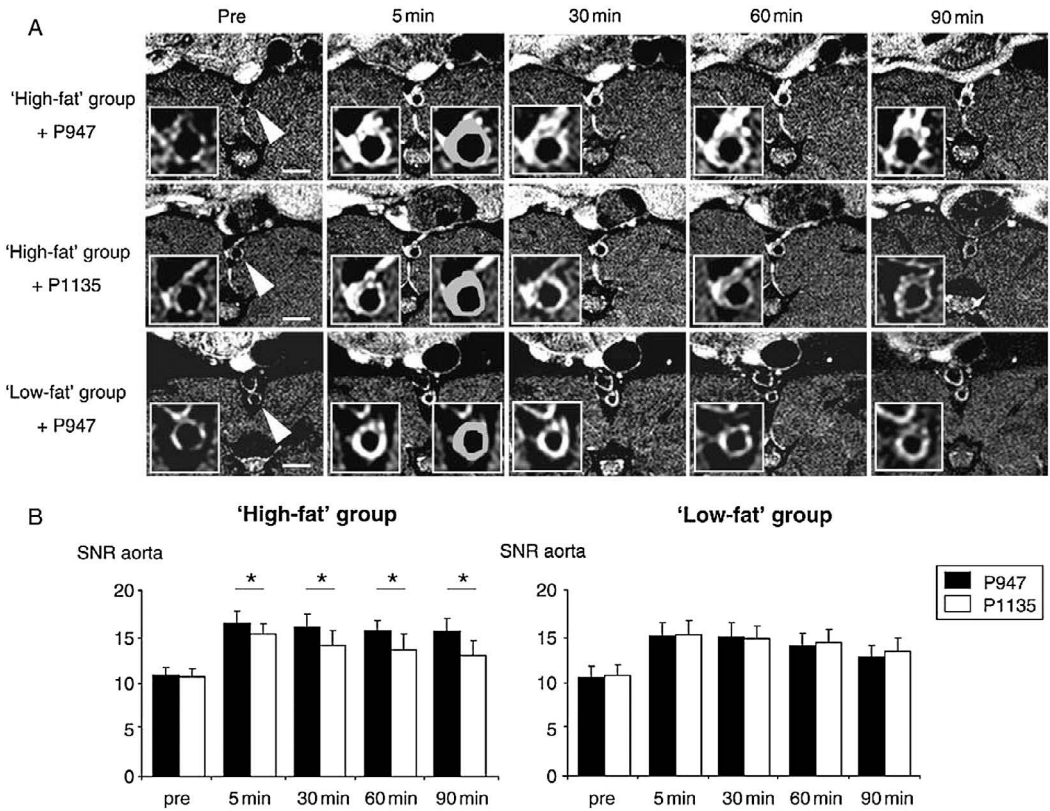
Figure 4. Kinetics of aortic wall enhancement after injection of P947 or P1135. (**A**) Note the strong and diffuse enhancement 5 minutes after injection of P947 or P1135 in the aortic wall of rabbits from both "high-fat" and "low-fat" groups detected with MRI. Aortic wall areas were therefore drawn manually at this imaging time point (right inserts). At later time points, the intensity of enhancement decreased faster in the aortic wall of rabbits from "high-fat" group after injection of P1135 and from "low-fat" group after injection of P947 as compared to rabbits from "high-fat" group after injection of P947. Bar width, 10 mm. (**B**) Kinetics of aortic wall enhancement in rabbits from "high-fat" and "low-fat" groups after injection of P947 or P1135 with the second MRI. In rabbits from the "high-fat" group, SNR of the aortic wall decreased at a slower rate after injection of P947 than after P1135. No such difference could be detected in rabbits from the "low-fat" group. *, $p = 0.03$; †, $p < 0.01$.

MMP-related gelatinolytic activity in atherosclerotic plaques

In situ zymography performed on arterial tissue cryosections showed intense gelatinolytic activities in the intima and adventitia of atherosclerotic plaques of rabbits from the "high-fat" group, whereas only weak gelatinolytic activity was detected in plaques of rabbits from the "low-fat" group (**Figure 5**). Strong enhancement in the aortic wall with MRI 90 minutes after the injection of P947 was associated to the presence of intense gelatinolytic activity with *in situ* zymography on corresponding cryosections of atherosclerotic plaques.
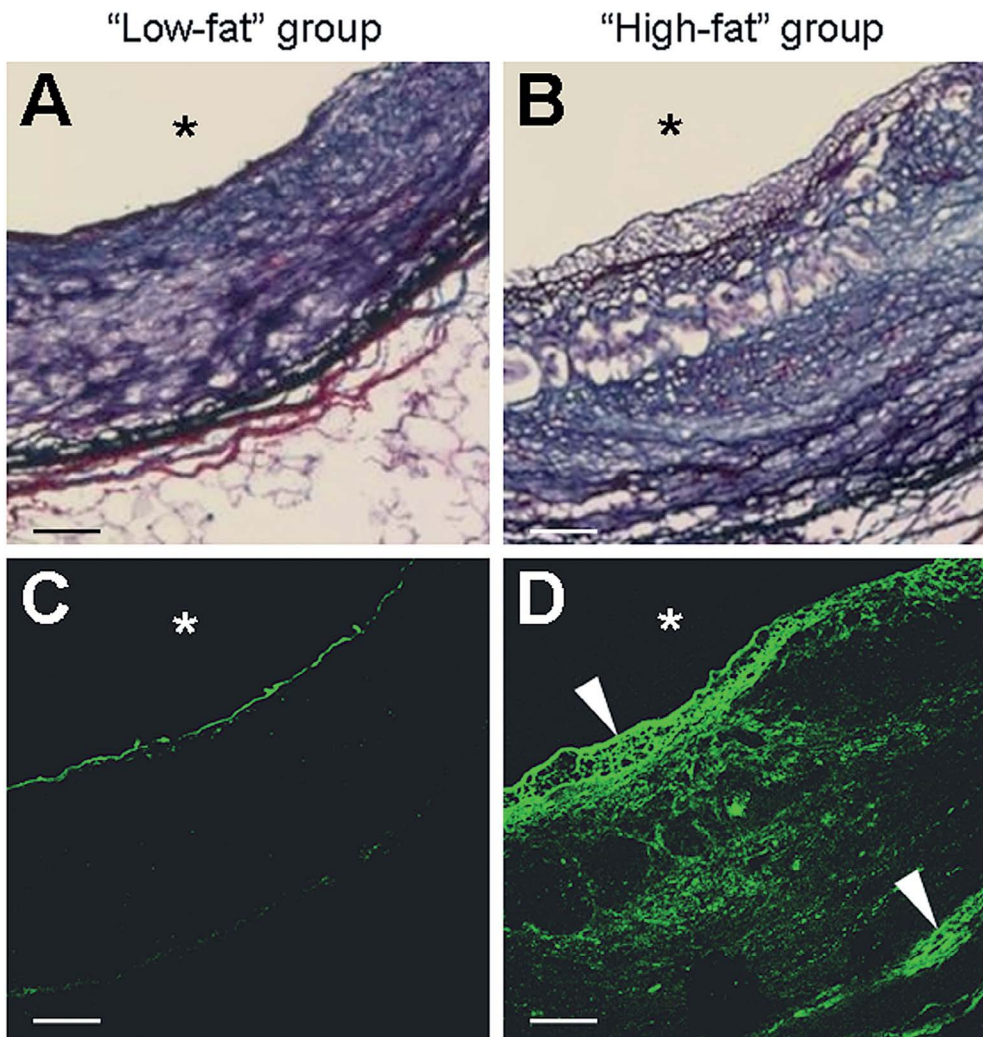
Figure 5. Representative *in situ* zymographies of atherosclerotic plaques from rabbits of "low-fat" and "high-fat" groups. Combined Masson's elastin staining (**A** and **B**) and *in situ* zymographies (**C** and **D**) of adjacent cryosections of atherosclerotic plaques from rabbits of the "low-fat" (**A**, **C**) or "high-fat" (**B**, **D**) groups corresponding to MRI sections displayed in Figure 2. Intense gelatinolytic activities (green fluorescence, white arrowheads) were detected in the fibrous cap and adventia of atherosclerotic plaques from rabbits of the "high-fat" group, whereas only weak fluorescence was detected in atherosclerotic plaques from rabbits of the "low-fat" group. Images of *in situ* zymographies were acquired using a confocal laser microscope with identical amplification gain settings. *, lumen. Bar width, 500 μm.

In situ zymography tests were repeated on adjacent cryosections of atherosclerotic plaques from the "high-fat" group after adding P947, P1135 or reaction buffer to the substrate solution (**Figure 6**). P947 but not P1135 inhibited gelatinolytic activities in atherosclerotic plaques. No fluorescence

was present on cryosections incubated with a solution lacking the DQ-gelatin. Independent experiments with five different aortic segments yielded similar results.
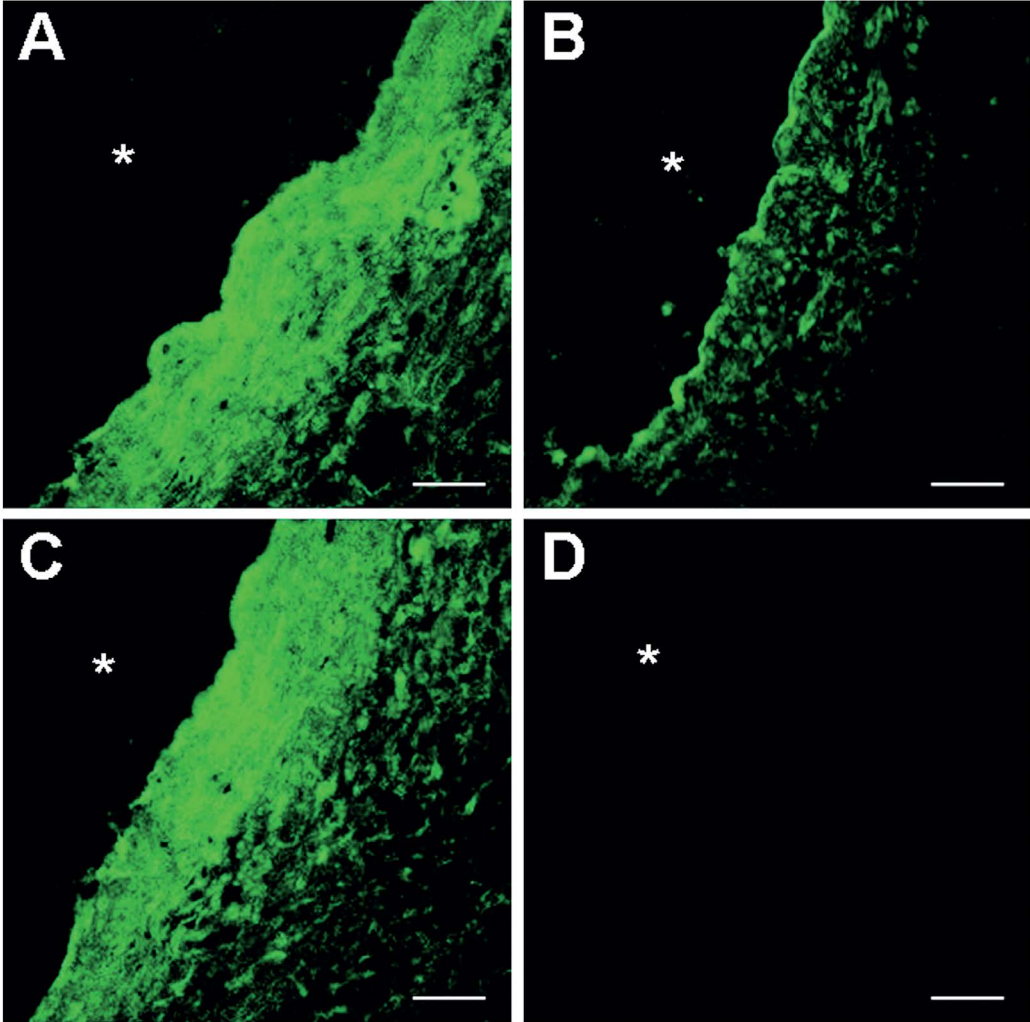
Figure 6. Representative example of competition studies with *in situ* zymography on adjacent cryosections of atherosclerotic plaques. (**A**) After incubation of cryosections with DQ-gelatin, an intense green fluorescence was detected in the intima of atherosclerotic plaques. (**B**) Addition of the MMP-specific contrast agent P947 strongly inhibited the fluorescent signal. (**C**) No inhibition could be detected after addition of the non-specific contrast agent P1135. (**D**) No fluorescence was present on cryosection incubated with a solution lacking the DQ-gelatin. All images were acquired using a confocal laser microscope with identical amplification gain settings. *, lumen. Bar width, 100 μm.

In addition, samples of culture media of aortic segments were run on gelatin zymography gels. Intense pro-MMP-9 (98 kDa), pro-MMP-2 (70 kDa), and active MMP-2 (60 kDa) gelatinolytic bands were detected in the conditioned media of atherosclerotic plaques (**Figure 7A**). Lower MMP-2 activities were measured in the conditioned media of atherosclerotic plaques from the "low-fat" group as compared to "baseline" and "high-fat" groups (**Figure 7B**; 737 ± 194 vs. 1718 ± 193 and 1472 ± 267 DU per milligram wet weight, respectively; p < 0.001). Pro-MMP-2 activities did not differ significantly in aortic segments from the three groups of rabbits ("baseline", 4336 ± 654; "high-fat", 4124 ±1132; "low-fat", 3153 ± 414; p = 0.09).

MMP activities measured in the incubation media of aortic segments were then compared to the enhancement measured in the aortic wall 90 minutes after injection of P947 with the MRI performed in the former two weeks in each rabbit (n = 15). A stronger correlation (**Figure 7C**) was observed between aortic wall enhancement with P947-enhanced MRI and MMP-2 activity than with pro-MMP-2 activity (r = 0.87; r = 0.28, respectively).
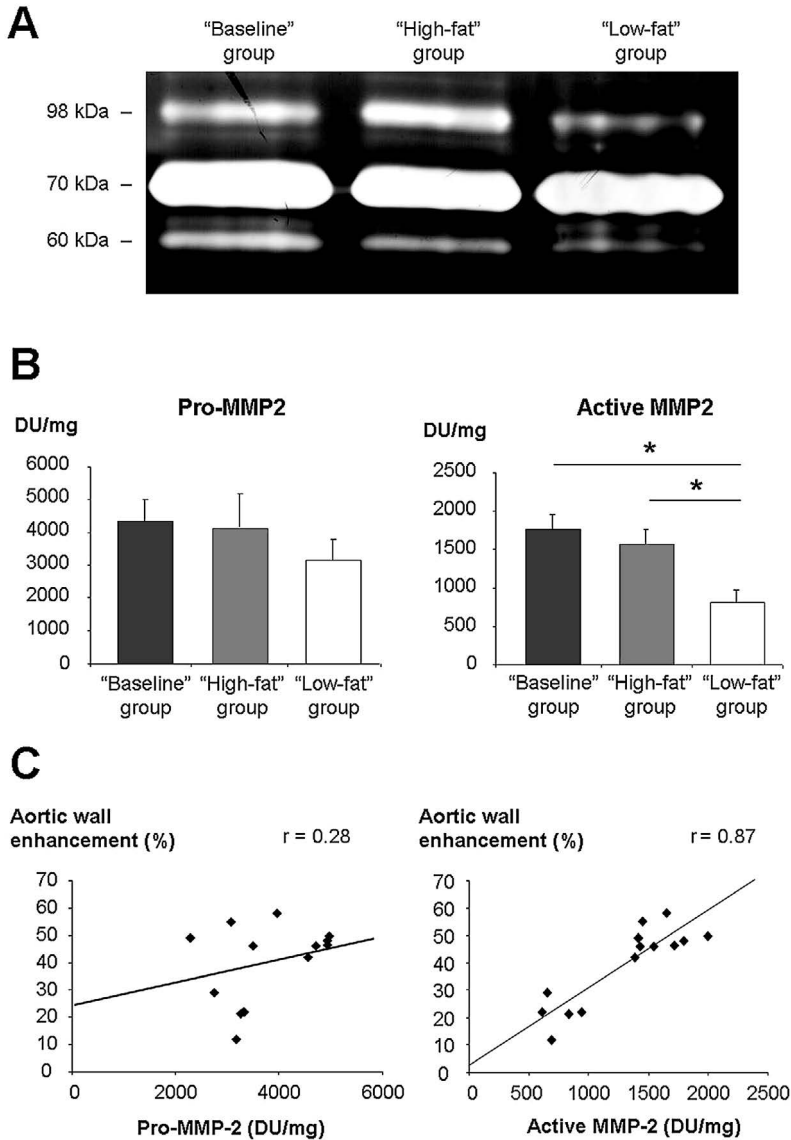
Figure 7. Quantification of MMP activity with SDS-PAGE gelatin zymography. A, Representative example of gelatin zymography showing pro-MMP-9 (98 kDa), pro-MMP-2 (70 kDa), and MMP-2 (60 kDa) gelatinolytic activities in conditioned media of aortic segments from the three groups of rabbits. MMP-2 gelatinolytic band was weaker in aortic segments from the "low-fat" group as compared to aortic segments from "baseline" and "high-fat" groups. (**B**) Significantly lower MMP-2 activities were measured in conditioned media of the "low-fat" as compared to either "baseline" or "high-fat" groups. Pro-MMP2 activities did not differ significantly in aortic segments from the three groups of rabbits. (**C**) Mean gelatinolytic activities measured in incubation media of aortic segments of each rabbit (n = 15) were compared to the enhancement measured in the aortic wall after injection of P947 with the MRI performed in the former two weeks in corresponding animals. A strong correlation was observed between P947-enhanced MRI and MMP-2 activity, whereas correlation was weaker with pro-MMP-2 activity. DU, densitometric units. *, p < 0.05.

DISCUSSION

In the present study, we showed that the intensity of enhancement 90 minutes after the injection of P947 significantly decreased in the aortic wall 4 months after switching rabbits from a hyperlipidemic to a chow diet, whereas the intensity of enhancement remained high in the aortic wall of rabbits maintained on a hyperlipidemic diet. Such changes were not detected with the contrast agent P1135, which lacks the MMP-specific peptide sequence. In addition, we found a strong correlation between the intensity of enhancement in the aortic wall with MRI 90 minutes after the injection of P947 and MMP-related enzymatic activity measured *ex vivo* with gelatin zymography in corresponding atherosclerotic plaques. These results demonstrate that P947 and a clinical MRI scanner can be used to distinguish non-invasively the effects of dietary manipulations upon variations of tissue MMP enzymatic activity within atherosclerotic plaques.

Specificity of P947 for MMPs
Specificity of P947 for MMPs present in atherosclerotic plaques has been tested using several strategies. First, a competition study was performed *ex vivo* in atherosclerotic aortic segments of rabbits and confirmed a significantly lower enhancement measured with MRI when the aortic segments had been pre-incubated with the free peptide forming P947[10]. This approach could however not be translated *in vivo* because of the low water solubility of the peptide. Second, a fluorescent form of P947 was synthesized by replacing the gadolinium by a europium molecule in the chelate and was injected *in vivo* in Apo E[-/-] mice. The fluorescent form of P947 accumulated in MMP-rich areas of atherosclerotic plaques identified by immuno-histology[11]. Fluorescent P947 synthesis had a very low yield and did not provide sufficient concentrations for *in vivo* injection in rabbits. In this study, the specificity of P947 for MMPs was therefore tested by comparing the enhancement obtained in the aortic wall of the same rabbits after injection of the contrast agent P947 and P1135 that has the same properties as P947 except that the sequence of four amino-acids constitutive of the MMP-inhibiting moiety was scrambled. A significantly higher retention of contrast agent was detected after injection of P947 as compared to P1135 in the aortic wall of rabbits from the "high-fat" group, which contained high gelatinolytic activities with zymography. In contrast, kinetics of aortic wall enhancement was similar after injection of P947 or P1135 in rabbits from the "low-fat" group, which contained low MMP activities with zymography. In addition, a strong correlation was found between the intensity of aortic wall enhancement after injection of P947 and the MMP-

related enzymatic activity measured in corresponding aortic segments. Taken together, these results pledge for a specific retention of P947 in MMP-rich aortic wall of rabbits.

Choice of imaging time point

The contrast agents evaluated in this study were of low molecular weight and were expected to be rapidly cleared out of atherosclerotic plaques in case of non-specific accumulation. In fact, a relatively slow wash-out of atherosclerotic plaques was detected after injection of P1135 and could be related to the presence of a gadolinium chelate, which is known to accumulate in atherosclerotic plaques[18]. Kinetics studies showed a faster decrease of aortic wall enhancement after injection of P1135 as compared to P947. The 90-minute imaging time point after injection of P947 seemed optimal to detect the specific retention of P947 in the aortic wall with a relatively low non-specific background enhancement and was therefore chosen as an end point in this study.

Imaging of adventitial MMP activity

In this study, the enhancement detected in the arterial wall with MRI 90 minutes after the injection of P947 was heterogeneous but predominated in areas close to the lumen and in the outer region of the aortic wall. *In situ* zymography confirmed the presence of gelatinolytic activities both in the fibrous cap close to the lumen and in the adventitia of corresponding aortic sections. MMP activities were measured in aortic segments that contained the adventitia. Therefore, the regions of interest drawn to measure aortic wall enhancement included also the outer area of the aortic wall. In fact, MMP activity in the adventitia could play a key role in positive remodeling of atherosclerotic plaques (i.e. development of plaques outwards) and reflect atherosclerotic plaque content. Positive remodeling of atherosclerotic plaques could initially be beneficial by preserving the lumen[19] but was also often found with intra-vascular ultrasound [20] and computed tomography[21] in ruptured coronary atherosclerotic plaques of patients presenting with acute coronary syndromes. Interestingly, coronary atherosclerotic plaques with an outward remodeling contained higher MMP activities in the adventitia than those with a constrictive remodeling[22]. Indeed, positive/outward remodeling was reported to characterize vulnerable plaques[23], and had been previously associated with other markers of plaque instability such as rich inflammatory infiltrate, and decreased collagen and smooth muscle cells in the caps and shoulders of atherosclerotic plaques[24]. In fact, detecting MMP-rich areas with P947-enhanced MRI may be easier in the adventitia than in the thin fibrous

cap of high-risk atherosclerotic plaques and could represent an additional noninvasive marker of plaque instability.

Early detection of aortic wall remodeling

MMPs have been strongly involved in plaque remodeling and stabilization of plaques[5]. In a previous study performed in the same rabbit model of atherosclerosis[15], lipid lowering by diet was followed 7 months later by a regression of atherosclerosis burden with a decrease in lipid component, an increase in the fibrosis component and negative remodeling of plaques. Indeed, reduced MMP activity in atherosclerotic plaques 16 months after switching rabbits from a hyperlipidemic to a chow diet suggests that a decreased catabolism contributes to arterial collagen accumulation[12]. In our study, a similar trend toward a regression of plaque burden was found 4 months after switching rabbits from high-cholesterol to a chow diet. In addition, a strong decrease of MMP gelatinolytic activity was detected in atherosclerotic plaques by both P947-enhanced MRI (*in vivo*) and *ex vivo* zymography as soon as 4 months after the change of diet. These results suggest that decreased gelatinolytic activity in atherosclerotic plaques after lowering plasma lipids could represent an early marker of the evolution of plaques towards stabilization.

Place of molecular MRI for detection of MMP activity in the arterial wall

In previous works[25-27], detection of MMP activity in the arterial wall of atherosclerotic mice was demonstrated using optical and nuclear imaging techniques. These techniques have however important limitations for the clinical evaluation of atherosclerotic plaques in humans. Optical imaging remains restricted to the evaluation of superficial structures or small animals because of light scattering caused by overlaying tissues; and nuclear imaging has a high sensitivity for the detection of radio-tracers but is limited by a spatial resolution of a few millimeters and the absence of anatomical images[28]. In contrast, some important features of atherosclerotic plaques (e.g., thin fibrous cap, large necrotic core or hemorrhage) can be identified in patients using MRI through their different intrinsic relaxation properties[7,8]. In addition to high-spatial resolution imaging, detection of biological activities using contrast agents targeting specific molecules involved in plaque destabilization would strongly improve the potential of MRI to identify plaques prone to rupture and monitor the effect of therapeutic or dietary interventions.

Study limitations
The interpretation of this study must consider several limitations. First, a relatively small number of animals were studied. One hurdle with low-molecular weight MR contrast agents is that they require micro-molecular concentrations to be detected with MRI[28]. At this stage of development of the contrast agent, synthesis of P947 was complex and therefore only a limited number of rabbits could be imaged. Second, competitive blocking of P947 with a version of P947 lacking gadolinium was not evaluated in this study. Nevertheless, regarding the high number of binding sites for MMP and the micro-molar affinity of P947 for MMP, competition studies would have required high concentrations of P947 lacking gadolinium to test this approach in rabbits, which were not available at this stage of development of the contrast agent. In addition, lack of gadolinium in the chelate can modify the electric charge of the molecule and change pharmacokinetics and properties of the contrast agent. Third, a first acquisition needs to be performed prior to contrast administration. Finally, the results obtained in an experimental model of atherosclerosis need to be validated in complex human atherosclerotic plaques. In a former study[10], a higher retention of P947 in human carotid endarteriectomies was however evidenced by *ex vivo* MRI in MMP-rich as compared to MMP-poor atherosclerotic plaques.

Perspectives
In summary, we demonstrate in the present study that P947-enhanced MRI distinguishes variations of MMP-related enzymatic activity within plaques as an effect of dietary changes in an experimental model of atherosclerosis. Translation of this imaging technology to the clinical field could give deeper insights into the role of MMPs in arterial wall remodeling *in vivo* and a clinical modality to image and monitor markers previously associated with plaque progression and instability. Thus, in association to morphological aspects of atherosclerotic plaques identified with MRI, P947 may help to identify patients with plaques prone to rupture who could benefit from early implementation of therapies aimed towards plaque stabilization.

REFERENCES

1. Virmani, R. et al. *J. Am. Coll. Cardiol.* 47(8 Suppl), C13-8 (2006).
2. Libby, P. et al. *Circulation* 104, 365-372 (2001).
3. Fuster, V. et al. *J. Am. Coll. Cardiol.* 46, 937-954 (2005).
4. Galis, Z.S., et al. *J. Clin. Invest.* 94, 2493-2503 (1994).
5. Pasterkamp, G., et al, *Arterioscler. Thromb. Vasc. Biol.* 24, 650-657 (2004).
6. Galis, Z.S., et al. *Circ. Res.* 90, 251-262 (2002).
7. Fayad, Z.A., et al. *Circulation* 101, 2503-2509 (2000).
8. Hatsukami, T.S., et al. *Circulation* 102, 959-964 (2000).
9. Briley-Saebo, K.C., et al. *J. Magn. Reson. Imaging* 26, 460-479 (2007).
10. Lancelot, E., et al. *Arterioscler. Thromb. Vasc. Biol.* 28, 425-432 (2008).
11. Amirbekian, V., et al. *Radiology* 251, 429-438 (2009).
12. Aikawa, M., et al. *Circulation* 97, 2433-2444 (1998).
13. Odake, S., et al. *Biochem. Biophys. Res. Commun.* 199, 1442-1446 (1994).
14. Hyafil, F., et al. *Nat. Med.* 13, 636-641 (2007).
15. Helft, G., et al. *Circulation* 105, 993-998 (2006).
16. Hyafil, F., et al. *Arterioscler. Thromb. Vasc. Biol.* 26, 176-181 (2006).
17. Frederiks, W.M. and Mook, O.R., *J. Histochem. Cytochem.* 52, 711-722 (2004).
18. Yuan, C., et al. *J. Magn. Reson. Imaging* 15, 62-67 (2002).
19. Glagov, S., et al. *N. Engl. J. Med.* 316, 1371-1375 (1987).
20. Maehara, A., et al. *J. Am. Coll. Cardiol.* 40, 904-910 (2002).
21. Hoffmann, U., et al. *J. Am. Coll. Cardiol.* 47, 1655-1662 (2006).
22. Pasterkamp, G., et al. *Atherosclerosis* 150, 245-253 (2000).
23. Schoenhagen, P., et al. *Curr. Atheroscler. Rep.* 5, 150-154 (2003).
24. Pasterkamp, G., et al. *J. Am. Coll. Cardiol.* 32, 655-662 (1998).
25. Deguchi, J.O., et al. *Circulation* 114, 55-62 (2006).

26. Schafers, M., et al. *Circulation* 109, 2554-2559 (2004).
27. Fujimoto, S., et al. *J. Am. Coll. Cardiol.* 52, 1847-1857 (2008).
28. Rudd, J.H., et al. *Arterioscler. Thromb. Vasc. Biol.* 29, 1009-1016 (2009).

Chapter 7

Reproducibility of black blood dynamic contrast-enhanced (DCE) MRI in aortic plaques of atherosclerotic rabbits

Based on

Author contribution: Esad Vucic: designed and performed experiments, analyzed data and revised the manuscript.

ABSTRACT

Purpose

To investigate the short-term reproducibility of black-blood dynamic contrast-enhanced (DCE) magnetic resonance imaging (MRI) in atherosclerotic rabbits to evaluate the potential of this technique to be a reliable readout of plaque progression and/or regression upon therapeutic intervention.

Materials and methods

Atherosclerotic rabbits were imaged at baseline and 24 hours later with DCE-MRI on a 1.5T MRI system. DCE-MRI images were analyzed by calculating the area under the signal intensity versus time curve (AUC). Intraclass correlation coefficients (ICCs) were used to evaluate interscan, intraobserver, and interobserver reproducibility. In addition, the test-retest coefficient of variation (CoV) was evaluated.

Results

Statistical analyses showed excellent interscan, intraobserver, and interobserver agreement. All ICCs were greater than 0.75, P < 0.01 indicating excellent agreement between measurements.

Conclusion

Experimental results show good interscan and excellent intra- and interobserver reproducibility, suggesting that DCE-MRIcould be used in preclinical settings as a read-out for novel therapeutic interventions for atherosclerosis. This preliminary work encourages investigating the reproducibility of DCE-MRI also in clinical settings, where it could be used for monitoring high-risk patients and in longitudinal clinical drug trials

INTRODUCTION

Cardiovascular disease accounts for approximately 30% of deaths worldwide. Among the different cardiovascular disorders, atherosclerosis remains the major cause of death and premature disability in developed societies[1,2]. Although conventional risk factors combined with risk scores are helpful in estimating cardiovascular risk in patients groups, they lack predictive power in identifying individual patients at high risk for cardiovascular events and may not provide any indication about the risk associated with a single atherosclerotic lesion[3]. Several studies have highlighted the role of

inflammation in the pathogenesis of atherosclerotic plaque. These studies indicate that plaque pathological behavior is determined not primarily by size and the level of luminal narrowing, but by plaque composition and inflammation. In particular, pathological studies indicate that plaques with large lipid cores, thin fibrous caps, and inflammatory cell infiltrates accompanied by an abundant plexus of neovessels might be more likely to rupture and precipitate acute clinical events[4,5]. The deeper understanding of the role of inflammation in the pathogenesis of atherosclerosis identifies new important markers for the detection and risk stratification of otherwise asymptomatic atherosclerotic lesions. Moreover, by identifying inflammation as a novel target for medical intervention, it opens new possibilities in the therapeutic management of atherosclerosis. While histological markers of plaque inflammation (such as inflammatory cell content and plaque neovascularization) are known and can be evaluated by histology in animal models, it is not feasible to assess them routinely in clinical practice or in either pre-clinical or clinical drug development studies. Therefore it would be of clinical relevance to develop non-invasive techniques that could investigate plaque physiology, and provide surrogate endpoints for the evaluation of progression/regression of disease and/or treatment efficacy. Among various imaging techniques, magnetic resonance imaging (MRI) and positron emission tomography (PET) have recently been proposed to investigate plaque neovascularization and inflammatory infiltrate, respectively[6-12]. The correlation between plaque ^{18}F fluorodeoxyglucose (^{18}F-FDG) uptake measured by PET and plaque macrophage content has been established in animals[13,14], and the reproducibility of this technique together with its potential to monitor the reduction in plaque inflammation after treatment have also been investigated[15]. These studies have shown that ^{18}F-FDG PET can reliably measure the degree of plaque inflammation in a non-invasive manner. Dynamic contrast enhanced (DCE) MRI is an imaging technique extensively used to study the vascularity of tumors[18].This technique takes advantage of the administration of clinically-available contrast agents (i.e., Gadolinium (Gd)-chelates), to quantify the extent of tissue blood supply and its associated physiological characteristics, such as permeability surface area product, extraction fraction, and blood flow. Based on the notion that inflamed, unstable atherosclerotic plaques are highly vascularized, DCE-MRI has also been applied to the study of neovascularization in atherosclerosis. Both "bright blood" and "black blood" techniques have been previously used in DCE-MRI of atherosclerosis. In "bright blood" techniques, the signal from flowing blood in the vessel lumen is preserved and this allows data analysis using model-based approaches. On the contrary in "black blood" approaches

this same signal is suppressed, thereby restricting the analysis to non model-based approaches. Black blood approaches however allows better delineation of the vessel wall. While bright blood techniques have been shown successful in quantifying plaque neovascularization in patients with carotid atherosclerosis[6-8], black blood techniques have been useful in studying animal models of disease[16], where it is imperative to achieve good wall delineation. In more detail, is has been shown that black blood T1 weighted (T1W) turbo spin echo (TSE) DCE-MRI analyzed by non model-based approaches can quantify neovessels in aortic plaques of atherosclerotic rabbits (correlation coefficient r = 0.89, p = 0.016)[16]. These data suggest that DCE-MRI could be useful as a read-out for plaque neovascularization and inflammation in pre-clinical animal studies and also in a clinical environment for monitoring atherosclerotic disease progression or regression in response to anti-inflammatory treatment.
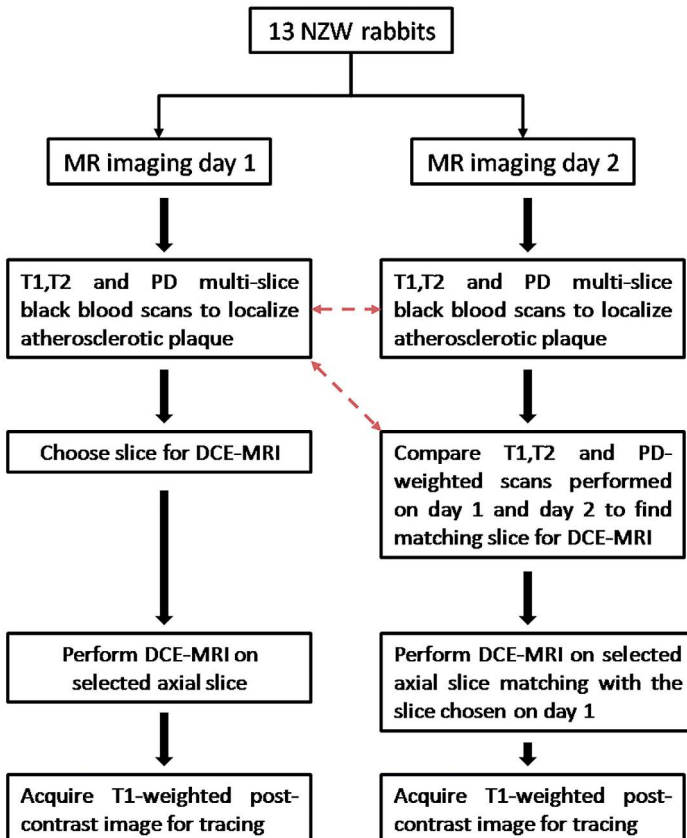
Figure 1. Flow chart followed during baseline and 24 hours scan.
Red dashed arrows indicate the scans compared during the 24 hours scan to find the slice matching with the one used for the dynamic contrast enhanced (DCE) MRI acquisition during the baseline scan.

However, in order for this technique to become a valuable tool in the clinic, more studies are still required. The reliability of this technique has been investigated in tumors, both in animal models and patients as well[17-22], but to our knowledge its short term reproducibility together with intra and inter observer variability still needs to be investigated in the context of atherosclerosis.

In the present work we tested the inter-scan variability together with intra and inter-observer agreement of black-blood DCE-MRI in atherosclerotic rabbits. The experiments performed in this study allowed assessing the reliability of DCE-MRI in a pre-clinical setting, and estimating samples size for the planning of future pre-clinical studies with adequate power.

METHODS

Animal Protocol

Aortic atherosclerotic plaques were induced in thirteen New Zealand White (NZW) male rabbits (mean age, 4 months; mean weight = 3.1 ± 0.2 kg; Covance, Princeton, NJ, USA) by a combination of 4 months of high cholesterol diet (4.7% palm oil and 0.3% (weeks 1 through 8) and 0.15% cholesterol (weeks 9 through 16); Research Diet Inc., New Brunswick, NJ, USA) and repeated balloon injury of the aorta (2 weeks and 6 weeks after starting the high-cholesterol diet). Aortic injury was performed from the aortic arch to the iliac bifurcation with a 4F Fogarty embolectomy catheter introduced through the femoral artery. All procedures were performed under general anaesthesia by an intramuscular injection of ketamine (20 mg/kg; Fort Dodge Animal Health, Overland Park, KS, USA), xylazine (5 mg/kg; Bayer Corp., Shawnee Mission, KS, USA) and acepromazine (0.5 mg/Kg; Boehringer Ingelheim Vetmedica, Inc. St. Joseph, USA). The protocol was approved by the Institute Animal Care and Use Committee of Mount Sinai School of Medicine, New York, NY, USA.

MR Imaging Protocol

All rabbits were scanned after completion of 4 months of high-cholesterol diet. During this time, all animals also underwent balloon injury of the aorta (2 weeks and 6 weeks after starting the high-cholesterol diet). Under anaesthesia, animals were imaged at baseline and 24 hours after baseline with the same MRI protocol. Imaging was performed using a 1.5 Tesla MRI clinical system (Siemens Sonata, Siemens Medical Solutions, Erlangen, Germany) using a knee coil for signal reception. On both occasions, to locate

atherosclerotic plaques, 3-mm thick sequential axial images of the aorta were obtained from the celiac trunk to the iliac bifurcation using 2D multi-slice black blood T1, T2 and PD-weighted (T1W, T2W, PDW) fast spin-echo sequences (TE, 5.6/39/5.6 ms, TR, 800/2000/2000 ms, inter-slice gap, 0.6 mm, field of view, 12x12 cm, matrix size, 256x256, echo train length, 7, and signal averages, 16). Spectral fat suppression was applied to null the signal from the peri-adventitial fat. DCE-MRI was performed on one selected axial slice using a black blood double inversion recovery (DIR) turbo spin echo (TSE) sequence (slice thickness, 3 mm, TE, 5.6ms, TR, 250 ms, field of view, 12x12 cm, matrix size, 256x256, echo train length, 15, signal averages, 1). A total of 100 images per rabbit were acquired, with a time resolution of 4.8 s. After a 24s delay from the beginning of the DCE-MRI acquisition (equivalent to 5 pre-contrast images), 0.2 mmol/Kg of Gd-DTPA (Magnevist) was injected with a power injector at a rate of 0.5mL/s followed by a 10 ml saline flush, through a marginal ear vein. After the DCE-MRI scan, a T1W post-contrast MR image of the same axial slice selected for DCE-MRI was acquired (slice thickness, 3 mm, TE, 5.6 ms, TR, 250 ms, field of view, 12x12 cm, matrix size, 256x256, echo train length, 15, signal averages, 16). This image was acquired with the same exact imaging parameters used for the DCE acquisition, except for the number of averages (16 instead of one), in order to clearly delineate the atherosclerotic vessel wall. After 24 hours, all animals were imaged with exactly the same protocol (2D T1W, T2W and PDW multi-slice black blood scans, followed by black blood T1W DCE-MRI and T1W post-contrast scans on a selected axial slice). On the second day, DCE-MRI was performed on an axial slice matching the one chosen on the first day of imaging. In order to ensure proper matching between slices T1W, T2W and PDW scans of both sessions were compared at the MRI console on the day of the second scan by simultaneously evaluating all images starting from the iliac bifurcation up to the renal arteries. Slice matching between the two imaging sessions was achieved by using anatomical fiducial markers such as the iliac bifurcation, the vertebral column and the renal arteries. Figure 1 illustrates the flow chart followed during imaging sessions on day 1 and day 2, while **Figure 2** shows PDW images of two matching slices chosen for DC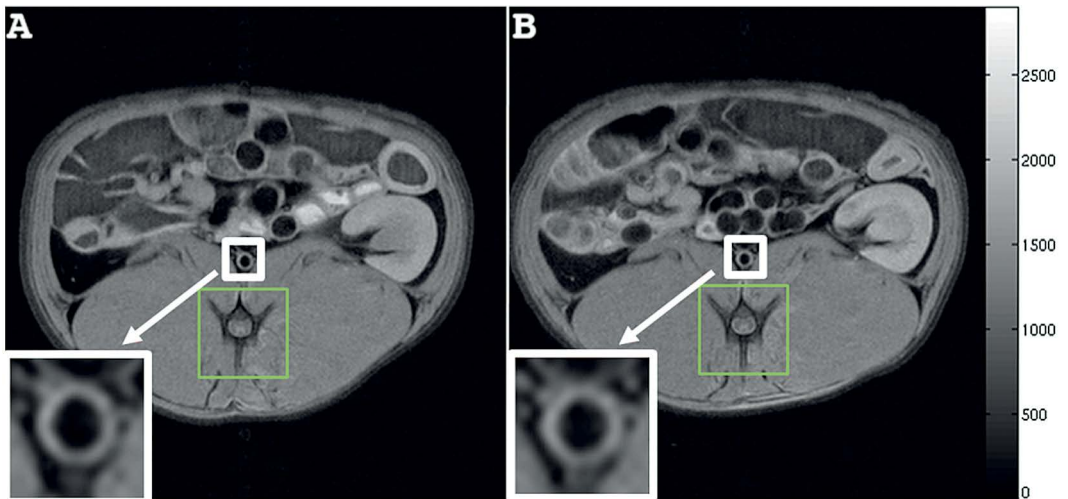E-MRI during day 1 (**Figure 2A**) and day 2 (**Figure 2B**) fiducial markers such as the iliac bifurcation, the vertebral column and the renal arteries. **Figure 1** illustrates the flow chart followed during imaging sessions on day 1 and day 2, while **Figure 2** shows PDW images of two matching slices chosen for DCE-MRI during day 1 (**Figure 2A**) and day 2 (**Figure 2B**).

Figure 2. Proton density weighted images (PDW) of the slice chosen for dynamic contrast enhanced (DCE) MRI of one representative rabbit. **Panel A** shows the slice chosen during the baseline scan. **Panel B** shows the corresponding slice chosen during the 24 hours scan. The white box and arrow indicate the abdominal aorta (also magnified at the bottom left of both panels). The green box indicates the vertebral spine, which was used as an anatomical fiducial marker to match the two slices.

DCE Image Analysis

The change of signal intensity in a region-of-interest (ROI) including the atherosclerotic plaque visible in the slice selected for DCE-MRI was evaluated with a custom made Matlab (The MathWorks, Inc., Natick, MA, USA) program. The area under the signal intensity versus time curve (AUC) was calculated at different time points (1, 2 and 7 minutes after injection of contrast agent) by numerical integration via the trapezoidal rule of the time series using the following equation:

$$AUC_{SI}(T) = \int_0^T (SI(t) - SI_{precontrast})dt \qquad [1]$$

where $SI(t)$ represents the signal intensity in one given pixel at time t, $SI_{precontrast}$ represents the average pre-contrast signal intensity value calculated as the pixel-by-pixel average intensity of the first 5 pre-contrast images and T = 1, 2 and 7 minutes after injection. AUC is a measure that expresses the uptake and retention of contrast agent in a tissue of interest. AUC calculated at 1 and 2 minutes after injection have been shown to correlate with plaques neovascularization in aortic plaques of NZW rabbits[16]. However, since both wash-in and wash-out kinetics contribute to this measure, we evaluated reproducibility of AUC calculated also at a later time point after injection (7 minutes), in order to capture both these aspects.

Assessment of DCE-MRI Reproducibility

In order to ensure proper calibration between scans performed on different days, the pre-contrast signal intensity in a reference tissue (resting skeletal peri-vertebral muscle) and in regions of background noise was evaluated for each animal in both scans. Care was taken not to choose regions of interest where the effect of the intra-muscular injection of anesthesia (defined as bright areas in T2 weighted images of the same slice) was visible. Skeletal muscle undergoes enhancement during contrast agent injection: however, since calibration was performed only on pre-contrast images and since contrast agent washes out in between scans, this does not affect the
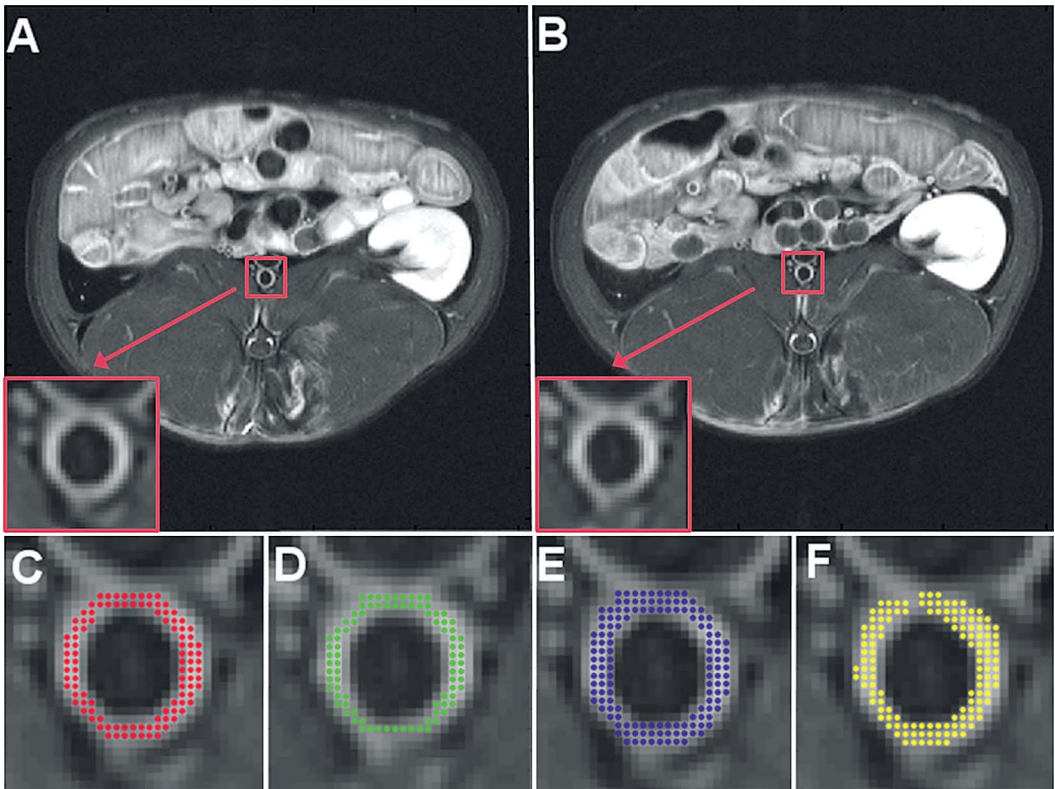
Figure 3. T1 weighted post-contrast images used for tracing or the vessel wall for dynamic contrast enhanced (DCE) MRI data analysis of the same atherosclerotic rabbit shown in **Figure 2** (panel A, day 1; panel B, day 2). The red box and arrow indicate the abdominal aorta (also magnified at the bottom left of both panels). Panel C shows the tracing of observer 1 for day 1 (area covered with red dots). Panel D shows the tracing of observer 1 for day 2 (area covered with green dots). The tracings shown in panel C and D were used to evaluate inter-scan variability. Panel E shows the repeated tracing of observer 1 for day 1 (area covered with blue dots). The tracings shown in panel C and E were used to evaluate intra-observer variability. Panel F shows the tracing of observer 2 for day 1 (area covered with yellow dots). The tracings shown in panel C and F were used to evaluate inter-observer variability.

calibration procedure. Regions of interest covering the whole atherosclerotic aortic vessel wall visible in the slice of interest were independently traced by two observers (respectively with 3 and 8 years experience in MR imaging of atherosclerosis) on T1W post-contrast images of the slice selected for dynamic contrast enhanced acquisition, in order to assess inter-scan and inter-observer variability. The size of the ROI varied from animal to animal, depending on the diameter of the aorta and vessel wall thickness. A typical size ROI was on average 100 pixels (**Figure 3**)*. In order to minimize recall bias, the tracing dataset was randomized for both observers and for both tracing sessions. **Figure 3** shows an example of the images used for tracings of one rabbit (**Figure 3A** – **first scan**; **Figure 3B** – **second scan**) and of the tracings of both observers (**Figure 3, C-F**).

Statistical Analysis
A paired t test was used to verify a potential difference in signal intensities between consecutive scans in the tissue of reference and in regions of background noise, in order to ensure adequate signal intensity calibration. Intra-class correlation coefficients (ICCs) with 95% confidence intervals were calculated to test the inter-scan variability, and inter-observer and intra-observer agreement using SPSS software (SPSS Inc., Chicago, Illinois). For inter-scan variability thirteen data-points were included in the analysis (one data point for each rabbit). For evaluation of intra-observer and inter-observer reproducibility twenty-six data points were included in the analysis (all tracings from both observers or repeated tracings from one observer for both scanning sessions). The average AUCs for scan 1 and scan 2, their average difference (defined as the average of the difference between AUC for scan 1 and scan 2 for each rabbit), as well as the CoV were calculated. The test-retest coefficient of variation (CoV) was calculated as the standard deviation of AUC derived from two consecutive scans on the same subject, divided by their mean, averaged across subjects. A priori power analysis was also performed. The power of a statistical test is defined as the probability that the test will not make type 2 errors. If the rate of type 2 errors, or false negatives, is defined as β, then the power is defined as $1-\beta$. By assuming a given statistical significance (defined as α) and effect size that needs to be detected, a priori power analysis can be used to determine an appropriate sample size to achieve adequate power. A priori power analysis was performed using **GPower** software, version 3.0 (Universitat Kiel, Germany) based on a 2-sample paired t test (2-sided) with $1-\beta$ (power) = 80% power and α = 5%. Bland–Altman plots with their corresponding limits of agreement were drawn to evaluate systematic measurement bias. The limit of agreement lines

were calculated as mean ± 1.96 SDs of the difference of AUC values in two consecutive scans.

RESULTS

No statistical difference was found between signal intensity values evaluated in the first scan and signal intensity values evaluated in the second scan (p = 0.29) for regions of peri-vertebral muscle. Similar calibrations performed on regions of background noise led to the same results (p = 0.84). This ensured adequate signal intensity calibrations among scans performed on different days. Statistical analyses showed excellent inter-scan, intra-observer and inter-observer agreement for all the parameters evaluated in the study. **Table 1** shows the intra-class correlation coefficient (ICC) for all the AUC measures evaluated (1, 2 and 7 minutes) for inter-scan, intra-observer and inter-observer variability: all ICC values for all parameters were greater than 0.75 (p < 0.01), indicating excellent agreement[23].

	AUC 1 min*	AUC* 2 min	AUC* 7 min
Inter-scan ICC[†]	0.840 (p = 0.002)	0.834 (p = 0.002)	0.768 (p = 0.009)
Intra-observer ICC[†]	0.997 (p < 0.001)	0.997 (p < 0.001)	0.996 (p < 0.001)
Inter-observer ICC[†]	0.983 (p < 0.001)	0.988 (p < 0.001)	0.991 (p < 0.001)

Table 1. Inter-scan, intra-observer and inter-observer agreement
* Area under the curve, [†] Intra class correlation coefficient

Table 2 shows inter-scan variability data for AUC 1, 2, and 7 minutes: the CoV show a test-retest variability of respectively 17% for AUC 1 minute, 16% for AUC 2 minutes and 11% for AUC 7 minutes, comparable to other DCE-MRI studies.

	AUC* 1 min	AUC* 2 min	AUC* 7 min
Scan 1 average	277.1 (79.8)	624.5(160.0)	2350.7(506.9)
Scan 2 average	280.4 (131.2)	640.5 (246.7)	2383.3 (682.7)
Average difference	-3.3 (77.4)	-16.0 (156.9)	-32.5 (521.6)
CoV[†]	17%	16%	11%

Table 2. AUC variability between scans
* Area under the curve, [†] Coefficient of variation

Figure 4 shows an example of two area under the curve (AUC) maps of one representative rabbit (same animal shown in Figure 2 and 3), calculated from respectively the first (**Figure 4, A**) and the second (**Figure 4, B**) scan. Both maps are represented with the same color scale and show great similarity, both overall and in the vessel wall (**Figure 4 A** and **B**, lower left panel).
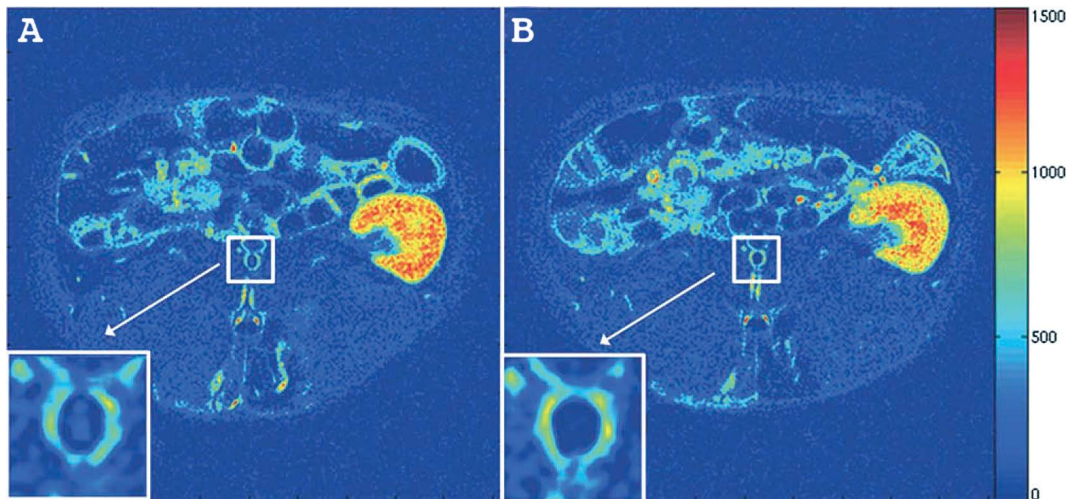

Figure 4. Area under the curve (AUC) maps (2 min) of the same atherosclerotic rabbit shown in **Figure 2** and 3 (**panel A, day 1; panel B, day 2**). The white box and arrow indicate the abdominal aorta (magnified at the bottom left of both panels). Both maps are presented with the same color scale, windowing and contrast. Hot colors indicate high AUC values, while cold colors indicate low AUC values.

Figure 5 shows plaque ROI curves from two representative rabbits captured from both imaging sessions and demonstrates a very similar plaque enhancement in both cases.
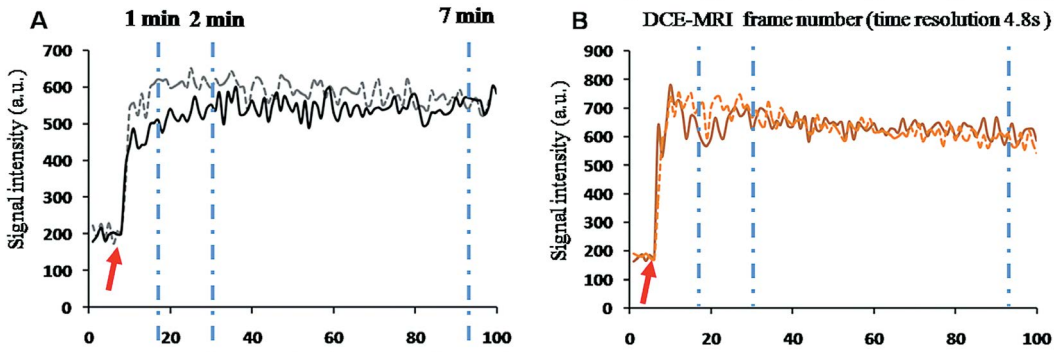
Figure 5. Signal intensity of plaque ROI curves. **Panel A:** plaque ROI curve for the same representative rabbit showed in previous figures. **Panel B:** plaque ROI curves for a second representative rabbit. X axis, frame number of DCE-MRI acquisition. Y axis, signal intensity (absolute units) of plaque ROI curve. Solid lines represent plaque ROI curves from DCE-MRI acquisition of day 1. Dashed lines represent plaque ROI curves for DCE-MRI acquisition of day 2. Dashed dotted light blue lines show the time points at which AUC was calculated (1, 2 and 7 minutes after injection). Baseline values were not subtracted in order to show that they are comparable between scans performed during different sessions. Red arrow indicates the time for beginning of calculation of AUC.
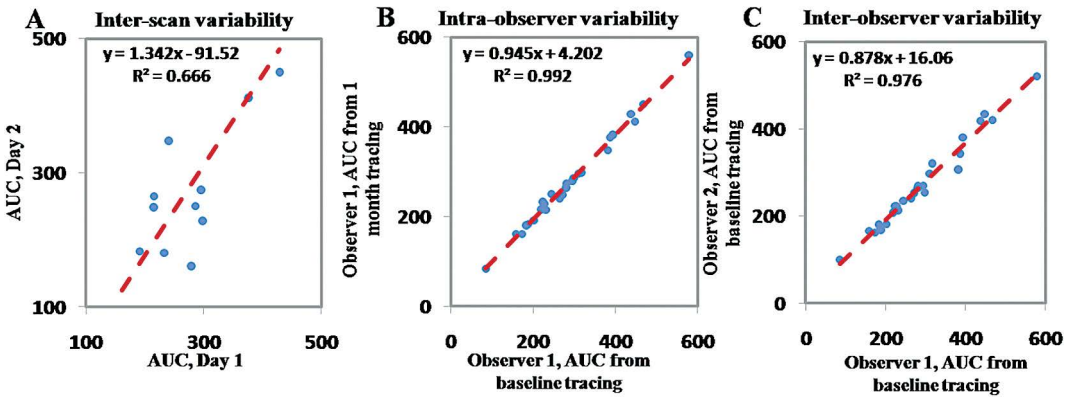
Figure 6. Correlations between: (**a**) AUC 1 minute evaluated on DCE-MRI scan of day 1 versus AUC 2 minutes evaluated on DCE-MRI scan of day 2 for the evaluation of interscan variability; (**b**) AUC 1 minute, baseline tracings of observer 1 versus 1 month tracings of the same observer for the evaluation of intraobserver variability; (**c**) AUC 1 minute, baseline tracings of observer 1 versus baseline tracings of observer for the evaluation of interobserver variability. Red dashed line indicates regression line. Both axes represent AUC values expressed in absolute units.
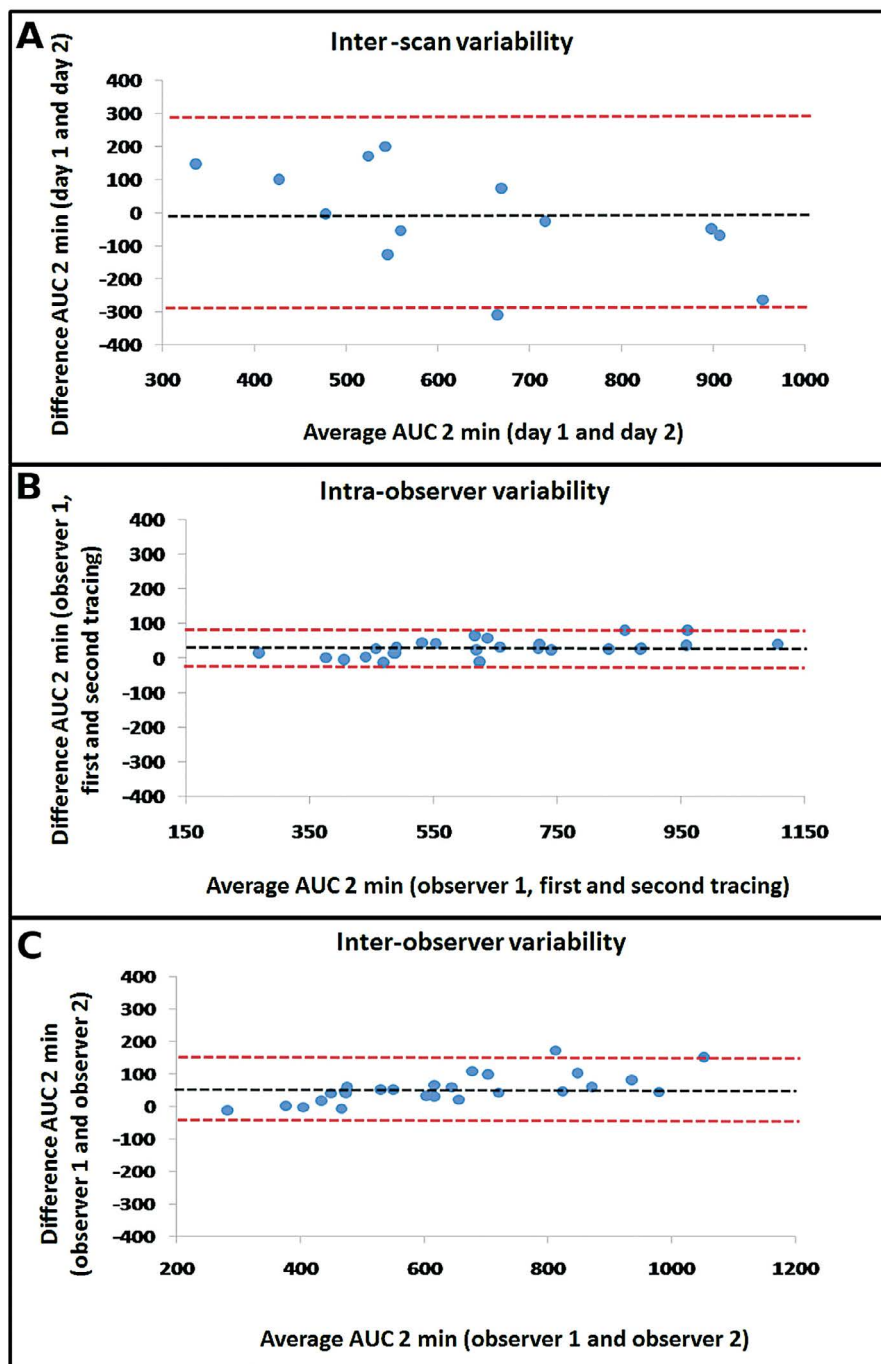
Figure 7. Bland–Altman plots for interscan (**a**), intraobserver (**b**), and interobserver (**c**) variability for AUC 2 minutes. The black dashed line represents the average difference between the two measurements, while the limits of agreement are drawn as red dashed lines (average difference ± 1.96 SDs). Both axes represent AUC values expressed in absolute units.

DISCUSSION

In this study we tested the short term reproducibility of black blood DCE-MRI for imaging of the abdominal aorta of atherosclerotic rabbits. Overall the study shows that the reliability of this technique compares well with other imaging techniques used to investigate atherosclerosis, such as [18]F- FDG PET[15,22] and non-contrast MRI[24,25]. ^{18}F-FDG PET is a nuclear medicine technique that has recently been proposed to investigate plaques inflammatory activity [6-12]. The correlation between plaque 18F–FDG uptake measured by PET and plaque macrophage content has been established in several animal studies[13,14]. In addition, Rudd et al.[15,22] have recently investigated the inter-scan, intra-observer and inter-observer reliability of ^{18}F-FDG PET for the study of the inflammatory activity of atherosclerotic lesions in aortas and in carotid, iliac and femoral arteries of patients. These studies showed excellent short term reliability of this technique, thus indicating its possible role as a surrogate marker of plaque inflammation in multicenter longitudinal trials[15,22]. Recent studies have shown that both black blood DCE-MRI non model-based derived parameters and ^{18}F-FDG standard uptake value (SUV) correlate positively with the degree of plaque neovascularization in the aorta of NZW atherosclerotic rabbits[16]. These studies suggest that DCE-MRI could also be used as a surrogate marker of plaque inflammation, while complementing or possibly even substituting the role of ^{18}F-FDG PET in the evaluation of plaque metabolic activity, without delivering ionizing radiation to imaging subjects. However, in order for this technique to become a valuable tool in the clinic its inter-scan, intra-observer and inter-observer variability need to be investigated. In the present study we investigated the short term reproducibility of DCE-MRI for imaging of the abdominal aorta of atherosclerotic rabbits. We showed excellent inter-scan reliability of the parameter AUC (**Tables 1,2** and **Figure 6**) for the investigation of atherosclerosis in the abdominal aorta of NZW atherosclerotic rabbits. In addition, inter and intra-observer variability was tested and also showed excellent agreement (**Table 1; Figure 7**). Table 2 provides the average AUCs for scan 1 and scan 2 and their average difference together with their standard deviations (in brackets). From these values it is possible to estimate the test-retest CoV, which shows a variability of respectively 17% for AUC 1 minute, 16% for AUC 2 minutes and 11% for AUC 7 minutes, comparable to other DCE-MRI studies. By relying on this information, a priori power analysis was also performed, in order to estimate the subject numbers that would be needed in drug trials to observe an effect of a desired magnitude. **Figure 8** shows an example of sample size calculation required to detect different changes induced by a hypothetical

drug, based on the data provided in **Table 2** for AUC 7 min. While these estimates do not take into account inter subject variability in the response to a given treatment or subjects drop-off from clinical studies, they do provide guidelines for the minimum sample size required while planning drug trials in animals in pre-clinical settings. One of the limitations of the present study is that DCE-MRI was performed only on one selected axial slice and therefore, the presented results rely on matching of chosen slices between the two imaging sessions. However, since DCE-MRI of the vessel wall imposes very high constraints in terms of in-plane spatial and time resolution, it usually allows only for limited slice coverage for every frame acquired. Therefore, visual matching between scans performed, for example, in longitudinal studies will most likely be always needed and the accuracy of this process will affect experimental results. In this study, we aimed to test the reproducibility of the "worst case scenario", in which, in order to maximize spatial and time resolution, slice coverage was sacrificed to only one axial slice. In addition, we aimed to test the reproducibility of a previously used protocol[16] which has been proven effective in correlating AUC from black blood DCE-MRI with neovessels count by histology. Despite the study limitations, our results show that this experimental setup could potentially be used in pre-clinical drug trials to evaluate experimental drug efficacy by MRI. These results are encouraging and suggest that, if DCE-MRI is proven to be equally reproducible in clinical settings, there is a potential role for this technique in the future clinical practice for the evaluation of high-risk patients and as a surrogate imaging marker in clinical drug trials. This technique could be used to non-invasively investigate metabolic activity of atherosclerotic plaques to assess the risk associated with atherosclerotic lesions, monitor disease progression and metabolic changes after treatment with conventional lipid-lowering or anti-inflammatory drugs.

In conclusion, DCE-MRI has been shown to correlate to plaque inflammation in atherosclerotic rabbits and has the potential to be useful for monitoring the response to drug therapy in pre-clinical studies. In order for DCE-MRI to be a good therapy read-out, this technique has to be sufficiently reproducible. This study investigates the inter-scan, intra and inter-observer reliability of DCE- MRI in the abdominal aorta of atherosclerotic NZW rabbits. Experimental results show excellent inter-scan, intra and inter-observer agreement (Table 1 and 2), suggesting that DCE-MRI could be used in pre-clinical settings as a read-out for novel anti-inflammatory therapies. In addition, this preliminary work encourages investigating the reproducibility and the application of this

technique also in clinical settings, where it could be used for monitoring high-risk patients and in longitudinal clinical drug trials.
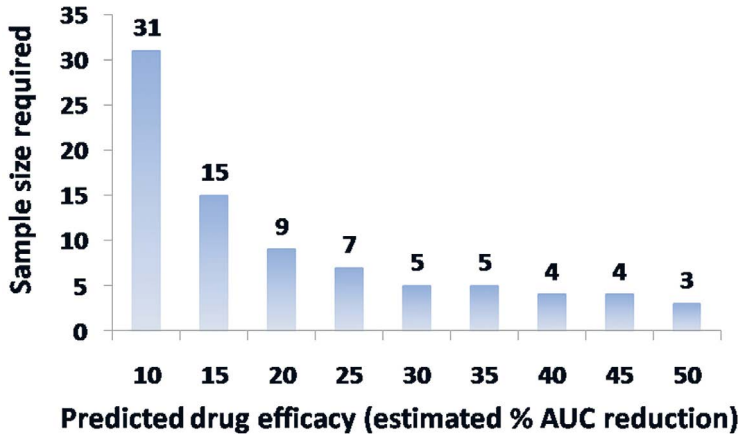

Figure 8. *A priori power analysis.*A priori power analysis for sample size calculation. The plot shows the minimum number of required subjects in a trials using dynamic contrast enhanced (DCE) MRI to detect changes in atherosclerotic plaques metabolic activity as a function of the estimated level of drug effect.

REFERENCES

1. Fauci, A.S., et al.17. Chapter 218. New York: McGraw Hill; 2008. *Harrison's principles of internal medicine.*
2. Lopez, A.D., et al. *Lancet* 367,1747–1757 (2006).
3. Hurks, R., et al. *Thromb. Haemost.*101, 48–54 (2009).
4. Davies, M.J., et al. *Br. Heart J.* 69, 377–381 (1993).
5. Moreno, P.R., et al. *Circulation* 90, 775–778 (1994).
6. Kerwin, W.S., et al. *Circulation* 107, 851–856 (2003).
7. Kerwin, W.S., et al. *Radiology.* 241, 459–468 (2006).

8.   Kerwin, W.S., et al. *Magn. Reson. Med*. 59, 507–514 (2008).

9.   Rudd, J.H., et al. *Trends. Cardiovasc. Med.* 15, 17–24 (2005).

10.   Rudd, J.H., et al. *Circulation* 105, 2708–2711 (2002).

11.   Davies, J.R., et al. *J. Nucl. Med*. 45, 1898–1907 (2004).

12.   Davies, J.R., et al. *J. Am. Coll. Cardiol.* 47(8 Suppl), C57–68 (2006).

13.   Zhang, Z., et al. *BMC Nucl. Med.* 6, 3 (2006).

14.   Ogawa, M., et al. *J. Nucl. Med.* 47,1845–1850 (2006).

15.   Rudd, J.H., et al. *J. Nucl. Med.* 49, 871–878 (2008).

16.   Calcagno, C., et al. *Arterioscler. Thromb. Vasc. Biol*. 1311–1317 (2008).

17.   Galbraith, S.M., et al. *NMR Biomed.* 15, 132–142 (2002).

18.   Padhani, A.R., et al. *NMR Biomed*. 15, 143–153 (2002).

19.   Jackson, A., et al. *Br. J. Radiol.* 76, 153–162 (2003).

20.   Roberts, C., et al. *J. Magn. Reson. Imaging.* 23, 554–563. (2006).

21.   Yankeelov, T.E., et al. *J. Magn. Reson. Imaging* 24, 1140–1147 (2006).

22.   Rudd, J.H., et al. *J. Am. Coll. Cardiol.* 50, 892–896 (2006).

23.   Eliasziw, M., et al. *Phys. Ther.* 74, 777–788 (1994).

24.   Saam, T., et al. *J. Magn. Reson. Imaging* 26, 344–352 (2006).

25.   El Aidi, H., et al. *Nat. Clin. Pract. Cardiovasc. Med.* 6, 219–228 (2009).

Chapter 8

Pioglitazone modulates vascular inflammation in atherosclerotic rabbits noninvasive assessment with FDG-PET-CT and dynamic contrast-enhanced MR imaging

Based on

Author contribution: Esad Vucic: designed and performed the experiments, analyzed data and wrote the manuscript.

ABSTRACT

Objectives
We sought to determine the anti-atherosclerotic properties of pioglitazone using multi-modality non-invasive imaging techniques.

Background
Inflammation is an essential component of vulnerable or high risk atheromas. Pioglitazone, a peroxisome proliferator–activated receptor-gamma (PPAR-γ)-agonist possesses potent anti-inflammatory properties. We aimed to non-invasively to quantify the anti-inflammatory effects of pioglitazone on atheroma using ^{18}F-fluorodeoxyglucose (^{18}F-FDG)-PET/CT and dynamic contrast enhanced MRI (DCE-MRI).

Methods
Atherosclerotic plaques were induced in the aorta of fifteen New Zealand White (NZW) rabbits by a combination of hyperlipidemic diet and two balloon endothelial denudations. Nine rabbits continued the same diet whereas six received pioglitazone (10mg/kg orally) in addition to the diet. Twelve animals underwent ^{18}F-FDG-PET/CT and fifteen animals underwent DCE-MRI at baseline, one and three months after treatment initiation. Concomitantly, serum metabolic parameters were monitored. After imaging was completed aortic histological analysis and correlation analysis was performed.

Results
^{18}F-FDG-PET/CT detected an increase in average standardized uptake value (SUV) in the control group ($p < 0.01$), indicating progressive inflammation, while stable SUV values were observed in the treatment group, indicating no progression. DCE-MRI detected a significant decrease in area under the curve (AUC) for the pioglitazone group ($p < 0.01$). Immunohistology of the aortas demonstrated a significant decrease in macrophage and oxidized phospholipid immunoreactivity in the pioglitazone group ($p = 0.04$ and $p = 0.01$, respectively) with respect to control animals, underlining the imaging results. Serum metabolic parameters showed no difference between groups. A strong positive correlation between SUV and macrophage density and AUC and neovessels was detected ($r^2 = 0.86$, $p < 0.0001$ and $r^2 = 0.66$, $p = 0.004$, respectively).

Conclusions

^{18}F-FDG-PET/CT and DCE-MRI demonstrate non-invasively the anti-inflammatory effects of pioglitazone on atheroma. Both imaging modalities appear suited to monitor inflammation in atherosclerosis.

INTRODUCTION

Cardiovascular disease (CVD) remains the major cause of morbidity and mortality worldwide[1] despite the widespread use of low density lipoproteins cholesterol (LDL-C) lowering therapies. Inflammation, mainly promoted by oxidized lipids in the vessel wall, plays a critical role in all stages of atherosclerosis, but is crucial in plaque rupture and thrombosis which causes the majority of acute coronary events[2,3]. "Vulnerable plaques" are characterized by a relatively large lipid core, thin fibrous cap and an abundance of inflammatory cells (especially macrophages) accompanied by neo-vascularization[4]. Currently, therapies targeting reversal cholesterol transport and inflammation, in particular recombinant HDL therapeutics and various nuclear receptor agonists, are being developed[5]. However, their translation into clinical practice has been difficult because of the lack of clinical outcome studies and validated surrogate endpoints[6].

The peroxisome proliferator–activated receptor gamma (PPAR-γ) belongs to a nuclear receptor superfamily of ligand-dependent transcription factors. Different cells involved in the pathogenesis of atherosclerosis, such as endothelial cells, smooth muscle cells, T-lymphocytes, dendritic cells and mainly macrophages express PPAR-γ-receptor[7,8]. Synthetic PPAR-γ-receptor ligands, thiazolidinediones (TZD), are used in clinical practice as oral antidiabetic agents. Besides their antidiabetic properties TZD have demonstrated in animal studies potent anti-atherosclerotic effects, by inhibiting the formation of atherosclerotic plaques[9,10]. However, some TZDs may increase the risk of myocardial infarction[11]. Pioglitazone, in contrast, in the large clinical secondary prevention trial PROactive (over 5000 subjects) demonstrated a significant reduction of all cause mortality, myocardial infarction and stroke in a diabetic patient population[12]. Two subsequent large trials (CHICAGO and PERISCOPE) showed decreased progression of carotid intima-media thickness (as assessed by surface and intra-vascular ultrasounds) after 18 months of treatment with pioglitazone. These two studies confirmed the significant vascular benefits of pioglitazone and highlighted the potential role of imaging in tracking the progression of disease or its regression upon therapeutic intervention. However, the imaging

techniques used in these studies do not give any information regarding changes in vascular inflammation induced by pioglitazone, which could help indentifying responsive patients much before anatomical changes become apparent. Non-invasive imaging techniques targeted towards quantifying inflammation, macrophage content and neovascularization of atherosclerotic vessels represent an attractive clinical tool. In an ideal scenario such techniques would allow accurate readout of vessel wall inflammation, delineating cardiovascular risk, guiding therapeutic decisions and defining the role of novel treatments and may therefore aid in risk stratification and provide surrogate therapeutic endpoints[13]. Recently, a study in mice showed that non-invasive optical molecular imaging techniques can detect changes in inflammation upon pioglitazone treatment[14]. However, the techniques used in these studies cannot be applied in a clinical setting because of the limited depth penetration possible with optical imaging. ^{18}F-FDG/PET and DCE-MRI are non-invasive clinically available techniques and have recently been validated as read-outs of vascular inflammation. ^{18}F-FDG/PET detected vascular macrophage content and DCE MRI neovascularization[15-18]. In this study we applied ^{18}F-FDG-PET/CT and DCE-MRI to characterize vascular inflammation and neovascularization and its changes during pioglitazone treatment in a rabbit model of atherosclerosis.

MATERIAL AND METHODS

Animal Model
Fifteen New Zealand White rabbits (NZW; Charles River Laboratories) at the age of 3 months (weight of 3.0 kg +/-0.1 kg) were fed a diet containing 0.3% cholesterol and 4.7% coconut oil for 3 months and 0.15% and 4.7% coconut oil thereafter. The development of atherosclerosis was further enhanced with a double balloon injury to the abdominal aorta at weeks 2 and 6 (19). At 4 months animals were divided into two groups (control, n = 9 and treatment n = 6). The treatment group received pioglitazone (10mg/kg bodyweight) mixed with the high fat diet for 3 months (**Figure 1**)[20]. Three age matched animals on chow diet served as non-atherosclerotic controls. Diets were prepared by Research Diet Inc. All procedures were performed under anesthesia by intramuscular injection of ketamine (20mg/kg; Ft Dodge Animal Health) and xylazine (5 mg/kg; Bayer). The protocol was approved by the Mount Sinai School of Medicine Institute Animal Care and Use Committee.

Serum Analysis and fast protein liquid chromatography (FPLC)

Blood was collected from 12 hour fasting animals at baseline, 4-, 5- and 7 months after high cholesterol diet and separated into serum per standard protocols[21]. Serum samples were analyzed immediately using commercial kits for cholesterol, triglycerides, glucose (Wako Chemicals) and insulin (Millipore). In addition, 200 µl of pooled serum at baseline and after 3 months of pioglitazone treatment was subjected to fast protein liquid chromatography to assess the cholesterol concentrations within lipoprotein subfractions. Serum was filtered through a membrane filter (0.22 um pore size) and injected onto two Superose-6 FPLC columns in series (FPLC system; Pharmacia Biotech). Columns were pre-equilibrated with buffer (0.15 M NaCl, 1 mM EDTA, pH 7.5). The flow rate was 0.3 ml/min, and 0.5 ml fractions were collected. Fractions were then assayed for cholesterol as described above.

Immunohistology

Macrophages were detected on adjacent slices by standard immunohistochemistry techniques. The total macrophage-rich (RAM-11-positive) area was quantified digitally as fraction of the media-intimal area (= macrophage density) per slice and expressed as average macrophage density per animal. Similarly, the areas for smooth muscle actin, apolipoprotein B-100 and oxidized phospholipids were evaluated. Neovessels were detected on a single, DCE image matched section with an anti-CD31 antibody as previously described[17].

After the last PET- and MRI imaging, rabbits were euthanized by an intravenous injection of sodium pentobarbital (120 mg/kg) (Sleepaway; Fort Dodge Animal Health). Abdominal aortas were excised and sectioned to match the PET imaged slices and immediately embedded in TissueTek® and placed on dry ice. Matching was achieved by excising the abdominal aorta between anatomical imaging landmarks (left renal artery and iliac bifurcation). After excision the aortic tissue was divided into the equal sized tissue parts matching the in vivo imaging slices. Individual slices (5 µm thick) were sectioned from blocks matched to the PET/CT axial slices. Macrophages were detected on adjacent slices by standard immunohistochemistry techniques using a monoclonal mouse antibody (mmAB; RAM-11,1:200; Dako). The total macrophage-rich (RAM-11-positive) area was quantified digitally as a fraction of the intimal area (= macrophage density) using a semi-automated analysis function of the ImageJ software (NIH) and then expressed as average macrophage density per each animal. Similarly, smooth muscle actin area (mmAB; 1A4,1:100; Dako), apolipoprotein B area (mmAB; MB47, 1:500) and

oxidized phospholipid area (mmAB; E06, 1:500) were evaluated[22]. Neovessels were stained with an mmAB anti-CD31 antibody (1:100, Dako)[17]. Primary antibodies were detected by peroxidase coupled secondary anti-mouse antibodies and a peroxidase detection reagent (IMMpress and NovaRED, respectively; Vector Laboratories). Secondary antibodies alone served as controls and did not lead to significant staining.

^{18}F-FDG-PET/CT

Six rabbits from each group were imaged using a combined PET/CT scanner (Discovery LS; GE Healthcare). PET images were acquired for 10 min, 3 h after intravenous injection of ^{18}F-FDG (37 MBq [1 mCi/kg])[19]. The images were acquired in 3-dimensional mode and the acquisition covered the area from the diaphragm to the iliac bifurcation. A Fourier iterative reconstruction of the PET data was used. In addition to a PET scan, a non–contrast-enhanced CT scan was obtained for each rabbit on the same scanner for attenuation correction and anatomical localization of the PET signal. The final reconstructed slice thickness was 4.25mm.

PET/CT Analysis

PET/CT data were displayed in 3 orthogonal planes on a GE Xeleris workstation. Maximal and mean SUVs were recorded on contiguous axial slices of the aorta between the left renal artery and the iliac bifurcation (average number of slices, 13.6) from ROIs encompassing the vessel wall. Results were expressed as the average SUV of the aorta per animal. All PET measurements were performed by an independent operator unaware of the results of MRI and immunohistology.

Anatomical and Dynamic Contrast-Enhanced MRI

Nine control rabbits and six pioglitazone treated rabbits were imaged under anesthesia using a 1.5 Tesla MRI system (Siemens Sonata, Siemens Medical Solutions) and a conventional knee coil. Sequential axial, 3-mm thick, images of the aorta were obtained from the left renal artery to the iliac bifurcation using T1-, T2- and PD- (proton density) weighted imaging sequences (slice thickness = 3 mm, TE 5.6/39/5.6 ms, TR 800/2000/2000 ms, inter-slice gap 0.6 mm, field of view 12x12 cm, matrix size 256x256, echo train length 7, and signal averages, 16/6/6). For all different sequences inferior and superior radiofrequency saturation pulses were added to null the signal from flowing blood in the inferior vena cava and aorta together with spectral fat suppression, to null the signal from the periadventitial fat.
DCE-MRI was performed on one selected axial slice using a black blood turbo

spin echo (TSE) sequence previously validated against histology[17] (slice thickness = 3 mm, TE = 5.6 ms, TR = 250 ms, field of view 12x12 cm, matrix size 256x256, with an in-plane resolution of 500x500 µm, suitable for imaging of the rabbit aorta). A total of 100 images per rabbit were acquired, with a time resolution of 4.8 s. After the acquisition of the 5th image, 0.2 mmol/kg of Gd-DTPA (Magnevist) was injected at a rate of 0.5 ml/s followed by a 10 ml saline flush, through a marginal ear vein. After the DCE-MRI scan, a T1-weighted post-contrast MR image of the same axial slice selected for DCE-MRI was acquired (slice thickness, 3 mm, TE, 5.6 ms, TR, 250 ms, field of view, 12x12 cm, matrix size, 256x256, echo train length, 15, signal averages, 16). This image was acquired with the same exact imaging parameters used for the DCE acquisition, except for the number of averages (16 instead of one), in order to clearly delineate the atherosclerotic vessel wall. One and three months after baseline scans all animals were imaged with exactly the same protocol. DCE-MRI was performed on an axial slice matching the one chosen for baseline imaging. Slice matching between the two imaging sessions was achieved by using anatomical fiducial markers such as the iliac bifurcation, the vertebral column and the renal arteries.

Anatomical multi-contrast (MC)-MRI and DCE-MRI Analysis

Average vessel wall area of the aorta between the left renal artery and iliac bifurcation was quantified on contiguous slices by manual tracing on T2 weighted images (VesselMass software, Leiden University Medical Center). DCE-MRI quantified the change of signal intensity in a ROI including the entire atherosclerotic plaque during the injection of the contrast agent with a custom made Matlab (The MathWorks) program. The area under the signal intensity versus time curve (AUC) was quantified at 1 and 2 minutes after injection of contrast agent by numerical integration[17].

Statistical Analysis

Numeric values are expressed as mean ± SD. $P < 0.05$ was considered significant. Continuous DCE and PET outcomes were modeled as linear functions of time for both treatment and control groups. A linear mixed model with random intercepts and compound symmetric covariance structure was used to estimate the regression equations for treatment and control groups while accounting for the correlation between repeated measurements made on each rabbit[23]. The models for PET outcomes were weighted by the number of slices analyzed in each animal. To test for differences among the treatment and control groups estimated by linear regression equations, an interaction term between treatment group and time was included in each

mixed model along with both main effects. If the interaction term was found to be statistically significant then pair-wise comparisons of treatment group slopes were estimated. All statistical analyses were performed using Proc Mixed in SAS Version 9.2. Average macrophage density per animal was correlated with average animal SUV max or AUC 1min of the corresponding animal. Neovessels were counted on a single section, matched to the DCE-MRI imaged slice, and were correlated with AUC_{1min} or average SUV max of the corresponding animal. AUC_{1min} and average SUV max from corresponding animals were correlated. All correlations were measured using Pearson testing after normality of the data was established. All histological data, animal characteristics data and non-linear regression imaging data were analyzed with a 2-tailed Student-t-test.

Power Analysis
Retrospective power was computed using SAS's Proc Mixed as previously described[24]. A separate exemplary dataset was created for each outcome by making N_i (the sample size in Group i where i is either control or treatment group) copies of the predicted mean measures (estimated from our mixed models presented herein) within each group at each time point. The same model in Proc Mixed was specified and run on the exemplary dataset after specifying the variance/covariance parameters estimated from our mixed models on the original data. The F-statistic for each outcome was saved from the table of Type 3 tests and an approximate non-centrality parameter (F-value x Numerator degrees of freedom) was computed along with a critical F-value by entering a specified alpha of 0.05 and the numerator and denominator degrees of freedom into the FINV function. Finally, the power was computed using critical F-value, non-centrality parameter, numerator and denominator degrees of freedom as inputs to the PROBF function.

RESULTS

Study design, animal characteristics and serum analysis
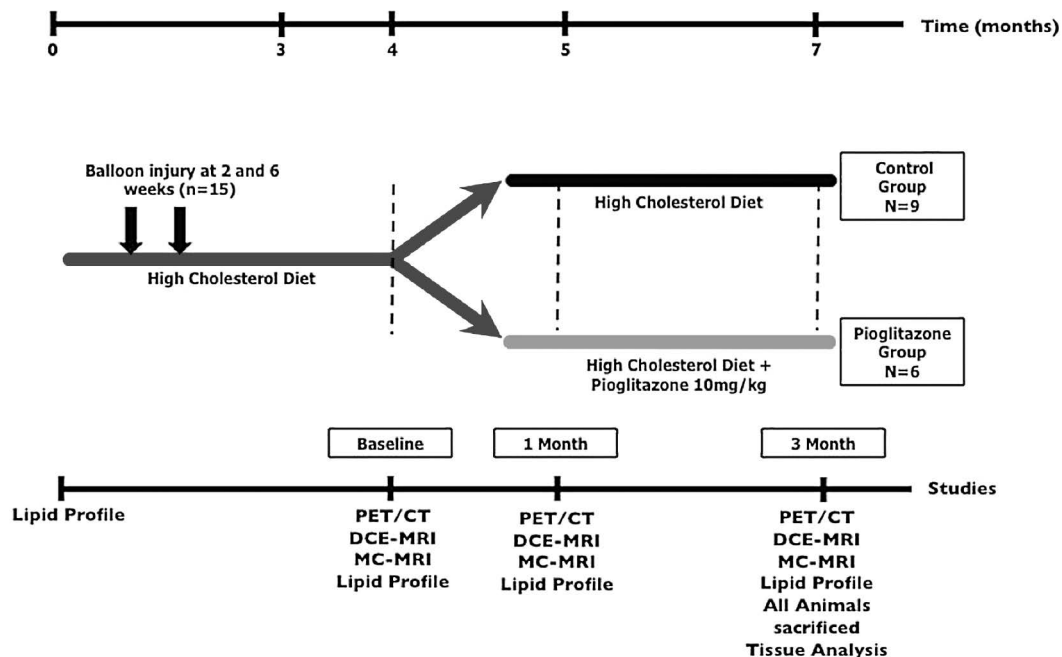The study design is depicted in **Figure 1**.

Figure 1. Study Design.Atherosclerosis was induced in 15 New Zealand White Rabbits through a combination of double balloon injury and high cholesterol diet. After 4 months diet first imaging scans and lipid profiles were performed (baseline) and animals were divided into two groups: control group and pioglitazone group. After a total of 5 months another round of imaging scans and lipid profiles (1 month imaging) were performed. The final imaging scans and lipid profiles were performed after a total of 7 months (3 month imaging). All animals were then immediately sacrificed and tissue analysis was performed.

After 4 months of high cholesterol diet significantly elevated total cholesterol levels were observed (**Table 1**). There were no significant baseline differences in total cholesterol between the control and pioglitazone treated groups prior to treatment initiation (**Table 1**). There were no statistically significant differences in fasting serum glucose or insulin levels and in non-fasting triglycerides in either group throughout the study. Both groups had nearly identical weights throughout the study (**Table 1**). FPLC at baseline and after 3-months revealed no significant difference in lipoprotein profiles after pioglitazone treatment (**Figure 2**).

Imaging Strategies for the Detection of Inflammation in Atherosclerosis

	control (n = 9)	PIO (n = 6)	p-value
weight (kg)			
t = 4 months	3.42 +/- 0.29	3.32 +/- 0.33	0.52
t = 5 months	3.47 +/- 0.31	3.29 +/- 0.40	0.32
t = 7 months	3.42 +/- 0.38	3.40 +/- 0.28	0.90
	control (n = 5)	PIO (n = 5)	
total Cholesterol (mg/dl)			
t = 4 months	1099 +/- 291	1220 +/- 197	0.35
t = 5 months	1158 +/- 282	1143 +/- 126	0.91
t = 7 months	1154 +/- 230	1278 +/- 159	0.27
triglycerides (mg/dl)*			
t = 4 months	147 +/- 126	165 +/- 168	0.87
t = 5 months	113 +/- 95	102 +/- 65	0.84
t = 7 months	172 +/- 163	105 +/- 17	0.52
glucose (mg/dl)			
t = 4 months	152 +/- 31	132 +/- 25	0.29
t = 5 months	178 +/- 40	156 +/- 43	0.32
t = 7 months	180 +/- 47	170 +/- 47	0.67
insulin (ng/dl)			
t = 4 months	0.52 +/- 0.37	0.49 +/- 0.45	0.91
t = 5 months	0.44 +/- 0.39	0.32 +/- 0.05	0.53
t = 7 months	0.23 +/- 0.13	0.21 +/- 0.06	0.79

Table 1. Animal Characteristics
Data for weight and fasting values for: total cholesterol, triglycerides*, glucose and insulin are presented for the control and pioglitazone (PIO) group in separate columns. P-values between the control and PIO group were determined with a student t-test and are shown on a separate column. Individual data except p-values are represented as means ± standard deviation. *= nonfasting.
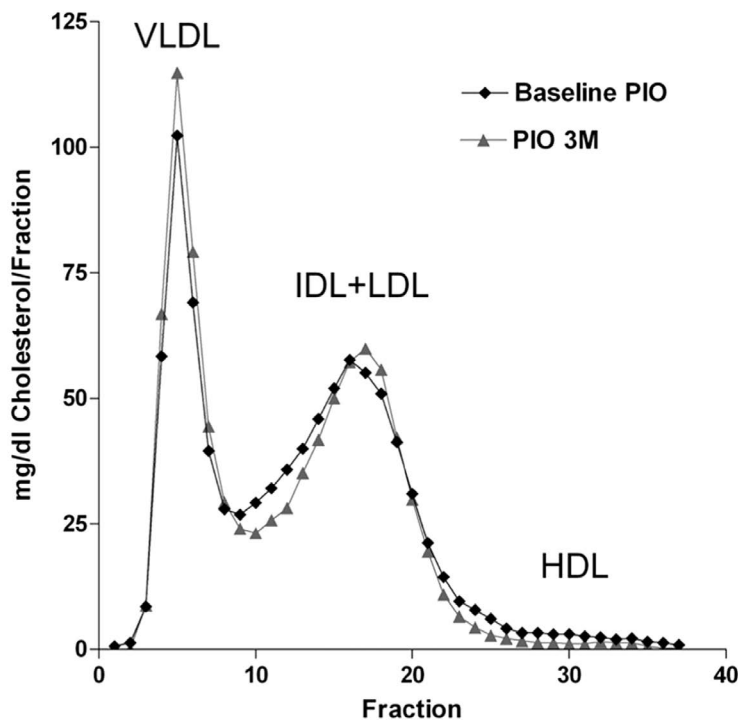
Figure 2. Size distribution of lipoprotein fractions in New Zealand White rabbits fed a high cholesterol diet and treated with pioglitazone at baseline (Baseline PIO; diamonds) and for three months (PIO 3M; triangles). Serum was pooled from five animals per group and fractionated with FPLC.

SUV correlates with tissue macrophage content and AUC correlates with neovascularization

We correlated the SUV $\overline{max}$ and AUC_{1min} respectively against macrophage density and neovessel counts and found a strong positive correlation (r^2 = 0.86, p < 0.0001 and r^2 = 0.66, p = 0.004, respectively; **Figure 3AB**) consistent with previous studies[17,24]. No strong correlation was found between SUV $\overline{max}$ and neovessel count and between AUC_{1min} and macrophage density (r^2 = 0.09, p = 0.37 and r^2 = 0.19, p = 0.18, respectively; **Figure 3CD)**. SUV $\overline{max}$ and AUC_{1min} did not strongly correlate (r^2 = 0.17, p = 0.18; **Figure 3E**).
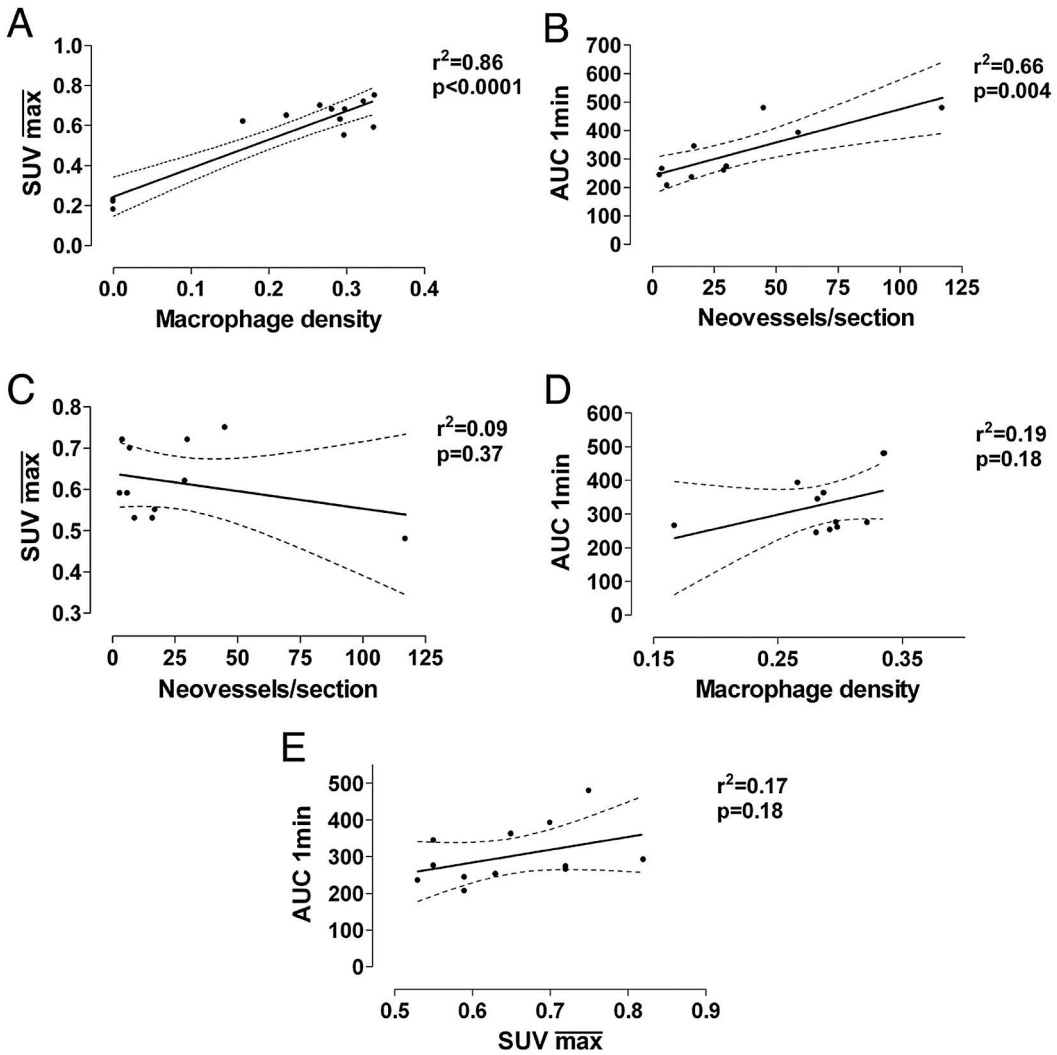
Figure 3. Regression Analysis. (**A**) Correlation between $\overline{max}$ standard uptake value (SUV $\overline{max}$) generated from FDG-PET/CT imaging and macrophage density (stained area/intimal area) from histological staining. (**B**) Correlation between mean AUC_{1min} generated from DCE-MRI imaging and neovessel count per histological section. (**C**) Correlation between mean standard uptake value (SUV) and neovessel count per histological section. (**D**) Correlation between mean AUC_{1min} generated from DCE-MRI imaging and macrophage density. (**E**) Correlation between mean standard uptake value (SUV) and mean AUC_{1min}. Black line, regression line; dashed line, 95% confidence interval.

Pioglitazone arrests inflammation progression as assessed by ^{18}F-FDG-PET/CT

Upon completion of baseline imaging, animals were divided into matched groups, one control group and one treatment group, with both groups

displaying similar baseline SUV $\overline{max}$ (0.64 ± 0.05 and 0.62 ± 0.12, p = 0.70; **Figure 4A** and **4C** and **bar graph**). The SUV versus time slope for the control group is positive, therefore indicating an increase of SUV $\overline{max}$ (p = 0.10) and $\overline{mean}$ (p = 0.02) over time. On the contrary the SUV versus time slope for the treatment group was not statistically different from zero (SUV $\overline{max}$, p = 0.70; SUV $\overline{mean}$, p = 0.92), indicating no significant progression in plaque inflammation. Comparison of the two slopes indicated a trend towards significance (SUV $\overline{max}$, p = 0.15; SUV $\overline{mean}$, p = 0.1). Comparison of SUV values between the two groups at 1 and 3 months showed significant differences (p < 0.05) for both SUV $\overline{max}$ and $\overline{mean}$. Non-atherosclerotic aged matched animals on chow diet show minimal SUV values.
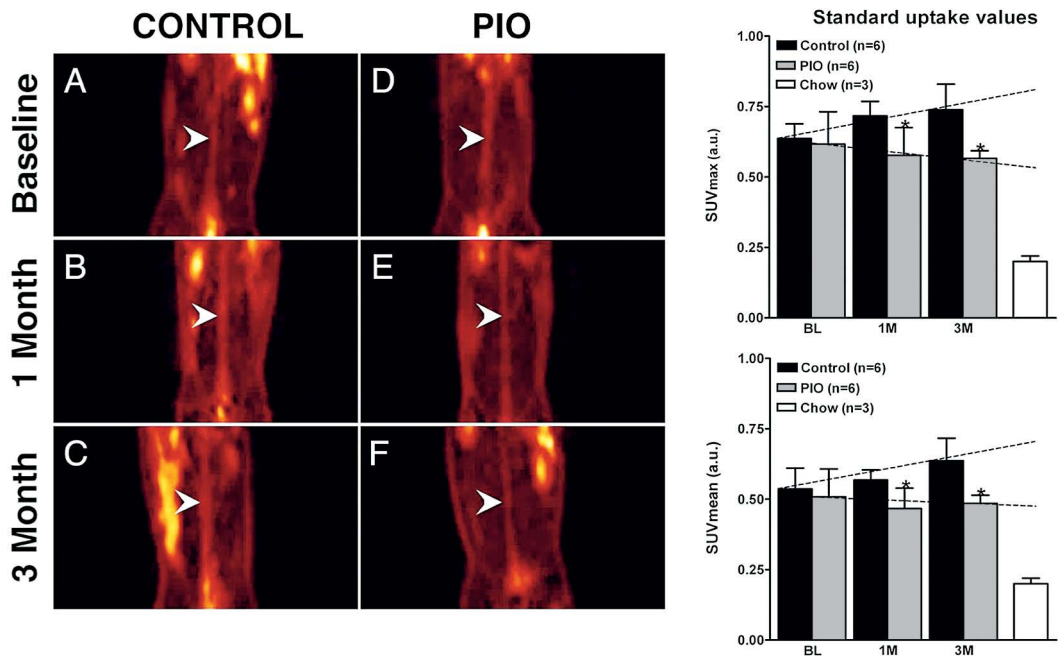

Figure 4. FDG-PET/CT. Left hand, (**A-F**), coronal PET images through the abdominal aorta (white arrow-heads) from one representative animal per group. (**A**) and (**D**), baseline control- and baseline pioglitazone (PIO) group. (**B**) and (**E**), 1-month control and 1-month PIO group. (**C**) and (**F**), 3-month control and PIO group. On the right hand side two bar graphs summarize the changes in SUVmax (top) and SUVmean (bottom) at baseline (BL), one month (1M) and three months (3M) for both groups. Right hand bar shows values for non-atherosclerotic chow fed animals. Values are represented as mean ± standard deviation. *p < 0.05 when comparing control and PIO group. Schematic slopes are indicated as dashed lines.

Pioglitazone decreases neovascularization as assessed by DCE-MRI

In analogy to the ^{18}F-FDG-PET/CT experiments, we applied DCE-MRI to assess inflammation and neovascularization in atherosclerotic plaques (**Figure 5**). The AUC versus time slope for the control group was not statistically different from zero for AUC measures (AUC_{1min}, p = 0.33; $AUC_{2\,min}$, p = 0.18). The AUC versus time slope for the treatment group was negative and significantly different from zero for all AUC measures (p < 0.01). A trend towards significance was found when comparing the control and treatment groups slopes (AUC_{1min}, p = 0.06; AUC_{2min}, p = 0.09). There was a significant difference between baseline and 3 month AUC values in the treatment group (AUC_{1min}, p = 0.01).
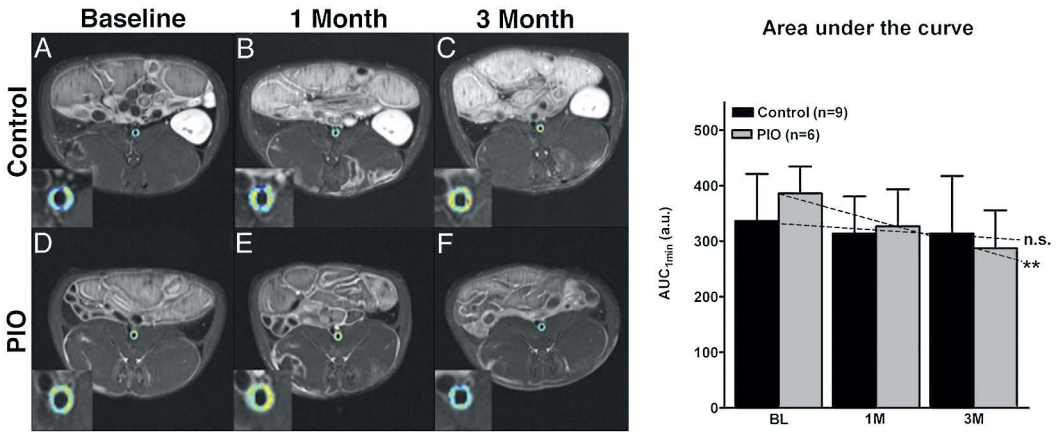

Figure 5. Dynamic-contrast-enhanced MRI. Left hand side, (**A-F**) show single slice axial T1 weighted MRI images with color encoded overlay of the contrast signal at one minute of the abdominal aorta with insert of the aorta. (**A**) and (**D**), baseline control and baseline pioglitazone (PIO) group. (**B**) and (**E**), 1-month control and PIO group (**C**) and (**F**), 3-month control- and pioglitazone group. Warm colors (orange to red) indicate higher AUC values and cold colors (green to blue) indicate lower AUC values. On the right hand side a bar graph summarizes the changes in the AUC at baseline (BL), one month (1M) and after three month (3M) for the control and PIO group. Values are represented as mean ± standard deviation. *p < 0.05 when comparing baseline and 3M in the PIO group. Schematic slopes are indicated as dashed lines; n.s.=non-significant and **p = 0.01 when comparing individual slopes against zero.

Pioglitazone has no effect on vessel wall area as assessed by MC-MRI

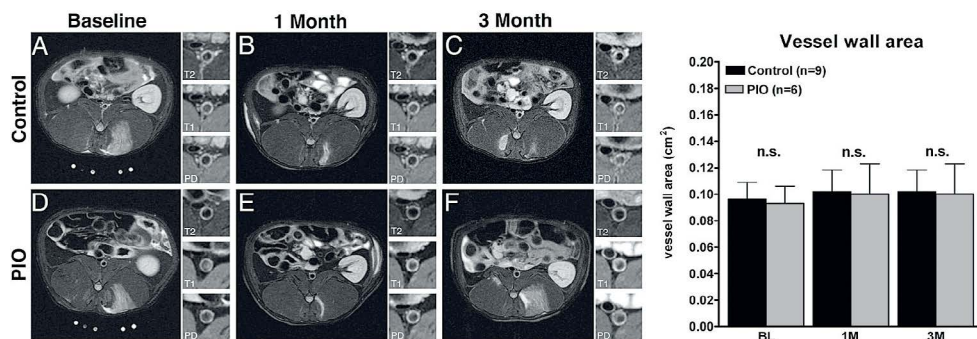Multi-contrast MRI showed no significant changes in aortic wall area in either group (**Figure 6**).

Figure 6. Multi-contrast-MRI. **(A-F)**, single slice axial T2 weighted representative MRI images with insert of the aorta with T2-, T1- and Proton Density (PD)-weighing. (**A**) and (**D**), baseline control and pioglitazone (PIO) group. (**B**) and (**E**), 1-month control and PIO group. (**C**) and (**F**): 3-month control and PIO group. Right hand side a bar graph summarizes the changes in the vessel wall area at baseline (BL), one month (1M)- and three month (3M) of either control or PIO group. Values are represented as mean ± standard deviation, n.s. = non-significant

Pioglitazone decreases plaque macrophages and oxidized phospholipids

Macrophage staining at the end of imaging study revealed a significant decrease in macrophage density within the pioglitazone group compared to control (0.25 ± 0.05 and 0.32 ± 0.02, (a.u.), respectively, P = 0.04; **Figure 7** and **8**). A trend towards lower apolipoprotein B density was detected in the pioglitazone group compared to control (0.28 ± 0.03 and 0.34 ± 0.07 (a.u.), respectively, p = 0.12; **Figure 7** and **8**). Pioglitazone treatment resulted in a 41% reduction in the oxidized phospholipid density compared to control (0.086 ± 0.026 and 0.146 ± 0.045 (a.u.), respectively, p = 0.03; **Figure 7** and **8**). Average smooth muscle actin density was identical between groups (0.24 ± 0.075 and 0.24 ± 0.078 (a.u.), respectively, p = 0.88; **Figure 7** and **8**). A trend towards lower neovessel content was observed in the pioglitazone treated group (p = 0.12; **Figure 7**).
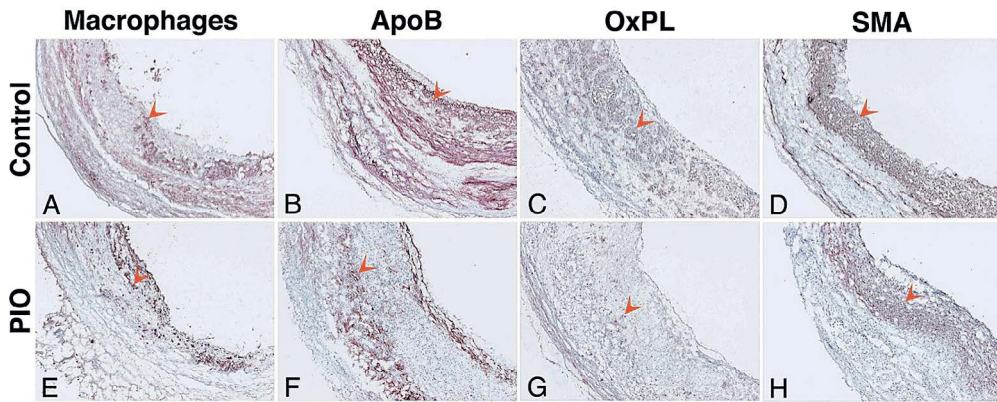
Figure 7. Immunohistology. Representative images of immunohistological staining of the abdominal aorta after 3 months of vehicle- (control; **A-D**) and pioglitazone (PIO) treatment (**E-H**). Staining (red-brown, red arrowheads) for macrophages (Mac; **A** and **E**), apolipoprotein B (ApoB; **B** and **F**), oxidized phospholipids (OxPL; **C** and **G**) and smooth muscle actin (SMA; **D** and **H**) is shown. Objective magnification: 10x. The lumen is on the right hand side from the tissue.
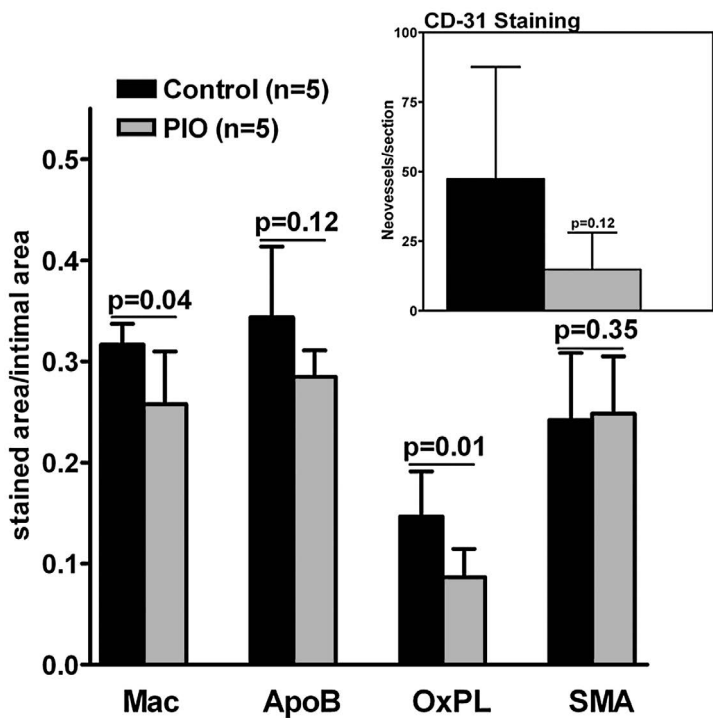

Figure 8. Summary Immunohistology
Macrophages (Mac), apolipoprotein B (ApoB), oxidized phospholipids (OxPL) and smooth muscle actin (SMA) staining at 3 months of vehicle and pioglitazone (PIO) treated animals. Insert shows CD-31 staining for neovessels. Values are represented as means ± standard deviation. Individual p-values between control and PIO group indicated above bar graph.

Power Analysis of ^{18}F–FDG–PET/CT and DCE–MRI

^{18}F-FDG-PET/CT determined SUV $\overline{max}$ values had 30% power to detect a difference between individual group slopes, 43% power to detect a group effect and 15% power to detect a time effect. SUV $\overline{mean}$ values had 40% power to detect a difference between individual group slopes, 37% power to detect a group effect and 45% power to detect a time effect.

DCE-MRI determined $AUC_{1\ min}$ values had 46% power to detect a difference between individual group slopes, 14% power to detect a group effect and 87% power to detect a time effect. $AUC_{2\ min}$ values had 39% power to detect a difference between individual group slopes, 15% power to detect a group effect and 92% power to detect a time effect.

DISCUSSION

In this study we show significant modulation in inflammation in aortic plaques of atherosclerotic rabbits as measured non-invasively by ^{18}F-FDG-PET/CT and DCE-MRI upon treatment with pioglitazone. The imaging results are confirmed by the histological findings, which show a strong correlation of macrophage density and neovessel content with imaging parameters. In addition, this study provides insight to the diagnostic strengths of both FDG-PET and DCE-MRI while tracking anti-atherosclerotic therapeutic intervention.

Previous studies have tested the potential of FDG-PET to track therapeutic intervention. Tahara et al.[26] investigated the effect of simvastatin on plaque inflammation by FDG-PET in the thoracic aorta of human subjects, while Ogawa et al.[27] investigated the effect of probucol on the aortic plaques of Watanabe heritable hyperlipidemic (WHHL) rabbits. In contrast with the work presented here, both these studies showed no significant increase in FDG uptake in the control groups while regression of inflammation was demonstrated by a significant decrease of FDG uptake over time in the treatments groups. This behavior is different from what we reported in our study, where we show progression of inflammation in the control group and no change in FDG uptake over time in the treatment group. However, some significant differences between this study and the ones described before must be noted. For example the dietary differences (dietary restrictions for patients and chow diet for rabbits as opposed to hyperlipidemic diet in this study with or without drug depending on the group) and the different rabbit model used (WHHL versus NZW). The only study in the literature investigating the use of DCE-MRI to track therapeutic intervention in atherosclerosis shows results

comparable to the ones presented here, although the time frame of the two studies is considerably different (48 hours versus 3 months of treatment)[28].

In addition to showing the ability of FDG-PET and DCE-MRI to track therapeutic intervention with pioglitazone, this study sheds light on the possible complementary role in future clinical applications of the two methodologies. For example, FDG-PET shows increase in plaque inflammation in the control group over time, while DCE-MRI measures do not change. Given the established correlation between FDG-PET and DCE-MRI with macrophages and neovessels respectively, this may reflect a difference in the change of these histological variables over time during plaque progression and may provide insight to the natural progression of aortic atherosclerosis in this specific rabbit model. More natural progression studies are needed to clarify this behavior and to plan future pre-clinical drug trials. The difference in FDG-PET and DCE-MRI measures in the treatment groups (impaired progression versus regression) may either reflect the different sensitivity of the techniques or a different impact of pioglitazone on the related histological variables (macrophages and neovessels respectively). In this last case the relationship between the two imaging techniques may be different for every new drug study planned with other therapeutic interventions.

Conclusions

In summary, we demonstrate the effectiveness of the PPARγ-agonist pioglitazone in promoting modulation of vascular inflammation in a rabbit model of atherosclerosis as evaluated by non-invasive imaging techniques and validated by histology. ^{18}F-FDG PET/CT and DCE-MRI were used in this case as surrogate imaging markers of vascular inflammation. Both techniques are already clinically available, which stresses the translational aspect of this study. Dedicated prospective outcome studies are underway which will clarify the role of plaque inflammation imaging in patients' risk stratification[29]. Furthermore, novel anti-atherosclerotic therapies are being developed and their role in clinical practice will need to be established. In this sense, the here described imaging tools may become potent armaments for improved drug development and their translation into clinical practice. Dedicated future clinical studies in non-diabetic patient populations will be needed to evaluate pioglitazone's effect in atherosclerotic disease.

Acknowledgements

REFERENCES

1. Dahlöf, B., *Amer. J. Cardiol.* 2105,3A-9A (2010).
2. Libby, P., et al. *J. Am. Coll. Cardiol.* 54, 2129-2138 (2009).
3. Ross, R., N. *Engl. J. Med*. 340, 115-126 (1999).
4. Fuster, V., et al. *J. Am. Co.l Cardiol*. 46, 937-954 (2005).
5. Natarajan, P., et al. *J. Am. Coll. Cardiol,* 55,1283-1299 (2010).
6. deGoma, E.M., et al. *J. Am. Coll. Cardiol.* 51, 2199-2211 (2008).
7. Marx, N., et al. *J. Immunol.* 164, 6503-6508 (2000).
8. Takata, Y., et al. *Circ. Res.* 91, 427-433 (2002).
9. Collins, A.R., et al. *Arterioscler. Thromb. Vasc. Biol.* 21, 365-371 (2001).
10. Li, A.C., et al. *J. Clin. Invest.* 106, 523-531 (2000).
11. Nissen, S.E., et al. *Arch. Intern. Med.*170, 1191-1201 (2010).
12. Dormandy JA, et al. *Lancet* 366, 1279-1289 (2005).
13. Rudd, J.H., et al. *Arterioscler. Thromb Vasc. Biol.* 29, 1009-1016 (2009).
14. Chang, K., et al. *Arterioscler. Thromb. Vasc. Biol.* 30, 1933-1939 (2010).
15. Tawakol A, et al. *J. Am. Coll. Cardiol.* 48, 1818-24 (2006).
16. Rudd, J.H., et al. *Circulation* 105, 2708-2711 (2002).
17. Calcagno, C., et al. *Arterioscler. Thromb. Vasc. Biol*. 28, 1311-1317 (2008).
18. Rudd, J.H., et al. *Circ. Cardiovasc. Imaging* 2, 107-115 (2009).
19. Hyafil, F., et al. *J. Nucl. Med.* 50, 959-965 (2009).
20. Joner, M., et al. *Arterioscler. Thromb. Vasc. Biol*. 27,182-189 (2007).
21. McVicar, J.P., et al. *PNAS.* 81, 1356-1360 (1984).
22. Torzewski, M., et al. *Arterioscler. Thromb. Vasc.. Biol* 24, 2307-2312 (2004).
23. Littell Ramon, C., et al. *SAS System for Mixed Models*. Cary, NC: SAS Institute Inc., 1996.
24. Stroup, W.W., *Proc. Biopharmaceutical Section. Am. Stat. Assoc*. 15-24, (1999).
25. Tawakol, A., et al. *J. Nucl. Cardiol.* 12, 294-301 (2005).
26. Tahara, N., et al. *J. Am. Coll. Cardiol.* 48, 1825-1831 (2006).
27. Ogawa, M., *J. Nucl. Med.* 247, 1845 (2006).

28. Lobatto, M.E., et al. *Mol. Pharm*. 7, 2020-2029. (2010).
29. Falk, E., et al*. Curr. Atheroscler. Rep*. 13, 359–366 (2011).

Chapter 9

Regression of inflammation in atherosclerosis by the LXR agonist R211945: a noninvasive assessment and comparison with atorvastatin

Based on

Author contribution: Esad Vucic: designed and performed the experiments, analyzed data and wrote the manuscript.

ABSTRACT

Objective
In this study, we aimed to non-invasively detect the anti-inflammatory properties of the novel LXR-agonist R211945.

Background
R211945, an LXR-agonist, induces reversal cholesterol transport and modulates inflammation in atherosclerotic plaques. We aimed to characterize with ^{18}F-fluorodeoxyglucose (^{18}F-FDG)-PET/CT and dynamic contrast-enhanced MRI (DCE-MRI) inflammation and neovascularization, respectively in atherosclerotic plaques upon R211945 treatment in comparison to atorvastatin and controls.

Methods
Twenty-one atherosclerotic New Zealand White (NZW) rabbits (control, R211945 (3 mg/kg orally) and atorvastatin (3mg/kg orally) groups). All groups underwent ^{18}F-FDG-PET/CT and DCE-MRI at baseline, 1 month and 3 months after treatment initiation. Concomitantly, serum metabolic parameters and histology were assessed. For statistical analysis, continuous DCE-MRI and PET/CT outcomes were modeled as linear functions of time by using a linear mixed model whereas the histological data, animal characteristics data and non-linear regression imaging data were analyzed with a 2-tailed Student-t-test.

Results
^{18}F-FDG-PET/CT detected a decrease in mean and maximal standardized uptake value (SUV) over time in the R211945 group (both $p = 0.001$) indicating inflammation regression. The atorvastatin group displayed no significant change ($p = 0.371$ and $p = 0.600$ respectively) indicating no progression or regression. The control group demonstrated an increase in SUV ($p = 0.01$ and $p = 0.04$ respectively) indicating progression. There was a significant interaction between time and group for mean and maximum SUV ($p = 0.0003$ and $p = 0.0016$ respectively). DCE-MRI detected a trend towards difference ($p = 0.06$) in area under the curve (AUC) in the atorvastatin group suggesting a decrease in neovascularization. There was no significant interaction between time and group ($p = 0.6350$ and $p = 0.8011$, respectively). Macrophage and apolipoprotein B immunoreactivity decreased in the R211945 and atorvastatin groups (each: $p < 0.0001$ and $p = 0.0004$,

respectively) and R211945 decreased oxidized phospholipid immunoreactivity (p = 0.02).

Conclusions

Noninvasive imaging with ^{18}F-FDG-PET, DCE-MRI and histological analysis demonstrate significant anti-inflammatory effects of the LXR-agonist R211945 in comparison to atorvastatin. The results suggest a possible role for LXR-agonists for the treatment of atherosclerosis.

INTRODUCTION

Cardiovascular disease (CVD) is the leading cause of mortality worldwide[1]. Atherosclerosis is the primary cause of cardiovascular disease and is caused by the accumulation of oxidized lipids in the arterial wall that triggers the accumulation of inflammatory cells, most prominently macrophages[2,3]. The ongoing recruitment of macrophages leads to the formation of fatty streaks and ultimately to the development of complex atherosclerotic plaques. Inflammation plays a central role at all stages of atherosclerosis and in particular when accompanied by neovascularization, promotes atherosclerotic plaque rupture and thrombosis which causes the majority of acute coronary events[4,5].

Currently, the mainstay for the treatment of atherosclerosis are LDL cholesterol lowering strategies, mainly using statins which reduce the mortality risk by only 30% to 40%[6]. Recently, strategies to further lower risk have been actively explored[7]. High density lipoproteins cholesterol (HDL-C) displays a strong inverse relation to CVD as demonstrated in multiple large epidemiological studies including the Framingham Heart Study[8]. The mechanism by which HDL exerts its protective effects is mainly mediated by reverse cholesterol transport[9], a process by which peripheral tissue cells actively excrete cholesterol and phospholipids through the ATP-binding cassette transporter A1 (ABCA1) leading to the formation of HDL. This process is controlled by ABCA1 and is directly regulated by liver-X-receptors (LXRs)[10]. In animal models of atherosclerosis, LXR-agonists attenuate the development and reverse existing atherosclerotitic plaques[11,12]. First generation LXR-agonists, despite potent anti-atherosclerotic effects, were accompanied by fatty liver accumulation and elevation of plasma triglycerides and LDL. Their translation into clinical practice was, therefore, limited[3]. R211945, an LXR agonist, is a potent inducer of ABCA1 in rodents and cynomolgus monkeys without causing liver and metabolic side effects.

We have demonstrated previously that multimodality molecular imaging using FDG-PET/CT and DCE-MRI have the ability to assess macrophage content/inflammation and neovascularization in atherosclerotic plaques at baseline and after therapeutic intervention[14-16]. In this study, we aimed to assess non-invasively with FDG-PET/CT and DCE-MRI the effects of the treatment with the LXR-agonist-R211945 on macrophage content/inflammation and neovascularization in atherosclerotic plaque in a rabbit model of atherosclerosis and to characterize its effects in comparison to treatment with atorvastatin.

MATERIAL AND METHODS

Animal Model
Atherosclerosis was induced in twenty-one age and weight matched New Zealand White rabbits (NZW; Charles River Laboratories) identically as previously described[14]. After 4 months of high-fat diet, animals were divided into three groups: control (n = 9) and two treatment groups (n = 6/each). Animals in the control groups were kept on high-fat diet only and animals from the treatment groups were administered either R211945 (3 mg/kg bodyweight) or atorvastatin (3 mg/kg bodyweight) mixed with the high fat diet for 3 months (**Figure 1**). Three baseline age matched animals on chow diet served as non-atherosclerotic controls at baseline and underwent PET/CT and macrophage histological staining for correlation between SUV and macrophage density. Diets were prepared by Research Diet Inc. All imaging and surgical procedures were performed under anesthesia by intramuscular injection of ketamine (20 mg/kg; Ft Dodge Animal Health) and xylazine (5 mg/kg; Bayer). The protocol was approved by the Mount Sinai School of Medicine Institute Animal Care and Use Committee.

Blood Analysis
Blood sampling was performed before diet initiation and at 4,5 and 7 months after diet initiation. Animals were fasted for 12 hours prior to blood collection and the obtained serum was analyzed using commercial kits for cholesterol, triglycerides, glucose (Wako Chemicals) and insulin (Millipore). Plasma levels of R211945 and atorvastatin were determined by mass spectrometry (Taylor Technology, Princeton, NJ)
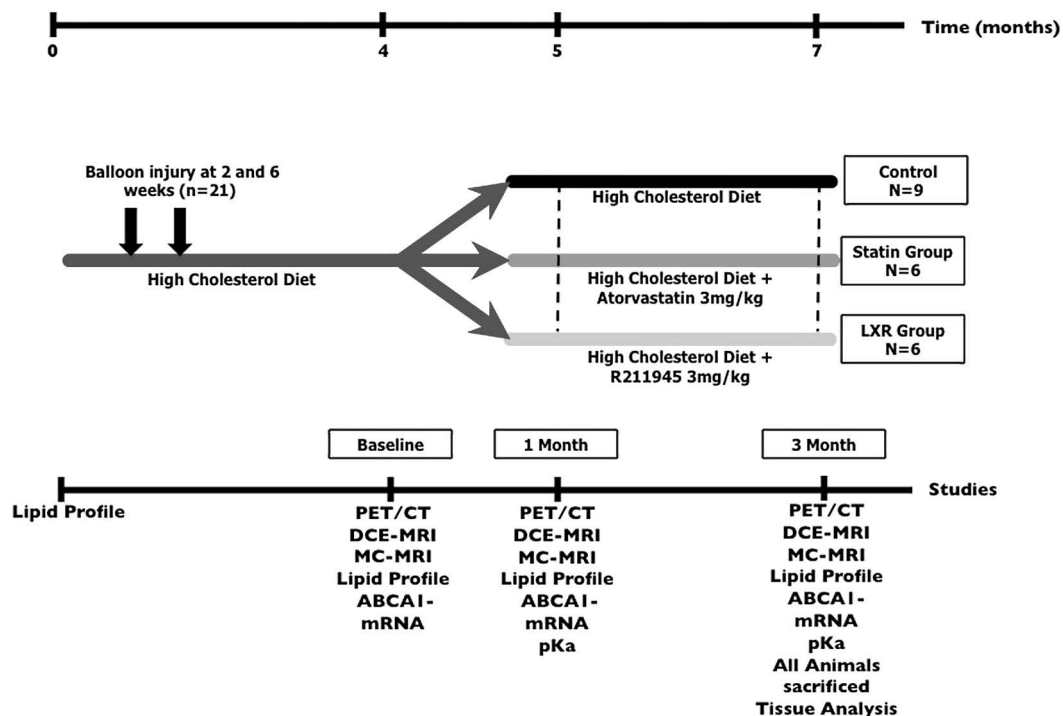
Figure 1. Study Design. Atherosclerotic New Zealand White rabbits at 4 months diet where imaging scans, lipid profiles and RNA analysis were performed (baseline). Animals were then divided into: control, atorvastatin and R211945 group. At 5 months (1 month imaging) and at 7 months (3 month imaging), imaging scans, lipid profiles, RNA analysis and drug pKa determination were performed. After last imaging all animals were immediately sacrificed and tissue analysis was performed.

Immunohistology

Standard immunohistochemistry techniques were used to quantify macrophages and neovessels in the vessel wall. Macrophages-rich areas were identified using RAM-11 staining and expressed as a fraction of the media-intimal area (macrophage density) per slice. The average macrophages density per animal was used in the statistical analysis. Areas of smooth muscle actin, apolipoprotein B-100 and oxidized phospholipids were evaluated in a similar fashion. Neovessels were identified using CD-31 staining as previously described, on the histological sections matching with the imaged DCE slice[15].

18F-FDG-PET/CT

PET images were acquired using a combined PET/CT scanner (Discovery LS; GE Healthcare). After injection of 37 MBq [1 mCi/kg] of FDG, three hours were allowed for the FDG to circulate, to lower ^{18}F-FDG blood activity. Subsequently, a non–contrast-enhanced CT scan was obtained for attenuation

correction and anatomical localization of the PET signal. PET images were acquired for 10 min in 3-dimensional mode. The acquisition covered the area from the diaphragm to the iliac bifurcation. Image reconstruction was performed using a Fourier iterative algorithm, giving a final reconstructed slice thickness of 4.25 mm.

PET/CT Image Analysis

PET/CT data were analyzed by an experienced observer blinded to the histology and MRI results, using a GE Xeleris workstation. PET/CT outcome variables were maximum and average standardized uptake values (SUVs) values. SUVs were recorded on contiguous axial slices in the aorta, starting from the left renal artery and until the iliac bifurcation by drawing circular ROIs encompassing the whole visible vessel wall. An average of 15 slices per animal was analyzed. The average maximum and mean SUV (SUV $\overline{max}$ and SUV $\overline{mean}$) per animal were used in the statistical analysis.

Anatomical and Dynamic Contrast Enhanced MRI

Rabbits were imaged using a 1.5 Tesla clinical MRI system (Siemens Sonata, Siemens Medical Solutions) using a conventional knee coil for signal reception. T1, T2 and proton density (PD) weighted images were acquired from the left renal artery to the iliac bifurcation to characterize atherosclerotic plaques[17]. DCE-MRI was acquired on one selected axial slice using a black blood turbo spin echo (TSE) after injection of 0.2 mmol/kg of Gd-DTPA (Magnevist®). This sequence has been previously validated against histology and demonstrated excellent reproducibility[14,15,17].

Anatomical multi-contrast(MC)-MRI and DCE-MRI Analysis

The average vessel wall area (VWA) was quantified by manual tracing of the vessel wall contours on contiguous T2-weighted slices of the aorta between the left renal artery and iliac bifurcation using VesselMass software (Leiden University Medical Center).

DCE-MRI data were analyzed using a custom made Matlab (The MathWorks) software. The area under the signal intensity versus time curve (AUC) of an ROI encompassing the whole aortic wall visible in the slice acquired at 1 and 2 minutes after contrast agent injection was calculated[17]. All MRI and DCE-MRI measurements were performed by independent operators blinded to the results of PET and immunohistology.

Statistical Power

Prior to begin of the study we performed calculations for the sample size for FDG-PET/CT imaging on data available from our group[16.] We obtained the statistical standard deviation for SUV max- values pre- and post- treatment (± 0.03 and ± 0.1, respectively) and the observed treatment effect (reduction in SUV of about 28%). Based on this data and other published data in rabbit[18], we estimated a 25% to 30% reduction in SUV for our study. The resulting sample size was between n = 3 and n = 4, to have 80% power to detect a difference based on a 2-sample paired t-test (2-sided) with 1-beta (power) = 80% power and alpha = 5%. We also took into account data from a human FDG-PET/CT reproducibility study[19]. Based on this data and a 25-30% estimated therapeutic effect, the sample size is between n = 5 to n = 7, to have 80% power to detect a difference based on a 2-sample paired t-test (2-sided) with 1-beta (power) = 80% power and alpha = 5%.

In terms of DCE-MRI, we based the sample size calculation on a reproducibility study in the same animal model used herein[17]. We assumed a similar reduction for AUC as for SUV of about 25%-30% upon treatment. The resulting sample size is between n = 5 to n = 7, to have 80% power to detect a difference based on a 2-sample paired t-test (2-sided) with 1-beta (power) = 80% power and alpha = 5%.

Statistical analysis - Linear mixed model

Continuous DCE-MRI and PET/CT outcomes were modeled as linear functions of time by using a linear mixed model. This approach allowed estimating the regression equation for each group, while accounting at the same time for the correlation between repeated measurements in each rabbit over time. In the case of PET outcomes, the models were weighted by the number of slices analyzed in each animal. In addition we tested for differences among the slopes of treatment and control groups estimated by linear regression equations by including an interaction term between treatment group and time was included in each mixed model along with both main effects. If the interaction term was found to be statistically significant then pair-wise comparisons of treatment group slopes were estimated. To adjust for multiple comparisons we used the Bonferroni-Holm step down procedure[20]. All statistical analyses were performed using Proc Mixed in SAS Version 9.2[21]. All histological data, animal characteristics data and non-linear regression imaging data were analyzed with a 2-tailed Student-t-test. Numeric values are expressed as mean ± SD. P-values < 0.05 were considered significant.

RESULTS

Animal characteristics and serum analysis

All animals exhibited significantly elevated total cholesterol levels after 4 months of high-fat diet (**Table 1**). Total cholesterol level of control and R211945 treated groups did not change whereas the atorvastatin group showed a reduction of 33% at 1 month and 34% at 3 months of treatment compared to baseline (**Table 1**). Weight and non-fasting triglycerides were not different between the groups (**Table 1**). Therapeutic plasma levels of both R211945 and atorvastatin were detected at 1- and 3 months by mass spectrometry (data not shown).

	control (n = 6)	Atorvastatin (n = 6)	R211945 (n = 6)	p-value (c/A)	p-value (c/R)
weight, kg					
t = 4 months	3.42 +/- 0.33	3.51 +/- 0.22	3.49 +/- 0.21	0.59	0.63
t = 5 months	3.48 +/- 0.31	3.47 +/- 0.33	3.48 +/- 0.26	0.95	0.97
t = 7 months	3.50 +/- 0.30	3.62 +/- 0.34	3.60 +/- 0.21	0.49	0.49
total Cholesterol (mg/dl)					
t = 4 months	1,099 +/- 315	1,278 +/- 196	1,228 +/- 223	0.41	0.49
t = 5 months	1,158 +/- 282	850 +/- 433	1,187 +/- 169	0.11	0.85
t = 7 months	1,124 +/- 200	843 +/- 270	1,119 +/- 142	0.04*	0.97
triglycerides (mg/dl)*					
t = 4 months	184 +/- 110	180 +/- 198	163 +/- 75	0.97	0.79
t = 5 months	113 +/- 95	163 +/- 80	129 +/- 102	0.41	0.82
t = 7 months	172 +/- 163	161 +/- 88	158 +/- 89	0.91	0.87
glucose (mg/dl)					
t = 4 months	140 +/- 27	121 +/- 12	156 +/- 41	0.23	0.49
t = 5 months	178 +/- 40	169 +/- 41	182 +/- 52	0.68	0.87
t = 7 months	180 +/- 47	201 +/- 53	173 +/- 27	0.48	0.81
insulin (mg/dl)					
t = 4 months	0.58 +/- 0.38	0.42 +/- 0.18	0.47 +/- 0.37	0.48	0.72
t = 5 months	0.28 +/- 0.06	0.38 +/- 0.13	0.29 +/- 0.13	0.14	0.85
t = 7 months	0.21 +/- 0.14	0.27 +/- 0.04	0.23 +/- 0.06	0.43	0.83

Table 1. Animal Characteristics. Fasting values for: total cholesterol, triglycerides*, glucose and insulin and weight for the control (c), atorvastatin (A) and R211945 (R) groups. P-values between the control and atorvastatin and R211945 groups are shown in a separate columns. Individual data except p-values are represented as means ± standard deviation. *= nonfasting.

R211945 regresses inflammation and atorvastatin arrests inflammation progression assessed by ^{18}F-FDG-PET/CT

Upon completion of baseline ^{18}F-FDG-PET/CT imaging, animals were divided into three matched groups (control, atorvastatin and R211945) and subsequently imaged at 1 and 3 months (**Figure 2**). The individual groups displayed similar baseline average SUV $\overline{max}$ (0.64 ± 0.05, 0.63 ± 0.09, and 0.64 ± 0.09, respectively) and identical SUV $\overline{mean}$ (0.54 ± 0.05, 0.54 ± 0.09, and 0.54 ± 0.08, respectively) (**Figure 2 and scatter plots**). By using a linear mixed model and adjusting for multiple comparison we found that SUV values of control animals showed significant difference compared to R211945 treated animals at 3 months after therapy initiation for both SUV $\overline{max}$ (p = 0.0007) and SUV $\overline{mean}$ (p = 0.0001). Upon treatment, the SUV versus time slope for the R211945 treatment group was negative and statistically different from zero for both SUV $\overline{max}$ and SUV $\overline{mean}$ (p = 0.001 and p = 0.0009, respectively) indicating regression. In comparison, SUV $\overline{max}$ and SUV $\overline{mean}$ versus time slopes for the atorvastatin treatment group were not statistically different from zero (p = 0.60 and p = 0.37 respectively), indicating halting of progression. In contrast, the SUV versus time slope for the control group was positive, SUV $\overline{max}$ (p = 0.04) and $\overline{mean}$ (p = 0.01), indicating progression. A significant difference of the slopes of R211945 with control for both SUV $\overline{max}$ (p = 0.0004) and SUV $\overline{mean}$ (p < 0.0001) was detected. **Figure 2, bottom** shows scatter plots and the SUV versus time slopes. There was a significant interaction between time and group (p = 0.0016 for SUV $\overline{max}$; p = 0.0003 for SUV $\overline{mean}$).
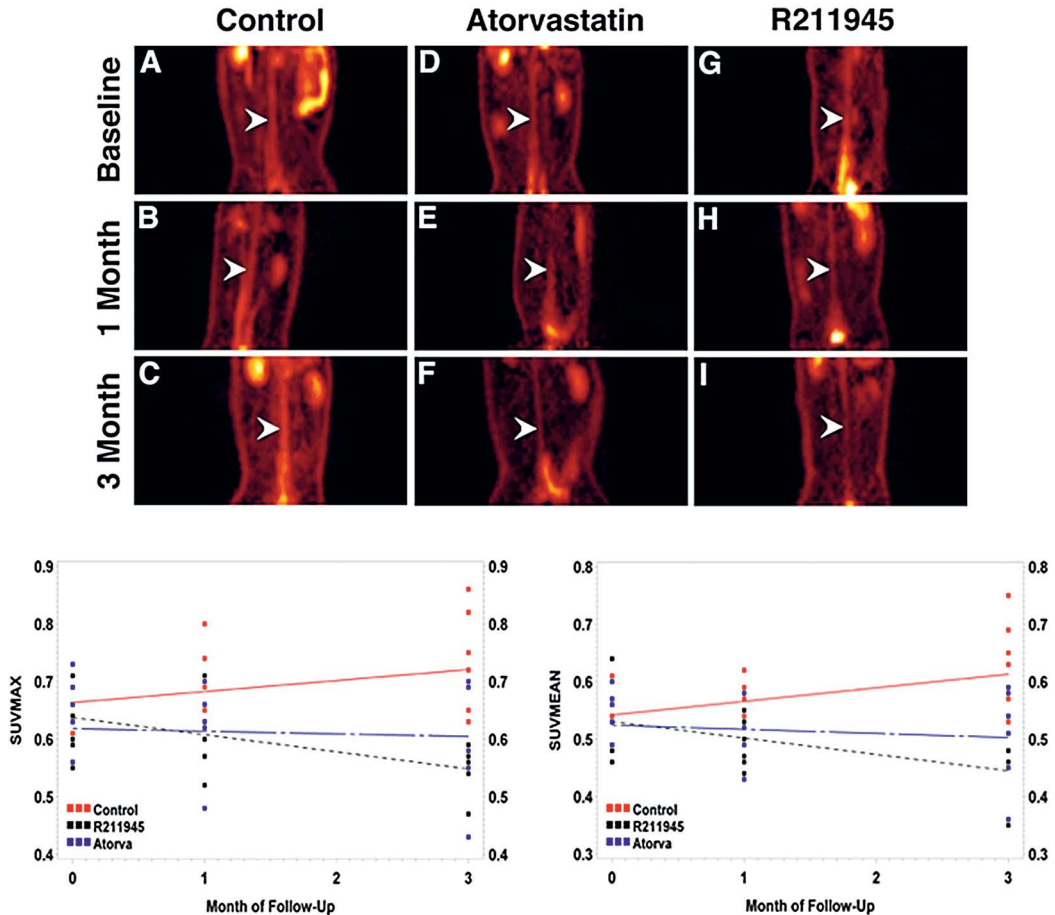
Figure 2. FDG-PET/CT. Coronal PET images through the abdominal aorta (white arrowheads) from one representative animal per group (**A-I**). Figure (**A**), (**D**), and (**G**), baseline all groups (control, atorvastatin and R211945, respectively). Figure (**B**), (**E**), and (**H**), 1-month all groups. Figure (**C**), (**F**), and (**I**), 3-month all groups. Bottom, summary showing scatter plots and SUV versus time slopes.

R211945 does not change neovascularization whereas atorvastatin shows a trend towards a decrease in neovascularization assessed by DCE-MRI

Figure 3 shows AUC maps from one representative rabbit from each group and the mean AUC 1 min values over time. **Figure 3 bottom**, the AUC versus time slopes for the R211945 group was negative but not statistically different from zero ($AUC_{1\ min}$, p = 0.14; $AUC_{2\ min}$, p = 0.10). The AUC versus time slope for the atorvastatin treatment group was negative and trended towards a significant difference from zero ($AUC_{1\ min}$, p = 0.06; $AUC_{2\ min}$, p = 0.06). The AUC versus time slope for the control group was not statistically different from

zero for AUC measures ($AUC_{1\,min}$, p = 0.40; $AUC_{2\,min}$, p = 0.20). There was no significant interaction between time and group (p = 0.6350 for $AUC_{1\,min}$; p = 0.8011 for $AUC_{2\,min}$).
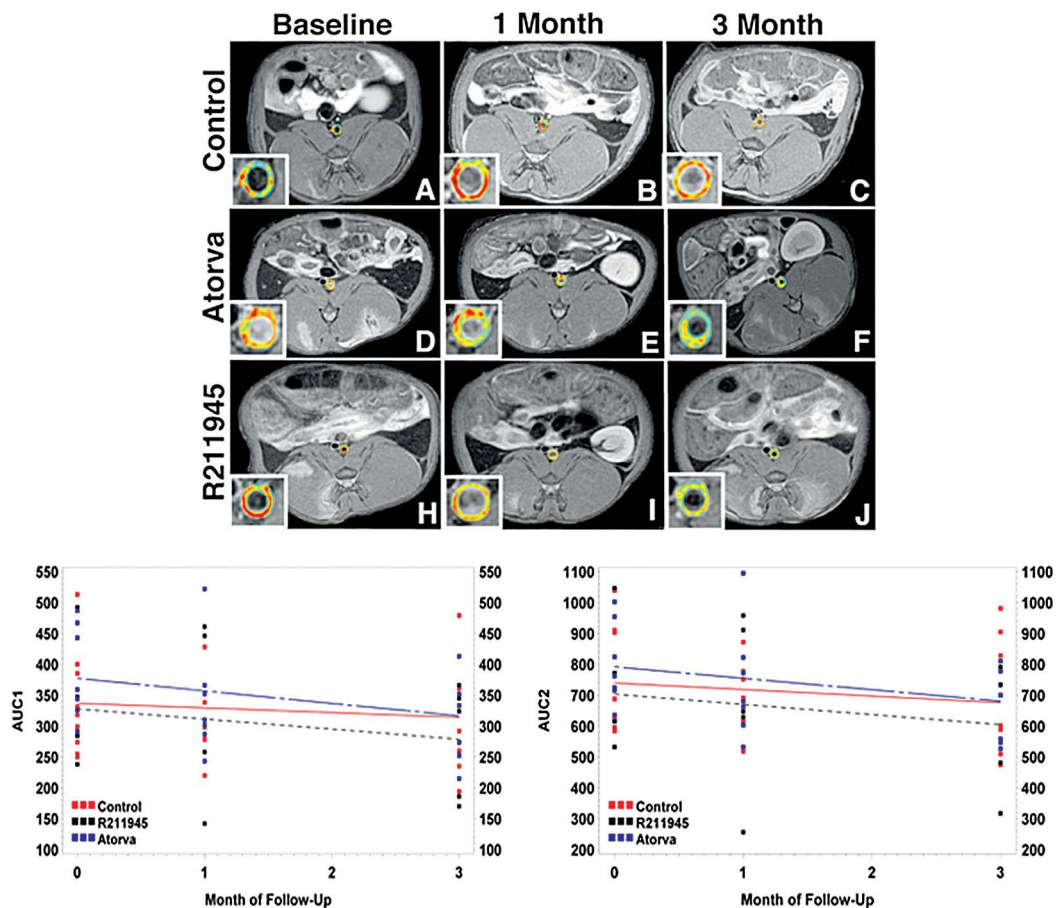

Figure 3. Dynamic-contrast-enhanced MRI. Single slice axial T1 weighted MRI images with color encoded overlay of the contrast signal at one minute of the abdominal aorta with insert of the aorta (**A-I**). (**A**), (**D**), and (**G**) baseline, all groups (control, atorvastatin (Atorva) and R211945, respectively). (**B**), (**E**), and (**H**), 1-month all groups. (**C**), (**F**), and (**I**), 3-month all groups. Warm colors (orange to red) indicate higher AUCs; cold colors (green to blue) indicate lower AUCs. **Bottom**, summary showing scatter plots and AUC versus time slopes.

R211945 and atorvastatin have no effect on vessel wall area as assessed by MC-MRI

Multi-contrast MRI revealed no significant changes in aortic wall area in either group (**Figure 4**).
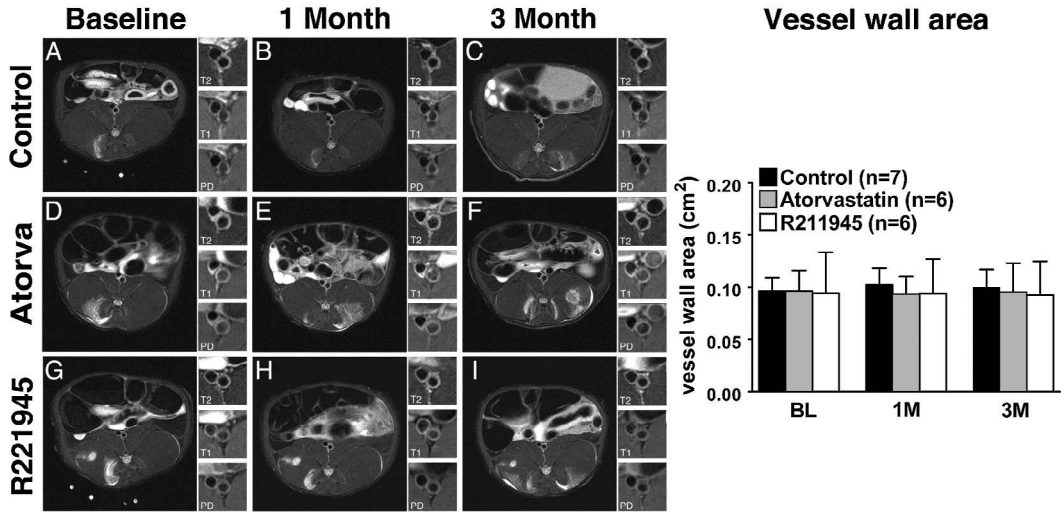
Figure 4. Multi-contrast-MRI. Single slice axial T2 weighted representative MRI images with insert of the aorta with T2-, T1- and Proton Density (PD)-weighing (**A-I**). (**A**), (**D**), and (**G**), baseline all groups (control, baseline atorvastatin (Atorva) and baseline R211945, respectively). (**B**), (**E**), and (**H**), 1-month all groups. (**C**), (**F**), and (**I**), 3-month all groups. Right, bar graph summary. Values are mean ± standard deviation.

R211945 and atorvastatin decrease macrophages, apoB and oxidized phospholipids in plaque

Aortic tissue analysis of the individual groups (**Figure 5** and **6**) showed a significantly lower macrophage density within the R211945 and atorvastatin group compared to control (0.22 ± 0.009, 0.217 ± 0.02 and 0.32 ± 0.009, (a.u.), respectively; $p < 0.0001$ and $p = 0.0004$, respectively) was observed. A significant lower apolipoprotein B density was detected in the R211945 and atorvastatin group compared to control (0.25 ± 0.05, 0.26 ± 0.07 and 0.33 ± 0.03 (a.u.), respectively; $p = 0.01$ and $p = 0.04$, respectively). R211945 treatment resulted in a 42% reduction in oxidized phospholipid density compared to control (0.076 ± 0.026 and 0.146 ± 0.045 (a.u.), respectively, $p = 0.02$) whereas atorvastatin treatment led to a reduction of 23% in oxidized phospholipid density (0.106 ± 0.026, $p = 0.08$ vs control). Average smooth muscle actin density was very similar between the R211945, atorvastatin and, control group (0.24 ± 0.075, 0.26 ± 0.078 and 0.27 ± 0.078 (a.u.), respectively; $p = 0.36$ and $p = 0.23$, respectively vs control). A trend towards lower neovessel content was observed in the R211945 and atorvastatin treated groups ($p = 0.12$ and $p = 0.12$, respectively vs control).
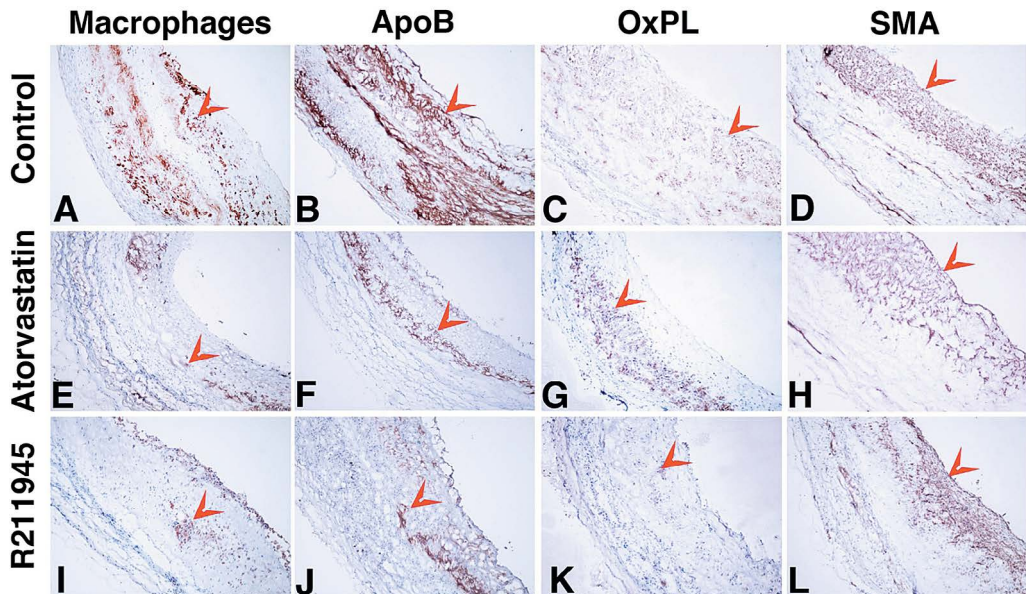
Figure 5. Representative immunohistological images of individual groups of the abdominal aorta at 3 months. Staining (red-brown, red arrowheads) for macrophages (Mac; **A,E,I**), apolipoprotein B (ApoB; **B**,**F,J**), oxidized phospholipids (OxPL; **C,G,K**) and smooth muscle actin (SMA; **D,H,L**) are shown. Objective magnification: 10x. The lumen is on the right hand side from the tissue.
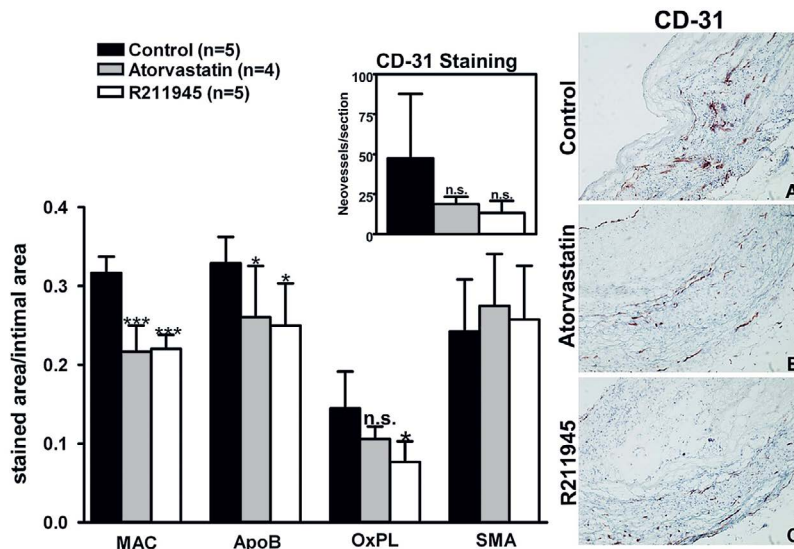

Figure 6. Summary Immunohistology. Left hand side, Macrophages (Mac), apolipoprotein B (ApoB), oxidized phospholipids (OxPL) and smooth muscle actin (SMA) staining at 3 months of control, atorvastatin and R211945 treated animals. Insert shows CD-31 staining for neovessels (individual p-values between control and treatment group are indicated). Right hand side, representative histological images after CD-31 staining for neovessels; control (**A**), atorvastatin (**B**) and R211945 (**C**). All values are means ± standard deviation; *P0.05, ***p < 0.001 and n.s. = non significant; control vs treatment groups.

SUV correlates with tissue macrophage content and AUC correlates with neovascularization

We found a strong positive correlation between maximal SUV and macrophages (r^2 = 0.86, p < 0.0001) and between AUC_{1min} and neovessels (r^2 = 0.51, p = 0.004) (**Figure 7AB**) consistent with previous studies[14,15].
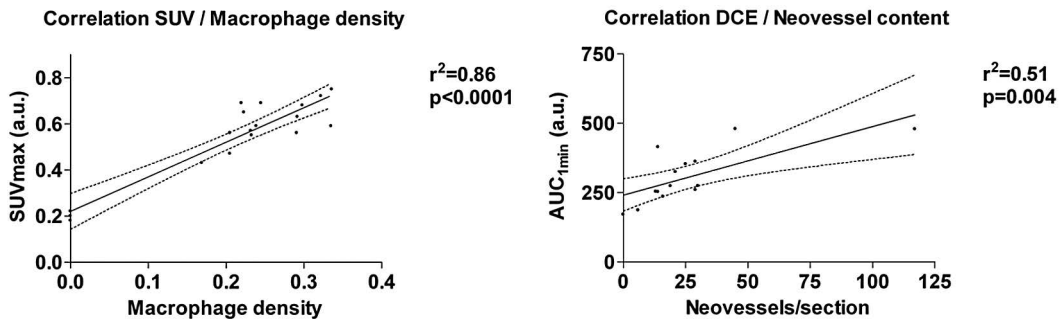

Figure 7. Correlation between average maximal standard uptake value (SUV) generated from FDG-PET/CT imaging and macrophage density (stained area/intimal area) from histological staining (**A**). Correlation between mean AUC_{1min} generated from DCE-MRI imaging and neovessel count per histological section (**B**). Black line, regression line; dashed line, 95% confidence interval.

R211945 induces ABCA1 expression

We evaluated ABCA1 expression, as the major LXR agonist target, for all groups (**Figure 8**). R211945 treatment lead to an increase in ABCA1 expression in peripheral blood of 101% at 1 month (p = 0.007 vs control) and 88% at 3 months (p = 0.01 vs control) whereas atorvastatin treatment led to a decrease of 17% at 1 month (p = 0.36 vs control) and 30% at 3 months (p = 0.01 vs control), consistent with previous studies[22,23]. Vehicle treatment did not result in an increase in ABCA1 expression.
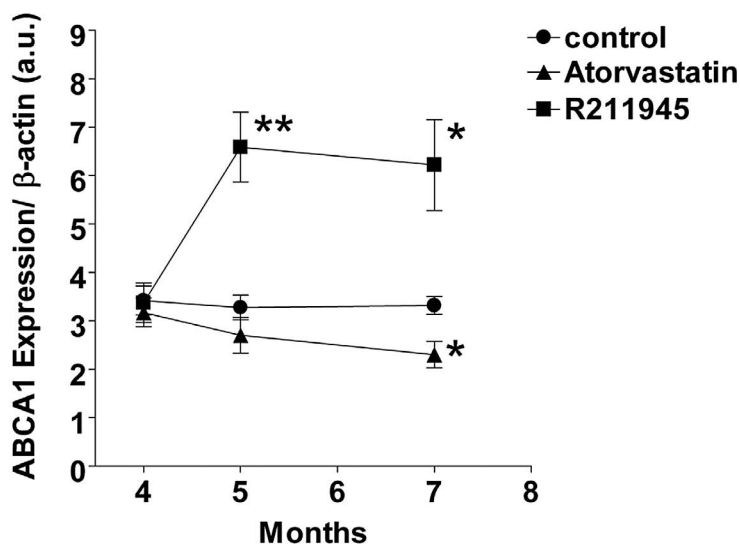
Figure 8. ABCA1 RNA expression in peripheral blood relative to β-actin at baseline (total 4 month), 1 month (total 5 month) and 3 month (total 7 month); *p < 0.05, **p < 0.01 control vs treatment group.

DISCUSSION

We demonstrate that the LXR-agonist-R211945 significantly regresses inflammation in plaques of atherosclerotic rabbits as quantified by ^{18}F-FDG-PET/CT. We observed, furthermore, with DCE-MRI a trend towards a decrease in neovascularization upon treatment with atorvastatin. The imaging results herein were confirmed by histological analysis and correlation assessment between imaging parameters and tissue macrophage density and neovessel content, respectively.

The potential to non-invasively monitor plaque inflammation and its changes following therapeutic intervention by ^{18}F-FDG-PET/CT and DCE-MRI has been shown in multiple studies[24-26]. We have recently demonstrated in the same animal model used herein the capability of both imaging modalities, ^{18}F-FDG-PET/CT and DCE-MRI, to assess reduction in inflammation and neovascularization upon pharmacological intervention[14,16]. Atorvastatin treatment lead in the current study to an arrest in increase of FDG uptake whereas R211945 induced a significant decrease of FDG uptake over time.

Histological analysis, revealed a similar macrophage density in both, the R211945- and atorvastatin group whereas only the R211945 group showed a significant decrease of SUV-values which was surprising as one would expect a lower macrophage content in the R211945 group given the observed reduction of SUV. One potential interpretation is a difference in the inflammatory state of the residual vessel wall macrophages as FDG uptake by macrophages is closely linked to their state of activation[26]. Interestingly, we observed a larger magnitude of oxidized phospholipid reduction in the R211945 group compared to the atorvastatin group. Lipid oxidation in plaque occurs partially through direct action of activated macrophages[27]. Furthermore, effects on smooth muscle cells, endothelial cells, T-cells and modulation of hypoxia may have been induced by R211945 leading to a more pronounced decrease in SUV-values as compared to atorvastatin[28].

Non-invasive DCE-MRI, demonstrated a trend in reduction of neovasculature in the atorvastatin group. Our results are consistent with human and animal studies where atorvastatin treatment results in neovessel regression via suppression of VEGF[29,30]. This result is, furthermore, consistent with our previous study where a trend for reduction in neovasculature upon treatment with the PPAR-γ-agonist pioglitazone was observed[14]. PPAR-γ-agonists, similar to statins, decrease neovascularization[31]. In contrast, the R211945 treated group did not show a significant reduction in neovasculature. The short-term application of an LXR-agonist, in contrast to atorvastatin and pioglitazone, has been shown to induce VEGF[32]. The pathophysiological role of LXR-induced VEGF is unclear at the moment. VEGF, however, is not only important in angiogenesis but is critical for the resolution of injury[33]. In addition, we did not assess VEGF or target tissue VEGF-receptor expression directly in our study and, therefore, cannot conclusively determine the effects of the LXR-agonist on VEGF.

Both atorvastatin and R211945 treatments did not reach statistical significance in for both the imaging and histological parameters which can be explained by the magnitude of the observed drug effect and the resulting power from the current sample size.

A potent induction of ABCA1 was observed in the R211945 treatment group. The previously described triglyceride increase by LXR agonists was absent in our study. Preliminary data demonstrate that R211945 preferentially acts on vasculature versus liver and shows, furthermore, selective nuclear co-factor

recruitment thereby limiting transactivation of lipogenic genes and as a result avoiding hepatic and metabolic side effects.

From an imaging standpoint, we show the capabilities of FDG-PET/CT and DCE-MRI to track non-invasively therapeutic intervention in atherosclerotic disease. This study supports the complementary role in future clinical applications of the two imaging techniques given the established correlation between ^{18}F-FDG-PET and DCE-MRI with macrophages/ inflammation and neovasculature, respectively.

Conclusions
In summary, we demonstrate the induction of regression of atherosclerosis in a rabbit model of atherosclerosis by an LXR-agonist without causing lipogenic side effects. 18F-FDG PET/CT and DCE-MRI were used in this study as markers of vascular macrophage content/inflammation and neovascularization. Both imaging techniques are non-invasive and clinically available and this study has, therefore, direct implications for the future assessment of interventions in atherosclerotic disease.

Disclosures
Tatsuo Tanimoto, Karen Brown and Masakatsu Kotsuma are employees of Daiichi Sankyo Inc.

REFERENCES

1. Dahlöf, B., *Amer. J. Cardiol.* 105:3A-9A (2010).
2. Steinberg, D. & Witztum, J.L., *Arterioscler. Thromb. Vasc. Biol.* 30, 2311-6. (2010).
3. Tsimikas, S., et al. *Curr. Pharm. Des.* 17, 27-37 (2011).
4. Ross, R., *N. Engl. J. Med.* 340, 115-126 (1999).
5. Hansson, G, K., *Atherosclerosis* 202, 2-10 (2009).
6. Libby, P., *J. Am. Coll. Cardiol.* 46, 1225-8 (2005).
7. Natarajan, P., et al. *J. Am. Coll. Cardiol.* 55, 1283-1299 (2010).
8. Gordon D., et al. *Circulation* 79, 8-15 (1989).
9. Tall, A.R., *Journal of Internal Medicine* 263, 256-273 (2008).
10. Venkateswaran, A., et al. *PNAS* 97, 12097-12102 (2000).
11. Calkin, A.C, and Tontonoz, P., *Arterioscler. Thromb. Vasc. Biol.* 30, 1513-1518 (2010).
12. Naik, S.U., et al. *Circulation* 113, 90-97 (2006).
13. Fievet, C., et al. *Biochem. Pharmacol.* 77, 1316-27 (2009).
14. Vucic, E., et al. *JACC Cardiovasc. Imaging* 4, 1100–1109 (2011).
15. Calcagno, C., et al. *Arterioscler. Thromb. Vasc. Biol.* 28, 1311-1317 (2008).
16. Lobatto, M.E., et al. *Mol. Pharm.* 7, 2020-2029 (2010).
17. Calcagno, C., et al. *Journal of Magnetic Resonance Imaging* 32, 191-198 (2010).
18. Ogawa, M., et al. *J. Nucl. Med.* 47, 1845 (2006).
19. Rudd, J.H., et al. *J. Am. Coll. Cardio.l* 50, 892-896. (2010).
20. Holm, S., *Scandinavian Journal of Statistics* 6, 65-70 (1979).
21. Littell, R.C., et al. *SAS System for Mixed Models*. Cary, NC: SAS Institute Inc., 1996.
22. Beyea, M.M., *J. Biol. Chem*. 282, 5207-5216 (2007).
23. Sone, H., et al. *Biochem. Biophys. Res. Commun*. 316, 790-4 (2004).
24. Ishii, H., *Clin. Ther.* 32, 2337-2347 (2011).
25. Tahara, N., et al. *J. Am. Coll. Cardiol.* 48, 1825-1831 (2006).
26. Mamede, M., et al. *Neoplasia* 7, 369-379 (2005).
27. Miller,Y.I., *Subcell. Biochem.* 51, 229-251 (2010).
28. Folco, E.J., et al. *J. Am. Coll. Cardiol.* 58, 603-14 (2011).
29. Alber, H.F., et al. *J. Am. Coll. Cardiol.* 39, 1951-5 (2002).
30. Bot, I., et al. *Atherosclerosis*; 214, 295-300 (2011).
31. Panigrahy, D., et al. *J. Clin. Invest.* 110, 923-32 (2002).
32. Walczak, R., et al. *J. Bio.l Chem.* 279, 9905-11 (2004).
33. Hoenig, M.R., et al. *Curr. Drug. Targets* 9, 422-35 (2008).

Chapter 10

Discussion

In this thesis imaging approaches ranging from preclinical nanoparticular and molecular imaging agents for MRI and CT for the detection of inflammatory plaque characteristics and markers of vulnerable plaques to clinically applicable imaging approaches for detection of inflammation using PET and MRI were presented.

Each imaging approach has potential advantages and limitations. MRI based approaches combine the high tissue contrast without radiation exposure and relatively high sensitivity with the use of nanoparticular contrast agents. The here presented, and for that matter, nanoparticular contrast agents for molecular MRI and CT, in general could prove difficult to translate to clinical applications[1]. A major limitation is the cost, which is partially related to expensive synthesis and the relatively high doses that need to be applied. Additionally, there are toxicity concerns which may further limit the use of nanoparticles as diagnostic agents[2]. These limitations could be overcome with further improvement in, sensitivity, safety, and cost[1]. In the near term, however, inflammation targeting nanoparticular agents could find application as therapeutic agents - so-called nanomedicines[3]. Indeed, analogs of the here introduced HDL nanoparticles have been successfully applied as therapeutic agents targeting inflammation in atherosclerosis[4-6]. Multiple other pre-clinical studies have been undertaken using nanomedicines to treat inflammation in atherosclerosis with promising results[7].

The here presented FDG-PET imaging approach to monitor therapeutic interventions has been successfully applied in multiple human trials[8]. It was used either in parallel with outcomes trials as well as more interestingly as a surrogate marker for therapeutic efficacy[9]. DCE-MRI was used together with FDG-PET to assess changes in inflammation in this thesis. Overall, it demonstrated lower sensitivity to detect changes of inflammation upon therapeutic intervention when compared to FDG-PET. This finding could to be related to the fact that each method measures different aspects of vascular inflammation[10]. Recent, technological advancements, however, could increase the sensitivity of DCE-MRI and, therefore, further enhance its capabilities for monitoring therapeutic interventions[11]. Currently, repeated radiation exposure

limits the widespread use of PET for the longitudinal monitoring of patients with atherosclerotic risk factors or established disease. The recent advent of hybrid PET/MRI, however, already decreases radiation exposure when compared to PET/CT. Near term, technological advancements are predicted to lead to additional dose reduction[12]. This could pave the way for longitudinally imaging in cardiovascular disease and thereby improve risk - and therapeutic response assessment.

The clinical effectiveness with reduction of ischemic events through IL1-β inhibition with canakinumab in the CANTOS (Canakinumab Anti-Inflammatory Thrombosis Outcome Study) trial has clearly established inflammation as a distinct therapeutic target in atherosclerosis[13]. IL1-β inhibition itself may not be clinically translatable as it has too many unwanted collateral effects e.g. increase in fatal infections. Given the extensive list of factors and different immune cells that promote inflammation in atherosclerosis, there are a plethora of potential therapeutic targets. Current molecular imaging of inflammation with multiple clinical available PET agents appears to be poised to provide valuable information to select the best drug targets and novel more specific tracers and techniques will further refine this technique in the future. Already, the clinically available agents FDG and NaF provide differential aspects of atherosclerotic plaque biology and inflammation and may, therefore, add to the understanding of atherosclerosis disease progression and risk[14]. Novel more specific imaging probes are in development and recently an activated macrophages specific probe has been described[15]. Apart from novel imaging probes artificial intelligence applying machine and deep learning has been introduced to analyze atherosclerotic plaques from data generated from routine coronary Computed Tomography Angiograms (CTA)[16]. This so called coronary CTA radiomics approaches reveal vast information about atherosclerosis plaque features that are present on routine coronary CTA scans but hidden from visual detection. In general, radiomics obtains quantitative metrics of spatial and textual properties from radiological images to create big-data datasets. It generates many, hundreds or more, different parameters per region of interest. From the dataset novel analytical methods using data mining can be applied to identify correlation between the derived parameters and clinical or outcome data. This technique has been shown to identify complex plaque morphologies on coronary CTA datasets[17]. Most recently, coronary CTA radiomics was compared against NaF-PET, invasive intravascular ultrasound (IVUS), and optical coherence tomography (OCT) to identify plaque markers of vulnerability[18]. In this study coronary CTA radiomics identified invasive and PET imaging markers of

plaque vulnerability and was superior to current clinical quantitative markers of plaque vulnerability. Similar to the radiomics approach with coronary CTA quantitative radiomics approaches have been undertaken with cardiovascular MRI[19]. T1- and T2 mapping radiomics to characterize atherosclerotic high risk plaque features and detect myocardial inflammation have been successfully applied, recently[20,21]. Both, CT and MRI radiomic techniques could reveal complex plaque pathobiology with current clinical imaging techniques without the need for inflammation targeted contrast agents. This could lead to a more comprehensive population based assessment and ultimately improved prevention and treatment strategies.

Imaging of inflammation may have targets beyond the vasculature itself. As outlined in the introduction, pro-inflammatory myelopoiesis is central to the atherosclerotic process[22-24]. Enhanced myelopoiesis activity was demonstrated in patients with chronic atherosclerosis[24] and the degree of metabolic activity/ inflammation in the bone marrow and particularly spleen correlates with acute- and future risk of adverse cardiovascular events[25,26]. Imaging of myelopoietic organs, immune cell trafficking (from the hematopoietic organs to the vasculature and egress out of the vasculature) and immune cell interconnection may, therefore, provide novel insights into the atherosclerotic process as well as the potential for more effective therapeutic approaches and preventive strategies[24,25,27-29].

The multiple levels at which the immune system participates in atherosclerosis and the multiple cellular interactions that take place constitute a challenge to selectively modulate the immune system where it promotes atherosclerosis while sparing the organisms general immune response capacity[30]. A major challenge is to identify the most specific targets in atherosclerosis[31]. This is underlined by the failure of the Cardiovascular Inflammation Reduction Trial (CIRT)[32] that tested low-dose methotrexate, a broad anti-inflammatory therapeutic, that, proved ineffective in reducing adverse cardiovascular events. It is, therefore, of critical importance to investigate the interplay of the systemic immune response with local vascular immune response in atherosclerotic plaques. This is an area where detail is still largely lacking[33]. Recently, atherosclerotic cell specific imaging approaches particularly large-scale time of flight cytometry (CyTOF) analysis, and cellular sequencing approaches such as Cellular Indexing of Transcriptomes and Epitopes by Sequencing (CITE-seq) and single-cell RNA sequencing (scRNA-seq) analysis have been introduced to study atherosclerotic plaques[33,34]. These large-scale diagnostic approaches have already revealed in much more detail the

composition of the atherosclerotic plaque microenvironment. A recent human study demonstrated differences in adaptive and innate immune system and immune dysregulation between stable and unstable carotid plaques[34]. Furthermore, differences between blood and plaque immune cell function were present.

Improved characterization of the plaque microenvironment will allow for the development of more specific imaging probes and inflammation targeting therapeutics. In oncology, the development of immune-imaging using molecular and nanoparticle probes has revolutionized cancer immune therapy by e.g. allowing real time assessment of therapeutic response, immune cell tracking and therapeutics delivery[35,36]. Immune imaging holds large potential for application in atherosclerosis as well, particularly if combined with therapeutic approaches[3]. Atherosclerosis, as a chronic maladaptive inflammatory condition constitutes a superb target for immune-modulatory therapies. Nanomedicines, currently, constitute the most advanced immune-modulatory therapeutic agents[37]. Ideally, immune-modulatory nanomedicines either as theranostics or sole therapeutic agents could target specific immune cells e.g. Macrophages, T cell, B cells or other immune cells as well as inflammatory mediators and elicit responses that are dependent on the microenvironment of individual atherosclerotic plaques or myelopoietic organ[7]. In other words the agents should be "smart". The elicited response, thereby, would be tailored to the inflammatory milieu of the individual plaque or organ. This approach would promise true precision medicine[38].

Altogether, imaging of inflammation in atherosclerosis will help to improve the detection of individuals at risk, help better characterize atherosclerosis pathobiology and lead to improved and personalized therapeutics and enable more effective early interventions and preventive strategies.

REFERENCES

1. Kiessling, F., et al. *Radiology* 273, 10–28 (2014).
2. Ajdary, M., et al. *Nanomaterials* 8, 634 (2018).
3. Mulder, W. J. M., et al., *Sci. Transl. Med.* 6, 239sr1–239sr1 (2014).
4. Duivenvoorden, R., et al. *Nat. Commun.* 5, 227 (2014).
5. Tang, J., et al. *Sci. Adv.* 1, e1400223 (2015).
6. Tang, J., et al. *PNAS.* 113, E6731–E6740 (2016).
7. Cervadoro, A., et al. *Front. Bioeng. Biotechnol.* 6, 177 (2018).

8.   Doris, M. K., Dweck, M. R. & Fayad, Z. A., *Curr. Opin. Lipidol.* 27, 605–614 (2016).
9.   Tarkin, J. M., Dweck, M. R. & Rudd, J. H. F., *Heart* 105, 567–578 (2019).
10. Calcagno, C., et al*. Eur. J. Nucl. Med. Mol. Imaging* 40, 1884–1893 (2013).
11. Wüst, R. C. I., et al. *Arterioscler. Thromb. Vasc. Biol.* 39*,* 841–849 (2019).
12. Robson, P. M., et al. *JACC Cardiovasc. Imaging* 10, 1165–1179 (2017).
13. Ridker, P. M., et al*. N. Engl. J. Med.* 377, 1119–1131 (2017).
14. McKenney-Drake, M. L., et al. *Eur. J. Nucl. Med. Mol. Imaging* 45, 2190–2200 (2018).
15. Park, S.-J., et al*. Nat Commun.* 10, 1111–7 (2019).
16. Kolossváry, M., et al*. J. Thorac. Imaging* 33, 26–34 (2018).
17. Kolossváry, M., et al*. Radiology* 293, 89–96 (2019).
18. Kolossváry, M., et al*. Eur. Heart J. Cardiovasc. Imaging* 20, 1250–1258 (2019).
19. Leiner, T., et al. *J. Cardiovasc. Magn. Reson.* 21, 61–14 (2019).
20. Shi, Z. et al. *Eur Radiol* 28, 3912–3921 (2018).
21. Baessler, B., et al*. Radiology* 289, 357–365 (2018).
22. Murphy, A. J. & Tall, A. R., *Eur. Heart J.* 37, 1113–1121 (2016).
23. Chistiakov, D. A., et al *J. Cell. Mol. Med.* 22, 1366–1382 (2018).
24. van der Valk, F. M., et al. *Eur. Heart J.* 38, 425–432 (2017).
25. Emami, H., et al. *JACC Cardiovasc. Imaging* 8, 121–130 (2015).
26. Kashiwazaki, D., *et al. J. Stroke Cerebrovasc. Dis.* 27, 3212–3217 (2018).
27. Vandoorne, K., *et al. Circ. Res.* 123, 415–427 (2018).
28. Nahrendorf, M., *et al. J. Am. Coll. Cardiol.* 65, 1583–1591 (2015).
29. Fayad, Z. A., et al. *J. Am. Coll. Cardiol.* 72, 2198–2212 (2018).
30. Wolf, D. & Ley, K., *Circ. Res.* 124, 315–327 (2019).
31. Zhao, T. X. & Mallat, Z., *J. Am. Coll. Cardiol.* 73, 1691–1706 (2019).
32. Ridker, P. M., *et al. N. Engl. J. Med.* 380, 752–762 (2019).
33. Clément, M. & Mallat, Z., *Cardiovasc. Res.* 114, 1306–1307 (2018).
34. Fernandez, D. M., *et al. Nat. Med.* 25, 1576–1588 (2019).
35. Mayer, A. T. & Gambhir, S. S., *J. Nucl. Med.* 59, 1174–1182 (2018).
36. Wang, P., *et al. Nanoscale Horiz.* 6, 24 (2020).
37. Duivenvoorden, R., *et al. Nat. Rev. Cardiol.* 16, 21–32 (2019).
38. Mulder, W. J. M. *et al. Acc. Chem. Res.* 51, 127–137 (2018).

Chapter 11

Curriculum Vitae

Esad Vucic was born on 16th November 1972, in Bar, Montenegro. His family moved to Germany when he was two years old. He grew up in Graben-Neudorf, Gechingen and Sindelfingen, all in the Southwest of Germany. After finishing an equivalent to a high school degree (German: Hochschulreife) in 1993 at the Mildred-Scheel-School in Böblingen in Germany, he studied Medicine at University of Leipzig and the Eberhard-Karls-University, Tübingen. His fascination for research let him to participate in ongoing research projects at the Department of Physiology at the University of Tübingen. He then continued his projects with a two month visiting clerkship at the Department of Physiology at Yale University, New Haven, USA. In 2002, he graduated from Medical University and upon graduation he continued the research that he had started during medical school with a postdoctoral fellowship at the Department of Physiology at Yale University. The research focused on cellular imaging techniques to study intracellular pH regulation and proton transport. The results of this research led to multiple presentation and a manuscript describing the proton and potassium exchange mechanism in gastric parietal cells. Upon completion of his postdoctoral fellowship, he started his medical training in internal medicine at SUNY Downstate, Brooklyn, New York and Mount Sinai St. Luke's & Mount Sinai West (formerly, St. Luke's Roosevelt), New York. His interest in research let him to procure research projects and because his ultimate goal was to become a cardiologist he reached out to Prof. Valentin Fuster at Mount Sinai Hospital whom he knew from a prior visiting clinical clerkship. Prof. Fuster referred him to Prof. Zahi Fayad where he felt his prior expertise in cellular imaging could be a good fit as the laboratory focused on translational and molecular imaging in cardiovascular disease. He then started to work in Prof. Fayad's laboratory, at the now, Biomedical Engineering and Imaging Institute, Icahn School of Medicine at Mount Sinai. There, he participated in various imaging projects focused on molecular imaging of atherosclerosis. His research was very productive despite him being a full time medical resident leading to several scientific presentations and co-autherships in multiple manuscripts. He, then, met Dr. Willem Mulder, now, Prof. Mulder, who joined the faculty at the Biomedical Engineering and Imaging Institute. Seeing his motivation for research, Prof. Mulder connected him to his former mentor Prof. Klaas Nicolay from Eindhoven

University of Technology to pursue a PhD in biomedical engineering. After he completed his residency in internal medicine in 2007, he joined Prof. Fayad's laboratory for full time research. At the same time from 2007 to 2012 he started a PhD project at Eindhoven University of Technology and the Icahn School of Medicine at Mount Sinai of which the results are presented in this dissertation. His work led to multiple publications and presentations at international conferences and to an investigator initiated grant from Takeda Pharmaceuticals. He continued his medical training in Cardiology from 2009 at the Mount Sinai Hospital, New York and in parallel completed his PhD research work and manuscripts. He then, furthermore, trained in Advanced Cardiac Imaging at the Massachusetts General Hospital in Boston and Cardiac Electrophysiology at New York University Langone Medical Center in New York. Since 2019, he is employed at the Newark Beth Israel Medical Center, Newark, New Jersey where he focuses on Advanced Cardiac Imaging.

Atherosclerosis is a chronic inflammatory disease that is triggered by the deposition of lipoproteins in the subendothelial space. Monocytes-macrophages are the principal immune cells within atherosclerotic lesions or "plaques" and both the innate and the adaptive immune system drive the disease process. Atherosclerosis is a slowly progressive sterile inflammatory disease that remains silent over long periods of time. Non–resolved inflammation through its destabilizing effects on atherosclerotic plaques triggers acute ischemic events leading to myocardial infarction and stroke. Both, are the principal causes of death worldwide and the incidence of atherosclerosis continues to increase despite effective lipid-lowering strategies. Currently, no effective diagnostic techniques exist to identify at highest risk individuals. Novel imaging approaches that allow assessment of inflammatory plaque activity could help risk stratify populations and identify who benefits most from preventive intervention, monitor therapy responses and identify the most promising therapeutic interventions. In this thesis, I will explore various imaging strategies from nanoparticular and small molecule-based MRI-and CT- contrast agents to detect inflammatory activity in atherosclerotic plaques as well as employ clinically applicable MRI and PET/CT imaging techniques to monitor the effects of therapeutic interventions on atherosclerotic plaque inflammation in atherosclerotic disease models.

TU/e EINDHOVEN UNIVERSITY OF TECHNOLOGY